Experiments with electrostatically trapped NO and N_2 molecules in high Rydberg states

Matthew Henry Rayment

Supervisor: *Prof. Stephen D. Hogan*

A thesis submitted for the degree of

Doctor of Philosophy

at

University College London.

Department of Physics and Astronomy

University College London

Wednesday 8th November, 2023

I, Matthew Henry Rayment, confirm that the work presented in this thesis is my own. Where information has been derived from other sources, I confirm that this has been indicated in the work.

Signature: _____

Date: _____

“The true delight is in the finding out rather than in the knowing”

Isaac Asimov

Abstract

In this thesis, nitric oxide (NO) and nitrogen (N_2) molecules, initially travelling in pulsed supersonic beams, have been laser photoexcited into long-lived Rydberg states in series that converge to selected rotational and vibrational states of the molecular cations. Molecules prepared in these excited states were subsequently guided, decelerated, and trapped, from an initial speed of 800 $\mathrm{m\,s^{-1}}$ in the laboratory-fixed frame of reference, using the travelling electric fields of a cryogenically-cooled chip-based Rydberg-Stark decelerator. Electrostatic trapping was achieved for up to 10 ms, and enabled the study of slow-decay processes of the long-lived Rydberg states these molecules over these previously inaccessible timescales. Measurements of the trap decay time constants, of the total population of trapped molecules, were made after excitation into Rydberg states with principal quantum numbers, n, between 32 and 50. For the experiments with NO, molecules were excited into Rydberg states converging to the $N^+ = 0$ to 6 rotational, and $v^+ = 0$ and 1 vibrational states of the $X^+\,^1\Sigma^+$ ground electronic state of the NO^+ cation. This allowed investigation of the effects of rotational and vibrational excitation on the decay dynamics of the long-lived Rydberg states. Although such rotational state selectivity was not possible in the excitation of the N_2 molecules to Rydberg states, long-lived Rydberg states converging toward the $v^+ = 0$ series limit were prepared and trapped in experiments, permitting comparison of the decay dynamics of long-lived Rydberg states of different species.

Impact statement

The work presented in this thesis represents the first experimental demonstration of the trapping of neutral NO and N_2 molecules. Additionally, these experiments extend the technique of Rydberg-Stark deceleration and trapping to species heavier than H_2 and He, through the use of a newly designed chip-based Rydberg-Stark decelerator. The electrostatic trapping of long-lived Rydberg states of NO and N_2 molecules has enabled the study of molecular Rydberg state decay processes on unprecedentedly long timescales of up to 10 ms, particularly when compared to the $\lesssim 10$ μs timescales on which the decay processes of these molecules had previously been studied, and allowed slow-decay processes to be observed. These results have therefore furthered the investigation of the physical properties of the atmospherically important NO and N_2 molecules, and demonstrated a means by which the motion of similar molecules could be controlled provided appropriate excitation schemes to long-lived Rydberg states are identified.

Acknowledgements

I wish to start by thanking my supervisor Prof. Stephen Hogan. During our discussions I have learned a lot from his vast array of knowledge on Rydberg atoms and molecules, and experimental Physics. In addition, his kindness, understanding, and willingness to give advice have been greatly appreciated over the course of my PhD. I would therefore like to thank him again for the opportunities he has given me during my time in the Rydberg group.

Also, during the PhD I have had the good fortune to meet and work with a large range of like-minded people in the Rydberg group. Although the working conditions in A27 cannot always be described as optimal, the presence of these people in this otherwise 'unusual' space has greatly enhanced my time during the PhD. The conversations on everything from Physics to music, the history of rounders, and plugs of world have significantly enriched these last four years, and resulted in me learning a lot in the process. I would therefore like to thank: Dr. Adam Deller, Dr. Alex Morgan, Dr. Klaudia Gawlas, Dan Walker, Jake Tommey, Luke Brown, Dr. Junwen Zou, Louise McCaul, Dr. Markus Fleck, Dr. Vincenzo Monachello, Mila Sedzielewski, and Julien Grondin.

Outside of the Rydberg group I would also like to thank Prof. David Cassidy. Both for the opportunity he gave me in my Masters year to undertake a project in his Positronium group, and more generally for the discussions, often in Housman, that I have had with him.

In addition, it has been a pleasure to know the members of the Positronium group during both my Masters year and PhD. They, along with the members of the Rydberg group, have contributed to the positive day-to-day experiences I have had

during my PhD. The trips made to the weekly food market, to play pool, and to pubs have all been highly enjoyable and appreciated, particularly during more stressful or busy times of the PhD. I therefore thank: Dr. Lokesh Gurung, Ross Sheldon, Dr. Tamara Babij, Sam Reeder, Rebecca Daly, and Dr. Don Newson.

For all of the 8 years I have been at UCL I have been involved with the UCL Jazz Society, particularly with their Big Band. In this time I have had the opportunity to perform in 18 shows, in venues ranging from the Jeremy Bentham Room to the Adelphi Theatre on the West End, and go on 3 short tours to Barcelona, Budapest, and Luxembourg. Furthermore, I was given the chance to learn how to arrange scores which were then performed in some of these shows, and organised two years' worth of summer gigs at the Print Room Café. All of this was only possible because of the kindness and inclusiveness of the people involved with the society, which has made being part of it such a pleasure, and I would therefore like to thank everyone I have met though it during my time at UCL. Similarly, I would like to thank the members of UCL Live Music Society I met through the society's Rhapsody showcase, and the members of the bands for UCL Musical Theatre Society's productions of Tick Tick Boom, American Idiot, and Legally Blonde, for the good times I had during these performances.

Lastly, and most importantly, I would like to thank my family for all the support and encouragement that they have given me throughout my PhD and more generally in life. It cannot be overstated how much this support has meant to me, and has been a significant factor in my ability to pursue my chosen path, even if it is Physics! I can do nothing more that express my immense gratitude for all that you have done for me.

Contents

1 Introduction **1**

2 Molecular Rydberg states **5**

2.1 General properties of Rydberg states 5

2.2 Rydberg states of diatomic molecules 7

2.2.1 Physical origin of intramolecular interactions 8

2.2.2 Decay processes of molecular Rydberg states 9

2.3 Previous experiments with Rydberg NO and N_2 molecules 11

2.3.1 NO 11

2.3.2 N_2 20

3 Stark effect **23**

3.1 Stark effect in atoms 23

3.2 Fluorescence lifetimes 26

3.3 Hund's angular momentum coupling schemes 30

3.4 Calculations of the Stark effect in Rydberg states of NO 32

3.4.1 Field-free Hamiltonian 33

3.4.2 Stark Hamiltonian 38

3.5 Lifetime calculations for NO 39

3.6 Calculations of the Stark effect in Rydberg states of N_2 43

4 Experimental techniques **47**

4.1 Principles of Rydberg-Stark deceleration 48

4.2 Experimental apparatus and methods 50

4.3 Numerical trajectory calculations 58

5 Trap decay measurements of $v^+ = 0$ Rydberg NO 63

5.1 Excitation scheme 63

5.2 State-dependent trap-decay rates of $v^+ = 0$ Rydberg NO molecules . 70

5.2.1 Experimental methods 70

5.2.2 Trap decay measurements 72

5.2.3 Decay rate measurements 81

5.2.4 Vibrational channel interactions 82

5.2.5 Rotational channel interactions 89

5.3 Conclusions 92

6 Vibrationally and rotationally excited Rydberg NO 95

6.1 Trap decay rates of vibrationally excited Rydberg NO 95

6.1.1 Experimental methods 95

6.1.2 Laser spectroscopy of $v^+ = 1$ Rydberg states 97

6.1.3 Trap decay rates 100

6.1.4 Deceleration and trapping field strengths 103

6.1.5 Vibrational autoionisation 105

6.2 Effects of rotational excitation on decay rates of Rydberg NO 108

6.2.1 Experimental methods 108

6.2.2 Results and discussions 110

6.3 Conclusions 119

7 Spectroscopy and electrostatic-trapping of Rydberg N_2 121

7.1 Ion-dip and photoabsorption spectroscopy of Rydberg states in N_2 . 122

7.1.1 Experimental methods 122

7.1.2 Excitation scheme 124

7.1.3 Results and discussions 126

7.2 Electrostatic-trapping Rydberg N_2 molecules 135

7.2.1 Experimental methods 135

7.2.2 Deceleration and trapping 136

7.2.3 Trap decay measurements 142
7.3 Conclusions 145

8 Conclusions and outlook **147**

Bibliography **153**

Chapter 1

Introduction

Cold and ultracold samples of diatomic molecules, and their ions, have a range of applications from tests of fundamental physics, to studies of chemical reactions at low temperatures. For example, cold and ultracold samples of polar molecules and molecular ions, such as ThO [1] and HfF^+ [2], have energy levels, and therefore transitions, that are sensitive to the electron electric dipole moment (eEDM). Precision measurements of these transitions enable limits to be placed on the value of an eEDM, which allows tests of "Standard Model" physics and its extensions [1–3]. Additionally, precision measurements of vibrational intervals in cold state-selected H_2, HD, D_2, and HD^+ have been used to constrain the strength of a "fifth force" [4], and proposals and measurements to place bounds on the time-dependence of fundamental constants, e.g., the proton-to-electron mass ratio, using transitions in molecules have been made [5–9]. Studies of inelastic and reactive collisions between molecules, or between atoms and molecules, have been performed with the aim of precisely measuring reaction potential energy surfaces and observing quantum effects such as tunnelling, resonant energy transfer, and the formation of exotic bound states [10–13].

To achieve low temperatures and long observation times for these types of studies, it is often necessary to control the motion of the molecules in the ground, or a long-lived excited, state. Molecules in states that possess non-zero electric dipole moments experience energy shifts in an external electric field. Forces can therefore be exerted on molecules in these states using inhomogeneous electric fields [14–

16]. Fields of this kind have been used to decelerate, and trap, "ground-state" polar molecules using multistage Stark decelerators [17, 18]. The first demonstration of the deceleration of a polar molecule was with CO in the metastable $a^3\Pi_1$ state using a Stark decelerator [19]. Similar deceleration and trapping experiments were also later performed using chip-based Stark decelerators [20, 21]. These techniques were also extended to decelerate other molecules, and enable crossed and merged beam collision experiments to be performed with high collision energy resolution [18]. Electrostatic trapping of polar molecules in metastable states allowed the decay time constants of these to be measured [18, 22]. Analogous techniques have been applied to prepare cold samples of paramagnetic molecules using inhomogeneous magnetic fields in multistage Zeeman decelerators [17]. In addition, optical based methods for the deceleration of ground state molecules have also been demonstrated [23–25]. However, for molecules with small or zero electronic or magnetic dipole moments, in the ground state, the methods of multistage Stark or Zeeman deceleration cannot be employed. In these cases excitation to Rydberg states, with large electric dipole moments, provides a potential means by which samples can be efficiently decelerated using inhomogeneous electric fields [17, 26].

The properties of Rydberg states of molecules, including their large electric dipole moments and their dependence on the characteristics of their molecular ion core, means that samples in these states are of interest in a range of research areas. For example, precision spectroscopy of Rydberg states of molecules has been used to measure properties of the parent neutral molecule [27–34]. In the case of H_2, Rydberg states were utilised in the precision measurement of the ionisation and dissociation energies [30], and of the ground state para- to ortho-H_2 energy interval [31], which allowed for tests of *ab inito* molecular structure calculations including effects of bound-state quantum electrodynamics [35, 36]. Similar measurements have also been performed for D_2 and HD [33, 34]. Spectroscopy of high-ℓ Rydberg states of molecules has also allowed the multipole moments of molecular ions to be inferred [37, 38].

Rydberg states of diatomic atmospheric molecules, including H_2, N_2, O_2, CO,

and NO, play a role in the physical and chemical dynamics of atmospheric and astrophysical plasmas, such as those found in the Earth's ionosphere, interstellar gas clouds, and comet tails [39–46]. The study of the properties and decay dynamics of Rydberg states of atmospheric molecules is therefore important in understanding recombination processes, including dissociative recombination, that involve Rydberg states [41, 47–49]. In the laboratory Rydberg molecules have been used to generate ultracold molecular plasmas [50, 51], the creation of which strongly depends on the decay dynamics of the excited Rydberg states [52, 53].

Molecules in Rydberg states are used in the state-of-the-art studies of chemical dynamics at low temperatures. This includes the study of ion-molecule reactions, such as the $H_2^+ + HD \rightarrow H_2D^+ + H$ and $H_2^+ + H_2 \rightarrow H_3^+ + H$ reactions, at collision energies < 100 mK [54–59], with observations of quantum capture and enhancement of these reaction rates at these low temperatures [59]. In these experiments, reactions occurred between the ion core of the Rydberg molecule and the neutral ground-state molecule, with the Rydberg electron shielding the reaction centre from heating by stray electric fields [54]. Rydberg states of small molecules also offer opportunities to explore the chemistry associated with ultra-long range Rydberg bimolecules, formed of a Rydberg molecule bound to a ground-state molecule through low-energy Rydberg electron scattering [13]. In addition, the excitation of Rydberg states in small molecules may offer opportunities to develop new laser based schemes for trace gas detection, in particular in the detection of trace amounts of NO [60, 61].

In many of the above research areas, it is desirable to prepare cold, velocity controlled or trapped samples of Rydberg molecules. This can be achieved by exerting forces on the excited molecules using inhomogeneous electric fields though the methods of Rydberg-Stark deceleration upon which this thesis is based. Prior to the work described here the only molecule for which Rydberg-Stark deceleration had been implemented was H_2 [17, 26, 62, 63], along with its isotopologues HD and D_2 [59, 64]. Deceleration and trapping of these and other Rydberg molecules enables; studies of slow decay dynamics of Rydberg states (including how they are

affected by intramolecular interactions), a means to perform low-temperature ion-molecule reactions in merged beam setups, and the possibility of preparing cold ground-state samples if the molecules are optically pumped back to the ground state following deceleration.

In this thesis, a brief background on Rydberg states of molecules, and examples of previous measurements performed with Rydberg states of NO and N_2, are given in Chapter 2. The Stark effect in atoms and diatomic molecules, specifically NO and N_2, is presented in Chapter 3. In Chapter 4, the principle of Rydberg-Stark deceleration, the experimental apparatus and techniques, and numerical trajectory calculations are described. Experiments that demonstrate the ability to prepare cold electrostatically-trapped samples of long-lived Rydberg-states of NO and N_2 molecules are described in Chapters 5 to 7. This enabled measurements of state-dependent slow-decay processes of these molecules from the trap, with the effect of rotational and vibrational excitation on these decays being investigated. Conclusions are drawn in Chapter 8.

Chapter 2

Molecular Rydberg states

2.1 General properties of Rydberg states

All neutral atoms and molecules possess Rydberg states, with their main distinguishing characteristic being that they consist of a highly excited electron in an orbital with a large principal quantum number, n, bound to an ion core by the Coulomb interaction. The energies of these states are given to first order by the Rydberg formula [65]

$$E_{n\kappa} = E_{\rm ion} - \frac{hcR_{\rm M}}{(n-\mu_\kappa)^2}, \tag{2.1}$$

where $E_{\rm ion}$ is the energy associated with the Rydberg series limit. Additionally, h is the Planck constant, c the speed of light in a vacuum, $R_{\rm M}$ is the Rydberg constant adjusted for the reduced mass of the atom or molecule, and μ_κ is the quantum defect, which has a dependence on the angular momentum quantum numbers, denoted in general by κ, of the Rydberg electron and ion core. The quantity $\nu = n - \mu_\kappa$ is referred to as the effective principal quantum number. A schematic diagram of Rydberg series converging to the ionisation thresholds of hydrogen (H^+), a non-hyrogenic atom (X^+), and a diatomic molecule (AB^+) are shown in Fig. 2.1.

Although the quantum defects can depend on multiple quantum numbers, the strongest dependence is on the orbital angular momentum of the Rydberg electron ℓ. It is therefore often possible to assume that $\mu_\kappa \approx \mu_\ell$. For hydrogenic atoms and single-electron atomic ions, e.g., H, D, Ps, He^+, and Li^{2+}, the quantum defects are $\mu_\ell = 0$ for all values of ℓ, reflecting the observed energy degeneracy of states of a

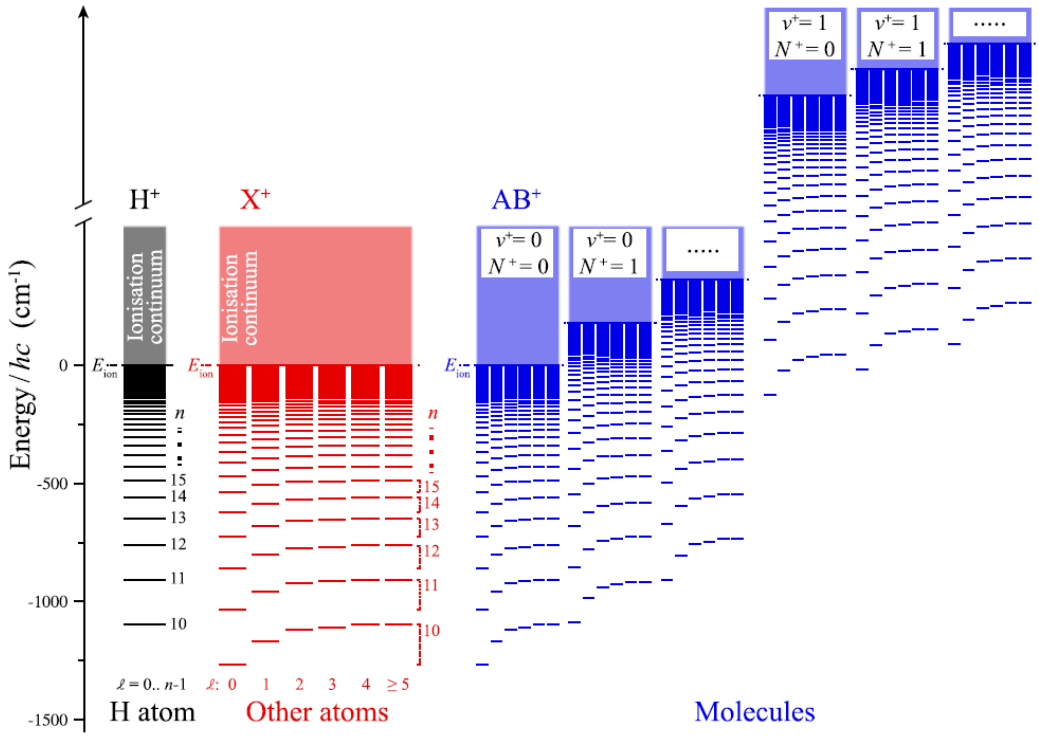

Figure 2.1: Schematic diagram of the Rydberg series in hydrogen (H), a non-hydrogenic atom (X), and in a diatomic molecule (AB). From Ref. 26.

given value of n in the absence of external electric or magnetic fields. The low-ℓ Rydberg states ($\ell \lesssim 3$) of non-hydrogenic atoms and molecules typically have non-zero quantum defects, i.e., $|\mu_\ell| > 0$. For these states the Rydberg electron penetrates the electron charge distribution of the ion core, which results in the Rydberg electron being incompletely shielded from the nuclear charge [66]. These states are therefore typically more strongly bound than an equivalent hydrogenic state of the same n for which $\mu_\ell = 0$. High-ℓ Rydberg states ($\ell \gtrsim 4$) can be considered approximately hydrogenic, i.e., $\mu_\ell \simeq 0$, and hence also degenerate in energy in the absence of external fields.

Many of the physical properties of Rydberg atoms and molecules exhibit a strong dependence on the value of the principal quantum number, n. Examples of such dependencies for the H atom are shown in Table 2.1. These properties, including large static electric dipole moments and long lifetimes, allow the motion of atoms and molecules in Rydberg states to be controlled using inhomogenous electric fields.

Table 2.1: Physical properties of Rydberg atoms and their n dependence [66]. Example values given for the H atom.

Property	n dependence	Values for H at: $n = 5$	$n = 25$
Binding energy (cm^{-1})	n^{-2}	4387.10	175.48
State separation [adjacent n] (cm^{-1})	n^{-3}	1754.84	14.04
Orbital radius (Å)	n^2	13.237	330.916
Maximum static electric dipole moment (D)	n^2	76.29	2288.82
Radiative lifetime[(a)] (μs)	n^3	0.1403	16.3279
Classical ionisation limit ($kV\,cm^{-1}$)	n^{-4}	513.661	0.822

[(a)] Values calculated from fluorescence lifetime of nf states in H.

2.2 Rydberg states of diatomic molecules

As can be seen in Fig. 2.1, the Rydberg energy level structure of diatomic molecules is more complex than in atoms. Because of the large mean orbital radius of the Rydberg electron, its motion can be considered, to first order, to be independent of the vibration or rotation of the ion core. This results in multiple Rydberg series converging to the different rotational (N^+) and vibrational (v^+) states of the molecular ion core (AB^+). In this scenario the energies of the Rydberg states are given by Eq. 2.1 with $E_{\rm ion}(v^+,N^+) = I_0 + E(v^+,N^+)$, where I_0 is the ionisation energy associated with the Rydberg series converging to the ground state of the molecular cation, and $E(v^+,N^+)$ is the rotational-vibrational energy of the v^+, N^+ state of the cation [43].

However, this first order approximation that leads to Eq. 2.1 is not sufficient to describe the energies of molecular Rydberg states, as it is usually necessary to also consider effects of intramolecular interactions between the Rydberg electron and molecular ion core. These interactions result in the coupling of states in Rydberg series that converge to different rotational and vibrational states of the molecular ion core and are associated with energy shifts. These types of intramolecular interactions can also play a significant role in determining the decay dynamics of the Rydberg states of molecules.

2.2.1 Physical origin of intramolecular interactions

A Rydberg electron can mostly be considered to be far from the molecular ion core, and therefore primarily experiences a pure Coulomb interaction with the net positive charge of the ion core. This results in the expression in Eq. 2.1. However, the Rydberg electron does have a finite probability of penetrating near to or inside the electron charge distribution in the core region, particularly for low-ℓ states [43]. When the Rydberg electron is close to the ion core it interacts strongly with the charge distribution of the core. These interactions can be described in terms of the interaction of the Rydberg electron with the electric multipole moments of the ion core. These results in perturbations to the energies given by Eq. 2.1 [43, 67–69]. These intramolecular interactions between the Rydberg electron and ion core allow the exchange of angular momentum, and therefore also energy, between the Rydberg electron and the ion core, resulting in the mixing of Rydberg states which converge to different rotational states of the ion core [43, 67–70].

However, the electron charge distribution of the molecular cation, and therefore also the multipole moments used to described it, is dependent on its internuclear separation, R [69, 71–74]. The interaction of the Rydberg electron with these R-dependent multipole moments can result in a mixing of Rydberg states that converge to different vibrational states of the ion core [69, 71, 72]. This represents a coupling between the electronic and vibrational motion of the molecule [69]. The mixing of Rydberg states which converge to different vibrational states of an ion core is generally much weaker than the mixing of Rydberg states that converge to different rotational states within a single vibrational series.

Another source of mixing between Rydberg states is the configuration mixing that occurs for low-ℓ states. This configuration mixing is a rotation-less mixing of states with low-ℓ character, that occurs in addition to mixings induced by the multipole interactions [67, 71, 75]. The configuration mixing reflects the presence a short-range interaction that affects low-ℓ Rydberg states that penetrate the electron charge distribution on the molecular ion core [70, 71, 75]. The combined effects of these interactions means that, even for high-ℓ molecular Rydberg states that may

appear ostensibly "atom like", the molecular characteristics can be important. The incorporation of effects of these types of interactions into calculations of the energy level structure of Rydberg states of molecules is discussed in Chapter 3.

2.2.2 Decay processes of molecular Rydberg states

Rydberg states of molecules can decay by both radiative and non-radiative processes. The intrinsic decay processes of Rydberg states of an isolated diatomic molecule (i.e., excluding decays induced by collisions, ionisation by external electric fields, or blackbody induced transitions) are; fluorescence, autoionisation, and predissociation.

All Rydberg states of molecules can decay by fluorescence to energetically lower lying states, i.e., $AB^* \rightarrow AB^{(*')} + h\upsilon$. Here AB^* represents the excited Rydberg state, $AB^{(*')}$ represents the state to which the Rydberg state spontaneously decays to (this can be an electronically excited state or the ground state), and $h\upsilon$ represents the photon (or photons) emitted. The total fluorescence decay rate of an individual Rydberg state is therefore determined by calculating the sum of the spontaneous emission decay rates to all energetically lower lying states. Fluorescence decay rates typically scale with n^{-3} for isolated low-ℓ states. However, states with higher values of ℓ have fluorescence decay rates that scale with up to n^{-5} [66], and in the case ℓ-mixed Rydberg-Stark states this dependence is $\sim n^{-4}$ [76]. For context, the hydrogenic field-free fluorescence lifetimes of np and nf states are on the order of 10 μs and 100 μs for $n \sim 40$, i.e., these states have fluorescence rates of $\sim 10^5$ s^{-1} and $\sim 10^4$ s^{-1}, respectively.

Autoionisation can occur when a bound state in one Rydberg series lies energetically above another Rydberg series limit, associated with a different quantum state of the ion core. In this scenario the bound state is located within the ionisation continuum of the other series. If there is an intramolecular interaction that couples bound and ionisation continuum states there is then a probability that the "bound" state collapses into the ionisation continuum and ionisation occurs, i.e., $AB^* \rightarrow AB^+ + e^-$ [43, 77, 78]. Autoionisation may therefore be viewed as a consequence of energy transfer from the nuclear degrees of freedom of the molecular ion

core to the Rydberg electron. In molecules, rotational or vibrational autoionisation of Rydberg states can occur. These arise following excitation of bound states for which the coupling to the ionisation continuum occurs predominantly by rotational or vibrational channel interactions, respectively. These intramolecular couplings are strongest for low-ℓ ($\ell \lesssim 3$) states, and result in larger autoionisation rates for these states. In NO, rotational autoionisation rates of $N^+ = 12$ np states are $\sim 10^{10}$ s^{-1} for $n \sim 40$ [79], and ng states in the $v^+ = 1$ series have vibrational autoionisation rates of $\sim 10^7$ s^{-1} for $n \sim 40$ [80].

In predissociation, energy is redistributed from the Rydberg electron to the nuclear degrees of freedom of the molecule, resulting from the interaction of Rydberg and valence state potential energy curves. In this case there is a finite probability of the "bound" state collapsing into the dissociation continuum leading to the dissociation of the neutral molecule into fragments, i.e., $\mathrm{AB}^* \rightarrow \mathrm{A} + \mathrm{B}^{(*)}$ [43, 77, 78]. In predissociation some of the internal energy of the molecule is transferred into the kinetic energy of the neutral fragments, which can be in the ground or an excited state [78]. The predissociation rates are strongly ℓ-dependent and are largest for $\ell \lesssim 3$ states in molecules. For example, in NO the predissociation rates of np and nf states are on the order of 10^9 s^{-1} and 10^8 s^{-1} for $n \sim 40$, these correspond to lifetimes of ~ 1 ns and ~ 10 ns, respectively [81, 82].

The probability, and therefore the associated decay rate, of these non-radiative processes occurring for states in an isolated molecule generally depends on the extent to which the Rydberg electron wavefunction penetrates into the electron charge distribution of the ion core [43, 78]. Therefore, the rates of these decay processes have an n- and ℓ-dependence. States of higher values of n and ℓ typically have slower decay rates. For uncoupled states in the absence of external fields, the n-dependence of the non-radiative-decay rates is $\sim n^{-3}$, reflecting the $n^{-3/2}$ dependence of the amplitude of the Rydberg electron wavefunction in the core region [43, 66, 78, 83]. The overall decay rate therefore also scales with $\sim n^{-3}$ for these states. However, coupling between Rydberg states induced by intramolecular interactions, and/or external electric fields, alter decay rates and can result in either

a change to the n-dependence, or a break-down of the typical n-scaling expected for "hydrogenic" species.

2.3 Previous experiments with Rydberg NO and N_2 molecules

In this section, previous experiments in which Rydberg state in NO and N_2 were studied are described. This includes a particular emphasis on previous studies of excited state decay dynamics, including non-radiative decay process of $\ell \leq 4$ Rydberg states in these molecules. The interpretation of the work reported in this thesis, with measurement timescales approximately two orders of magnitude larger than those accessible in previous studies, requires an understanding of these previous results, and the mechanisms leading to the decay of low-ℓ Rydberg states.

2.3.1 NO

The excitation of high Rydberg states in NO using resonance enhanced two-colour two-photon $X\,^2\Pi_{\Omega''}(v'', J'') \rightarrow A\,^2\Sigma^+(v', N', J') \rightarrow n\ell X^+\,^1\Sigma^+(v^+, N^+)$ excitation schemes was first demonstrated in experiments performed by Ebata *et al.* [84] and Seaver *et al.* [85] in 1983. Using this type of multiphoton excitation scheme to populate high Rydberg states, the decay dynamics of these states were studied using a combination of spectroscopy and the direct measurement of the lifetimes. Typically such experiments centred on the properties of optically accessible low-ℓ states, for which $\ell \leq 4$.

The lifetimes of high-n ($n = 40$ to 122) Rydberg states in NO, excited on np(0) and nf(2) resonances from the intermediate $A\,^1\Sigma^+(N' = 0, J' = 1/2)$ state, were measured by Vrakking and Lee [81, 82], with and without the application of external electric fields. These lifetimes were measured, following excitation to spectrally-resolved high-n states, by monitoring the change in the excited state population with time using delayed pulsed electric field ionisation (PFI), see Fig. 2.2(a). The corresponding lifetimes were extracted by fitting exponential functions to the experimental data, from which a value for the decay time constant was obtained.

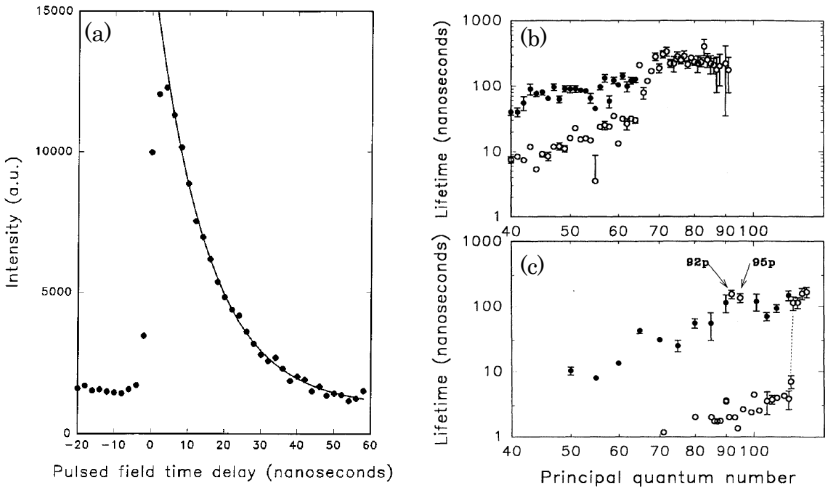

Figure 2.2: (a) Example of decay curve measured for the 50f(2) Rydberg state using delayed PFI. The continuous curve is a single exponential function fit to the data at times > 5 ns. Measured lifetimes of states excited on (b) nf(2), or (c) np(0) resonances from the intermediate $A\,^1\Sigma^+(N' = 0, J' = 1/2)$ state in nominally zero electric field (open circles) and in DC electric fields of ~ 20 mV cm^{-1} to 2 V cm^{-1} (filled circles) - see text for details. Figure adapted from Refs. 81 and 82.

The measured lifetimes for states excited on nf(2) and np(0) resonances are seen in Fig. 2.2(b) and (c), respectively, with the measurements either preformed in nominally zero electric field (open circles) or in weak applied fields (filled circles).

For the nf(2) measurements recorded in nominally zero electric field [Fig. 2.2(b)], the lifetimes below $n \simeq 65$ scaled with n^3, as expected of field-free low-ℓ Rydberg states. The lifetimes of these states were on the order of ten nanoseconds, which suggested that the decay of the molecule was dominated by fast predissociation rather than fluorescence. However, for $n = 65$ to 70 the lifetimes measured on the nf(2) resonances increased, to ~ 100 ns, before plateauing at a maximum value of ~ 400 ns at $n \simeq 80$. This increase in the lifetime at high values of n reflected the presence of stray electric fields in the apparatus. For non-degenerate low-ℓ Rydberg states ($\ell \lesssim 3$) a finite electric field is required to induce ℓ-mixing with the degenerate high-ℓ manifold [denoted $n(2)$ for $N^+ = 2$], with the field required to cause complete ℓ-mixing $F_{\rm mix} \propto |\mu_\ell| n^{-5}$, where μ_ℓ is the quantum defect of the low-ℓ state. The $n(2)$ high-ℓ states have longer lifetimes than the nf(2) states in zero electric field, with their lifetimes dominated by fluorescence rather than predissociation.

Therefore ℓ-mixed Rydberg states prepared by photoexcitation in the presence of an electric field have longer lifetimes than pure nf(2) states. However, in the experiments associated with Fig. 2.2, stray electric fields were reduced to $\sim 10\,\mathrm{mV\,cm^{-1}}$. These fields were therefore only comparable to the electric field required to induce strong ℓ-mixing of the nf(2) states with $n(2)$ states at high values of n. Hence, the increase in the measured lifetimes between $n = 65$ and 70 was attributed to the stray field becoming sufficient to completely mix the nf(2) and $n(2)$ states in this range of values of n. The slight decrease in the lifetimes of states with $n \gtrsim 80$ was attributed in part to further mixing with ns or nd states at these higher values of n. The ns and nd Rydberg states are also short lived with high predissociation rates.

A similar trend was observed in the np(0) states in nominally zero electric field [Fig. 2.2(c)]. (i) The lifetimes below $n \simeq 116$ are short, i.e., < 10 ns, because of the high predissociation rates of states with p character in NO, but increase with n, and (ii) a sharp increase in lifetime to the order of 100 ns is seen for $n \geq 116$. As with photoexcitation on nf(2) resonances, discontinuities in the n-dependence of the measured decay times is attributed to effects of ℓ-mixing in the $\sim 10\,\mathrm{mV\,cm^{-1}}$ stray electric fields in the apparatus.

For the 92p(0) and 95p(0) states in Fig. 2.2(c), the lifetimes measured are on the order of 100 ns, as opposed to the < 10 ns lifetimes of the surrounding states. The larger lifetimes of these two states was explained by Bixon and Jortner [86] to be the consequence of charge-dipole interactions between the Rydberg electron and the NO^+ ion core. These interactions strongly couple an np(0) state and an accidentally near degenerate n'd(1) state, which, if the electric field is sufficiently large, will mix with the longer-lived high-ℓ $n'(1)$ states. In this situation, the np(0) state acts as a 'doorway state' though which the longer lived $n'(1)$ states are populated. In the cases of the excitation on the 92p(0) and 95p(0) resonances, long-lived $80(1)$ and $82(1)$ states are populated by this mechanism, respectively.

In the measurements in Fig. 2.2(b) and (c), the strength of the applied electric field in the apparatus was set for each value of n to cause significant mixing with the degenerate high-ℓ states. The longer lifetimes observed for these same values

of n indicates that this ℓ-mixing occurred. The measured lifetimes of the ℓ-mixed states photoexcited on the np(0) resonances were then in line with the $\sim n^4$ scaling expected for ℓ-mixed Stark states. For the optically accessible ℓ-mixed states with nf(2) character, the lifetimes were observed to 'saturate' for $n \gtrsim 70$. This 'saturation' was attributed to enhanced mixing with the short-lived predissociative states with $\ell \leq 2$ that occurs in higher fields at low values of n, or at higher values of n in fields of a similar strength.

Measurements and calculations reported by Goodgame *et al.* [71] of the Stark effect in $v^+ = 1$ Rydberg states in NO with values of n between 10 and 20, and therefore located above the $v^+ = 0$ series limit, allowed for additional studies of intramolecular interactions, and excited state lifetimes from the spectral linewidths. These Rydberg states were accessed through the intermediate $A\,^2\Sigma^+(v' = 1, N', J')$ state, with $N' = 0$, $J' = 1/2$ or $N' = 2$, $J' = 5/2$, in the presence of electric fields up to 1000 $\mathrm{V\,cm^{-1}}$. An example of the spectra recorded in this work can be seen in Fig. 2.3. In this case, excitation occurred though the $A\,^2\Sigma^+(v' = 1, N' = 0, J' = 1/2)$ state. From a comparison of the calculated and measured spectral linewidths, the lifetimes of the low-ℓ states with $v^+ = 1$ and values of n between 10 and 20 were estimated in this work to be between ~ 1 ps and ~ 50 ps. These lifetimes are dominated by fast non-radiative decay processes that include contributions from predissociation and vibrational autoionisation.

Further studies of Rydberg states of NO in electric fields were later carried out by Jones *et. al.* [87] and Patel *et. al.* [88]. These works focused on effects of intramolecular interactions and the Stark structure of $v^+ = 0$ Rydberg states. Laser photoexcitation spectra recorded, in electric fields of up to 150 $\mathrm{V\,cm^{-1}}$ with detection using the complementary methods of pulsed electric field ionisation, and analysis of the predissociation fragments by laser photoionisation. These measurements, when combined with calculations, allowed intramolecular interactions between optically accessible np(N^+) or nf(N^+) states, and neighbouring high-ℓ states to be studied. In addition, they allowed the determination of the distribution of np(N^+) and nf(N^+) character among the ℓ-mixed Stark states in the presence of electric

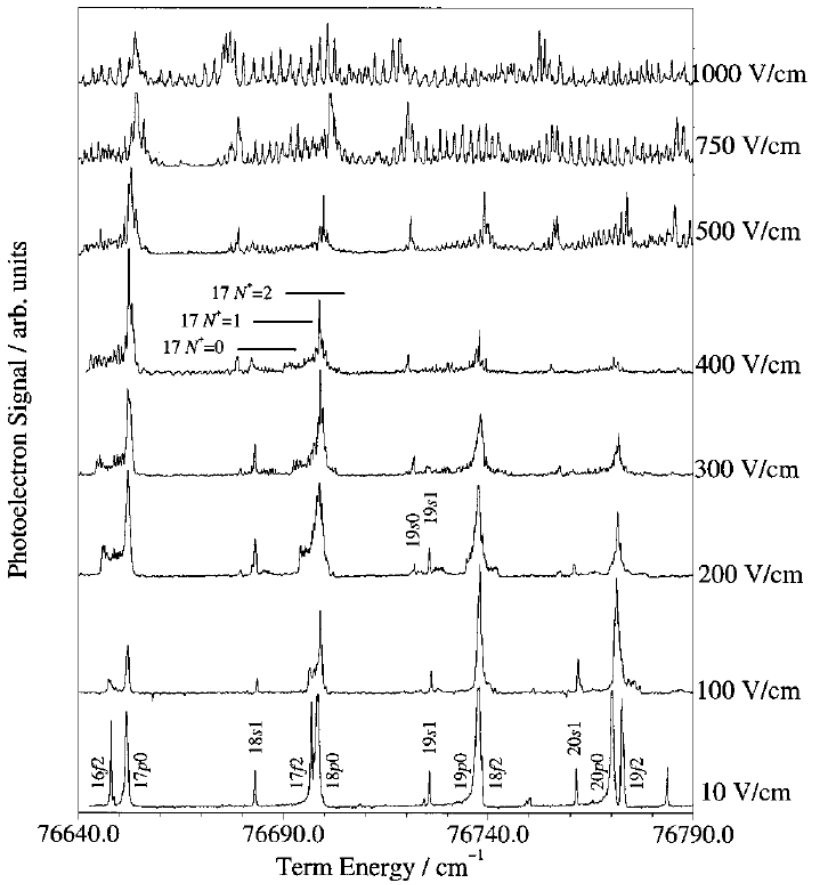

Figure 2.3: Stark spectra of $v^+ = 1$ Rydberg states in NO excited from the $A\,^1\Sigma^+(N' = 0, J' = 1/2, v' = 1)$ intermediate state. From Ref. 71.

fields. The implementation of the two detection methods also highlighted the importance of predissociation on the decay of the states excited and how this changes in the presence of an electric field.

Rotational autoionisation, vibrational autoionisation, and predissociation of the higher-ℓ, ng Rydberg states in NO have also been investigated in experiments conducted by Fujii and Mortia [89]. The ng states, with either $v^+ = 0$ or 1, were prepared in these experiments by excitation from 4f Rydberg states, with $v' = 0$ or 1. These 4f states were accessed from the ground state in a resonance-enhanced two-colour two-photon transition through the A state. Detection of the molecules in Rydberg states in these experiments was achieved by delayed PFI at times between 50 ns and 3 μs after laser photoexcitation. In this work only states with $n \gtrsim 55$

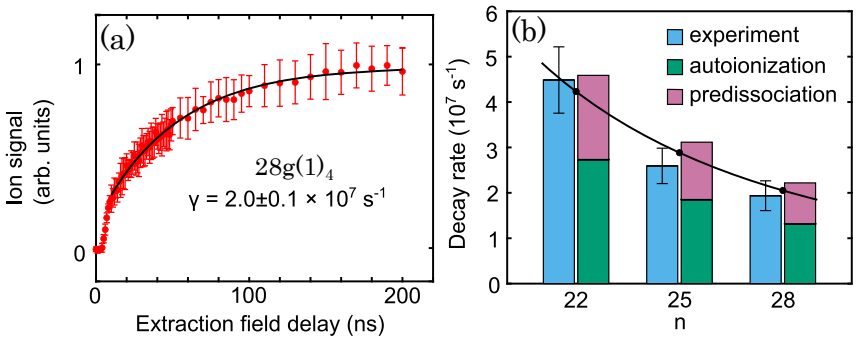

Figure 2.4: (a) Example of measured NO^+ signal recorded following autoionisation of the $28g(1)_4$ Rydberg state in NO. (b) Comparison of the measured ng-state decay rates (blue bar), averaged over all values of N^+ and N, and calculated total decay rates (stacked green and purple bars for the autoionisation and predissociation contributions, respectively). The black line and points represent a fit to the experimental data to show the n^{-3} dependence. Figure adapted from Ref. 80.

could be detected by PFI, and these states had lifetime on the order of 1 μs. This is significantly shorter than the $\sim$ 300 μs fluorescence lifetime expected at these values of n. The dominant decay process of the ng Rydberg states in these experiments was therefore identified as fast predissociation. In measurements of $v^+ = 0$, $N^+ = 12$, ng Rydberg states, molecules in states with $n \lesssim 55$ were detected by delayed PFI. This indicated that the molecules in these states decayed by rotational autoionisation. In addition, this autoionisation process was concluded to be faster than predissociation in these states. In this work, a sharp increases in the autoionisation rate was observed at the thresholds associated with the onset of $\Delta N^+ = -6$, -4, and -2 rotational autoionisation.

Further investigation of vibrational autoionisation rates of $v^+ = 1$ ng Rydberg states was carried out recently by Barnum *et al.* [80]. The ng Rydberg states were accessed in their experiments using the same photoexcitation scheme as Fujii and Mortia [89], with a spectral resolution of 0.05 cm^{-1} sufficient to observe the electronic fine structure. The decay of the molecules was monitored by delayed PFI, with a field that was selected to prevent ionisation of the bound Rydberg states, so that only ions produced by autoionisation were detected. An example of the measured NO^+ ion signal for the $n\ell(N^+)_N = 28g(1)_4$ state reported in this work is shown in Fig. 2.4(a). As seen from the data in Fig. 2.4(b), the measured decay

rates followed an n^{-3} dependence. In the analysis of this work, autoionisation decay rates were computed using a long-range charge-multipole interaction model to described the electrostatic interactions between the Rydberg electron and the NO^+ ion core. When combined with the known predissociation rate of the $v^+ = 0$, ng Rydberg states, the calculated total decay rates $\gamma_{\text{tot.}} = \gamma_{\text{dis.}} + \gamma_{\text{auto.}}$ [green and purple bars in Fig. 2.4(b)] were in good agreement with the measured rates. This indicated that ~ 70 % of the decay of the $v^+ = 1$ ng states occurs because of autoionisation, with the remaining ~ 30 % being from predissociation.

Recently, experiments by Deller and Hogan [90] demonstrated the possibility of preparing hydrogenic Rydberg states in NO with lifetimes in excess of $10\,\mu$s. In the experiments, the molecules were photoexcited using two counter propagating lasers to $v^+ = 0$ Rydberg states, with values of n between 40 and 100, from the ground $X^2\Pi_{1/2}(v'' = 0, N'' = 1, J'' = 3/2)$ state through the $A^2\Sigma^+(v' = 0, N' = 0, J' = 1/2)$ intermediate state. The excited molecules travelled for 126 μs, over a distance of ~ 100 mm, before detection. In this work, only states with lifetimes $\gtrsim 10$ μs were detected. An example of a Rydberg spectrum recorded in this way is seen in Fig. 2.5. This shows that long-lived Rydberg states were consistently populated by photoexcitation on the nf(2) resonances. On some np(0) resonances, e.g., the 65p(0) resonance, long-lived states were also accessible.

Because the field-free nf(2), or np(0), Rydberg states decay on time scales < 100 ns by fast non-radiative processes, they are therefore too short-lived to be observed in the spectrum in Fig. 2.5. Consequently, a combination of ℓ- and M_N-mixing must have occurred to populate high-$|M_N|$ states without any short-lived $\ell \lesssim 3$ character. Such states therefore have fluorescence-dominated lifetimes ≥ 10 μs. This M_N-mixing can be caused by the presence of time-varying electric-fields or collisions close to the time of photoexcitation [76, 91].

The spectrum in Fig. 2.5 is dominated by transitions to nf(2) Rydberg states because of their small quantum defects ($\mu_{\text{f}} \simeq 0.02$), and the associated requirement for only weak electric fields to cause strong ℓ-mixing. In contrast, the larger quantum defects of the np(0) states ($\mu_{\text{p}} \simeq 0.7$) meant they did not efficiently mix with

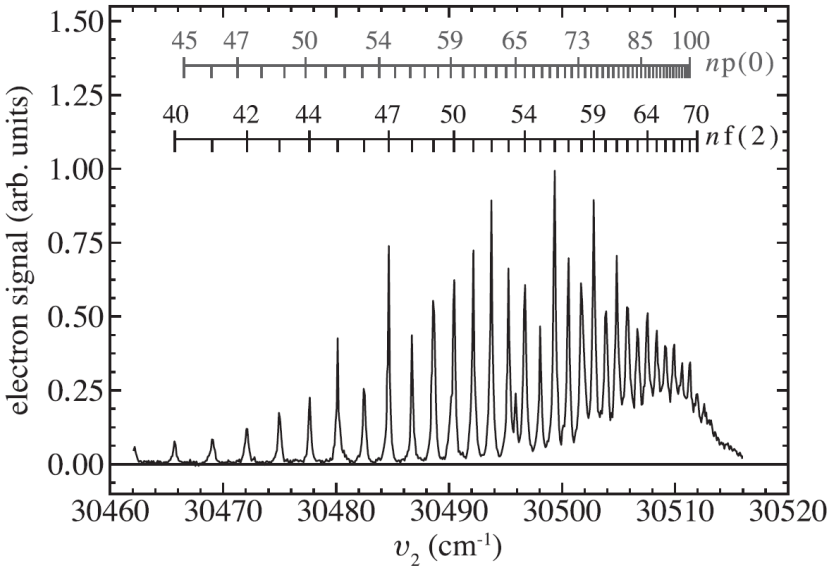

Figure 2.5: Laser photoexcitation spectrum of high Rydberg states in NO recorded by delayed PFI 126 μs after photoexcitation. When recording this spectrum the molecules were excited through the $A^2\Sigma^+(v'=0, N'=0, J'=1/2)$ intermediate state. From Ref. 90.

high-ℓ states of the same N^+ series. They only led to the population of long-lived states where there are accidental degeneracies with these states in another N^+ series [67, 86].

This work also utilised a two-dimensional spectroscopy technique, based on photoexcitation and state-selective electric field ionisation, to characterise the excited state populated 126 μs after excitation. The two-dimensional spectra of these long-lived Rydberg states can be seen in Fig. 2.6. The white bands in this figure represent the range of diabatic ionisation electric fields expected for hydrogenic Rydberg-Stark states in the $N^+ = 0$ to 4 rotational series. As the states excited on nf(2) resonances are seen to predominantly ionise within the $N^+ = 2$ range of ionisation fields, it was concluded that hydrogenic high-$|M_N|$ states with $N^+ = 2$ were populated. On some resonances, the range of ionisation fields corresponds to states in multiple N^+ series. This indicates accidental degeneracies that, through a combination of charge-multipole interactions and electric-field-induced mixing, lead to the population of states in different N^+ series. For states populated following photoexcitation on np(0) resonances, for $n \lesssim 70$ the range of ionisation fields indicates

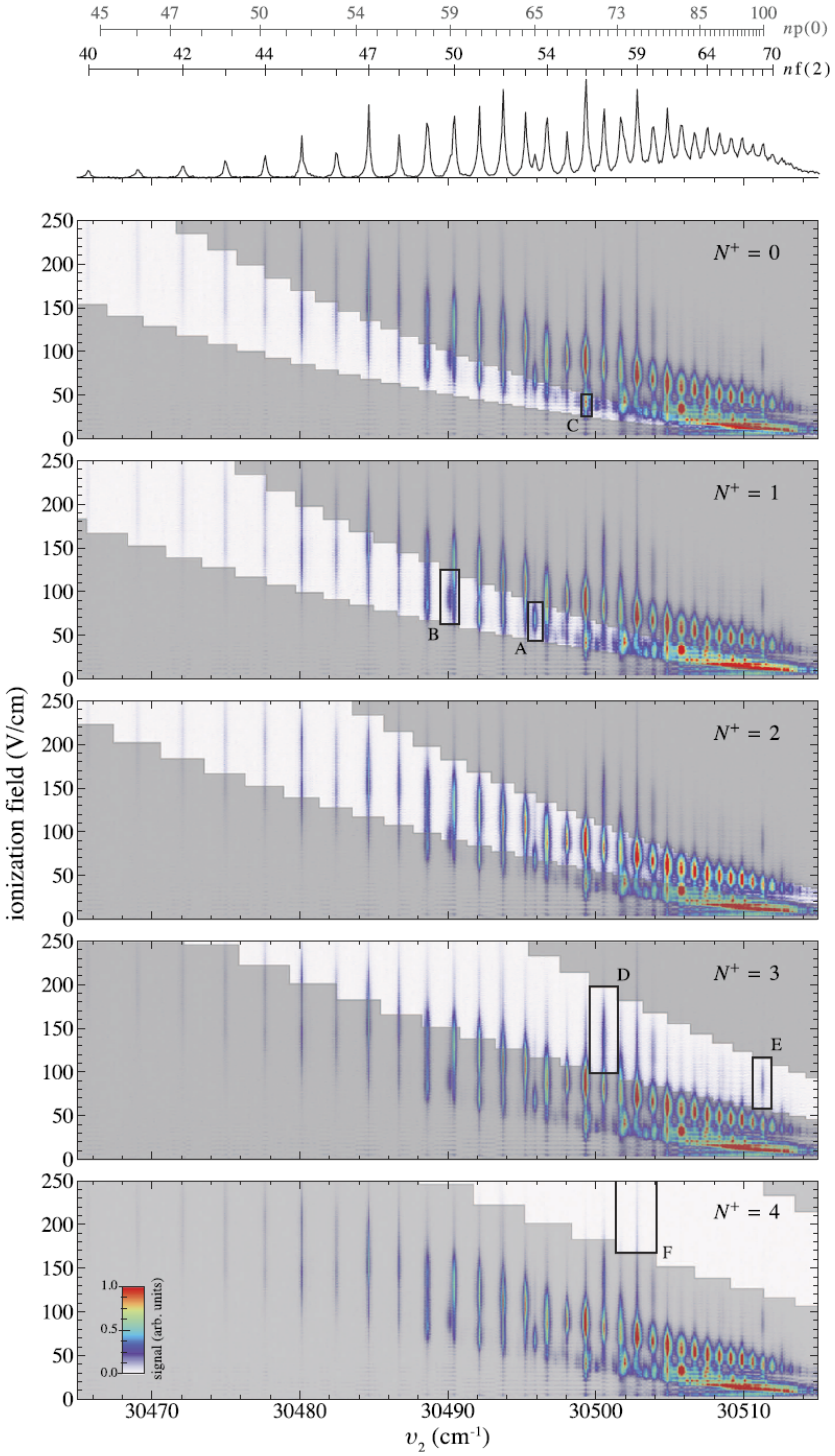

Figure 2.6: Two-dimensional spectra, recorded by state-selective electric field ionisation, of long-lived Rydberg states in NO with detection 126 μs after photoexcitation. The white regions in the lower panels correspond to the range of diabatic ionisation fields expected for hydrogenic Rydberg-Stark states in the $N^+ = 0$ to 4 rotational series. From Ref. 90.

that the long-lived states are of $N^+ = 1$ character. This is consistent with the population of hydrogenic $n'(1)$ states through the combined effects of charge-dipole interactions and electric-field-induced mixing. For $n \gtrsim 70$, from $\upsilon_2 \gtrsim 30510$ cm^{-1} in Fig. 2.6, a band of long-lived hydrogenic states with $N^+ = 0$ character is seen. This corresponded to a spectral region in which the stray electric fields in the experiment were sufficiently strong for electric-field-induced ℓ-mixing of the np(0) states with high-ℓ states in the $N^+ = 0$ series to have occurred.

2.3.2 N_2

High Rydberg states in N_2 have not been as extensively studied as those in NO. However, experiments have been performed to excite Rydberg states of N_2 either directly in single-photon transitions from the ground state [92–94], or using resonance-enhanced multiphoton excitation schemes [95, 96]. The experiments in the literature centred on spectroscopy of low-ℓ ($\ell \leq 3$) Rydberg states, but also included investigations into effects of rotational autoionisation. Here studies of the singlet Rydberg states in N_2 are summarised. However, it is worth noting that high-n triplet Rydberg states in N_2 have also been studied following laser excitation from the metastable $E\,^3\Sigma_g^+$ state [97].

Experiments in which Rydberg states converging to the $X^+\,^2\Sigma_g^+$ ground electronic state of N_2^+ were prepared by direct single-photon excitation from the $X\,^1\Sigma_g^+$ ground state were carried out by Huber and Jungen [92]. In this work, tuneable extreme ultraviolet (XUV) radiation, with wavelengths of ~ 80 nm, allowed the excitation of singlet np and nf Rydberg states. In the spectra reported, np Rydberg states with $N^+ = 0$, 1, and 2 were observed for $n \lesssim 40$. Analysis of these data using a multichannel quantum defect theory (MQDT) model allowed Hund's-case-(b) quantum defects for the np states to be determined, as well as the ionisation wavenumber of N_2 of 125667.032 ± 0.065 cm^{-1}. However, spectra recorded using this method can be complex, because multiple rotational states of the ground electronic state are populated, leading to difficulties in assignment of all Rydberg states.

To reduce the complexity of the spectra, excitation of high-n singlet Rydberg

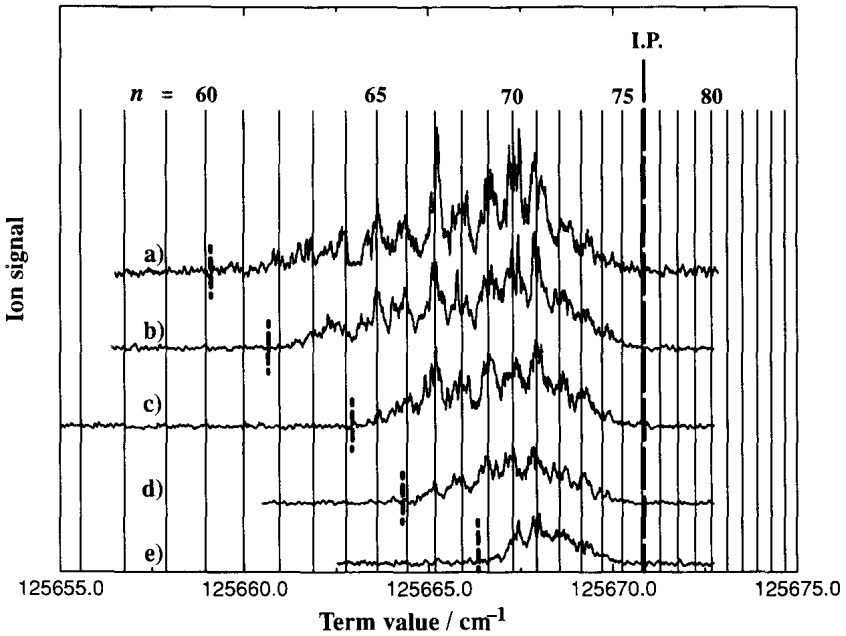

Figure 2.7: Example of Rydberg spectra recorded after excitation through the $a''\,^1\Sigma_g^+$ intermediate state. Calculated energies for $np(N^+ = 3)$ Rydberg states are shown. Spectra (a) to (e) were recorded using PFI fields of between 6.67 $V\,cm^{-1}$ and 1.00 $V\,cm^{-1}$, respectively. A constant dc field of 0.1 $V\,cm^{-1}$ is present for all spectra. The dashed vertical lines indicate the approximate wavenumbers for which the electric field ionisation rate is $> 10^9$ s^{-1} in the PFI field. From Ref. 96.

states in N_2 was also carried out by resonance-enhanced multiphoton excitation through the $a''\,^1\Sigma_g^+$ state (the nominal $3s\sigma$ Rydberg state), by Merkt *et al.* and Mackenzie *et al.* [95, 96]. In these works, delayed PFI was used to detect only Rydberg states with $n \gtrsim 50$. This simplified the spectra, allowing easier assignment of the spectral features. Ions produced by direct photoionisation and by electric field ionisation were separated in the experiments using a weak dc electric field. Prompt photo-ions were accelerated in this process through a smaller potential difference than the ions from Rydberg state field ionisation, and therefore arrived at the MCP later. Example spectra recorded by PFI, in a dc electric field of 0.1 $V\,cm^{-1}$ is shown in Fig. 2.7. In these spectra, transitions to np Rydberg states with $N^+ = 3$ are observed. The range of Rydberg states detected increased as the strength of the ionisation field increased. The dashed vertical lines in these spectra indicate the approximate wavenumbers at which the hydrogenic electric field ionisation rate was

calculated to be $> 10^9$ s^{-1}.

The excitation of np Rydberg states in N_2 by multiphoton excitation has also been used to investigate decay dynamics of high-n Rydberg states [95]. In that work delayed PFI over times up to ~ 25 μs was used to monitor the change in the number of Rydberg N_2 molecules present, and to measure spectra with detection 7 μs after photoexcitation. Rydberg states converging to either odd or even values of N^+ were investigated, within the restrictions imposed by nuclear spin statistics in N_2 and N_2^+. These nuclear spin statistics mean that the $N^+ = 0$ ($N^+ = 1$) ionisation limit is the lowest ionisation limit for even (odd) values of N^+, such that autoionisation only occurs for Rydberg states with $N^+ \geq 2$ ($N^+ \geq 3$). Weak dc electric fields present in these experiments meant that individual Rydberg resonances were not resolved for $n \gtrsim 65$. For $N^+ = 0$ ($N^+ = 1$) Rydberg states, populated following excitation of optically accessible np states, no Rydberg molecules were detected with $n \lesssim 100$. This indicated that any molecules in these states must have decayed by predissociation into neutral atoms that were not detected by PFI, since decay by fluorescence is not expected to play a significant role on the experimental timescales. For $n \gtrsim 100$, ℓ-mixing in the residual uncancelled stray electric field in the apparatus resulted in general in a decrease in the effects of predissociation. However, the decay rates of the Rydberg states with $n \gtrsim 200$ increased because of electric field and collisional ionisation. For $N^+ = 2$ ($N^+ = 3$) Rydberg states, populated though the optically accessible np states, rotational autoionisation was observed. For states with $n \lesssim 100$ approximately 30 % of the molecules decayed by fast autoionisation in < 500 ns, with the remaining ~ 70 % decaying by predissociation. The observation of molecules that predissociate, as opposed to decay by more rapid autoionisation, is attributed to the population of Rydberg states that have no autoionisation channels and that therefore could not decay by this means. For $n \gtrsim 100$, the molecules excited were observed to decay in a biexponential manner, with a faster decay at early times and a slower decay at later times. The early decay time constant was observed to scale with $\sim n^4$ as expected for ℓ-mixed Rydberg-Stark states. The slower decay at later times was attributed to ℓ- and m_ℓ-mixing.

Chapter 3

Stark effect

In this chapter, Section 3.1 and 3.2 provide a description of the Stark effect in Rydberg states of atoms, how it can be calculated, and the fluorescence lifetimes of these Rydberg states. An explanation of Hund's angular momentum coupling schemes of importance in calculating the energy level structure in high-n Rydberg states of diatomic molecules is then presented in Section 3.3. Details of the calculations of the energy-level structure and Stark effect in such Rydberg states in NO are then given in Section 3.4. In Section 3.5 calculations of the lifetimes of these Rydberg-Stark states in NO using input from the Stark effect calculations are then discussed. Example calculations of the Stark effect in N_2 are presented in Section 3.6. The contents of Sections 3.4 and 3.5 are based on work published in Ref. 98, with appropriate adaptations made to conform with the requirements of this thesis.

3.1 Stark effect in atoms

In an electric field, the energy levels in atoms can be shifted from their zero-field values by the Stark effect [66]. In general, the total atomic Hamiltonian accounting for the Stark effect can be expressed as

$$\hat{H}_{\rm tot} = \hat{H}_0 + \hat{H}_{\rm Stark}, \tag{3.1}$$

where $\hat{H}_0$ and $\hat{H}_{\rm Stark}$ represent the field-free and Stark Hamiltonians, respectively. The field-free Hamiltonian for an atom with a single excited Rydberg electron is

diagonal in an $|n,\ell,m_\ell\rangle$ basis, and the matrix elements are given by

$$\langle n,\ell,m_\ell|\hat{H}_0|n,\ell,m_\ell\rangle = E_{\text{ion}} - \frac{hcR_M}{(n-\mu_\ell)^2}, \tag{3.2}$$

i.e., the Rydberg formula in Eq. 2.1. For an electric field of $\vec{F} = (0,0,F_z)$, the Stark Hamiltonian is expressed as $\hat{H}_{\text{Stark}} = eF_z\hat{z}$ [26, 66], where e is the electron charge. Because the field-free basis and Hamiltonian are conveniently described in spherical polar coordinates, it is also appropriate to express the Stark Hamiltonian as $\hat{H}_{\text{Stark}} = eF_z r\cos\theta$, where r and θ representing the radial and angular coordinates of the Rydberg electron [26, 66]. The matrix elements of the Stark Hamiltonian can then be written as

$$\langle n',\ell',m'_\ell|\hat{H}_{\text{Stark}}|n,\ell,m_\ell\rangle = eF_z\langle \ell',m'_\ell|\cos\theta|\ell,m_\ell\rangle\langle n',\ell'|r|n,\ell\rangle, \tag{3.3}$$

where $\langle \ell',m'_\ell|\cos\theta|\ell,m_\ell\rangle$ and $\langle n',\ell'|r|n,\ell\rangle$ represent the angular and radial integrals, respectively.

As the angular integral in Eq. 3.3 is expressible as the integration of three spherical harmonic functions over all solid angles,[1] the value of $\langle \ell',m'_\ell|\cos\theta|\ell,m_\ell\rangle$ can be written in terms of the product of two Wigner-3J symbols with [99–101]

$$\langle \ell',m'_\ell|\cos\theta|\ell,m_\ell\rangle = (-1)^{m_\ell}\sqrt{(2\ell'+1)(2\ell+1)}\begin{pmatrix}\ell' & 1 & \ell\\ -m'_\ell & 0 & m_\ell\end{pmatrix}\begin{pmatrix}\ell' & 1 & \ell\\ 0 & 0 & 0\end{pmatrix}, \tag{3.4}$$

in which the $\begin{pmatrix}\end{pmatrix}$ parentheses represent the Wigner-3J symbols. From Eq. 3.4, the

[1] Given that $\langle \ell',m'_\ell|\cos\theta|\ell,m_\ell\rangle \equiv (-1)^{m'_\ell}\sqrt{\frac{4\pi}{3}}\int \mathrm{Y}_{\ell'-m'_\ell}(\theta,\phi)\mathrm{Y}_{10}(\theta,\phi)\mathrm{Y}_{\ell m_\ell}(\theta,\phi)\,\mathrm{d}\Omega$, with the general identity [99, 100]

$$\int \mathrm{Y}_{\ell_1 m_{\ell_1}}(\theta,\phi)\mathrm{Y}_{\ell_2 m_{\ell_2}}(\theta,\phi)\mathrm{Y}_{\ell_3 m_{\ell_3}}(\theta,\phi)\,\mathrm{d}\Omega = \sqrt{\frac{(2\ell_1+1)(2\ell_2+1)(2\ell_3+1)}{4\pi}}\begin{pmatrix}\ell_1 & \ell_2 & \ell_3\\ m_{\ell_1} & m_{\ell_2} & m_{\ell_3}\end{pmatrix}\begin{pmatrix}\ell_1 & \ell_2 & \ell_3\\ 0 & 0 & 0\end{pmatrix}.$$

selection rules for the interactions with the electric fields lead to non-zero matrix elements when

$$\Delta\ell = \pm 1, \Delta m_\ell = 0, \tag{3.5}$$

i.e., ℓ is no longer a good quantum number with the resulting eigenstates being of mixed ℓ character. The radial integral in Eq. 3.3 can be solved exactly for hydrogenic atoms, but for atoms with non-zero quantum defects the integral must be calculated numerically using, for example, the Numerov method [102]. The total energies of the atomic levels in the presence of an electric field are obtained then by diagonalising the total Hamiltonian, $\hat{H}_{\rm tot}$.

Examples of the Stark effect in Rydberg states of the H atom and the singlet Rydberg states of He are shown in Fig. 3.1. For the case of H, the Hamiltonian can be solved analytically using parabolic coordinates [66], where total energies can be expanded in terms of the external field, such that to second order

$$\begin{aligned} E_{n,k,m_\ell} = & E_{\rm ion} - \frac{hcR_{\rm M}}{(n-\mu_\ell)^2} + \frac{3}{2}nkea_0F_z \\ & - \frac{1}{16}n^4\left[17n^2 - 3k^2 - 9m_\ell^2 + 19\right]\frac{e^2a_0^2}{E_{\rm Har}}F_z^2, \end{aligned} \tag{3.6}$$

where $k = n_1 - n_2$ is an index characterising the Stark states, with n_1 and n_2 being the parabolic quantum numbers, and $E_{\rm Har} = 2hcR_{\rm M}$ is the Hartree energy. The index k can take values from $k = -(n - |m_\ell| - 1)$ to $+(n - |m_\ell| - 1)$ in steps of 2. For non-hydrogenic atoms, such as He, the energies are not exactly described by Eq. 3.6 because of the non-zero quantum defects (especially of the low-ℓ states). Particularly noticeable is that when the Stark states with neighbouring values of n begin to overlap; in H the resulting energy level crossings are exact in the $|n,\ell,m_\ell\rangle$ basis, while in He and other non-hydrogenic atoms these crossing are not exact but are instead avoided crossings. The size of these avoided crossings decreases if the low-ℓ states with large non-zero quantum defects are absent from the Stark manifold. These low-ℓ states can be removed if the value of $|m_\ell|$ is increased from 0 to a value greater than that of the low-ℓ states with significant non-zero quantum defects.

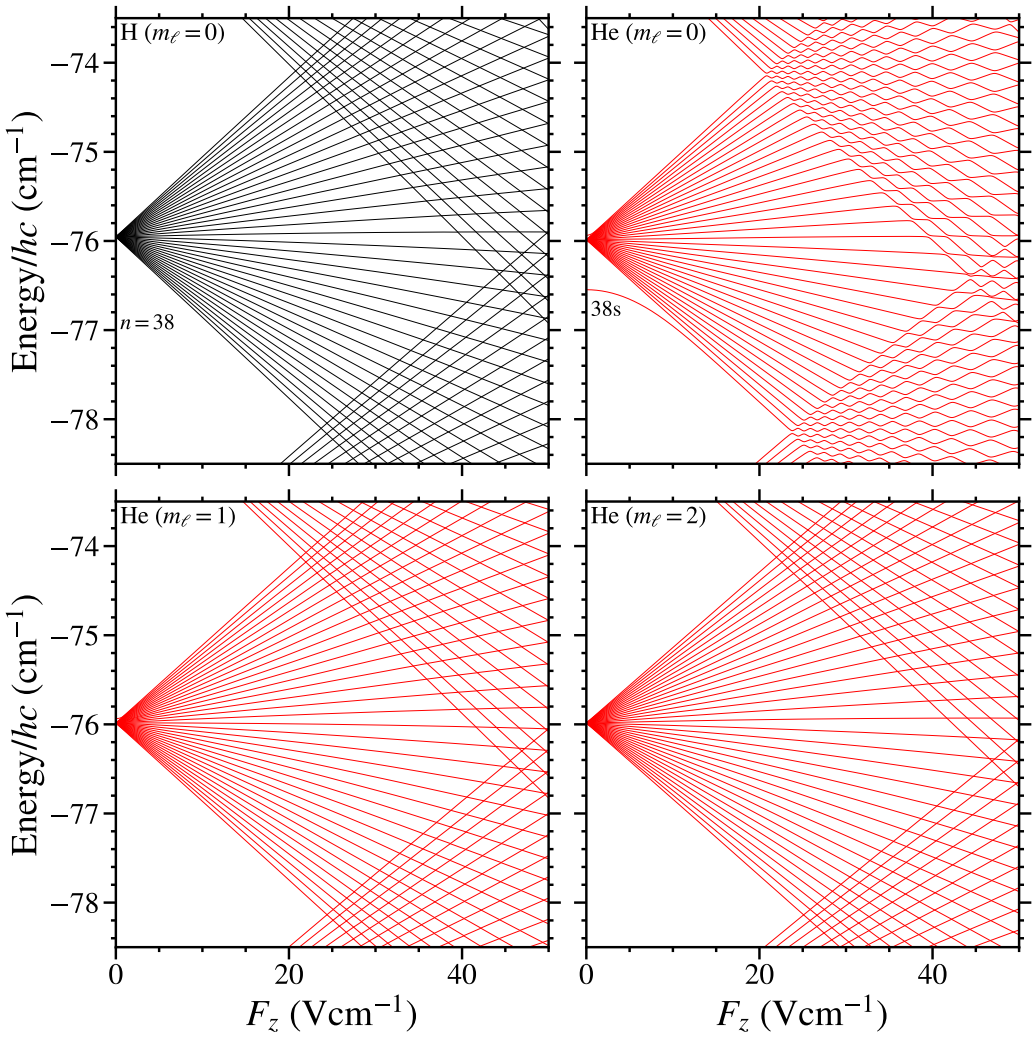

Figure 3.1: Stark effect in Rydberg states of H (black) and He (red) atoms around $n = 38$ for the values of m_ℓ indicated. The calculations presented in this figure were performed using Eqs. 3.1 to 3.4, with the eigenvalues calculated by diagonalisation of the total Hamiltonian (Eq. 3.1) at each value of the electric field, F_z. The calculations for He were carried out for the singlet Rydberg states, with quantum defects drawn from Ref. 103. All energies are relative to the Rydberg series limit.

3.2 Fluorescence lifetimes

Atoms in electronically excited states can decay by spontaneous emission of a photon and subsequent de-excitation to an energetically lower-lying state. In zero-field and within the electric dipole approximation, the spontaneous emission rate from a state $|n,\ell,m_\ell\rangle$ to an energetically lower-lying state $|n',\ell',m'_\ell\rangle$ is given by the

Einstein-A coefficient [104]

$$A_{n'\ell'm'_\ell,n\ell m_\ell} = \frac{e^2\omega^3_{n'\ell'm'_\ell,n\ell m_\ell}}{3\hbar c^3\pi\varepsilon_0}\left|\langle n',\ell',m'_\ell|\hat{r}_q|n,\ell,m_\ell\rangle\right|^2, \tag{3.7}$$

where $\omega_{n'\ell'm'_\ell,n\ell m_\ell} = (E_{n\ell m_\ell} - E_{n'\ell'm'_\ell})/\hbar$. The dipole matrix elements in Eq. 3.7 can be expressed in terms of Wigner-3J symbols as [99–101]

$$\begin{aligned}\langle n',\ell',m'_\ell|\hat{r}_q|n,\ell,m_\ell\rangle = &(-1)^{m'_\ell}\sqrt{(2\ell'+1)(2\ell+1)} \\ &\times \begin{pmatrix} \ell' & 1 & \ell \\ -m'_\ell & q & m_\ell \end{pmatrix}\begin{pmatrix} \ell' & 1 & \ell \\ 0 & 0 & 0 \end{pmatrix}\langle n',\ell'|r|n,\ell\rangle,\end{aligned} \tag{3.8}$$

where the value of q reflects the polarisation of the light ($q = 0$ being linearly polarised light, and $q = \pm 1$ being circularly polarised light), and $\langle n',\ell'|r|n,\ell\rangle$ is a radial integral. The selection rules associated with these electric dipole transitions are that

$$\Delta\ell = \pm 1, \Delta m_\ell = 0, \pm 1, \tag{3.9}$$

where $\Delta m_\ell = 0$ (± 1) transitions occur through the emission of a linearly (circularly) polarised photon. To calculate the total spontaneous emission, i.e., fluorescence, decay rate of an $|n,\ell,m_\ell\rangle$ state, the sum of the decay rates to all electric dipole allowed energetically lower lying states is computed, i.e.,

$$\gamma^{(\mathrm{fl})}_{n\ell m_\ell} = \sum_{n'\ell'm'_\ell} A_{n'\ell'm'_\ell,n\ell m_\ell}, \tag{3.10}$$

where this sum extends over all polarisations of light. The spontaneous emission lifetimes are then given by the inverse of the total decay rate, i.e.,

$$\tau^{(\mathrm{fl})}_{n\ell m_\ell} = 1/\gamma^{(\mathrm{fl})}_{n\ell m_\ell}. \tag{3.11}$$

The fluorescence lifetimes of field-free atomic Rydberg-states are highly dependent on the values of n and ℓ, but m_ℓ does not affect the lifetime of a given field-free state in free-space. Examples of the ℓ-dependence of the fluorescence

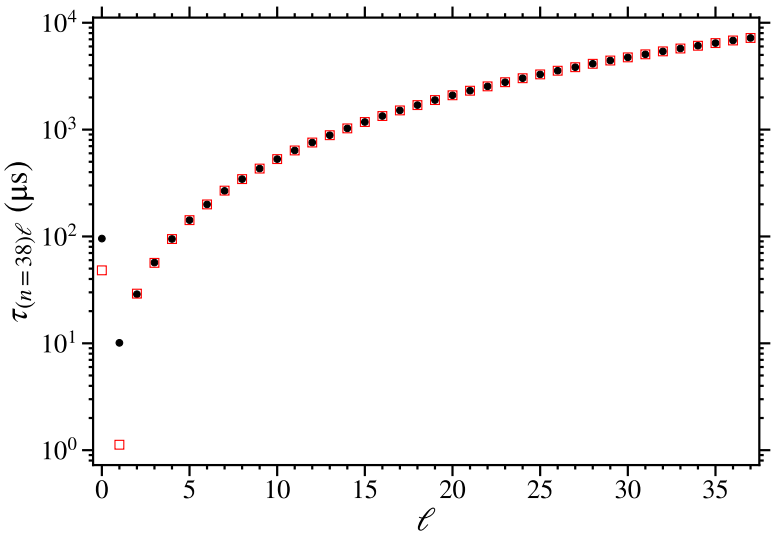

Figure 3.2: Calculated fluorescence lifetimes, $\tau_{n\ell}$, of field free $n = 38$ Rydberg states of H (black circles) and singlet He (red open squares).

lifetimes of the Rydberg states in H and He with $n = 38$ are shown in Fig. 3.2. The longer lifetimes for larger values of ℓ primarily reflects the $\omega^3_{n'\ell'm'_\ell,n\ell m_\ell}$ dependence of the Einstein-A coefficients. This is because, the highest-angular-frequency transitions are then to the lowest possible $\ell' = \ell - 1$ state for all states except the $\ell = 0$ state, where the highest-angular-frequency transition is to the lowest lying $\ell' = 1$ state. Therefore the largest value of $\omega_{n'\ell'm'_\ell,n\ell m_\ell}$ decreases as the value of ℓ increases resulting in smaller decay rates, and longer lifetimes [66]. The n-dependence of the fluorescence lifetimes depends on the value of ℓ. For the low-ℓ states, the fluorescence lifetimes scale with n^3, reflecting the n-dependence of the overlap of the Rydberg wavefunction with the lowest lying state with $\ell' = \ell - 1$ (or $\ell' = 1$ for $\ell = 0$), that are separated by the largest transition frequency. The value of $\omega_{n'\ell'm'_\ell,n\ell m_\ell}$ for transitions to this lowest-lying state is approximately constant as $n \to \infty$ [66]. For the outermost $\ell = n - 1$ states however, the lifetimes scale with n^5 because the only possible electric-dipole allowed decay permitted is to the state with $n' = n - 1$ and $\ell' = n' - 1$. In this case $\omega_{n'\ell'm'_\ell,n\ell m_\ell} \propto n^{-3}$ and the dipole matrix elements are approximately proportional to n^2 [66]. For non-hydrogenic atoms, the lifetimes of the low-ℓ states differ from those of the H atom because of their non-zero quantum defects, and the different transition frequencies to the lowest lying state, whereas

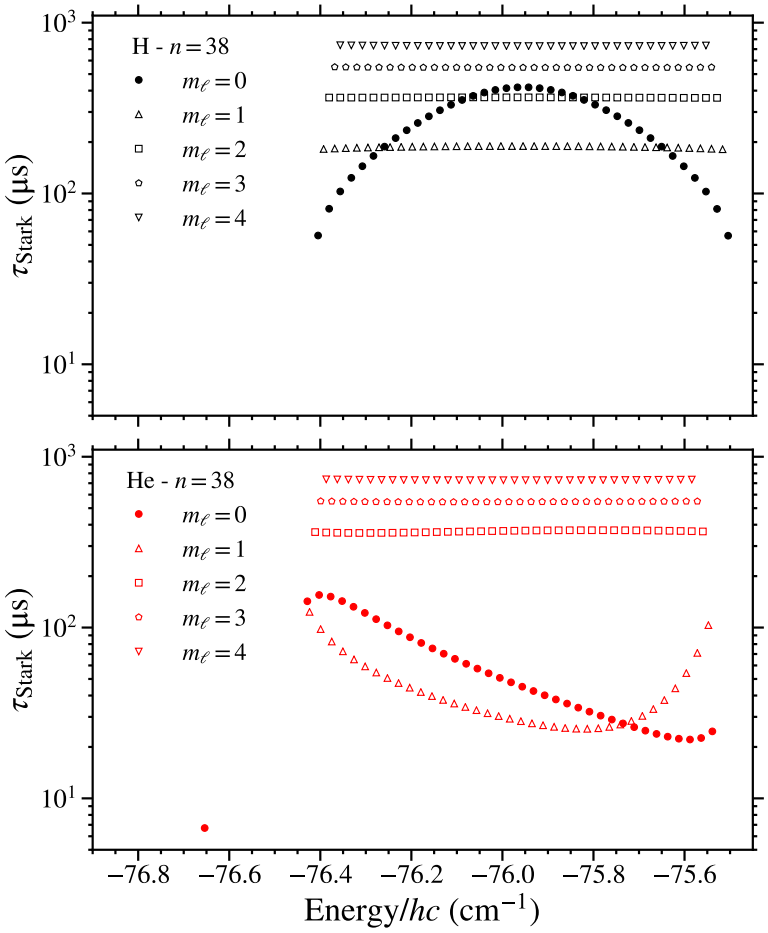

Figure 3.3: Calculated fluorescence lifetimes of $n = 38$ Stark states, in a field of 5 V cm^{-1}, for H and singlet He.

higher-ℓ states with quantum defects of $\mu_\ell \simeq 0$ in non-hydrogenic atoms have lifetimes that behave hydrogenically.

For Rydberg-Stark states, the ℓ-mixed character results in lifetimes that reflect the distribution of ℓ-character present. The fluorescence decay rates of atoms in a Stark state $|i\rangle$ can be determined by decomposing the state to identify the contributions from each field-free basis state, $|j\rangle = |n_j, \ell_j, m_{\ell j}\rangle$, using

$$\gamma_i^{(\mathrm{fl})} = \sum_j \left|c_{ij}(F_z)\right|^2 \gamma_j^{(\mathrm{fl})}, \tag{3.12}$$

where $c_{ij}(F_z) = \langle i|j(F_z)\rangle$ are coefficients of the eigenvector calculated for a field F_z. The eigenvector elements can be obtained by diagonalisation of the total Hamil-

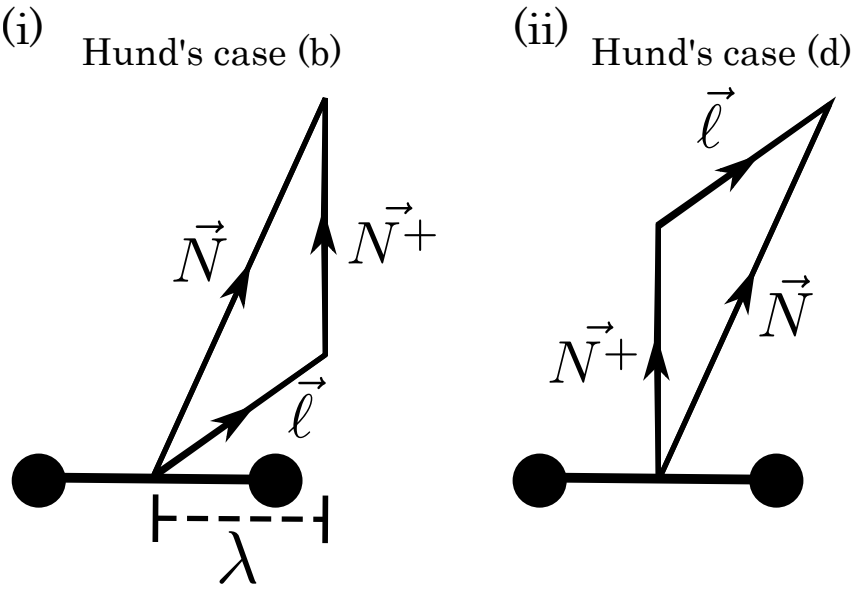

Figure 3.4: Schematic diagram of (i) Hund's-case-(b), and (ii) Hund's-case-(d) idealised angular momentum coupling schemes.

tonian, $\hat{H}_{\rm tot}$, and the field free decay rates $\gamma_j^{(\rm fl)}$ can be calculated using Eq. 3.10. Examples of H and He Stark-state lifetimes, for $n = 38$ and $m_\ell = 0$ to 4 are shown in Fig. 3.3 for a field of 5 $\mathrm{V\,cm^{-1}}$. In both cases as the value of $|m_\ell|$ increases the Stark-state lifetimes also increase. This reflects the fact that at higher values of $|m_\ell|$ shorter-lived low-ℓ character states (see Fig. 3.2) are not available to mix into the Stark states. This results in longer lifetimes for higher $|m_\ell|$. For a given Rydberg-Stark state, the fluorescence lifetimes scale with approximately n^4, reflecting the ℓ-mixed character of these states [76, 91].

3.3 Hund's angular momentum coupling schemes

In Rydberg states of molecules it is necessary to consider how the orbital angular moment of the Rydberg electron couples to the rotational angular moment of the ion core. This is achieved through the idealised Hund's coupling cases. For the Rydberg states of the molecules of interest in this thesis, consideration of the Hund's case (b) and Hund's case (d) is required [77, 105]. The descriptions given here are restricted to diatomic molecules.

In Hund's case (b) and Hund's case (d) the angular momenta considered are the orbital angular momentum of the Rydberg electron, $\vec{\ell}$, and the angular momen-

tum of the ion core excluding spin, $\vec{N}^+$, which sets the rotational energy scale.[2] The total angular momentum excluding spin is $\vec{N} = \vec{N}^+ + \vec{\ell}$ [68, 77, 78, 105]. Schematic diagrams of these coupling cases can be seen in Fig. 3.4. In the Hund's-case-(b) limit the rotational energy-level splitting is smaller than the electronic energy-level splitting, with the Rydberg electron's orbital angular momentum strongly coupled to internuclear axis of molecular ion core [43, 77]. In this instance the quantum number representing the projection of the Rydberg-electron's orbital angular momentum vector along the internuclear axis, λ, is a well defined quantum number [43, 70]. However, N^+ is not a good quantum number because Rydberg states of different N^+ are strongly mixed in the Hund's-case-(b) limit [43]. In Hund's case (d) the electronic energy-level splitting is small compared to the rotational splitting, and the coupling between $\vec{\ell}$ and $\vec{N}^+$ dominates over the coupling between $\vec{\ell}$ and the internuclear axis of molecular ion core [77, 105]. In this case the quantum number N^+ is well defined, whereas λ is no longer a good quantum number.

For each Hund's coupling case the angular momentum basis state wavefunctions is expressed in terms of a distinct set of good quantum numbers. Excluding spin and the spin projection onto a fixed z-axis, which are common to both cases and are not important to the discussions presented here, the Hund's-case-(b) and Hund's-case-(d) basis states can be expressed as $|\ell, \lambda, N, \Lambda, M_N\rangle$ and $|\ell, N^+, \Lambda^+, N, M_N\rangle$, respectively [43, 77]. Here Λ^+ represents the projection of the total orbital angular momentum of the molecular ion core, $\vec{N}^+$, onto the internuclear axis [77, 78, 106, 107]. $\Lambda = \Lambda^+ + \lambda$ is the projection of the total orbital angular momentum, $\vec{N}$, onto the internuclear axis for the Rydberg state of the neutral molecule [106, 107]. The projection of the total angular momentum on a fixed external z axis, M_N, is well defined in Hund's case (b) and Hund's case (d). However, the projection of $\vec{\ell}$ along the z axis, m_ℓ, is not well defined, even in Hund's case (d) [71, 77]. The Hund's-case-(d) basis states are therefore expressed as a sum

[2] Explicitly $\vec{N}^+ = \vec{R}^+ + \vec{L}^+$, where $\vec{R}^+$ and $\vec{L}^+$ are the rotational and total electron orbital angular momentum of the ion core (excluding spin), respectively [78]. $\vec{R}^+$ is defined as being in the direction perpendicular to the internuclear axis [105]. Hence the projection of $\vec{N}^+$ along the internuclear axis is equivalent to the projection $\vec{L}^+$, which is denoted as Λ^+.

over the possible m_ℓ and M_{N^+} (the projection of $\vec{N}^+$ along the z axis) combinations, for fixed values of N and M_N [77]. This sum is expressed as [77],

$$|\ell, N^+, \Lambda^+, N, M_N\rangle = \sum_{m_\ell, M_{N^+}} (-1)^{\ell+N^+-M_N}\sqrt{2N+1}\begin{pmatrix} \ell & N^+ & N \\ m_\ell & M_{N^+} & -M_N \end{pmatrix} |\ell, m_\ell, N^+, \Lambda^+, M_{N^+}\rangle. \quad (3.13)$$

The Wigner 3J symbol, in Eq. 3.13, dictates that $|\ell - N^+| \leq N \leq \ell + N^+$, and $M_N = m_\ell + M_{N^+}$.

Although the probability density, integrated over a spherical shell, of the Rydberg electron is largest far from the ion core, where the Hund's-case-(d) coupling scheme applies, there is a finite probability of the Rydberg electron penetrating, or closely approaching, the molecular ion core. In this region the stronger coupling of the Rydberg electron to the ion core is more appropriately described by the Hund's-case-(b) coupling scheme. Rydberg states therefore represent an intermediate case between the Hund's-case-(b) and Hund's-case-(d) idealised angular momentum coupling schemes [105]. To link the wavefunction of the Rydberg electron between the Hund's-case-(b) and Hund's-case-(d) regions a transformation is required to allow multichannel quantum defect theory (MQDT) to be employed as a means of calculating the effects of intramolecular interactions [70, 71, 108, 109]. Alternatively, the effect of intramolecular interactions can be accounted for by directly considering the interaction of the Rydberg-electron in a Hamiltonian approach described using a set of Hund's-case-(d) basis states with the multipole moments of the molecular ion core [67–69]. A combination of these approaches was employed in the calculations reported in this thesis, which are described below.

3.4 Calculations of the Stark effect in Rydberg states of NO

To aid the interpretation of the results of the experiments presented in this thesis, calculations of the energy-level structure and lifetimes of the Rydberg states in NO

in the presence of externally applied electric fields were performed. The methods used in these calculations follow those reported in Refs. 70, 71, 88, and 110, and involved determining the eigenvalues and eigenvectors of the Hamiltonian matrix describing the interaction of the molecule with an external electric field. Although these calculations are presented for the case of NO, the method can also be applied to other diatomic molecules whose Rydberg states can be described well by Hund's case (d), such as the singlet Rydberg states in N_2.

The calculations presented here were performed in the $|n\ell N^+ N M_N\rangle$ Hund's-case-(d) basis. In this basis the total Hamiltonian can be expressed as,

$$\hat{H}^{(\mathrm{d})}_{\mathrm{tot}} = \hat{H}^{(\mathrm{d})}_0 + \hat{H}^{(\mathrm{d})}_{\mathrm{Stark}}, \tag{3.14}$$

where $\hat{H}^{(\mathrm{d})}_0$ and $\hat{H}^{(\mathrm{d})}_{\mathrm{Stark}}$ represent the field-free and Stark Hamiltonians, respectively. $\hat{H}^{(\mathrm{d})}_{\mathrm{Stark}}$ contains all contributions arising from the presence of the the external electric field.

3.4.1 Field-free Hamiltonian

For Rydberg states in NO, the field-free Hamiltonian, $\hat{H}^{(\mathrm{d})}_0$ in Eq. 3.14, contains diagonal contributions that represent the energies of the unperturbed Hund's-case-(d) eigenstates. These were calculated using the Rydberg formula (Eq. 2.1). Off-diagonal contributions to $\hat{H}^{(\mathrm{d})}_0$ arise from the interactions of the Rydberg electron with the electric dipole moment, electric quadrupole moment, and electric polarisability of the NO^+ ion core [67–69]. They also contain contributions from the multi-electron character of NO^+ which because of short range interactions causes $\mathrm{s}\sigma - \mathrm{d}\sigma$ configuration mixing [70, 71] (σ represents the $\lambda = 0$ projection of the Rydberg electron orbital angular momentum vector onto the internuclear axis).

The general approach used here to construct the matrix $\hat{H}^{(\mathrm{d})}_0$ follows that presented by Goodgame *et. al.* [71], which itself is based on the work of Fredin *et. al.* [70] on the determination of off-diagonal elements of the field-free Hamiltonian from a first order approximation to MQDT. Off-diagonal matrix elements arising from the interaction of the Rydberg electron with the electric dipole moment of the

NO^+ ion were calculated using the method described by Bixon and Jortner [67, 86].

To construct the Hamiltonian, $\hat{H}_0^{(\mathrm{d})}$, it is separated into a diagonal part, $\hat{H}_{\mathrm{diag}}^{(\mathrm{d})}$, a part that accounts for the interaction of the Rydberg electron with the static electric dipole moment of the NO^+ ion core, $\hat{H}_{\mathrm{dip}}^{(\mathrm{d})}$, and a part that accounts for the combination of the interaction of the Rydberg electron with the electric quadrupole moment and higher order multipole moments of NO^+, and the $\mathrm{s}\sigma - \mathrm{d}\sigma$ configuration mixing, $\hat{H}_{\mathrm{multi}}^{(\mathrm{d})}$, i.e.,

$$\hat{H}_0^{(\mathrm{d})} = \hat{H}_{\mathrm{diag}}^{(\mathrm{d})} + \hat{H}_{\mathrm{dip}}^{(\mathrm{d})} + \hat{H}_{\mathrm{multi}}^{(\mathrm{d})}. \tag{3.15}$$

The Hamiltonian $H_{\mathrm{diag}}^{(\mathrm{d})}$ is diagonal in the $|n\ell N^+ N M_N\rangle$ basis with matrix elements given by,

$$\begin{aligned}&\langle n\ell N^+ N M_N|\hat{H}_{\mathrm{diag}}^{(\mathrm{d})}|n\ell N^+ N M_N\rangle \\ &\quad = hc\left[W_{v^+} + B_{v^+}^+ N^+\left(N^+ + 1\right) - D_{v^+}^+\left[N^+\left(N^+ + 1\right)\right]^2 - \frac{R_{\mathrm{NO}}}{\nu^2}\right].\end{aligned} \tag{3.16}$$

Here, W_{v^+} is the ionisation wavenumber of the Rydberg series converging to the ground electronic state of the NO^+ cation with vibrational quantum number v^+. For $v^+ = 0$ this has a value of $W_0 = 74721.7\ \mathrm{cm}^{-1}$ [71, 88]. For larger values of v^+ the ionisation wavenumber was determined from the vibrational energy of the NO^+ cation given by [78]

$$G_{v^+}^+ = \omega_{\mathrm{e}}^+\left(v^+ + \frac{1}{2}\right) - \omega_{\mathrm{e}}\chi_{\mathrm{e}}^+\left(v^+ + \frac{1}{2}\right)^2, \tag{3.17}$$

with ω_{e}^+ and $\omega_{\mathrm{e}}\chi_{\mathrm{e}}^+$ the equilibrium vibrational constant and the equilibrium anharmonic vibrational constant, respectively. Hence, for $v^+ > 0$

$$W_{v^+} = W_0 + (G_{v^+}^+ - G_0^+), \tag{3.18}$$

and in the $\mathrm{X}^+\,{}^1\Sigma^+$ state of NO^+ $\omega_{\mathrm{e}}^+ = 2376.42\ \mathrm{cm}^{-1}$ and $\omega_{\mathrm{e}}\chi_{\mathrm{e}}^+ = 16.262\ \mathrm{cm}^{-1}$ [72], such that $W_1 = 77065.6\ \mathrm{cm}^{-1}$ [71]. Also in Eq. 3.16, $B_{v^+}^+$ and $D_{v^+}^+$ are the rotational and centrifugal distortion constants for NO^+. These are weakly dependent on the

value of v^+ since [78]

$$B^+_{v^+} = B^+_{\rm e} - \alpha^+_{\rm e}\left(v^+ + \frac{1}{2}\right), \tag{3.19}$$

where $B^+_{\rm e}$ is the equilibrium rotational constant, and $\alpha^+_{\rm e}$ is the rotational-vibrational coupling constant. In the $X^+\,^1\Sigma^+$ state of NO^+ $B^+_{\rm e} = 1.99727$ cm^{-1} and $\alpha^+_{\rm e} = 0.01889$ cm^{-1} [72]. For $v^+ = 0$ and 1 the values the rotational constants are therefore $B^+_0 = 1.987825$ cm^{-1} and $B^+_1 = 1.968935$ cm^{-1}, respectively [72, 88]. Here $D^+_{v^+}$ is assumed to be approximately constant over the vibrational states of interest with a value of $D^+_0 = 5.64\times10^{-6}$ cm^{-1} [72, 88].

The Rydberg constant adjusted for the reduced mass of NO required in Eq. 3.16 is $R_{\rm NO} = 109735.31$ cm^{-1}, and in this expression $\nu = n - \mu^{\rm (d)}_{\ell,(N^+,N)}$ represents the effective principal quantum number calculated using the Hund's-case-(d) quantum defects $\mu^{\rm (d)}_{\ell,(N^+,N)}$. These quantum defects, $\mu^{\rm (d)}_{\ell,(N^+,N)}$, depend strongly upon the value of ℓ, but are also weakly dependent on the values of N^+ and N as shown below.

The elements of the Hamiltonian matrix $\hat{H}^{\rm (d)}_{\rm dip}$ are given by [67, 69, 86],

$$\begin{aligned}\langle n\,\ell\,N^+\,N\,M_N|\hat{H}^{\rm (d)}_{\rm dip}|n'\,\ell'\,N^{+\prime}\,N'\,M_N'\rangle \\ = \frac{-e\mu_{\rm NO^+}}{4\pi\varepsilon_0}\langle\nu\,\ell|r^{-2}|\nu'\,\ell'\rangle f(\ell N^+ N M_N;\ell' N^{+\prime} N' M_N'),\end{aligned} \tag{3.20}$$

where e is the electron charge, ε_0 is the vacuum permittivity, $\mu_{\rm NO^+}$ is the electric dipole moment of NO^+ in a coordinate system with its origin at the centre of mass of the molecule, and $\langle\nu\ell|\,r^{-2}\,|\nu'\ell'\rangle$ is a radial integral. The angular integral,

$$\begin{aligned}&f(\ell N^+ N M_N;\ell' N^{+\prime} N' M_N') \\ &\quad=(-1)^{\ell'+\ell+N'}\sqrt{(2N^++1)(2N^{+\prime}+1)}\sqrt{(2\ell+1)(2\ell'+1)} \\ &\quad\times\begin{Bmatrix} N' & N^+ & \ell \\ 1 & \ell' & N^{+\prime}\end{Bmatrix}\begin{pmatrix} N^+ & 1 & N^{+\prime}\\ 0 & 0 & 0\end{pmatrix}\begin{pmatrix}\ell & 1 & \ell'\\ 0 & 0 & 0\end{pmatrix}\delta_{N,N'}\delta_{M_N,M_{N'}},\end{aligned} \tag{3.21}$$

where the terms in the large ( ) and { } parentheses represent Wigner 3J and 6J symbols, respectively, and $\delta_{N,N'}$ and $\delta_{M_N,M_{N'}}$ are Kronecker delta functions. $\hat{H}^{\rm (d)}_{\rm dip}$

leads to interactions between Hund's-case-(d) basis states for which,

$$\Delta\ell = \pm 1;\ \Delta N^{+} = \pm 1;\ \Delta N = 0;\ \Delta M_N = 0. \tag{3.22}$$

The radial integral, in Eq. 3.20, was calculated using the Gilbert-Child [67, 111] near-threshold approximation with a finite quantum defect such that,

$$\langle \nu\,\ell | r^{-2} | \nu'\,\ell' \rangle = 2a_{\rm NO}^{-2} \left(\nu\nu'\right)^{-3/2} \left(\lambda_\ell + \lambda_\ell{}' + 1\right)^{-1} \frac{\sin\left[\pi\left(\lambda_\ell - \lambda_\ell{}'\right)\right]}{\pi\left(\lambda_\ell - \lambda_\ell{}'\right)}, \tag{3.23}$$

where $\lambda_\ell = \ell - \mu^{(\rm d)}_{\ell,(N^+,N)}$, and $a_{\rm NO}$ is the Bohr radius adjusted for the reduced mass of NO. This charge-dipole interaction is strongest between low-ℓ states, i.e., states with large non-zero quantum defects. In these calculations, a static electric dipole moment for NO^+ of $\mu_{NO^+} \simeq 0.4$ D was used. This was based on the value reported from calculations, at the equilibrium internuclear separation, for the $X^+\,^1\Sigma^+$ state [73, 112–115].

The elements of the Hamiltonian matrix $\hat{H}^{(\rm d)}_{\rm multi}$ can be expressed as [71] ,

$$\begin{aligned}\langle n\,\ell\,N^+\,N\,M_N | \hat{H}^{(\rm d)}_{\rm multi} | n'\,\ell'\,N^{+\prime}\,N'\,M_N{}' \rangle \\ = -\frac{2hcR_{\rm NO}}{\nu^{3/2}\nu'^{3/2}} H^{(N)}_{\ell N^+,\ell' N^{+\prime}} \delta_{N,N'} \delta_{M_N,M_N{}'},\end{aligned} \tag{3.24}$$

with,

$$H^{(N)}_{\ell N^+,\ell' N^{+\prime}} = \sum_\Lambda A^{(N\ell)}_{N^+\Lambda} H^\Lambda_{\ell\ell'} A^{(N\ell')}_{N^{+\prime}\Lambda}, \tag{3.25}$$

where $A^{(N\ell)}_{N^+\Lambda}$ represents the Hund's-case-(b) to Hund's-case-(d) frame transformation, and $H^\Lambda_{\ell\ell'}$ are Hund's-case-(b) matrix elements.

For Rydberg states converging to the $^1\Sigma^+$ state of NO^+ with $\Lambda^+ = 0$ (Λ^+ is the projection of the total electron orbital angular momentum vector of the NO^+ cation onto the internuclear axis which, for a Σ state, is zero), the projection of the total orbital angular momentum vector in the neutral NO molecule onto the internuclear

Table 3.1: NO Hund's-case-(b) quantum defects, $\mu_{\ell\Lambda}^{(\mathrm{b})}$, for $\ell \leq 3$ from Ref. 88.

		Λ			
		0	1	2	3
ℓ	0	0.210			
	1	0.7038	0.7410		
	2	0.050	-0.053	0.089	
	3	0.0182	0.0172	0.00128	0.0057

axis is $\Lambda = \lambda$ [70]. With this in mind $A_{N^+\Lambda}^{(N\ell)}$ can be expressed as [63, 71, 77, 106],

$$A_{N^+\Lambda}^{(N\ell)} = (-1)^{\ell+\Lambda-N^+} \begin{pmatrix} \ell & N & N^+ \\ -\Lambda & \Lambda & 0 \end{pmatrix} \sqrt{2N^+ + 1} \sqrt{\frac{2}{1+\delta_{\Lambda 0}}}. \tag{3.26}$$

Note that the Rydberg-electron spin and spin projection are common to Hund's case (b) and Hund's case (d) so do not appear in these transformations [77].

In NO, the configuration mixing predominantly occurs between the sσ ($\ell = 0, \Lambda = 0$) and dσ ($\ell = 2, \Lambda = 0$) Hund's-case-(b) basis states, and therefore results in ℓ-mixing of the Rydberg eigenstates. In Hund's case (b), the corresponding matrix elements, that account for these effects of configuration mixing, are [70, 71],

$$H_{\ell\ell'}^{\Lambda} = \begin{cases} \frac{1}{2}\left(\mu_{\mathrm{s}\sigma}^{(\mathrm{b})} - \mu_{\mathrm{d}\sigma}^{(\mathrm{b})}\right) \sin 2\theta_{\mathrm{sd}} & \text{if } \ell = 0,2;\ \ell' = 2,0;\ \Lambda = 0 \\ \mu_{\mathrm{s}\sigma}^{(\mathrm{b})} \cos^2\theta_{\mathrm{sd}} + \mu_{\mathrm{d}\sigma}^{(\mathrm{b})} \sin^2\theta_{\mathrm{sd}} & \text{if } \ell = \ell' = 0;\ \Lambda = 0 \\ \mu_{\mathrm{s}\sigma}^{(\mathrm{b})} \sin^2\theta_{\mathrm{sd}} + \mu_{\mathrm{d}\sigma}^{(\mathrm{b})} \cos^2\theta_{\mathrm{sd}} & \text{if } \ell = \ell' = 2;\ \Lambda = 0 \\ \mu_{\ell\Lambda}^{(\mathrm{b})} & \text{otherwise } (\ell = \ell'), \end{cases} \tag{3.27}$$

where $\theta_{\mathrm{sd}} = -38.7^\circ$ is the sσ – dσ mixing angle [70], and $\mu_{\ell\Lambda}^{(\mathrm{b})}$ are the Hund's-case-(b) quantum defects. Taking this into account the complete sets of selection rules for the intramolecular interaction accounted for in $H_{\mathrm{multi}}^{(\mathrm{d})}$ are,

$$\Delta\ell = 0, \pm 2;\ \Delta N^+ = \pm 2;\ \Delta N = 0;\ \Delta M_N = 0, \tag{3.28}$$

where the $\Delta\ell = \pm 2$ interactions only occur between basis states with $\ell = 0$ and $\ell' = 2$, and *vice versa*. The Hund's-case-(b) quantum defects, $\mu_{\ell\Lambda}^{(\mathrm{b})}$, used in the

calculations are listed in Table 3.1. To obtain the Hund's-case-(d) quantum defects, $\mu^{(\mathrm{d})}_{\ell,(N^+,N)}$, required in the determination of ν in Eqs. 3.16, 3.20, and 3.24, a frame transformation was performed such that,

$$\mu^{(\mathrm{d})}_{\ell,(N^+,N)} = \sum_{\Lambda=0}^{\ell} \left(A^{(N\ell)}_{N^+\Lambda}\right)^2 H^{\Lambda}_{\ell\ell}. \tag{3.29}$$

3.4.2 Stark Hamiltonian

In an electric field $\vec{F} = (0,0,F_z)$, the Hund's-case-(d) Hamiltonian in Eq. 3.15 can be extended to include contributions from the Stark effect. The resulting perturbation, $\hat{H}^{(\mathrm{d})}_{\mathrm{Stark}} = eF_z\hat{z}$, has matrix elements given by [63, 71, 116],

$$\begin{aligned}
&\langle \nu\,\ell N^+ N M_N|\hat{H}^{(\mathrm{d})}_{\mathrm{Stark}}|\nu'\,\ell' N^{+\prime} N' M_N{}'\rangle \\
&\qquad = eF_z(-1)^{N-M_N+N'+N^++\ell+1}\sqrt{(2N+1)(2N'+1)} \\
&\qquad\quad \times \begin{pmatrix} N & 1 & N' \\ -M_N & 0 & M_N{}' \end{pmatrix} \begin{Bmatrix} \ell & N & N^+ \\ N' & \ell' & 1 \end{Bmatrix} \langle \nu\,\ell||r||\nu'\,\ell'\rangle \delta_{N^+,N^{+\prime}},
\end{aligned} \tag{3.30}$$

where the integral,

$$\langle \nu\,\ell||r||\nu'\,\ell'\rangle = \begin{cases} -(\ell+1)^{1/2}\langle \nu\,\ell|r|\nu'\,\ell+1\rangle & \text{if } l' = l+1 \\ \ell^{1/2}\langle \nu\,\ell|r|\nu'\,\ell-1\rangle & \text{if } l' = l-1 \end{cases}. \tag{3.31}$$

This perturbation leads to non-zero off-diagonal couplings between states, within the same rotational series, for which $\Delta\ell = \pm 1$, i.e., between states for which,

$$\Delta\ell = \pm 1;\ \Delta N^+ = 0;\ \Delta N = 0, \pm 1\ (\ 0 \not\to 0);\ \Delta M_N = 0. \tag{3.32}$$

The radial integrals $\langle \nu\,\ell|r|\nu'\,\ell'\rangle$ on the right-hand side of Eq. 3.31 were evaluated using the Numerov method [102] with a pure Coulomb potential. Stepwise integration was performed inwards from large r to either the inner classical turning point of the Rydberg electron orbit, or the polarisability radius, r_α, of the NO^+ ion core, whichever was encountered first. The polarisability radius, r_α, was taken to

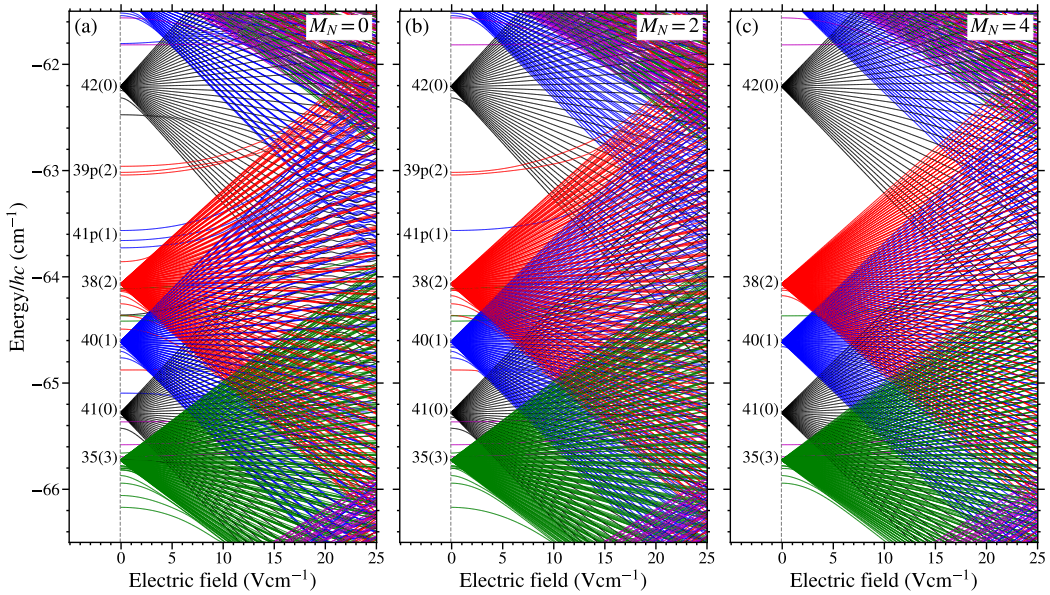

Figure 3.5: Calculated Stark maps for $v^+ = 0$ Rydberg states in NO with (a) $M_N = 0$, (b) $M_N = 2$, and (c) $M_N = 4$. The wavenumbers on the vertical axis are shown relative to the $v^+ = 0$, $N^+ = 0$ series limit.

be $r_\alpha \simeq (\alpha_{NO^+})^{1/3}$ [102], where $\alpha_{NO^+} \simeq 8$ a.u. is the electric dipole polarisability of the NO^+ cation [117, 118].

An example of a Stark map calculated by diagonalising $\hat{H}^{(d)}_{tot}$, and encompassing the wavenumber region around the field-free 38(2) state, is displayed in Fig. 3.5. The energy-level structure for states with $M_N = 0$, 2, and 4 are displayed in Fig. 3.5(a), (b), and (c), respectively. The quantum numbers used to label the individual states on the left-hand side of each panel in this figure indicate the dominant character in zero electric field. In this labelling scheme, a distinction is made between non-degenerate low-ℓ ($\ell \leq 3$) states, for which the dominant ℓ character can be determined in weak fields, and high-ℓ ($\ell \geq 4$) degenerate states. For context, atomic Stark effect calculations can achieve accuracies of ~ 30 MHz for electric fields up to the Inglis–Teller limit [119]. In NO similar calculations to those presented here have been tested to lower precision [71, 88].

3.5 Lifetime calculations for NO

Using the eigenvectors obtained following diagonalisation of $\hat{H}^{(d)}_{tot}$, the lifetimes of the Rydberg states in NO in the presence of an electric field could be determined.

Table 3.2: Predissociation rate parameters, $R_{\mathrm{dis}}(\ell)$, for $v^+ = 0$ states in NO (see text for details).

ℓ	$R_{\mathrm{dis}}(\ell)\,(\mathrm{s}^{-1})$	Refs.
0	9.42×10^{13}	[86]*
1	3.03×10^{14}	[82, 86]
2	1.88×10^{14}	[86]*
3	8.10×10^{12}	[82, 86]
4	1.60×10^{11}	[89, 110]

* Arbitrarily partitioned in Ref. 86 from $[R_{\mathrm{dis}}(0) + R_{\mathrm{dis}}(2)]/2\pi c \simeq 1500\ \mathrm{cm}^{-1}$.

Knowledge of the rates of decay by fluorescence, $\gamma_{\mathrm{fl}(k)}$, and predissociation, $\gamma_{\mathrm{dis}(k)}$, of each basis state, denoted $|k\rangle = \left|n_k\,\ell_k\,N_k^+\,N_k\,M_{Nk}\right\rangle$, allowed the total decay rate of an eigenstate $|i\rangle$ of $\hat{H}_{\mathrm{tot}}^{(\mathrm{d})}$ to be expressed as,

$$\gamma_{0(i)} = \sum_k |c_{ik}(F_z)|^2 \left(\gamma_{\mathrm{fl}(k)} + \gamma_{\mathrm{dis}(k)}\right), \tag{3.33}$$

where $c_{ik}(F_z) = \langle k|i(F_z)\rangle$ are the coefficients of the corresponding eigenvector in the electric field F_z.

In this calculation the fluorescence decay rates $\gamma_{\mathrm{fl}(k)} = 1/\tau_{\mathrm{fl}(k)}$ of the basis states were calculated by considering the Einstein-A coefficients of the hydrogenic Rydberg states in zero field. These values are expected to be correct to within an order of magnitude, with better agreement for higher values of ℓ. The effect of ℓ-mixing was then accounted for through the dependence of $c_{ik}(F_z)$ on the field strength (see Section 3.2).

The predissociation rates, $\gamma_{\mathrm{dis}(k)}$, required in Eq. 3.33 are dependent upon ν_k and ℓ_k. This dependence can be expressed as [86],

$$\gamma_{\mathrm{dis}(k)} = \frac{R_{\mathrm{dis}}(\ell_k)}{\nu_k^3}, \tag{3.34}$$

where $R_{\mathrm{dis}}(\ell_k)$ is the predissociation rate parameter for a basis state with $\ell = \ell_k$. The predissociation rate parameters for Rydberg states in the $v^+ = 0$ series that are available in the literature for values of $\ell \leq 4$, and used in the calculations described

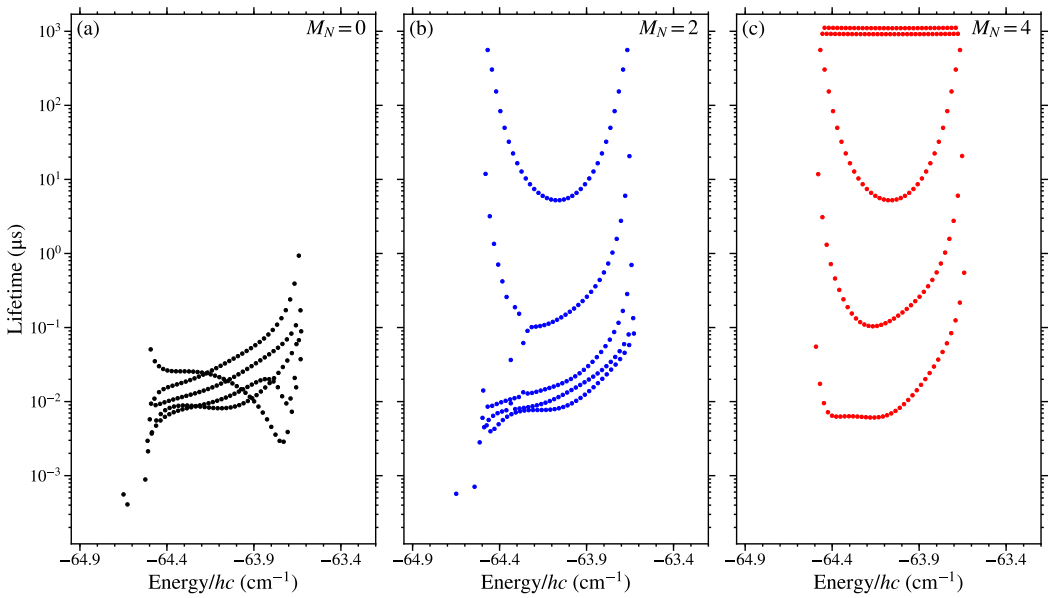

Figure 3.6: Calculated lifetimes of Rydberg-Stark states in NO with $n = 38$, $N^+ = 2$, and $v^+ = 0$ for (a) $M_N = 0$, (b) $M_N = 2$, and (c) $M_N = 4$. For each value of M_N, the $2N^+ + 1 = 5$ Stark manifolds are shown, with the calculated lifetimes determined using Eq. 3.33, which also depend on the ℓ-mixed character (see text for details). The wavenumbers on the horizontal axis are shown relative to the $v^+ = 0$, $N^+ = 0$ series limit. All calculations were performed for an electric field of 5 V cm^{-1}.

here, are presented in Table 3.2, and are expected to be accurate to within an order of magnitude. For higher values of ℓ, $R_{\rm dis}(\ell)$ was assumed to be zero in these calculations, because currently explicit measurements of predissociation rates for higher-ℓ states are absent in the literature. This absence of higher-ℓ predissociation rate parameters, and therefore the assumption that higher-ℓ states do not have a significant predissociation rate, is the primary limitation of the lifetime calculations performed here.

The calculated lifetimes, $\tau_{0(i)} = 1/\gamma_{0(i)}$, of the $n = 38$, $N^+ = 2$ Rydberg states in the $v^+ = 0$ series with $M_N = 0$, 2, and 4 in NO are shown in Fig. 3.6(a), (b), and (c), respectively. In each panel, the $2N^+ + 1 = 5$ Stark manifolds can be identified. All calculations shown in this figure were performed for an electric field of 5 V cm^{-1}. For low values of $|M_N|$, i.e., $|M_N| \leq 2$, contributions from predissociation dominate the decay of the excited states and the lifetimes of the states in the different Stark manifolds overlap. For larger values of $|M_N|$, predissociation plays a less important

role, and the corresponding states decay predominantly by fluorescence.

The high predissociation decay rates of the low-ℓ ($\ell \leq 3$) basis states, which are between $\sim 10^8$ s^{-1} and $\sim 5 \times 10^9$ s^{-1} for $n = 38$, dominate over the fluorescence decay rates ($\sim 10^4$ s^{-1} for $n = 38$) of these states. On the other hand, for high-ℓ basis states ($\ell \geq 4$) the total decay rates are smaller, with fluorescence rates ranging from $\sim 10^2$ s^{-1} to $\sim 10^4$ s^{-1} and predissociation rates $< 3 \times 10^6$ s^{-1}, which decrease with decreasing values of ℓ. Because of the lack of available predissociation rate data for higher ℓ states, only the predissociation of basis states with $\ell \leq 4$ was considered in calculations. With this in mind, mixed states, with some high-ℓ character and some low-ℓ character, can have significantly reduced lifetimes compared to those of the higher-ℓ states in zero-electric-field. This can be seen in Fig. 3.6(a), where all possible ℓ values are present for $M_N = 0$, with significant low-ℓ character mixed into all Stark states. The lifetimes of states with $M_N = 0$ are all < 1 μs, i.e., they decay predominantly by predissociation even in weak electric fields.

When $|M_N| > 0$ not all low-ℓ basis states contribute to the ℓ-mixed Stark states. However individual low-ℓ states are not absent from all Stark manifolds with the same value of $|M_N|$. Contributions from basis states with particular values of N^+ and ℓ reduce when $|M_N| > |N^+ - \ell|$, and are completely absent when $|M_N| > N^+ + \ell$. Therefore, in the example case with $N^+ = 2$, to prevent $\ell \leq 3$ basis states mixing into at least one of the Stark manifolds populated, it is necessary for $|M_N|$ to be greater than or equal to 2. The effect this has on the lifetimes can be seen in Fig. 3.6(b) and (c). When $M_N = 2$ [Fig. 3.6(b)], only one of the $N^+ = 2$ Stark manifolds has no $\ell \leq 3$ character. This manifold is easily identifiable as that with lifetimes between ~ 10 μs and ~ 1 ms. The shorter lifetimes towards the centre of this manifold reflect the presence of an $\ell = 4$ component which causes decay by predissociation.

For the case in which $M_N = 4$ [Fig. 3.6(c)], the Stark manifolds are clearly distinguishable by the lifetimes of their component states. In the manifold with the shortest lifetimes (~ 10 ns) the lowest-ℓ basis states present are those for which $\ell = 2$. Whereas, in the manifold with the longest lifetimes (~ 1 ms) $\ell \geq 6$. In between these extreme cases the lowest ℓ basis state present lies between these values. In

Table 3.3: Singlet N_2 Hund's-case-(b) quantum defects, $\mu_{\ell\Lambda}^{(b)}$, for $\ell \leq 2$ from Ref. 120.

		Λ		
		0	1	2
ℓ	0	0.900		
	1	0.608	0.684	
	2	0.13	-0.07	0.03

these data it is therefore possible to distinguish between manifolds of states that decay predominantly by predissociation and contain low-ℓ ($\ell \leq 3$) character, and those with only high-ℓ ($\ell \geq 4$) character for which decay by fluorescence dominates. The asymmetry in the lifetimes of the states of the Stark manifolds with $\ell \leq 3$ character in Fig. 3.6, arises because the low-ℓ states are not degenerate with those of higher ℓ in zero-field.

3.6 Calculations of the Stark effect in Rydberg states of N_2

For the singlet Rydberg states of N_2, that converge to the $X^+\,^2\Sigma_g^+\,(v^+, N^+)$ ground state of the ion core, similar Stark effect calculations to those in Section 3.4 were performed. Hund's case (d) is an appropriate choice of basis for these calculations, particularly because $S = 0$ for the singlet states. Since N_2 and N_2^+ have no electric dipole moment in their ground states, the field-free Hamiltonian for the Rydberg states of N_2, given by Eq. 3.15, does not contain contributions from charge-dipole interactions. As a result $\hat{H}_0^{(d)} = \hat{H}_{diag}^{(d)} + \hat{H}_{multi}^{(d)}$, where $\hat{H}_{diag}^{(d)}$ and $\hat{H}_{multi}^{(d)}$ are given by Eqs. 3.16 and 3.24, respectively. In addition to this, Rydberg series in N_2 that converge to even or odd values of N^+ are isolated from each other because these series are associated with the ortho and para forms of N_2, with ortho-para interconversion being forbidden [95].

The Hund's-case-(b) quantum defects, required in calculating $\hat{H}_{multi}^{(d)}$ and in calculating the Hund's-case-(d) quantum defects using Eq. 3.29, are listed in Table 3.3 for $\ell \leq 2$. Since the contributions of $s\sigma - d\sigma$ mixing have not been studied in the literature for high Rydberg states, this was not accounted for in the calculations.

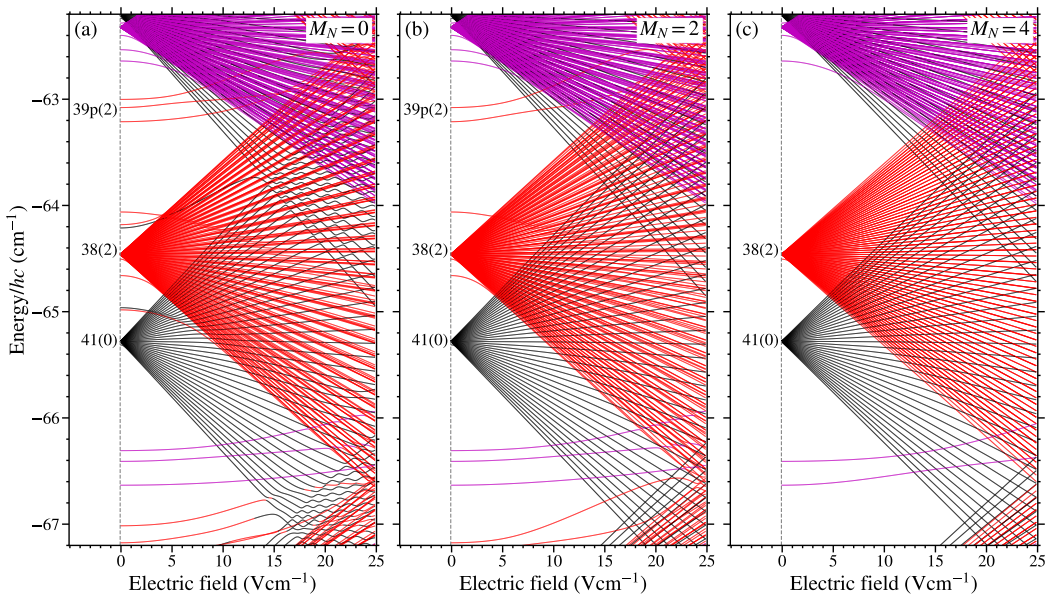

Figure 3.7: Calculated Stark maps for $v^+ = 0$ Rydberg states in N_2 with (a) $M_N = 0$, (b) $M_N = 2$, and (c) $M_N = 4$. Only states with even values of N^+ are shown. The wavenumbers on the vertical axis are shown relative to the $v^+ = 0$, $N^+ = 0$ series limit.

The Hund's-case-(b) quantum defects for Rydberg states with $\ell = 3$ were not available in the literature. However, the Hund's-case-(d) quantum defect for these states is known to be ~ 0.01 [94]. This value was therefore used for all $\ell = 3$ states in the calculations. States with $\ell \geq 4$ were assumed to have Hund's-case-(d) quantum defects of zero. In calculating $\hat{H}^{(\mathrm{d})}_{\mathrm{diag}}$, the Rydberg constant corrected for the reduced mass of N_2 was $R_{N_2} = 109735.17$ cm^{-1}, the ionisation wavenumber for states in the $v^+ = 0$ series was $W_0 = 125667.0$ cm^{-1}, and the rotational and centrifugal distortion constants of the N_2^+ cation with $v^+ = 0$ were $B_0^+ = 1.92234$ cm^{-1} and $D_0^+ = 6.106 \times 10^{-6}$ cm^{-1}, respectively [92, 94, 121].

With this information the Stark effect in the Rydberg states of N_2 was then calculated in the same way as in Section 3.4, using Eq. 3.30 to account for the perturbations to the zero-field Hamiltonian that arise from the external electric field. An example of a Stark map, calculated in this way, is shown in Fig. 3.7 for the wavenumber region encompassing the field-free 38(2) state. Because of the restrictions imposed by the nuclear-spin statistics, only even values of N^+ were considered in these calculations. The energy-level structure for states with $M_N = 0$, 2, and 4

is displayed in Fig. 3.7(a), (b), and (c), respectively. Unfortunately, unlike the case of NO, where a significant body of literature exists on the predissociation rates of the low-ℓ Rydberg states, the predissociation decay rates for even the low-ℓ ($\ell \lesssim 3$) Rydberg states in N_2 are not available. Consequently the lifetimes of the Rydberg states in the presence of electric fields could no be determined.

Chapter 4

Experimental techniques

The possibility of controlling the motion of atoms and molecules in Rydberg-Stark states, with large static-electric dipole moments, arises because forces can be exerted on samples in these states using inhomogeneous electric fields. This idea was first suggested by Wing [15] and Breeden and Metcalf [16] in the 1980s. Experiments to control the motion of Rydberg atoms in this way were then first reported in 2001 by Townsend *et al.* [122]. In this work, beams of krypton atoms in selected Rydberg-Stark states were deflected using the inhomogeneous electric field above two oppositely charged cylindrical electrodes. Since then, a wide range of tools for guiding, decelerating, and trapping Rydberg atoms and molecules have been implemented which rely on the same general principles [26]. Since all neutral atoms and molecules with a stable ion core possess Rydberg states, these methods can in principle allow for the control of the motion of any species for which excitation to these states can be achieved. Previously, Rydberg-Stark deceleration and guiding experiments have been performed to control the motion of H [123–127], D [128], H_2 [62, 63, 129–131], HD [59, 64], D_2 [64], He [132–137], Ar [138, 139], Kr [122], and Ps [140–142]. Of these only H, D, H_2, and He were electrostatically trapped following Rydberg-Stark deceleration [62, 63, 125, 128, 134–136].

The experiments described in this thesis utilised the technique of Rydberg-Stark deceleration to prepare samples of cold trapped diatomic molecules in highly-excited Rydberg states. Specifically, a chip-based transmission-line Rydberg-Stark decelerator was used [133, 134, 143]. The techniques described below can allow

for a species independent means of trapping cold samples of atoms or molecules, provided they can be efficiently excited to Rydberg-Stark states with large electric dipole moments ($\gtrsim$ 1000 D), and lifetimes $\gtrsim$ 10 μs. This species-independent means of preparing cold samples of atoms or molecules is particularly desirable for studies involving molecules for which other methods of cooling or trapping cannot be used, e.g., there are no convenient closed-cycling laser cooling transitions available, no ground-state electric or magnetic dipole moments, or where buffer gas cooling is not efficient [144].

4.1 Principles of Rydberg-Stark deceleration

As discussed in Chapter 3, in an electric field, $\vec{F}$, the Rydberg states of an atom or molecule undergo a Stark shift [66]. Examples of the Stark shifts of high-Rydberg states of NO and N_2 can be seen in Figs. 3.5 and 3.7, respectively, for $M_N = 0$, 2, and 4. The total energy of these Rydberg-Stark states can be considered to be

$$E_{\rm tot} = E_0 + E_{\rm Stark}, \tag{4.1}$$

where E_0 is the field-free energy and $E_{\rm Stark}$ corresponds to the shift in the energy because of the Stark effect. For hydrogenic Rydberg states [labelled $n(N^+)$ in Figs. 3.5 and 3.7] this Stark shift is approximately linear in small electric fields [66], and can be expressed as,

$$E_{\rm Stark} = -\vec{\mu}_{\rm elec} \cdot \vec{F}, \tag{4.2}$$

where $\vec{\mu}_{\rm elec}$ is the static electric dipole moment of the Rydberg-Stark state.

If a molecule in a Rydberg-Stark state is located in an inhomogeneous electric field, a force is exerted on it in the direction that minimises its potential energy, $E_{\rm tot}$. Since the field-free energy, E_0, in Eq. 4.1 has no dependence on the electric field, the force exerted on the molecule depends only on the Stark shift and is given by,

$$\vec{f} = -\vec{\nabla}\left(E_{\rm Stark}\right). \tag{4.3}$$

For states with linear Stark shifts,

$$\vec{f} = \vec{\nabla}\left(\vec{\mu}_{\text{elec}} \cdot \vec{F}\right). \tag{4.4}$$

Therefore, states with positive (negative) energy shifts, i.e., $E_{\text{Stark}} > 0$ ($E_{\text{Stark}} < 0$), are known as low-field-seeking [LFS] (high-field seeking [HFS]), because the force exerted on a molecule in these states acts in the direction of smaller (larger) electric fields. If a molecule in a LFS state travels from a region of small to large electric field, its potential energy increases and hence its kinetic energy decreases, because of the Stark effect. This leads to deceleration of the molecule. This force can be utilised to trap sufficiently cold/slow moving molecules in LFS Rydberg-Stark states around electric field minima.

However, it is not necessarily possible to use arbitrarily large electric fields to decelerate and trap molecules in Rydberg-Stark states. Firstly, in large electric fields the probability of electric field ionisation increases, with the field required for ionisation scaling with n^{-4} [26, 66, 90, 145]. Secondly, the presence of non-degenerate low-ℓ states in the Stark manifold, which occurs for low values of $|M_N|$, can result in large avoided crossings where states of adjacent n cross. This can be seen for NO [N_2] in Fig. 3.5(a) [Fig. 3.7(a)] when $M_N = 0$. The probability of traversing these large avoided crossings adiabatically is generally high, and the molecule then goes from being LFS to HFS (or *vice versa*) as the energy shift around the avoided crossing switches from being positive to negative (or *vice versa*). The electric fields that can be used for deceleration and trapping in cases where large avoided crossing are encountered must therefore be limited to those below the crossings. These are typically the fields associated with the Inglis-Teller limit $F_{\text{IT}} = F_0/(3n^5)$ [where $F_0 = 2hcR_M/ea_M$, with R_M and a_M are the Rydberg constant and Bohr radius adjusted for the reduced mass] where the n and $n+1$ manifolds first cross [66]. However, if low-ℓ states with large quantum defects are removed from the Stark manifolds, which can be achieved by exciting states of high-$|M_N|$, these avoided crossings are significantly smaller, see Fig. 3.5(c) [Fig. 3.7(c)] for $M_N = 4$ in NO [N_2]. In this situation the probability of traversing the avoided crossings diabati-

cally is high and the energy shift of the molecule remains of the same sign on either side of the crossing, which allows efficient deceleration in larger electric fields and the removal of significantly more kinetic energy per unit distance in a field gradient.

The finite lifetimes of Rydberg-Stark states also impose limitations on the particular states that can be decelerated and trapped. To decelerate molecules in Rydberg states their lifetimes must be at least comparable to the time it takes to implement the deceleration process. As typical timescales for deceleration in the experiments described here are $\sim 100\,\mu$s, the states used for deceleration must have lifetimes significantly in excess of $\sim 10\ \mu$s. Deceleration can therefore only be effectively achieved using states with high-$|M_N|$ which have lifetimes several orders of magnitude larger than those of low-$|M_N|$, because of the removal of the fast predissociative low-ℓ character from the Stark-manifold, as is discussed in Section 3.5 and shown in Fig. 3.6 for the case of NO.

Molecules in Rydberg states with high values of $|M_N|$, i.e., $|M_N| \gtrsim 3$, can be populated selectively using resonance-enhanced multi-photon excitation schemes with circularly polarised laser radiation, as has been demonstrated for the case of H_2 molecules [62, 63]. Alternatively, similar high-$|M_N|$ states can be populated by M_N-mixing in weak time varying electric fields [76, 91], that can originate from the presence of charged particles or electrical noise close to the time of photoexcitation. In this case deceleration and trapping of the molecules acts to filter out those in these long-lived high-$|M_N|$ states. This filtering of the molecules in long-lived Rydberg states occurs because of the finite time required for the deceleration, and because of the requirement to undergo diabatic transversal of the avoided crossings in the deceleration fields, which also only occurs with a high probability for high values of $|M_N|$.

4.2 Experimental apparatus and methods

A schematic diagram of the apparatus used in the experiments can be seen in Fig. 4.1. A pulsed supersonic beam of NO or N_2 molecules was generated, with a mean longitudinal speed $\bar{v}_z \simeq 800\,\mathrm{m\,s^{-1}}$, using a pulsed value (Parker series 9 pulse

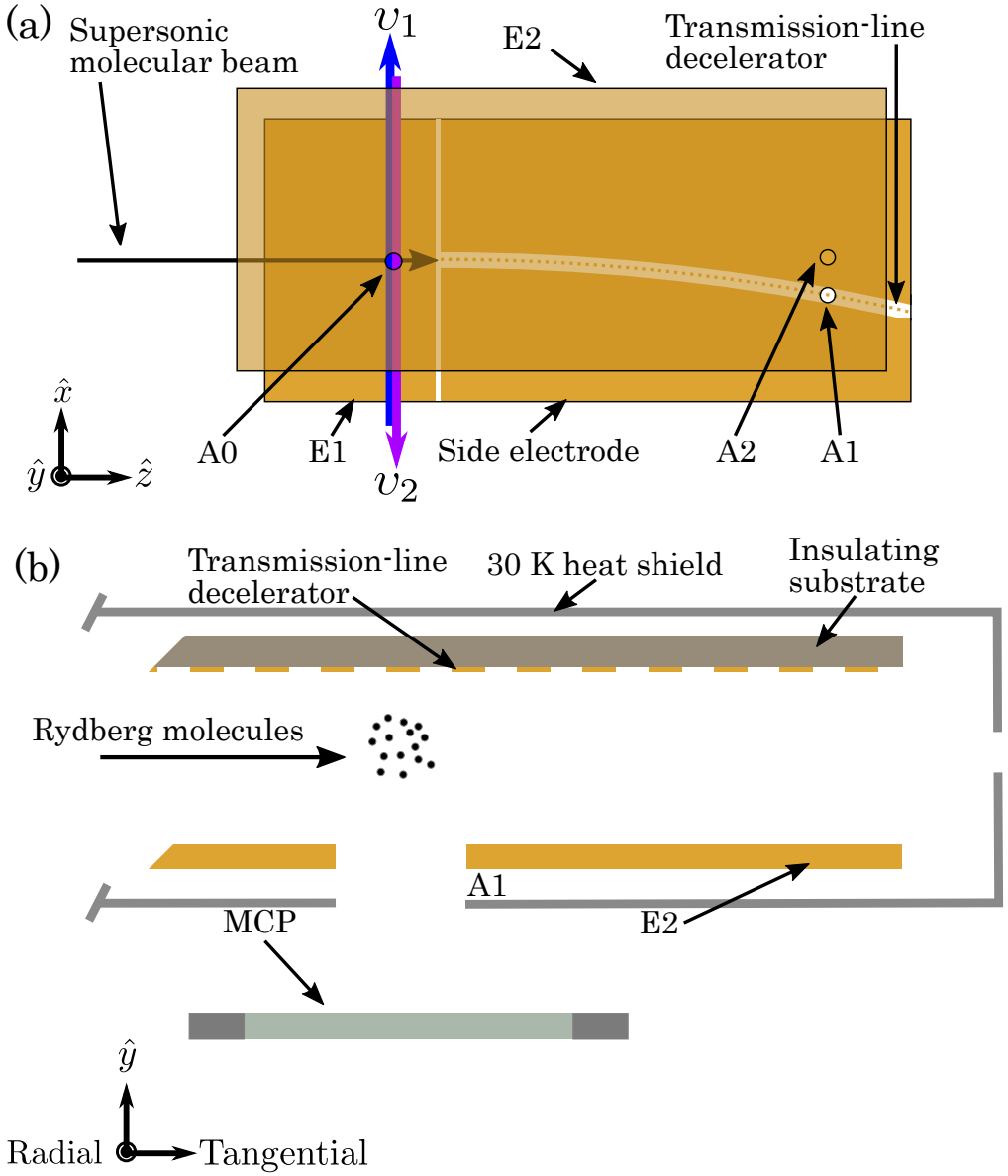

Figure 4.1: Schematic diagram (not to scale) of the chip-based Rydberg-Stark decelerator used in the experiments, (a) in the *xz*-plane, and (b) in the plane along the decelerator axis close to the detection region. The radial and tangential directions to the decelerator axis are indicated in panel (b). E1 and E2 represent metallic electrodes. A0, A1, and A2 are 2-mm-diameter detection apertures in electrode E2.

value with 0.5-mm orifice, $\sim$ 2 to 4 bar stagnation pressure, $\sim$ 200 μs pulse width) operated at a repetition rate of 25 Hz. After passing through a 2-mm-diameter skimmer, the molecular beam entered into a cyrogenically cooled ($\sim$ 30 K) region of the apparatus containing the chip-based transmission-line Rydberg-Stark decelerator [133, 134]. The background pressure in the experiment, after the 2-mm-diameter

skimmer, was $\sim 10^{-8}$ to 10^{-7} mbar.

The Rydberg-Stark decelerator consisted of two parallel horizontal planes separated from each other by 3 mm. The lower plane was a solid copper electrode, E2 in Fig. 4.1. The upper plane consisted of etched double-sided silver-plated copper electrode structure on an insulating arlon substrate. The front of the upper plane consisted of: (i) a rectangular excitation electrode E1; (ii) a curved array of 115 square electrodes, with 0.5 mm sides, separated from each other by a 0.5 mm insulating gap; and (iii) two side electrodes. Electrical contact between the electrodes in the array where made on the back of the upper plane, using an etched circuit with silver filled through-hole-vias. The circuit on the back side was laid out to connect every 6^{th} electrode in the array together, i.e., electrode j was connected to electrode $(j+5)$. The electrode array therefore consists of 23 groups of $N = 5$ electrically independent electrodes which had a spatial periodicity of $L = 5$ mm. This number of electrically independent electrodes was chosen to give a reasonable balance between minimising changes in the vertical displacement of the electric field minima as the trap moves [133], and the technical complexity of having many potential sources and amplifiers. The radius of curvature of the electrode array was $R = 518.5$ mm. Apertures A0, A1, and A2 were 2-mm-diameter holes in electrode E2 through which ions or electrons could be extracted following pulsed electric field ionisation (PFI). Aperture A1 was located above the 101^{st} electrode in the array, and was used for *in situ* detection of molecules that were decelerated or trapped. The alignment of the apparatus, and the molecular beam, was optimised with the decelerator off by detection of the molecules above apertures A0 and A2. A0 was located at the photoexcitation position, ~ 4 mm away from the centre of the 1^{st} electrode in the deceleration array, and A2 at same z-position as A1 but at the same x-position as A0, i.e., on the molecular beam axis.

Laser photoexcitation to Rydberg states was performed between the electrodes E1 and E2. The particular photoexcitation schemes used for NO and N_2 are described in the following chapters. However, in general the molecules were excited to high-n Rydberg-Stark states by the fundamental, frequency-doubled, or

frequency-tripled outputs of two Nd:YAG pumped dye lasers with wavenumbers υ_1 and υ_2, with full-width-at-half-maximum (FWHM) spectral widths of ~ 0.2 cm^{-1}, and FWHM temporal widths of ~ 8 ns. The lasers were not focused into the excitation region of the experiment unless specified in the following chapter. The fundamental wavenumbers of the dye lasers were monitored using a fibre-coupled wavelength meter with an absolute accuracy of ± 0.005 cm^{-1}.

After photoexcitation the excited bunches of Rydberg molecules travelled ~ 4 mm before being loaded into a single travelling electric field trap of the transmission-line decelerator. The 3-dimensional electric field traps were generated by applying time dependent potentials of the form,

$$V_j(t) = V_0 \sin\left[-\frac{2\pi j}{N} + 2\pi f_{\rm osc}(t)t + \phi\right], \tag{4.5}$$

to the $j^{\rm th}$ electrode in the array, and a constant potential of $-V_0/2$ to E2. In Eq. 4.5: V_0 is the amplitude of the potentials applied to the electrode array, $f_{\rm osc}(t)$ is a time dependent oscillation frequency of the potentials, and ϕ is a constant phase. The $N = 5$ independent oscillating potentials were generated at a low voltage using arbitrary waveform generators and then amplified using 5 MHz bandwidth amplifiers. The potentials generated were linearly ramped on from an amplitude of zero to V_0 in a time of 4 μs. The maximum value of V_0 was limited to 150 V by the maximum peak-to-peak voltage output of the high frequency amplifiers. An example of the electric field distribution within the decelerator structure, calculated by finite element methods in the SIMION software package, for $V_0 = 149$ V is shown in Fig. 4.2.

By appropriately choosing the time-dependence of $f_{\rm osc}(t)$ it was possible to guide at a constant speed, decelerate, or trap molecules in LFS Rydberg-Stark states. The general form of $f_{\rm osc}(t)$ was chosen to be,

$$f_{\rm osc}(t) = \frac{1}{L}\left(v_{\rm i} + \frac{1}{2}a_{\rm t}t\right), \tag{4.6}$$

where $v_{\rm i}$ is the initial speed of the trap, set such that $v_{\rm i} \simeq \bar{v}_z$, and $a_{\rm t}$ is the tan-

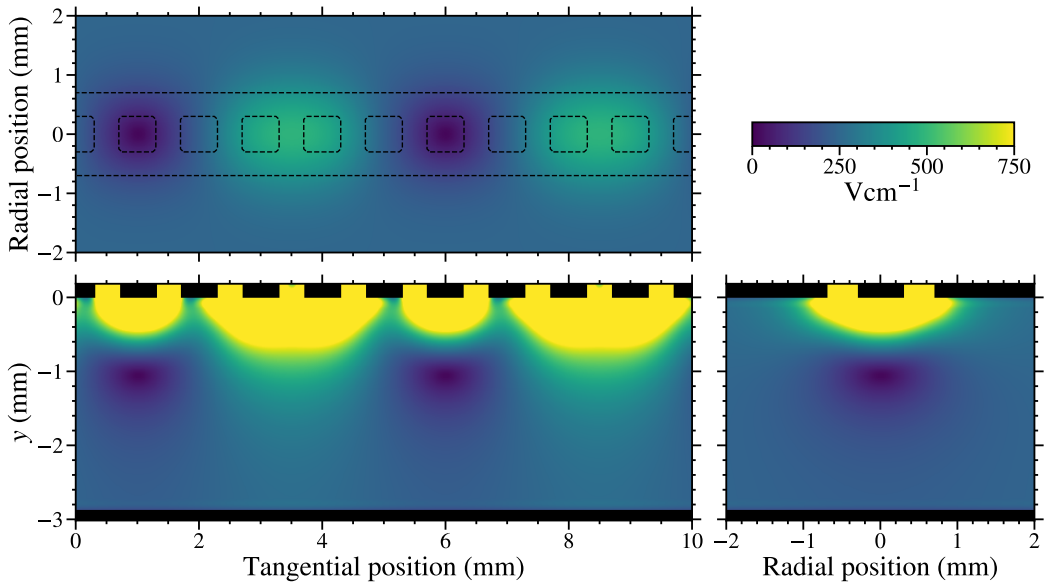

Figure 4.2: Example of the amplitude of the electric fields beneath a section of the transmission-line decelerator electrode array, for $V_0 = 149$ V. The slices shown intersect the minimum of the field distribution. The black regions represent electrodes and the dotted lines are the projected positions of the electrodes.

gential acceleration of the trap. Guiding at a constant speed was achieved by setting $a_t = 0\,\mathrm{m\,s^{-2}}$ such that the trap moves at a constant speed v_i. Deceleration of the trap, i.e., $a_t < 0\,\mathrm{m\,s^{-2}}$, was achieved by chirping the oscillation frequency of the applied potentials. The amount of chirp required was set by the desired final velocity of the trap, v_f, at the position 101st electrode, i.e., above A1, with $a_t = \left(v_f^2 - v_i^2\right)/2d$, where $d \simeq 100$ mm is tangential distance from the initial position of the travelling trap in which the molecules are transported to the centre of aperture A1. Electrostatic trapping was achieved by decelerating the traps such that $v_f = 0\,\mathrm{m\,s^{-1}}$, with the trap brought to rest above the detection aperture A1. The curved geometry of the transmission-line decelerator was chosen to minimise collisions between the Rydberg molecules undergoing deceleration and undecelerated molecules in the trailing edge of the supersonic beam. However, this meant that molecules in the travelling traps also experience a centripetal acceleration of $a_c = v^2(t)/R$, where $v(t) = v_i + a_t t$.

The molecules were detected *in situ* within the transmission-line decelerator by pulsed electric field ionisation (PFI). This was implemented by the application

of a pulsed potential of up to +500 V, with a rise time of $\sim$ 50 ns, to the side electrodes [see Fig. 4.1]. The resulting molecular cations were then accelerated through aperture A1, out of the cryogenic region of the apparatus, and collected on a room temperature microchannel plate (MCP) detector. By varying the time at which the PFI potential was applied, relative to the time of photoexcitation, time-of-flight (TOF) distributions of guided or decelerated Rydberg molecules were obtained. For molecules electrostatically trapped above A1 the change in the PFI signal, at times after the trap was brought to rest, reflecting the decay of molecules from the trap and their motion.

To obtain information on the distribution of Rydberg states populated, i.e., the range of states with different values of n, at the time of ionisation, state selective ionisation (SFI) was implemented using a slowly rising pulsed ionisation potential. This had a time dependence that could be expressed as $V_{\rm ramp} = V_{\rm max}[1-\exp(-t/\tau_{\rm ramp})]$, where $\tau_{\rm ramp}$ was 1 - 5 μs. When this slowly rising potential was applied, with $V_{\rm max} < 0$, to ionise the trapped molecules the resulting electrons were accelerated through A1 and collected at the MCP detector. The electron's shorter flight time to the MCP detector (typically $\lesssim$ 10 ns), than the molecular cations (typically $\sim$ 1 μs), permitted the most direct mapping of the detected electron signal to the applied potential at the time of ionisation [146].

Examples of measured TOF distributions, recorded with the decelerator on and off, are shown in Fig. 4.3 for NO molecules excited into Rydberg states with predominantly $n = 43$, $N^+ = 2$ character. The mean initial longitudinal speed of the molecular beam in the experiment was determined to be $\bar{v}_z = 810$ m s^{-1} from the TOF distribution with the decelerator off, by detection above aperture A2. With the decelerator on, and programmed for an initial trap speed of $v_i = 795$ ms^{-1}, guiding and deceleration were achieved. The decrease in the amplitude of the TOF distributions with increased deceleration $|a_{\rm t}|$ results from: (i) the finite lifetime of the Rydberg states populated, (ii) the reduced phase-space acceptance of the decelerator for larger values of $|a_{\rm t}|$, and (iii) the geometry of the *in situ* detection region [134].

Electrostatic trapping of NO molecules was achieved using a deceleration of

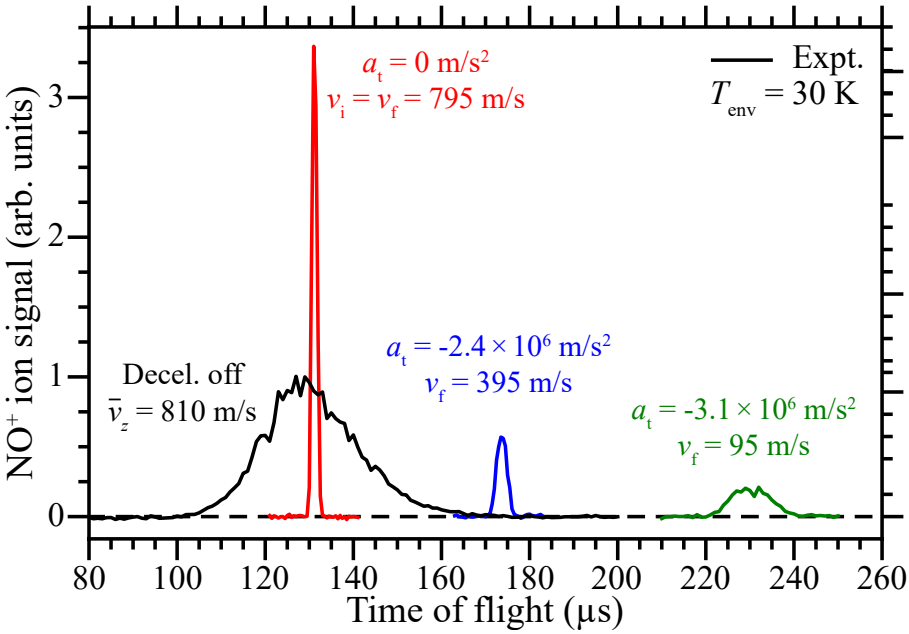

Figure 4.3: Measured TOF distributions from the time of photoexcitation of NO molecules into Rydberg states with predominantly $n = 43$, $N^+ = 2$ character ($\upsilon_1 = 44193.99$ cm^{-1} and $\upsilon_2 = 30475.08$ cm^{-1}). The TOF distribution recorded with the decelerator off and detected above aperture A2 is indicated by the continuous black curve. The other TOF distributions were measured with the decelerator on and programmed for an initial speed $v_i = 795$ m s^{-1} and decelerated to the final velocities indicated. All measurements were recorded with the apparatus cooled to ~ 30 K, $V_0 = 125$ V. Adapted from Ref. 143.

$a_t = -3.15 \times 10^6$ m s^{-2}. Under these condition, the trap was brought to rest above aperture A1 at a time ~ 250 μs after photoexcitation. Changes in the NO$^+$ ion signal at times later than this reflected the decay of the molecules from the trap. Example measurements of the decay of the molecules from the trap, recorded with the apparatus operated at temperatures $T_{env} = 295$ K and 30 K, are shown in Fig. 4.4. These data were normalised for comparison since fewer molecules where trapped with $T_{env} = 295$ K than when $T_{env} = 30$ K. By fitting a single exponential between trapping times of 50 μs and 350 μs (see Fig. 4.4) it can be seen that at 295 K the trap decay occurs much quicker than at 30 K. When $T_{env} = 295$ K the decay of the molecules from the trap is strongly affected by blackbody photoionisation [126, 137], which reduces the decay time constant when compared to that recorded for $T_{env} = 30$ K. As a result, the data recorded at 295 K reaches the level of background noise after ~ 600 μs, while it was possible to trap molecules for

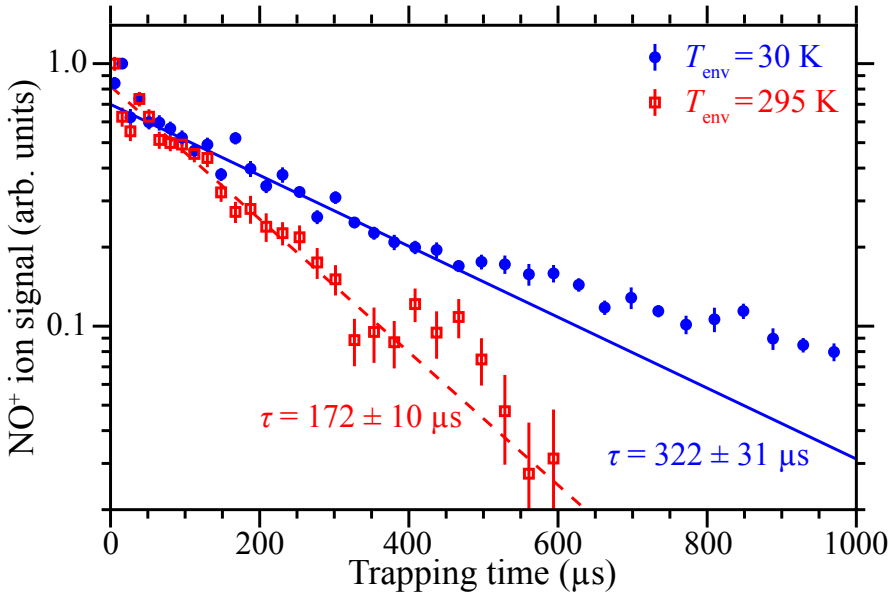

Figure 4.4: Decay of electrostatically trapped Rydberg NO molecules, initially excited into Rydberg states with predominantly $n = 43$, $N^+ = 2$ character ($\upsilon_1 = 44193.99$ cm^{-1} and $\upsilon_2 = 30475.08$ cm^{-1}), recorded with the apparatus operated at 295 K, or cooled to 30 K (as indicated). The trapping time of 0 μs indicates the time at which the electrostatic trap was brought to rest in the laboratory frame of reference, at a time 250 μs after photoexcitation. The continuous (dashed) line represents the single exponential fit to the data between trapping times of 50 μs and 350 μs. For both measurements $V_0 = 125$ V. From Ref. 143.

times up to 1 ms when $T_{\rm env} = 30$ K. The effects of blackbody induced transitions during deceleration and trapping were therefore minimised by performing the experiments at $T_{\rm env} = 30$ K. The number of molecules trapped per experimental cycle was estimated from the detected ion signal and electron counts to typically be ~ 10 - 100 at this temperature, such that the number density in the trap was $\sim 10^4$ - 10^5 cm^{-3}. This low density of molecules in the trap meant that effects of collisions within the trap should not significantly affect the measured trap decay rates, and collisions with background gases can also be neglected. Electric field ionisation is also not expected to significantly affect the measured trap decay rates. Numerical particle trajectory calculations (described below in Section 4.3), that include a Monte-Carlo treatment of the electric field tunnel ionisation process at each time step, indicate that electric field ionisation contributes < 1 s^{-1} to the total decay rate of the molecules from the trap for the range of values of n studied here.

4.3 Numerical trajectory calculations

To aid the interpretation of the experimental data, numerical particle trajectory calculations were performed. In these calculations the electric field distribution for a section of the decelerator, such as that shown in Fig. 4.2, was calculated by finite element methods in the software package SIMION. Trajectory calculations were then performed in the moving frame of reference of the travelling electric field traps, which is centred on the electric field minimum of the trap that the molecules were loaded into. In this moving frame of reference, the total potential energy, at the position $\vec{r}$, where $\vec{r} = (0,0,0)$ is the position of the electric field minimum, can be expressed as by [128, 133, 147]

$$V_{\mathrm{tot}}(\vec{r}) = V_{\mathrm{Stark}}(\vec{r}) + V_{\mathrm{pseudo}}(\vec{r}) \tag{4.7}$$

where $V_{\mathrm{Stark}}(\vec{r})$ is the Stark potential energy, and $V_{\mathrm{pseudo}}(\vec{r})$ is pseudo-potential that accounts for the acceleration of trap in this moving frame of reference. The Stark energy at the position $\vec{r}$ is given by the first order Stark effect (see Eq. 3.6), i.e., $V_{\mathrm{Stark}}(\vec{r}) = \frac{3}{2} nkea_0 |\vec{F}(\vec{r})|$ where $|\vec{F}(\vec{r})|$ is the magnitude of the electric field at position $\vec{r}$. The pseudo-potential, for a moving frame of reference centred on the electric field minimum of the trap, is given by [128, 133, 147]

$$V_{\mathrm{pseudo}}(\vec{r}) = m\vec{a}_{\mathrm{trap}} \cdot \vec{r}, \tag{4.8}$$

where m is the mass of the molecule, $\vec{a}_{\mathrm{trap}}$ is the acceleration of the trap, and $\vec{r}$ is the position relative to the electric field minimum. For the transmission-line Rydberg-Stark decelerator described here, there is both tangential and centripetal acceleration in the directions along and perpendicular to the array of electrodes, respectively. The tangential and centripetal accelerations are $a_{\mathrm{t}} = \left(v_{\mathrm{f}}^2 - v_{\mathrm{i}}^2\right)/2d$ and $a_{\mathrm{c}} = v^2(t)/R$, respectively, as described in Section 4.2. An example of the effect of the pseudo-potential on the trapping potential experienced by NO molecules in the moving frame of reference is shown in Fig. 4.5.

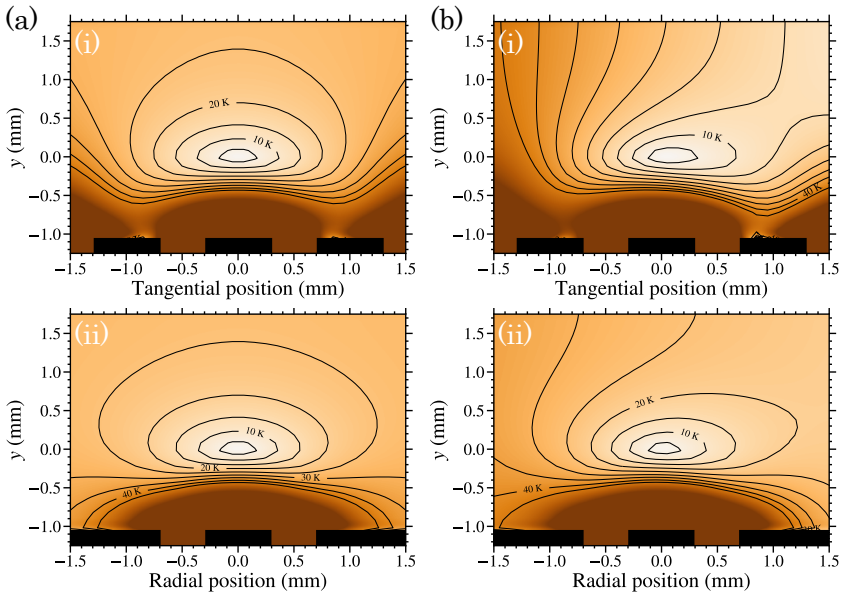

Figure 4.5: Total potential energy of NO molecules, in a hydrogenic $n = 38$, $k = 33$ Rydberg-Stark state with a static electric dipole moment of 4781 D, in the frame of reference of the electrostatic trap when it is: (a) stationary, and (b) experiencing tangential and centripetal accelerations of $a_t = -3.15 \times 10^6$ m s^{-1} and $a_c = -1.21 \times 10^6$ m s^{-1}, respectively. Panels (i) and (ii) show the 2D-slices of the potential through the electric field minimum for planes in the y-tangential and y-radial directions, respectively. The tangential and radial directions to the decelerator axis are as indicated in Fig. 4.1(b). Isopotential-energy curves for $V_{tot}(\vec{r})/k_B$, where k_B is the Boltzmann constant, are shown in 5 K intervals. All positions are given relative to the position of the minimum of the electric field of the trap.

Classical numerical particle trajectory calculations were then performed, in the moving frame of reference of the trap, using the velocity Verlet algorithm (leapfrog variant) [148, 149]. In this algorithm the position $\vec{r}_j(t)$, and velocity $\vec{v}_j(t)$, of the j^{th} molecule at time t, subjected to an acceleration of $\vec{a}_j(t)$ in a time step Δt were updated at each new time $t + \Delta t$ using

$$\vec{r}_j(t+\Delta t) = \vec{r}_j(t) + \vec{v}_j(t) + \frac{1}{2}\vec{a}_j(t)\Delta t^2 \tag{4.9}$$

$$\vec{v}_j(t+\Delta t) = \vec{v}_j(t) + \frac{1}{2}\left[\vec{a}_j(t) + \vec{a}_j(t+\Delta t)\right]\Delta t, \tag{4.10}$$

where $\vec{a}_j(t+\Delta t)$ was calculated at position $\vec{r}_j(t+\Delta t)$. The force exerted on the molecule at time t, was obtained from the local gradient of the total potential in the

moving frame of reference, i.e.,

$$\vec{f}(\vec{r}_j(t)) = -\vec{\nabla}\left[V_{\rm tot}(\vec{r})\right]|_{\vec{r}=\vec{r}_j(t)}\,, \tag{4.11}$$

where $V_{\rm tot}(\vec{r})$ is given by Eq. 4.7. However, as $V_{\rm tot}(\vec{r})$ is time dependent, because of the time dependence of the centripetal acceleration of the trap, $a_{\rm c}$, it was also updated at each time step. Once the trap came to rest, i.e., when $t \geq 2d/v_i$ for a final velocity of $v_f = 0$ m s^{-1}, the total potential $V_{\rm tot}(\vec{r})$ no longer depends on time and has no contributions from $V_{\rm pseudo}(\vec{r})$.

Electric field ionisation of the molecules during the deceleration and trapping processes was accounted for in the trajectory calculations using Monte-Carlo methods. Since the molecules that were decelerated and trapped were high-$|M_N|$ Rydberg states, which have been previously observed in NO to ionise hydrogenically with the avoided crossings in the Stark map traversed diabatically [90], their electric field tunnel ionisation rates can be approximated using the hydrogenic electric field ionisation rate [145, 150],

$$\Gamma_{nn_1n_2m_\ell} = \frac{E_{\rm Har}}{\hbar}\frac{(4R)^{2n_2+m_\ell+1}}{n^3 n_2!(n_2+m_\ell)!}\exp\left[-\frac{2}{3}R - \frac{1}{4}n^3\frac{ea_0|\vec{F}|}{E_{\rm Har}}\right.$$
$$\left.\times\left(34n_2^2 + 34n_2m_\ell + 46n_2 + 7m_\ell^2 + 23m_\ell + \frac{53}{3}\right)\right], \tag{4.12}$$

where

$$R = \frac{1}{ea_0\sqrt{E_{\rm Har}}}\frac{(-2E_{nn_1n_2m})^{3/2}}{|\vec{F}|} \tag{4.13}$$

and $E_{nn_1n_2m} = -[E_{\rm Har}/(2n^2)] + E_{\rm Stark}$, with $k = n_1 - n_2$ the difference between the parabolic quantum numbers n_1 and n_2, and $E_{\rm Har} = 2hcR_{\rm M}$ is the Hartree energy where $R_{\rm M}$ is the Rydberg constant adjusted for the reduced mass. The ionisation rate of a Rydberg-Stark state $|nkm_\ell\rangle$ was determined using Eq. 4.12 and the relation that $n_2 = (n-k-|m_\ell|-1)/2$ in the calculation.[1] For a molecule in an electric field $|\vec{F}(\vec{r}_j(t))|$ at time t, the probability of surviving without ionising in the time step Δt

[1] This relation can be derived from the relations that $k = n_1 - n_2$ and $n = n_1 + n_2 + |m_\ell| + 1$ [66].

was obtained from

$$P_{\Delta t}(\vec{r}_j(t)) = \exp\left[-\Gamma_{\text{ion}}(\vec{r}_j(t))\,\Delta t\right] \tag{4.14}$$

where $\Gamma_{\text{ion}}(\vec{r}_j(t))$ was calculated using Eq. 4.12. In the Monte-Carlo approach the value of $P_{\Delta t}(\vec{r}_j(t))$ was then compared a random number, P_{Rand}, between 0 and 1 sampled from a uniform distribution. If $P_{\text{Rand}} \geq P_{\Delta t}(\vec{r}_j(t))$, the molecule was considered to ionise in that time-step, whereas if $P_{\text{Rand}} < P_{\Delta t}(\vec{r}_j(t))$ the molecule was not field ionised and the calculation continued.

Numerical particle trajectory calculations for between 15000 and 30000 molecules were performed for NO Rydberg molecules, with a mass of $m_{\text{NO}} = 4.98263 \times 10^{-26}$ kg. These calculations were primarily performed for values of n between 30 and 50 for the outermost $m_\ell = 4$ LFS Stark-states, i.e., the $k = n-5$ Stark state. The trajectories of the molecules were calculated for the full deceleration period and for trapping times up to $t_{\text{trap}} = 400$ μs. In the calculations presented here, the initial trap velocity was set to $v_i = 795$ m s^{-1} with $v_f = 0$ m s^{-1} and $d = 100.25$ mm. The trapping potentials applied to electrodes were determined by Eq. 4.5 with $V_0 = 149$ V and a constant potential of $-V_0/2$ applied to electrode E2. The initial positions of the molecules were generated from a Gaussian distribution, centred on $\vec{r} = (0,0,0)$ with a standard deviation of $\sigma = 0.5$ mm in each dimension. Similarly, the initial velocities in the moving frame of reference of the trap were also sampled from a Gaussian distribution, centred on $\vec{v} = (0,0,\bar{v}_z - v_i)$, where $\bar{v}_z = 810$ m s^{-1}, with a standard deviation of $\vec{\sigma}_{\vec{v}} = (2,2,90)$ m s^{-1}.

One important output from these calculations was that, for the range of values of n studied here, the majority (~ 99 %) of losses by electric field ionisation occurred during deceleration before the trap was brought to rest, i.e., at times < 250 μs. Approximately 95 % (64 %) of these losses occur within 100 μs (50 μs) of the deceleration process starting. The effect of electric field ionisation on the decay of molecules from the stationary electrostatic trap was studied in a general way by introducing a Monte-Carlo trap decay at a rate of $\gamma_{\text{trap}} = 3.3 \times 10^3$ s^{-1} (i.e., with a decay time constant of $\tau_{\text{trap}} = 300$ μs) to represent the decay of the excited molecules, e.g., by spontaneous emission or predissociation, in addition to the

Monte-Carlo treatment of the electric field ionisation. A fit of a single exponential function with a decay rate γ_{fit} to the resulting number of trapped molecules between trapping times of $t_{\text{trap}} = 50$ μs and 350 μs with and without inclusion of electric field ionisation were performed. The difference between the values of γ_{fit} in these two cases was < 1 s^{-1} across the range of values of n investigated. Therefore it was concluded that electric field ionisation does not play a significant role in the measured total decay rates of the molecules from the trap. Finally, the numerical particle trajectory calculations were used to calculate the mean time-averaged field experienced by molecules in the trap. This was found to be approximately 95 V cm^{-1} with a standard deviation of 30 V cm^{-1}. These values were approximately constant across the range of values of n investigated here.

Chapter 5

Trap decay measurements of $v^+ = 0$ Rydberg NO

Detailed studies of high Rydberg states of NO are of interest to atmospheric physics [41–44] and ultracold molecular plasma dynamics [50–53]. In addition, the significant body of work in the literature, and the range of intramolecular interactions that occur in the Rydberg states of NO make it an ideal candidate for studies of the properties, and slow decay dynamics, of molecular Rydberg states. In this chapter, Section 5.1 provides a general overview of the laser photoexcitation schemes used to excite NO molecules into the high-n Rydberg states. Section 5.2 is based on work published in Ref. 98, but adapted to the requirements of this thesis. This section contains a description of experiments performed to trap long-lived Rydberg NO molecules, in series converging to the $v^+ = 0$ state of the NO^+ cation. Conclusions are then drawn in Section 5.3.

5.1 Excitation scheme

In the experiments described in this thesis NO molecules were excited into high Rydberg states using the resonance-enhanced two-colour two-photon

$$\mathrm{X}\,^2\Pi_{\Omega''}(v'', J'') \rightarrow \mathrm{A}\,^2\Sigma^+(v', N', J') \rightarrow n\ell\,\mathrm{X}^+\,^1\Sigma^+(v^+, N^+) \tag{5.1}$$

excitation scheme [84, 85, 88, 90, 151]. Here, $\mathrm{X}\,^2\Pi_{1/2}$ is the ground electronic state of NO, $\mathrm{A}\,^2\Sigma^+$ is the intermediate state, and $n\ell\,\mathrm{X}^+\,^1\Sigma^+$ represents the high-n

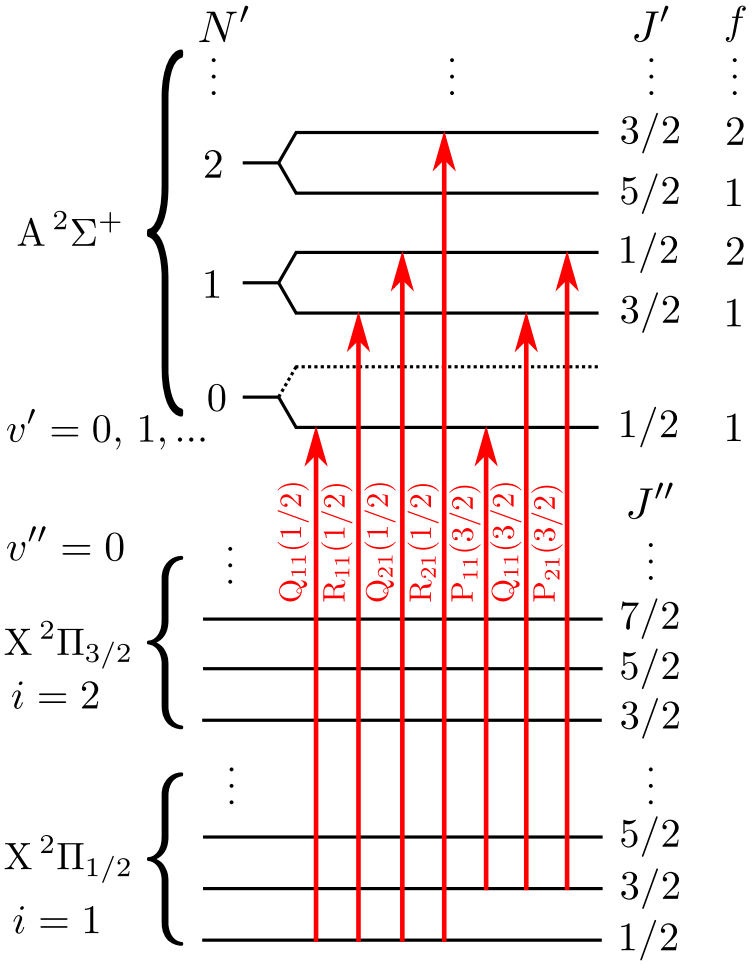

Figure 5.1: Schematic diagram of sublevels in the $X\,^2\Pi_{1/2}$ and $X\,^2\Pi_{3/2}$ states and the $A\,^2\Sigma^+$ intermediate state in NO. Examples of allowed transitions from the ground to intermediate states are indicated by the vertical arrows.

Rydberg states that converge to the ground electronic state of the NO^+ molecular cation.

In the ground $X\,^2\Pi_{\Omega''}(v'', J'')$ state, which is most closely described by Hund's case (a), J'' is the total angular momentum quantum number including spin, Ω'' is the projection of $\vec{J}''$ onto the internuclear axis, and v'' is the vibrational quantum number. The total angular momentum excluding spin N'' is not a well defined quantum number for the X state. As is depicted in the schematic energy level diagram in Fig. 5.1, the rotational energy levels of the ground state are split into two spin-orbit components for which $\Omega'' = 1/2$ and $3/2$ [88, 105, 151, 152]. The wavenumber interval between the $X\,^2\Pi_{1/2}$ and $X\,^2\Pi_{3/2}$ levels is ~ 125 cm^{-1} [153, 154]. In each of these levels, rotational states with quantum numbers $J'' \geq \Omega''$ are

present at wavenumbers given, to first order, by $B''J''(J''+1)$ [78, 105] where $B'' \simeq 1.7$ cm^{-1} [72].

The $A\,^2\Sigma^+(v', N', J')$ state in NO is the nominal 3sσ Rydberg state and is best described by Hund's case (b). For the $A\,^2\Sigma^+(v', N', J')$ state, J' is the total angular momentum quantum number including spin, N' is the total angular momentum quantum number excluding spin, and v' is the vibrational quantum number. In the A state, the rotational energy is predominately determined by the value of N' such that, to first order, $E'_{\text{rot.}}/hc = B'N'(N'+1)$ [78, 105] with $B' \simeq 2.0$ cm^{-1} [72]. Each rotational state is split, because of spin-rotation interactions into two levels for which $J' = N' \pm 1/2$, as shown schematically in Fig. 5.1, for the same value of N' [88, 105, 151, 152]. However, this spin-rotation splitting is ~ 0.005 cm^{-1} [155, 156], and is therefore much smaller than the wavenumber interval between adjacent rotational states. The lifetime of the A state is ~ 200 ns [157].

The $X\,^2\Pi_{\Omega''}(v'', J'') \rightarrow A\,^2\Sigma^+(v', N', J')$ ground-to-intermediate-state transitions are single-photon transitions driven in the experiments described here by laser radiation at wavenumber, υ_1. Examples of available, electric dipole allowed, $X \rightarrow A$ transitions are shown schematically in Fig. 5.1. These are labelled using the $\Delta J_{fi}(J'')$ notation [152, 158], in which P, Q, and R correspond to $\Delta J = -1$, 0, and $+1$, respectively. The subscripts f and i indicate the spin-rotation and spin-orbit levels of the A and X states, respectively. For the ground state $i = 1$ represents the $X\,^2\Pi_{1/2}$ level and $i = 2$ the $X\,^2\Pi_{3/2}$ level. For the $A\,^2\Sigma^+$ state $f = 1$ and $f = 2$ correspond to $J' = N' + 1/2$ and $J' = N' - 1/2$ level, respectively [152].

Examples of measured spectra of $X\,^2\Pi_{1/2}(v'' = 0) \rightarrow A\,^2\Sigma^+(v' = 0)$ transitions are shown in Fig. 5.2. These were recorded using one-colour $(1+1)$ and two-colour $(1+1')$ resonance-enhanced multi-photon ionisation (REMPI) spectroscopy. The wavenumbers indicated by the labelled vertical bars were calculated using the electronic, rotational, and vibrational constants for the X and A states, see Table 5.1, provided in Refs. 121 and 159. In the spectra in Fig. 5.2 transitions between states with the same values of J'' and N', but different values of J' were not spectrally resolved, i.e., the Q_{11} and P_{21}, along with the R_{11} and Q_{21} transitions, because

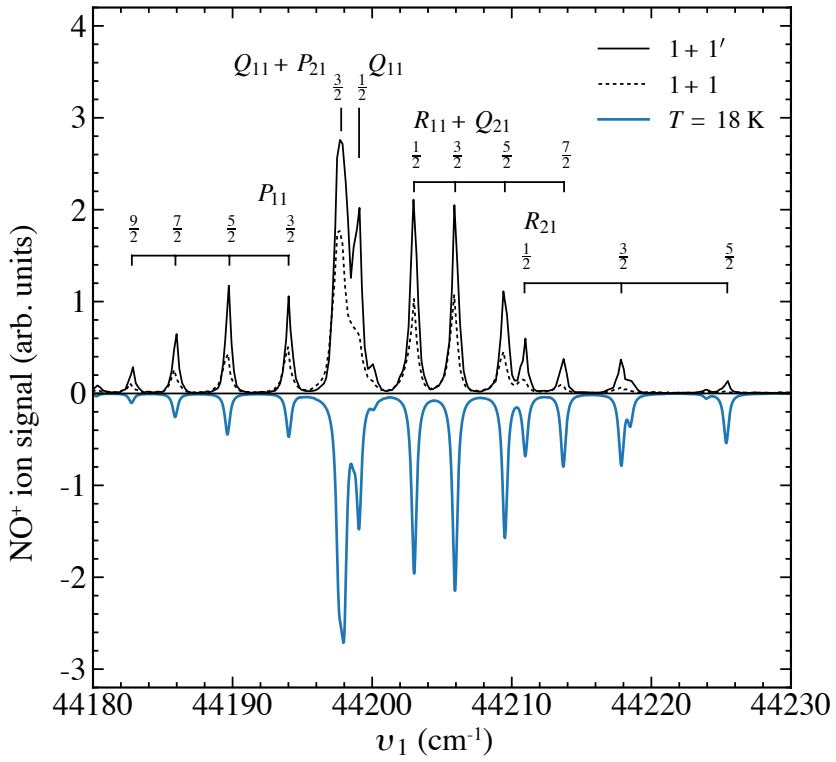

Figure 5.2: Example one-colour $(1+1)$ [black dotted line] and two-colour $(1+1')$ [solid black line] REMPI spectra of the $v''=0 \rightarrow v'=0$ case of the $X^2\Pi_{1/2} \rightarrow A^2\Sigma^+$ transition in NO. The calculated spectrum [inverted continuous blue line] is also shown for a rotational temperature of 18 K. Adapted from Ref. 90.

of the small spin-rotation splitting in the A state. The P_{11} and R_{21} transitions were spectrally resolved. However, $X^2\Pi_{\Omega''}(v'',N'',J'') \rightarrow A^2\Sigma^+(v',N',J')$ transitions for which $\Delta v \neq 0$ are also possible, reflecting the non-zero overlap of the vibrational wavefunctions of these two electronic states. An example of a $(1+1')$ REMPI spectrum of the $X^2\Pi_{1/2}(v''=0) \rightarrow A^2\Sigma^+(v'=1)$ transition is shown in Fig. 5.3. For the experiments reported in this thesis, both the $X^2\Pi_{1/2}(v''=0,J'') \rightarrow A^2\Sigma^+(v'=0,N',J')$ and the $X^2\Pi_{1/2}(v''=0,J'') \rightarrow A^2\Sigma^+(v'=1,N',J')$ transitions were used for resonance-enhanced multi-photon excitation of high-n Rydberg states.

To determine which Rydberg states can be accessed from the $A^2\Sigma^+$ state in the $A^2\Sigma^+(v',N',J') \rightarrow n\ell X^+{}^1\Sigma^+(v^+,N^+)$ transition, it is necessary to consider the selection rules that arise from: (i) the conservation of angular momentum, (ii) the required change in parity in the electric dipole allowed transitions from the

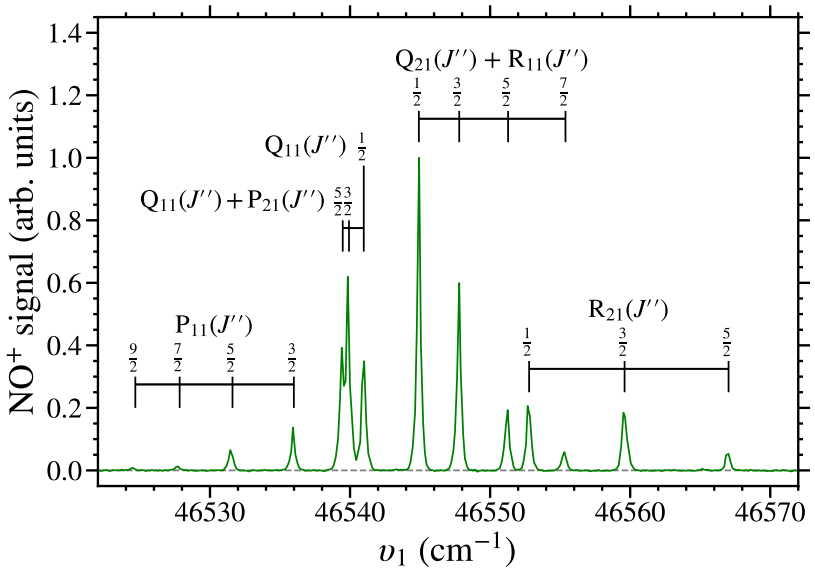

Figure 5.3: Two-colour (1+1′) REMPI spectrum of the $X\,^2\Pi_{1/2}\,(v''=0) \rightarrow A\,^2\Sigma^+\,(v'=1)$ transitions in NO. From Ref. 160.

Table 5.1: Electronic, vibrational, and rotational constants of the $X\,^2\Pi_{1/2}$ and $A\,^2\Sigma^+$ states in $^{14}N^{16}O$. All quantities are given in cm^{-1}. Values from Refs. [121, 159].

Quantity	$X\,^2\Pi_{1/2}$	$A\,^2\Sigma^+$
T_e	0	43965.7
ω_e	1904.2	2374.31
$\omega_e\chi_e$	14.075	16.159
B_e	1.67195	1.9965
α_e	0.0171	0.01915
D_e	5.4×10^{-7}	5.4×10^{-6}

$A\,^2\Sigma^+$ to high-n Rydberg states, and (iii) the electron orbital angular momentum character decomposition of the $A\,^2\Sigma^+$ state. Since the high-n Rydberg states of interest here converge to the closed-shell[1] $X^+\,^1\Sigma^+\,(v^+,N^+)$ state of the NO^+ cation, Hund's case (d) is the most appropriate angular momentum coupling scheme with which to describe them. The total angular momentum of the high-n Rydberg states can therefore be expressed as $\vec{J}=\vec{N^+}+\vec{\ell}+\vec{s}$, where $\vec{N^+}$ is the rotational angular momentum of the ion core, and $\vec{\ell}$ and $\vec{s}$ are the Rydberg electron orbital and spin angular momentum, respectively [71, 77, 88].

[1] Where the sum of individual electron orbital and spin angular momentum are both zero.

Explicitly, Rydberg states that have a non-zero probability of single-photon electric dipole excitation from the intermediate $A\,^2\Sigma^+$ state satisfy the conditions imposed by the conservation of angular momentum, i.e., that $\vec{J} = \vec{J}' + \vec{\gamma}$ where $\vec{\gamma}$ is the photon angular momentum, and the requirement that parity changes between the $A\,^2\Sigma^+$ state and the high-n Rydberg state, i.e., that $p^+ p' = -1$, where $p^+ = (-1)^{N^+ + \ell}$ and $p' = (-1)^{N'}$ [43, 71, 153, 161].[2] Since $s = 1/2$ for the Rydberg electron, these single-photon transitions must therefore satisfy the conditions that $|N^+ - J'| \leq \ell + 3/2$ and $N^+ + J' \geq |\ell - 3/2|$ [71].

However, although a range of electric-dipole transitions are allowed, they do not necessarily occur with a significant probability. Propensity rules must be applied to determine which of the allowed transitions occur with significant intensity in experiments. The relevant propensity rules in this case are that: (i) strong transitions follow the rotation spectator model, in which all the photon angular momentum is imparted to the excited electron and not to the molecular ion core [71, 153, 162]; and (ii) the spin of the excited electron is conserved in strong transitions from the intermediate state to the Rydberg states [71, 153]. From these considerations, the Rydberg electron orbital and spin angular momentum are therefore given by $\vec{\ell} = \vec{\ell}' + \vec{\gamma}$ and $\vec{s} = \vec{s}'$, respectively, where $\vec{\ell}'$ and $\vec{s}'$ represent the orbital and spin angular momentum of the electron in the intermediate state, respectively [71, 153]. Combining these two conditions with the conservation of total angular momentum, and the observation that the total spin and Rydberg-electron spin are equivalent, i.e., $\vec{S}' = \vec{s}'$, in the $A\,^2\Sigma^+$ state because all more tightly bound electrons are in closed shells, results in the final condition that $\vec{N}' = \vec{N^+} + \vec{\ell}'$ for these transitions. Therefore, the complete set of the propensity rules for strong transitions from the intermediate $A\,^2\Sigma^+$ state to high-n Rydberg states is [71, 153],

$$\Delta\ell = \pm 1, \tag{5.2}$$

$$\left|N' - \ell'\right| \leq N^+ \leq N' + \ell', \tag{5.3}$$

[2] More generally the parity of states described by Hund's case (b) is given by $p = (-1)^{N-\Lambda+q}$, where q is the orbital reflection symmetry index and $q = 0$ for all states of all symmetries other than the Σ^- state for which $q = 1$ [77, 78].

Table 5.2: Optically accessible Hund's-case-(d) basis states [$n\ell(N^+)$] based on propensity rules (Eqs. 5.2 - 5.4) for transitions, from the different ℓ' character components of the $A\,^2\Sigma^+$ intermediate state with rotational quantum number N'.

N'	$\ell'=0$	$\ell'=2$	$\ell'=1$
0	np(0)	np(2), nf(2)	ns(1), nd(1)
1	np(1)	np(1), np(3), nf(1), nf(3)	ns(0), ns(2), nd(0), nd(2)
2	np(2)	np(0), np(2), np(4), nf(0), nf(2), nf(4)	ns(1), ns(3), nd(1), nd(3)
3	np(3)	np(1), np(3), np(5), nf(1), nf(3), nf(5)	ns(2), ns(4), nd(2), nd(4)
4	np(4)	np(2), np(4), np(6), nf(2), nf(4), nf(6)	ns(3), ns(5), nd(3), nd(5)
5	np(5)	np(3), np(5), np(7), nf(3), nf(5), nf(7)	ns(4), ns(6), nd(4), nd(6)
6	np(6)	np(4), np(6), np(8), nf(4), nf(6), nf(8)	ns(5), ns(7), nd(5), nd(7)

$$N^+ + \ell + N' = \text{odd}. \tag{5.4}$$

In addition, the vibrational quantum number is not likely to change in the transitions, i.e., $v^+ = v'$, since the Franck-Condon factor significantly favours $\Delta v = 0$ transitions because of the similarity of the potential energy surfaces of the Rydberg and $A\,^2\Sigma^+$ states [88].

At this point it is necessary to consider the mixed ℓ' and ℓ character of the $A\,^2\Sigma^+$ state and the high-n Rydberg states, respectively. An excited electron in the $A\,^2\Sigma^+$ state is predominantly of 3sσ character, although the state is better described as a mixture of orbitals with different ℓ' character. The $A\,^2\Sigma^+$ state has 94.0 % s character, 5.4 % d character, 0.3 % p character, and 0.3 % higher ℓ' character [163, 164]. Therefore, considering the propensity rules (Eqs. 5.2 - 5.4), the distribution of ℓ' character of the intermediate state determines which Hund's-case-(d) basis states, $n\ell(N^+)$, can be accessed in single-photon electric-dipole-allowed transitions from the $A\,^2\Sigma^+$ state. Table 5.2 gives examples of these accessible Hund's-case-(d) basis states. Although all transitions listed are possible, they do not occur with equal strength. For example, it has been observed that the transition moments of the $d' \rightarrow n\text{f}(N^+)$ transitions are significantly larger than those for the $d' \rightarrow n\text{p}(N^+)$ transitions [71, 88]. In addition, the dominant transitions from the $N' = 0$ ($J' = 1/2$) level of the intermediate $A\,^2\Sigma^+$ state are to the np(0) and nf(2) Rydberg states [71, 88]. Furthermore, the Rydberg states are not of a pure $n\ell(N^+)$ character. This is a consequence of the effects of intramolecular interactions. The

efficiency with which particular Rydberg states can be excited using this excitation scheme therefore depends on the strengths of the transitions from the intermediate state to different Hund's-case-(d) basis states, and the composition of the Rydberg state in terms of these basis states.

5.2 State-dependent trap-decay rates of $v^+ = 0$ Rydberg NO molecules

5.2.1 Experimental methods

For the experiments discussed in this section, the methods of Rydberg-Stark deceleration were implemented, using the general approach described in Chapter 4. In the case of interest here, the molecules were excited using the resonance-enhanced two-colour two-photon

$$\begin{aligned} &\mathrm{X}^2\Pi_{1/2}\left(v''=0, J''=3/2\right) \\ &\qquad\rightarrow \mathrm{A}^2\Sigma^+\left(v'=0, N'=0, J'=1/2\right) \\ &\qquad\qquad\rightarrow n\ell\,\mathrm{X}^{+\,1}\Sigma^+\left(v^+=0, N^+\right) \end{aligned} \quad (5.5)$$

excitation scheme [84, 85, 88, 90], depicted in Fig. 5.4. This was performed using the frequency-tripled and doubled outputs of two Nd:YAG pumped dye lasers. The frequency-tripled output of the first laser was set to $\upsilon_1 = 44193.99$ cm^{-1} ($\equiv 226.275$ nm) [with an energy of ~ 10 μJ/pulse], to drive the X $\rightarrow$ A transition. The frequency-doubled output of the second laser was tuned over the wavenumber range from $\upsilon_2 = 30420$ cm^{-1} to 30500 cm^{-1} ($\equiv 328.7$ nm to 327.8 nm) [with an energy of ~ 1.6 mJ/pulse, collimated to a beam waste of $\sim$ 2-mm], to Rydberg states with np(0) and nf(2) character from the $\mathrm{A}^2\Sigma^+$ intermediate state. At the time of photoexcitation, gated time-varying electric potentials could be applied to electrode E1 (see Fig. 4.1) to enhance population transfer to long-lived ℓ-mixed Rydberg-Stark states.

The electrostatically trapped molecules in these experiments were detected

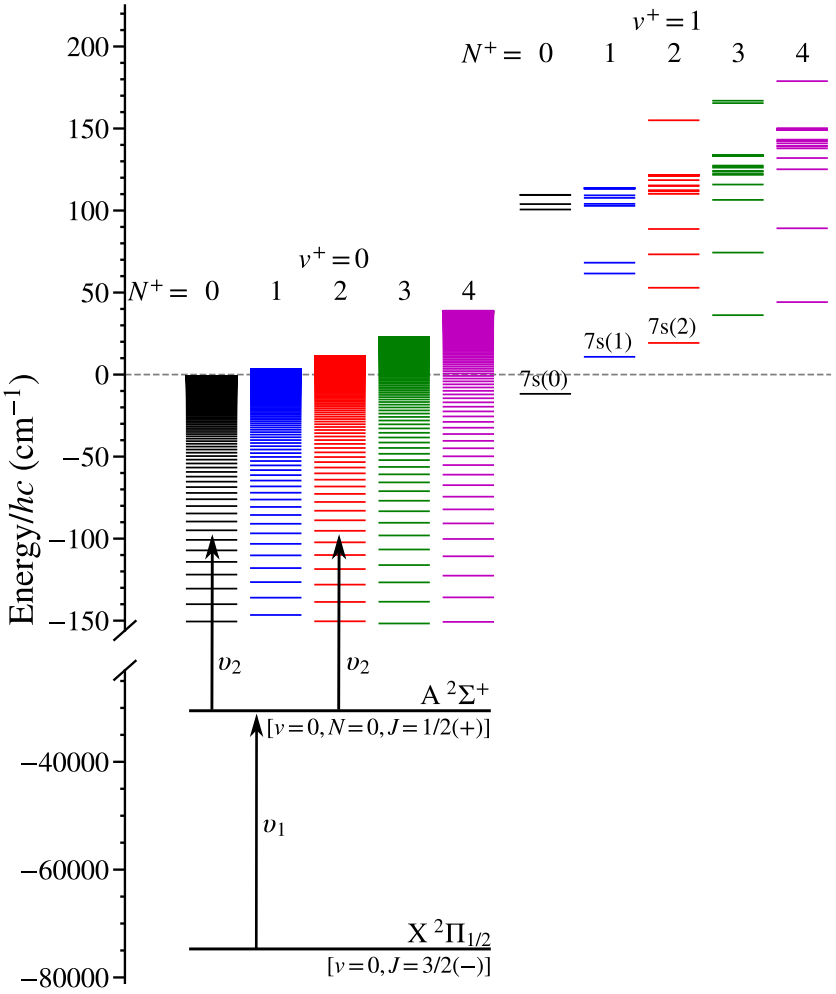

Figure 5.4: Resonance-enhanced two-colour two-photon excitation scheme employed in the preparation of Rydberg states in NO converging to the lowest vibrational state ($v^+ = 0$) of the NO^+ ion core. Low-n states in the $v^+ = 1$ series that are located close to the $v^+ = 0$, $N^+ = 0$ series limit are also shown.

in situ within the cyrogenically cooled decelerator structure by PFI upon the application of a pulsed potential of +500 V to the side electrodes [see Fig. 4.1], as described in Chapter 4. The resulting NO^+ ions were then collected at an MCP detector operated at room temperature for collection. To obtain information on the populations of the Rydberg states at the time of ionisation, slowly-rising pulsed potentials could also be applied to perform SFI. These potentials had the form $V_{\mathrm{Ramp}}(t) = V_{\mathrm{max}}[1 - \exp(-t/\tau)]$, with the time constant $\tau = 4.4$ μs and $V_{\mathrm{max}} = -220$ V. Under these detection conditions electrons produced by the ionisation of the Rydberg molecules were accelerated to the MCP detector.

5.2.2 Trap decay measurements

To measure rates of decay of electrostatically trapped Rydberg NO molecules, laser photoexcitation and Rydberg-Stark deceleration were performed as described in Chapter 4. When the traps in which the molecules were confined were brought to rest, at time $t_{\text{trap}} = 0$ μs in the following, detection by PFI was performed for times up to $t_{\text{trap}} = 1$ ms. Examples of the results of such trap decay measurements, for molecules photoexcited on the 38f(2) resonance ($\upsilon_2 = 30458.37$ cm^{-1}), can be seen in Fig. 5.5. These data demonstrate that Rydberg NO molecules can be efficiently decelerated and electrostatically trapped for times on the order of 1 ms. There are two main components to the decay observed in these data: (i) At early trapping times, i.e., for times $t_{\text{trap}} \lesssim 400$ μs, a fast reduction in signal is observed. This reflects the decay of the Rydberg states predominantly populated upon photoexcitation. (ii) At later times the rate of decay of molecules from the trap slows down. This suggests the presence of a small fraction of molecules in Rydberg states with longer lifetimes that remain in the trap at late times [143, 165].

The data represented by the orange open squares in Fig. 5.5 correspond to measurements made upon laser photoexcitation in nominally zero electric field, $V_{\text{Mod}} = 0$ V. As discussed in Chapter 4, the high-$|M_N|$ Rydberg-Stark states filtered out by deceleration and trapping, are populated following the interaction of excited molecules with time-varying stray electric fields close to the time of photoexcitation [76, 91]. To explore this process further, the application of rapidly-varying fields in the excitation region when the laser radiation is present was investigated, to see if this could be used to enhance population transfer into higher-$|M_N|$ states. The effect of this sinusoidal field modulation, generated by applying a gated few-cycle oscillating electric potential to electrode E1 (i.e., the field was in the direction perpendicular to electrodes E1 and E2, see Fig. 4.1) with an amplitude of $V_{\text{Mod}} = 7.5$ V and a frequency of 50 MHz for a time of 50 ns at the time of photoexcitation, can be seen by comparing the data recorded with (blue circles) and without (orange open squares) this modulation applied. These data are shown in Fig. 5.5 with the measured NO^+ ion signal at $t_{\text{trap}} = 0$ μs normalised to 1 for both

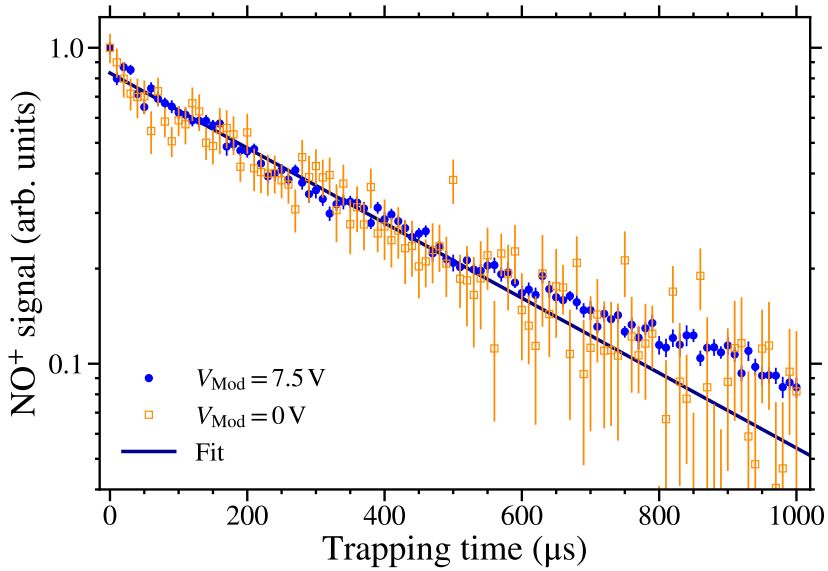

Figure 5.5: Decay of trapped Rydberg NO molecules photoexcited on the 38f(2) resonance at $\upsilon_2 = 30458.37$ cm^{-1} with ($V_{\mathrm{Mod}} = 7.5$ V) and without ($V_{\mathrm{Mod}} = 0$ V) a 50 MHz gated sinusoidal potential applied to the electrode E1 at the time of photoexcitation (see text for details). For both measurements $V_0 = 149$ V and the data were normalised to a value of 1 for the NO$^+$ signal recorded at time $t_{\mathrm{trap}} = 0$ μs. An example of a fitted exponential function, encompassing the times from $t_{\mathrm{trap}} = 0$ and 500 μs, to the trap decay data recorded with $V_{\mathrm{Mod}} = 7.5$ V is shown. All measurements were recorded with the apparatus cooled to ~ 30 K.

measurements. The field modulation resulted in a factor of ~ 30 increase in the NO$^+$ signal from molecules in long-lived high-$|M_N|$ Rydberg-Stark states detected by PFI, when compared to that obtained for $V_{\mathrm{Mod}} = 0$ V, and hence an increase in the number of molecules in long-lived Rydberg-Stark states that were trapped. This meant that upon the application of the field modulation, molecules could be observed in the trap for times in excess of 1 ms, whereas without this field modulation the NO$^+$ signal reduced to the level of the background noise after a trapping time of ~ 500 μs. The application of the short pulsed field modulation did not change the measured decay time constants from the trap at early times. An exponential function fit to both sets of data in Fig. 5.5, for trapping times between 0 and 500 μs, resulted in decay time constants of 366 ± 6 μs and 377 ± 21 μs with and without the modulation, respectively. It was therefore concluded that the applied short few-cycle pulsed modulation to the electric field close to the time of laser photoexcitation re-

sulted in population transfer to Rydberg-Stark states with similar characteristics to those populated solely as a result of effects of electric field noise, and the presence of ions or electrons around the time of photoexcitation. All measurements discussed in the following were performed with the field modulation applied.

To obtain state-dependent information on the rate of decay of the trapped molecules single exponential functions were fit to experimental data, of the kind in Fig. 5.5, over a range of early trapping times to obtain the trap-decay time constant, τ_{decay}. To validate the fitting procedure, and minimise spurious effects arising from the motion of the molecules in the trap, the range of trapping times over which the fit was performed was tested to ensure the stability of values of τ_{decay} obtained. This was done for molecules excited on the 38f(2) resonance as shown in Fig. 5.6(a). In Fig. 5.6(b) the variation in the values of τ_{decay} obtained for fixed fit start times of 50 μs or 100 μs, and a range of fit end times can be seen. For fit end times up to $\sim$ 350 μs the value of τ_{decay} remains constant within the the experimental uncertainties. However at later end times, the value of τ_{decay} gradually increases as the experimental data deviates from a single exponential function. This change in the decay time constant at later trapping times reflects the fact that a range of Rydberg-Stark states are populated close to the time of photoexcitation and the trap decay dynamics are no longer dominated by molecules in one particular set of states [165]. Molecules in shorter lived states decay more quickly from the trap, and therefore at later times only molecules in states with longer lifetimes remain. To minimise the effects of these decay dynamics on the values of τ_{decay}, the fit end time was chosen to be 350 μs for all analysis described below.

Fig. 5.6(c) shows the values of τ_{decay} obtained for a range of fit start times. For trapping times $\leq$ 50 μs the value of τ_{decay} varied with the fit start time. This behaviour is a consequence of the motion of the molecules in the trap after it was brought to rest [136, 143]. During deceleration, the molecules are generally located ahead of the electric field minima of the travelling traps [133]. After a trap is stopped the molecules oscillate with a period of $\sim$ 50 μs, as they evolve to fill it. From these considerations, the start time of the fitting process was therefore set to

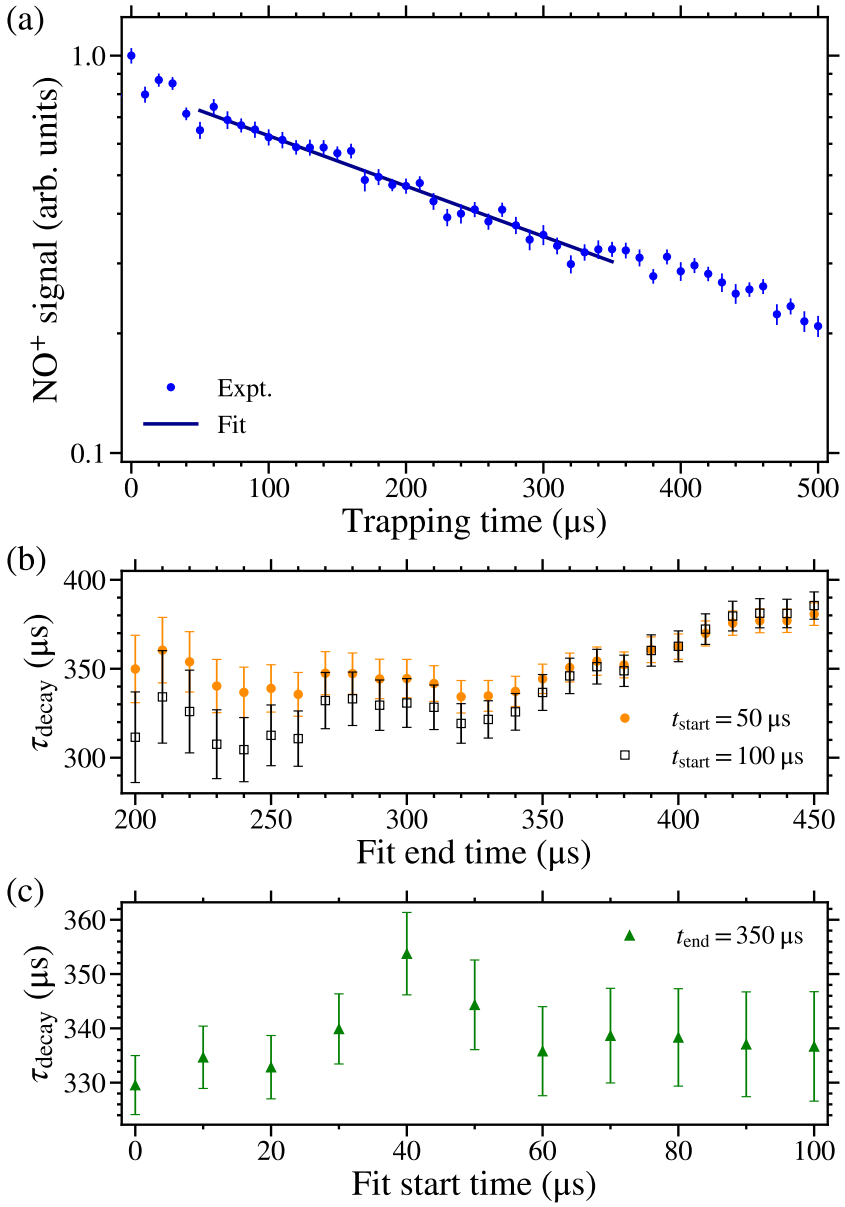

Figure 5.6: (a) Measured decay of Rydberg NO molecules, excited on the 38f(2) resonance, from the electrostatic trap, with an example of a fitted exponential function encompassing the times from $t_{\text{trap}} = 50$ μs to 350 μs. (b) The variation in τ_{decay} associated with fitting between 50 μs (orange circles) or 100 μs (black open-squares) and the fit end times indicated on the horizontal axis. (c) The variation in τ_{decay} associated with fitting between the fit start times indicated on the horizontal axis, and 350 μs.

50 μs.

To ascertain the range of Rydberg states suitable for decelerating and electrostatically trapping, a laser photoexcitation spectrum, shown in Fig. 5.7, was

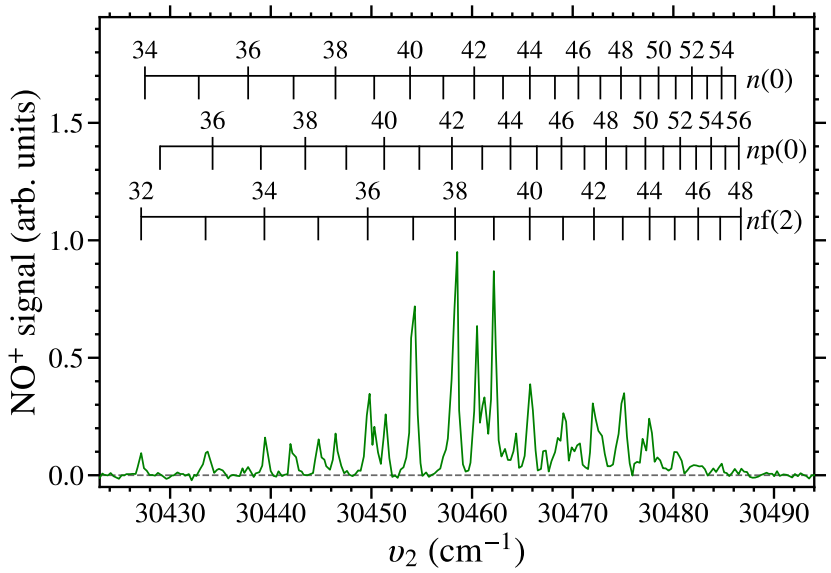

Figure 5.7: Laser photoexcitation spectrum of long-lived Rydberg states in NO recorded after deceleration and trapping for $t_{\text{trap}} = 350$ μs, with $\upsilon_1 = 44193.99$ cm^{-1}, and $V_0 = 149$ V.

recorded with detection after a trapping time of $t_{\text{trap}} = 350$ μs. The spectral intensities of each of the features in this spectrum reflect the combined contributions from the efficiency with which long-lived LFS hydrogenic Rydberg-Stark states were populated, the deceleration and trap loading efficiencies, and the excited state decay rates. The reduced spectral intensities at lower values of n in this spectrum reflect the n^2 dependence of the maximal electric dipole moments of the Rydberg states, that reduce the deceleration and trapping efficiency for lower n states. The spectral intensities in Fig. 5.7 also reduce for high values of n. This is a consequence of the lower threshold for electric field ionisation during deceleration and trap loading, and, in this particular case with NO, the lifetimes of the states.

The deceleration and trapping efficiency of the NO molecules depends on effects of intramolecular interactions between the optically accessible $n\text{p}(0)$ or $n\text{f}(2)$ states, and nearby ℓ-mixed hydrogenic Rydberg-Stark states. The resonances associated with transitions to the $n\text{f}(2)$ states in Fig. 5.7 arise because of their close proximity to, and mixing with, the $n(2)$ hydrogenic Stark states [90, 143]. Spectral features that arise as a result of mixing of the $n\text{p}(0)$ states with hydrogenic Stark states are also observed. Despite the $n\text{p}(0)$ states being shorter lived than the

nf(2) states [81, 82], the hydrogenic states populated in both cases are long lived. Two manifolds of ℓ-mixed hydrogenic Stark states are accessible upon excitation because of mixing with the np(0) states. These are (i) $n'(1)$ hydrogenic Stark states for which $n' \neq n$ that mix as a result of intramolecular charge-dipole interactions and accidental near degeneracies with np(0) states [86, 90]. These coincide with resonances denoted np(0) in Fig. 5.7. (ii) $n(0)$ hydrogenic Stark states that mix with the $[n+1]$p(0) states in the electric fields present close to the time of photoexcitation. These states are denoted $n(0)$ in Fig. 5.7.

The use of SFI to detect trapped Rydberg NO molecules allowed information on the time-evolution of the excited state populations to be obtained. To achieve this, PFI was performed by turning off the trapping potentials, resulting in nominally zero electric field, and ~ 1 μs later applying a slowly-rising ionising potential $V_{\rm Ramp}(t)$ to the side electrodes of the decelerator. Although diabatic transitions from the trapped LFS to HFS states are possible when the trapping potentials are turned off, these are not expected to result in any change in the principal quantum number, n, of the states initially trapped. The time-dependence of $V_{\rm Ramp}(t)$ is shown Fig. 5.8(a). The electron signal recorded by single-event counting at a trapping time of $t_{\rm trap} = 0$ μs, for molecules excited on the 38(2) and 43(2) resonances, are shown in Fig. 5.8(b)(i). From these data the electron detection times, and hence the ionisation fields of the molecules in each of these states, can be distinguished. The maxima in the signals recorded following excitation on the 38(2) and 43(2) resonances, occur at $t_{\rm Ramp} \sim 5.9$ μs [$V_{\rm Ramp}(5.9\ \mu{\rm s}) \sim -160$ V] and ~ 3.3 μs [$V_{\rm Ramp}(3.3\ \mu{\rm s}) \sim -110$ V], respectively. Since the maximum signal associated with the 43(2) resonance occurs earlier than that associated with the 38(2) resonance, it is concluded that excitation on the 43(2) resonance leads to ionisation in smaller electric fields. This is expected from the n-dependence of the ionisation field and previous detailed measurements of the electric field ionisation dynamics of long-lived hydrogenic states in NO [90]. The width of the distributions in Fig. 5.8(b)(i) reflect the combined effects of a distribution of Stark states present in the trap at the time of SFI, the inhomogeneity of the ionisation field caused by the electrode

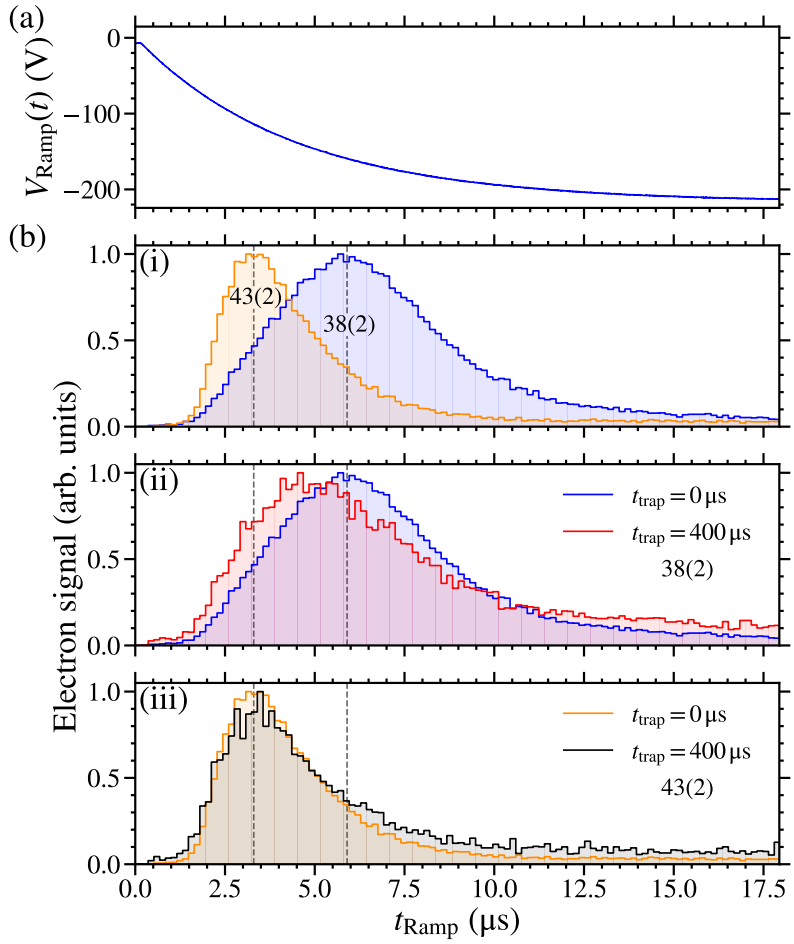

Figure 5.8: (a) The potential $V_{\mathrm{Ramp}}(t)$ applied to the side electrodes (Fig. 4.1) during SFI. (b) Electron signals recorded by single-event counting following excitation of NO molecules on (i) the 38(2) and 43(2) resonances after a trapping time of $t_{\mathrm{trap}} = 0$ μs, (ii) the 38(2) resonance at $t_{\mathrm{trap}} = 0$ μs and $t_{\mathrm{trap}} = 400$ μs, and (iii) the 43(2) resonance at $t_{\mathrm{trap}} = 0$ μs and $t_{\mathrm{trap}} = 400$ μs.

geometry in the decelerator, and the motion of the molecules in this time-varying inhomogeneous electric field after the trap was switched off. The tails in the electron signals at late times in Fig. 5.8(b)(i) are attributed in part to secondary electron generation following SFI.

The expected ratio of the ionisation fields for LFS hydrogenic Rydberg-Stark states with different values of n was determined from the ionisation field, $F_{\mathrm{ion}}(n)$, of the outermost LFS Stark state [66, 145],

$$F_{\mathrm{ion}}(n) = 2F_0/9n^4, \tag{5.6}$$

in which $F_0 = 2hcR_{\rm NO}/ea_{\rm NO}$. For the $43(2)$ and $38(2)$ states, this ratio was $F_{\rm ion}(43)/F_{\rm ion}(38) = 0.6$. This value is comparable to the ratio of the values of $V_{\rm Ramp}(t)$ at the maxima of the electron distribution for the molecules excited on the $43(2)$ and $38(2)$ resonances of $V_{\rm Ramp}(3.3\ \mu{\rm s})/V_{\rm Ramp}(5.9\ \mu{\rm s}) \sim 0.7$. It is therefore concluded that the molecules trapped in these states are predominately undergoing diabatic electric field ionisation [90].

Using the SFI detection scheme, information on the evolution of the excited state populations was also obtained by comparing the electron signals recorded when $t_{\rm trap} = 0\ \mu$s and 400 μs. This was done for the $38(2)$ and $43(2)$ resonances with the resulting electron time-of-flight distributions, scaled so that the signal maximum in each case was 1, shown in Fig. 5.8(b)(ii) and (b)(iii), respectively. For molecules excited on the $43(2)$ resonance, no significant change in the general form of the electron TOF distribution was observed between $t_{\rm trap} = 0\ \mu$s and 400 μs. For molecules excited on the $38(2)$ resonance this was not the case. Under these conditions when $t_{\rm trap} = 400\ \mu$s the maximum of the electron signal occurred at $t_{\rm Ramp} \sim 4.8\ \mu$s [$V_{\rm Ramp}(4.8\ \mu{\rm s}) \sim -140$ V], i.e., approximately 1.1 μs before that recorded when $t_{\rm trap} = 0\ \mu$s. This suggests that the molecules detected at late times in this case are in higher-n states. From the ratio of the corresponding values of $V_{\rm trap}(t)$, this shift in the maximum of the electron signal was estimated to correspond to a change in n of $\sim +2$.

By carrying out numerical particle trajectory calculations under conditions that match those in the experiments (see Section 4.3), the typical distribution of maximal electric fields experienced by molecules in the trap was determined. The mean of this distribution was ~ 150 V cm^{-1}. To estimate the electric field ionisation rates of the trapped NO molecules in the experiments, it was determined that for hydrogenic Rydberg-Stark states with $n = 38$, $|m| = 4$, $k = +33$ ($n = 43$, $|m| = 4$, $k = +38$), tunnel ionisation occurs at a rate of $\sim 10^{-30}$ s^{-1} ($\sim 10^{-3}$ s^{-1}) in this field [145] ($k = n_1 - n_2$ is the difference in the parabolic quantum numbers n_1 and n_2 obtained by solving the Schrödinger equation for a pure Coulomb potential in parabolic coordinates [66]). Additionally, explicit inclusion of electric field ionisation into the

particle trajectory simulations, see Section 4.3, indicated that the contribution from electric field ionisation to the observed trap decay rates was < 1 s^{-1}. Hence, it is concluded that electric field ionisation arising from the motion of molecules in the trap does not affect the distribution of states with these values of n over time.

In a similar vein, for hydrogenic Stark states with $n = 38$, $|m_\ell| = 4$, $k = +33$ ($n = 43$, $|m_\ell| = 4$, $k = +38$), the $\Delta n = \pm 1$ and ± 2 blackbody transitions rates at 30 K are calculated to be $\sim 9 \times 10^2$ s^{-1} and $\sim 4 \times 10^2$ s^{-1} ($\sim 7 \times 10^2$ s^{-1} and $\sim 3 \times 10^2$ s^{-1}), respectively. At this temperature these depopulation rates scale approximately with n^{-2}. However, because the molecules are trapped ~ 2 mm above a 2-mm-diameter aperture in the heat shield surrounding the decelerator (A1 in Fig. 4.1), the blackbody field that the molecules interact with has a room temperature component. From the position of the minimum of the trap the 2-mm-diameter aperture subtends approximately 0.25 of the total solid angle. Modifications to the blackbody spectrum arising from the dimensions of the electrode structure are not accounted for in the following. At 300 K the $\Delta n = \pm 1$ and ± 2 blackbody depopulation rates, for $n = 38$, $|m_\ell| = 4$, $k = 33$ ($n = 43$, $|m_\ell| = 4$, $k = 38$), are $\sim 1 \times 10^4$ s^{-1} and $\sim 5 \times 10^3$ s^{-1} ($\sim 7 \times 10^3$ s^{-1} and $\sim 3 \times 10^3$ s^{-1}), respectively. Therefore the total $\Delta n = \pm 1$ and ± 2 blackbody depopulation rates for these states at the position of the trap are estimated to be below $0.75\gamma_{BB}(30\text{ K}) + 0.25\gamma_{BB}(300\text{ K})$ and hence $\sim 3 \times 10^3$ s^{-1} and $\sim 1 \times 10^3$ s^{-1} ($\sim 2 \times 10^3$ s^{-1} and $\sim 1 \times 10^3$ s^{-1}), respectively. These blackbody transition rates are similar for both $n = 38$ and $n = 43$. Therefore any blackbody-induced changes in the electron distribution, measured by PFI, are not expected to differ for the molecules excited to the $38(2)$ and $43(2)$ states. Consequently, the change in the $n = 38$ electron distribution with trapping time [see Fig. 5.8(b)(ii)] is interpreted to arise from the initial population of the Rydberg states close to the time of photoexcitation and before deceleration and trapping. Excited states with longer lifetimes remain in the trap for longer times. Therefore if an ensemble of molecules is prepared in a set of states with different lifetimes, the measured distribution of these changes over time. This behaviour has been discussed previously by Seiler *et. al.* in the interpretation of experiments with electrostati-

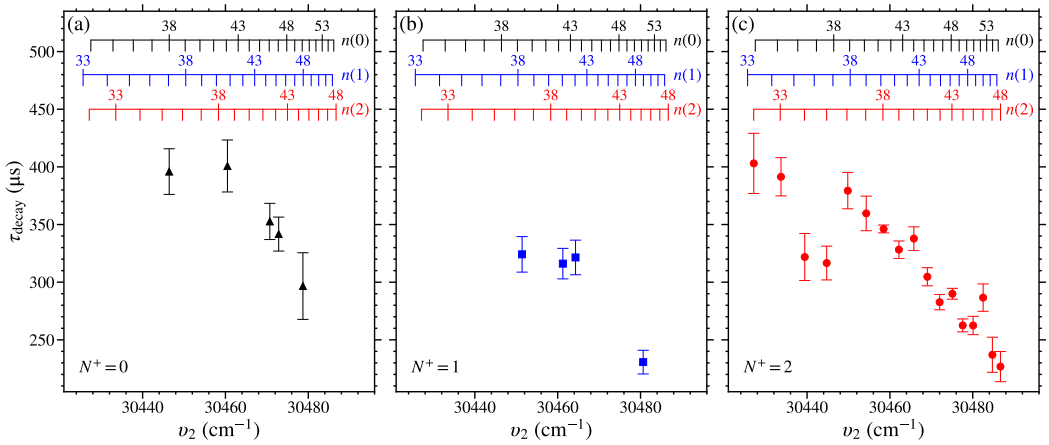

Figure 5.9: Measured values of τ_{decay} of Rydberg-Stark states in NO with (a) $N^+ = 0$, (b) $N^+ = 1$, and (c) $N^+ = 2$. In all measurements $V_0 = 149$ V.

cally trapped Rydberg H atoms [165]. In the case of interest here, this suggests that excitation of the NO molecules on the 38f(2) resonance resulted in the population of at least two Rydberg states with different values of $n(N^+)$, while excitation on the 43f(2) resonance lead predominantly to the population of states with a single values of $n(N^+)$.

5.2.3 Decay rate measurements

Measurements of the trap decay time constants, τ_{decay}, for NO molecules in $n(0)$, $n(1)$, or $n(2)$ Stark states were performed for values of n between 32 and 50. The value of τ_{decay} in each case was determined by fitting a single exponential function to the experimental data between $t_{trap} = 50$ μs and 350 μs, as described in Section 5.2.2. The error weighted mean of up to 6 separate measurements of τ_{decay} for each set of values of $n(N^+)$ were calculated, with the uncertainty on this weighted mean also calculated. These values of τ_{decay} obtained for the $n(0)$, $n(1)$, and $n(2)$ states, with $V_0 = 149$ V, can be seen in Fig. 5.9. For reference, the decay time constants of the 38(2) and 43(2) states in this figure were $\tau_{decay} = 346.2 \pm 3.4$ μs and 290.0 ± 4.7 μs, respectively.

From the measured trap decay times in Fig. 5.9 it is seen that there is a general trend for the measured value of τ_{decay} to decreases with increasing values of n, and therefore also increasing excitation wavenumber, υ_2. This behaviour occurs for

states in each N^+ series studied. For the $n(0)$ and $n(1)$ states this trend is seen for $n \geq 40$. For the $N^+ = 2$ series, the general reduction in the value of τ_{decay} with n begins at lower values of n. But for $n = 34$, 35, 40, 43, 45, and 46, deviations from this general behaviour are observed. For $n = 34$ and 35 the measured values of τ_{decay} are shorter than those of the surrounding states that follow the general trend. While, for $n = 40$, 43, 45, and 46 the measured values of τ_{decay} are longer.

In the hydrogen atom, the fluorescence lifetimes of ℓ-mixed Rydberg states scale approximately with n^4 [66, 76, 91]. Therefore, the observed general reduction in τ_{decay} with n for long-lived 'hydrogenic' Rydberg-Stark states in NO in Fig. 5.9 indicates that intramolecular interactions with short-lived states must occur. The significance of these interactions must in general increase with n. However, for particular values of n at which deviations from this general trend occur, additional contributions from interactions with more energetically localised states must arise.

5.2.4 Vibrational channel interactions

The general reduction in the measured values of τ_{decay} as the value of n, and hence υ_2, increases in the data in Fig. 5.9, is attributed to the effects of weak intramolecular interactions. A possible explanation of the origin of these intramolecular interactions is that they involve the mixing of the high-n Rydberg states with $v^+ = 0$ with short-lived low-n electronic states in series that converge to the $X^+\,^1\Sigma^+(v^+ = 1, N^+)$ state of NO^+. As can be seen in the energy-level diagram in Fig. 5.4, the $n = 7$ states in the $v^+ = 1$ series lie above, but close to, the $v^+ = 0$, $N^+ = 0$ series limit. The lifetimes of these states in the $v^+ = 1$ series are dominated by fast non-radiative decay processes, i.e., a combination of predissociation and vibrational autoionisation [71]. They have lifetimes of ~ 1 ps and hence spectral widths of ~ 5 cm^{-1} [71, 166]. Studies have been reported previously of the $\Delta v^+ \neq 0$ vibrational channel interactions in NO between Rydberg states in series converging to the $v^+ = 1$ series limit, and the $v^+ = 0$ continuum that give rise to autoionisation [71, 167]. In the case of interest here effects these same vibrational channel interactions seen between states with $v^+ = 0$ and $v^+ = 1$ below both series limits.

To estimate the scale of the effects of these vibrational channel interactions in the experiments here, calculations of τ_{decay} were performed including contributions from the $v^+ = 0$ fluorescence and dissociation decay rates, as described in Chapter 3 Section 3.5. In these calculations the interactions between states in the $v^+ = 0$ and $v^+ = 1$ series were treated semi-empirically. The amount of low-n, $v^+ = 1$ character mixed into a $v^+ = 0$ Rydberg-Stark state $|i\rangle$ was assumed to follow the amplitude of a Lorentzian function,

$$L_{(N^+)}(E_i) = a_{(N^+)} \left[\frac{(\Gamma_{v^+=1}/2)^2}{(E_i/hc - E_{v^+=1}/hc)^2 + (\Gamma_{v^+=1}/2)^2} \right], \tag{5.7}$$

at the off-resonance wavenumber E_i/hc of the Rydberg-Stark states for which the trap decay time was measured. $E_{v^+=1}/hc$ is the wavenumber of the peak of the Lorentzian function, $\Gamma_{v^+=1}$ is the $v^+ = 1$ spectral width ($\Gamma_{v^+=1} = 1/2\pi c\tau_{v^+=1}$ where $\tau_{v^+=1} \sim 1$ ps), and $a_{(N^+)}$ is a scaling factor. In the interpretation of the experimental data in Fig. 5.9, $E_{v^+=1}$ and $a_{(N^+)}$ were chosen to be fit parameters. Their values depended on the dominant N^+ character of the state $|i\rangle$. The total decay rate, $\gamma_{\text{tot}(i)}$, of the state $|i\rangle$ was then considered to be,

$$\gamma_{\text{tot}(i)} = \left[1 - L_{(N_i^+)}(E_i)\right] \gamma_{0(i)} + L_{(N_i^+)}(E_i)\gamma_{v^+=1}, \tag{5.8}$$

where $\gamma_{v^+=1} = 1/\tau_{v^+=1}$ is the $v^+ = 1$ decay rate, and $\gamma_{0(i)}$ is given by Eq. 3.33. The decay time constant of the state $|i\rangle$ was then $\tau_{\text{tot}(i)} = 1/\gamma_{\text{tot}(i)}$. This approach allowed the $v^+ = 1$ character of the $n(N^+)$ Stark states prepared in the experiments to be estimated.

Because the data in Fig. 5.9 were recorded for times greater than 250 μs after laser photoexcitation, the decay rates after this time were calculated using a similar procedure to that employed by Bixon and Jortner [86]. This involved considering the population of all accessible short and long lived $n(N^+)$ Stark states, each of which decay exponentially. The resulting exponential functions were summed,

$$P(t) = \sum_i \exp\left(-t/\tau_{\text{tot}(i)}\right), \tag{5.9}$$

to give the total excited state population, $P(t)$, where $t = 0$ μs corresponds to the photoexcitation time. A single exponential function was then fit to the results of these calculations between $t = 300$ μs and 600 μs, i.e., between the times corresponding to $t_{\text{trap}} = 50$ μs to 350 μs. Because the deceleration and trapping process only accepted the outer LFS Rydberg-Stark states, this procedure was implemented for the outer quarter of the Stark manifold for each value of $n(N^+)$ to obtain the calculated time constant τ_{calc}.

Calculations of τ_{calc} were carried out using fixed values of the electric field, F_z, and M_N. The value of F_z was taken to be equal to the time-averaged field experienced by the molecules in the electrostatic trap that are obtained from numerical particle trajectory calculations, as described in Section 4.3. For $V_0 = 149$ V this field was $F_z = 95$ V cm^{-1}, and was approximately constant across the range of values of n studied. The values of M_N were restricted to $|M_N| > |N^+ - 3|$ such that at least one of the $2N^+ + 1$ Stark manifolds, for each $n(N^+)$, contained no short-lived $\ell \leq 3$ character, i.e., for $N^+ = 0$, 1, and 2, $M_N \geq 4$, 3, and 2, respectively.

The decay time constants, τ_{calc}, where first calculated without including effects of vibrational channel interactions (i.e., $a_{(N^+)} = 0$ in Eq. 5.7). In this case only the intrinsic $v^+ = 0$ fluorescence and dissociation decay rates were considered. For the $n(2)$ $v^+ = 0$ states, the resulting time constants are shown for $M_N = 2$ to 5 in Fig. 5.10(a). From these data it is seen that when only $v^+ = 0$ fluorescence and dissociation decay rates were included the value of τ_{calc} increases with n, as would be expected in an atom. This does not however reflect the general trend observed in the experimental data in Fig. 5.9.

To determine the values of $E_{v^+=1}$ and $a_{(N^+)}$ for each N^+ series, a fit was performed of τ_{calc} to τ_{decay}. In this fitting process the reduced chi-squared $\chi^2 = \sum_n \left(\tau_{\text{decay}}(n) - \tau_{\text{calc}}(n)\right)^2 / \Delta\tau_{\text{decay}}(n)^2$ was minimised in each N^+ series. For $N^+ = 0$ and 1, all measured values of n were used in the fitting process. For $N^+ = 2$, the fitting was performed for the data points between $n = 36$ and 48 where the values of τ_{decay} change smoothly. The values of τ_{decay} of the 40(2), 43(2), 45(2), and 46(2) states were not included in the fit because of their deviation from the general

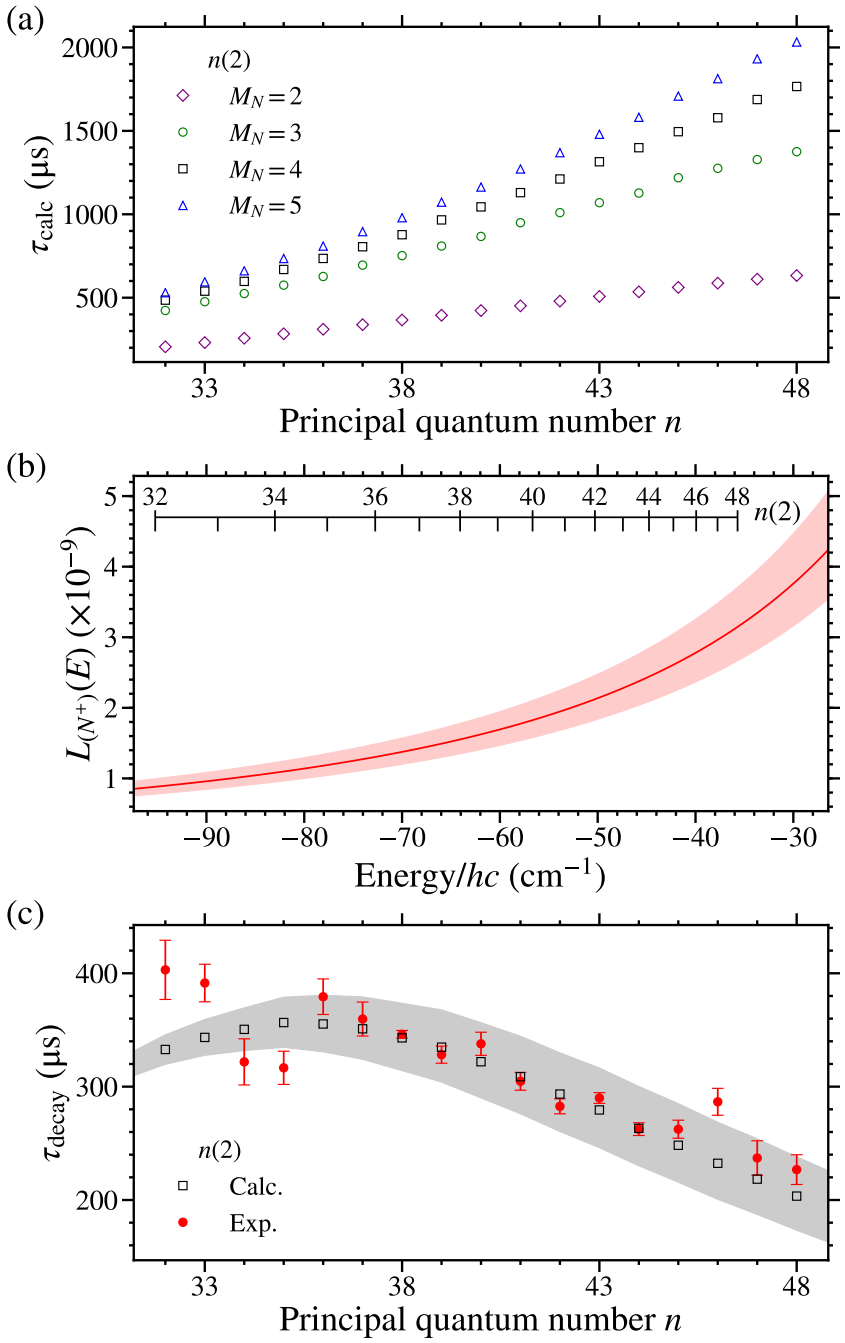

Figure 5.10: (a) Calculated decay time constants, τ_{calc}, excluding effects of vibrational channel interactions for $M_N = 2$, 3, 4, and 5 LFS $n(2)$ Rydberg-Stark states in NO. (b) Fraction of $v^+ = 1$ ($\tau_{v^+=1} \sim 1$ ps) character mixed into the $n(2)$ $v^+ = 0$ Stark states. The red shaded region represents the uncertainty in the fit parameters (see text for details). (c) Comparison of the experimentally measured values of τ_{decay} for $n(2)$ states (filled red circles) with calculated values of τ_{calc} for LFS $n(2)$, $M_N = 4$ Stark states including effects of vibrational channel interactions (open black squares). The grey shaded region represents the uncertainty in τ_{calc} resulting from the uncertainty in the fit parameters.

Table 5.3: Parameters associated with the Lorentzian function in Eq. 5.7, representing the strength of the vibrational channel interactions between the short-lived ($\tau_{v^+=1} \sim$ 1 ps) low-n states with $v^+ = 1$ and the high Rydberg states with $v^+ = 0$, obtained by minimising the reduced chi-squared of τ_{calc} with respect to τ_{decay} for the different N^+ hydrogenic series separately. The fitting process was performed with the data recorded for $V_0 = 149$ V. Values of $M_N = 4$ and $F_z = 95$ V cm^{-1} were used in the calculations.

N^+	$E_{v^+=1}/hc\,(\text{cm}^{-1})$	$a_{(N^+)}/10^{-6}$
0	-7 ± 7	0.18 ± 0.08
1	45 ± 10	3.0 ± 0.7
2	31 ± 3	2.0 ± 0.2

trend followed at surrounding values of n. A value of $M_N = 4$ was used in determining τ_{calc} because it is the smallest value of M_N for which all N^+ series considered contain at least one set of Stark states without any short lived low-ℓ ($\ell \leq 3$) character. The values of $E_{v^+=1}$ and $a_{(N^+)}$ which resulted in the minimum chi-squared, χ^2_{min}, can be seen in Table 5.3. The uncertainties on these values were estimated by considering the change required in $E_{v^+=1}$ or $a_{(N^+)}$ to increase the chi-squared to $\chi^2 = \chi^2_{\text{min}} + 1$.

Comparison of the best-fit values of $E_{v^+=1}$ in Table 5.3 with the energy-level structure in Fig. 5.4 shows that the peaks of the Lorentzian functions, which approximately represent the positions of the $v^+ = 1$ ($\tau_{v^+=1} \sim 1$ ps) states mixed into the $v^+ = 0$ Stark states, lie close to or above the $v^+ = 0$, $N^+ = 0$ series limit and are in the vicinity of the calculated energies of the $(n = 7)\,\text{X}^+\,^1\Sigma^+\,(v^+ = 1, N^+)$ states. From the values of $E_{v^+=1}$ and $a_{(N^+)}$, in Table 5.3 and Eq. 5.7 it can be estimated that the fraction of short lived ($\tau_{v^+=1} \sim 1$ ps) $n = 7$, $v^+ = 1$ character mixed into the $n(N^+)$ $v^+ = 0$ Stark states is between 10^{-10} and 10^{-9}. For example, a 10^{-9} contribution from a short-lived state with a lifetime of 1 ps, mixed into a long-lived state with a lifetime of 1 ms, yields a total decay rate of 2000 s^{-1} and a lifetime of 500 μs.

Fig. 5.10(b) shows the fraction of $(n = 7)\,\text{X}^+\,^1\Sigma^+\,(v^+ = 1, N^+)$ character mixed into the predominantly $v^+ = 0$, $N^+ = 2$ Rydberg states below the $v^+ = 0$, $N^+ = 0$ series limit as given by Eq. 5.7. The shaded region corresponds to the

range of mixing fractions that arise from the uncertainty in the fit parameters. As can be seen in Fig. 5.10(b) the fraction of this $n = 7$, $v^+ = 1$ character mixed into the $n(2)$ Stark states increases by approximately a factor of 5 over the wavenumber range studied. In Fig. 5.10(c) the effects of these vibrational channel interactions on the values of τ_{calc} for the $n(2)$ states (black squares) can be seen, and these results are compared to the measured values of τ_{decay} (red circles). The gray shaded region in this panel of Fig. 5.10 corresponds to the uncertainty in τ_{calc} arising from the uncertainty in the fit parameters. The calculated decay time constant obtained for the $38(2)$, $M_N = 4$ [$43(2)$, $M_N = 4$] state using this approach was $\tau_{\text{calc}} = 343 \pm 30$ μs [$\tau_{\text{calc}} = 279 \pm 35$ μs]. It can be seen in Fig. 5.10(c) that, in contrast to the case in which only $v^+ = 0$ fluorescence and dissociation rates were considered [Fig. 5.10(a)], this type of vibrational channel interaction leads to a dependence of the excited state decay times on the value of n that follows the trend observed in the experiments. The contributions from this interaction to the excited state decay rates are $\sim 10^3$ s^{-1}.

To aid in this interpretation of the experimental observations as arising from vibrational channel interactions, a two state quantum mechanical model was implemented. To approximate the interaction between a $v^+ = 0$ and $v^+ = 1$ state, a 2×2 Hamiltonian, H_{vib}, was constructed,

$$H_{\text{vib}} = \begin{pmatrix} E_{v^+=0} & I_{\text{vib}} \\ I_{\text{vib}} & E_{v^+=1} \end{pmatrix}, \tag{5.10}$$

where $E_{v^+=0}$ and $E_{v^+=1}$ represent the energies of the $v^+ = 0$ and $v^+ = 1$ states, respectively, and I_{vib} represents the strength of the interaction. Within the harmonic oscillator approximation, $\Delta v^+ = 1$ mixing occurs when an interaction is present that causes the Hund's-case-(b) quantum defects to have a non-zero derivative with respect to the internuclear separation R, when evaluated at the equilibrium internuclear distance R_e, i.e., $\left.\frac{\mathrm{d}\mu_{\ell\Lambda}^{(\mathrm{b})}}{\mathrm{d}R}\right|_{R=R_{\mathrm{e}}} \neq 0$. [27, 28, 71, 72, 77, 168]. For the Rydberg states of NO the dependence of $\mu_{\ell\Lambda}^{(\mathrm{b})}$ on R arises as a result of the interaction of the Rydberg electron with the R-dependent multipole moments of the NO^+ ion

core [71, 73]. The off-diagonal matrix elements associated with this interaction, $I_{\rm vib}$ in Eq. 5.10, can therefore be estimated by considering the interaction between the $|n\ell N^+ N M_N v^+ = 0\rangle$ and $|n'\ell' N^{+\prime} N' M_{N'} v^{+\prime} = 1\rangle$ Hund's-case-(d) basis states. This interaction can be expressed as [77]

$$I_{\rm vib} \simeq -\frac{2hcR_{\rm NO}}{\nu^{3/2}\nu'^{3/2}}\delta_{\ell,\ell'}\delta_{N,N'}\delta_{M_N,M_{N'}}\sum_{\Lambda} A^{(N\ell)}_{N^+\Lambda}\beta^{\Lambda}_{v^{+\prime},v^+}(\ell)\,\sec^2\left[\pi\,\mu^{(\rm b)}_{\ell\Lambda}\Big|_{R=R_{\rm e}}\right]A^{(N\ell)}_{N^{+\prime}\Lambda}, \tag{5.11}$$

where, for $\Delta v^+ = 1$,

$$\beta^{\Lambda}_{v^++1,v^+}(\ell) = \left.\frac{{\rm d}\mu^{(\rm b)}_{\ell\Lambda}}{{\rm d}R}\right|_{R=R_{\rm e}}\sqrt{\frac{(v^++1)\hbar}{2\mu_{\rm red}\omega_{\rm e}}}, \tag{5.12}$$

with $\mu_{\rm red}$ and $\omega_{\rm e}$ the reduced mass and vibrational frequency of NO^+, respectively. The units of the coupling given by Eq. 5.11 are introduced through the density of Rydberg states as in the first order approximation of MQDT [27, 70]. It is assumed that the values of the Hund's-case-(b) quantum defect at the equilibrium internuclear distance, $\mu^{(\rm b)}_{\ell\Lambda}\Big|_{R=R_{\rm e}}$, are small because $\ell \geq 4$, and hence $\sec^2\left[\pi\,\mu^{(\rm b)}_{\ell\Lambda}\Big|_{R=R_{\rm e}}\right] \simeq 1$. The derivatives of the quantum defects, for $\Lambda \leq 2$, were obtained by considering the low-n, R-dependent quantum defects calculated in Ref. 73. For $\Lambda \geq 3$, it was assumed that $\left.\frac{{\rm d}\mu^{(\rm b)}_{\ell\Lambda}}{{\rm d}R}\right|_{R=R_{\rm e}} = 0$. Values of $I_{\rm vib}$ were then determined by considering the interactions between states for which $v^+ = 0$, $N^+ = 2$, and $n = 38$, and those for which $v^+ = 1$, $N^+ = 0$ and 4, $n = 7$, and $\ell = 4$ and 5. Following this approach the interaction strength $I_{\rm vib}$ was calculated to be between $I_{\rm vib}/hc \simeq 1\times10^{-3}$ cm^{-1} and 5×10^{-2} cm^{-1}. The effect of this interaction on the $v^+ = 0$ and $v^+ = 1$ states was then determined by considering that $(E_{v^+=1} - E_{v^+=0})/hc \sim 100$ cm^{-1}, and calculating the eigenvalues and eigenvectors of the Hamiltonian in Eq. 5.10. The resulting mixed states contain 10^{-10} to 10^{-7} of the minority component, i.e., the absolute values of amplitudes of the minority component in the wavefunctions are 10^{-5} to $10^{-3.5}$. These mixing fractions are consistent with those expected from the measured trap decay times. Using this two-state model it can also be estimated that the vibrational channel interaction considered here would give rise to wavenumber

shifts of the $v^+ = 0$ and $v^+ = 1$ states of $\sim 10^{-8}$ cm^{-1} to 10^{-5} cm^{-1} (i.e., frequency shifts of $\sim$ 100 Hz to 100 kHz).

5.2.5 Rotational channel interactions

To interpret the trap decay time constants for the individual Rydberg states that deviate from the general trend in Fig. 5.9, i.e., that τ_{decay} decreases with increasing n, it is necessary to consider the role of rotational channel interactions between states with $v^+ = 0$. As discussed by Bixon and Jortner [86], and in Section 5.2.2, the hydrogenic Stark states populated by photoexcitation in the experiments here are those that undergo intramolecular interactions with nearby optically accessible np(0) or nf(2) states. These interactions can be induced solely by external electric-fields, as is the case for $n(2)$ states that mix with nf(2) states, or by a combination of intramolecular charge-multipole interactions and external electric-fields, that occur, for example, in the case of $n(1)$ states populated because of accidental degeneracies between np(0) and n'd(1) states (where $n' \neq n$), with the n'd(1) states further mixing with the $n'(1)$ hydrogenic states. Although population of $n(N^+)$ and $n'(N^{+'})$ states, at near accidental degeneracies, could occur in a coherent way the measurements presented here are not sensitive to this effect.

In Fig. 5.9(c) the measured values of τ_{decay} for the 40(2), 43(2), and 45(2) Rydberg-Stark states are larger than expected from the behaviour of the surrounding states. These $n(2)$ hydrogenic Stark states are populated because of the effects of mixing with the nf(2) states. However, the charge-quadrupole interactions that couple states for which $\Delta N^+ = \pm 2$ and $\Delta \ell = 0$ lead to mixing between nf(2) and n'f(0) states, which, in the presence of an electric field also mix with the $n'(0)$ states. This type of interaction with intramolecular and external field contributions leads to the population of $n'(0)$ states upon photoexcition if they are energetically close to an nf(2) resonance. Hence, because of accidental degeneracies with $n'(0)$ states, photoexcitation on the 40f(2), 43f(2), and 45f(2) resonances leads to the population of both the 40(2) and 44(0), the 43(2) and 48(0), and the 45(2) and 51(0) states, respectively. Since the $n'(0)$ states have longer decay time constants than the $n(2)$ states at a particular excitation wavenumber (see Fig. 5.9), trapped molecules in

these states have larger values of τ_{decay} than those excited on resonances where only $n(2)$ states are populated. This increase in the observed decay time constant also depends on the ratio of the $n(2)$ and $n'(0)$ state populations.

Further deviations from the general trend in the values of τ_{decay} in Fig. 5.9 are also seen for the $34(2)$ and $35(2)$ states. In these cases, charge-dipole interactions that couple states for which $\Delta N^+ = \pm 1$ and $\Delta\ell = \pm 1$ lead to mixing of the $n\text{f}(2)$ and $n'\ell'(3)$ states. These result in the population of $n'(3)$ states, in addition to $n(2)$ states, upon photoexcitation. Consequently, excitation on the $34\text{f}(2)$ and $35\text{f}(2)$ resonances leads to the population of both the $34(2)$ and $32(3)$, and the $35(2)$ and $33(3)$ states, respectively. The reduced decay time constants observed for $n = 34$ and 35 in Fig. 5.9(c), when compared to the surrounding states, suggests that the $32(3)$ and $33(3)$ states have shorter lifetimes than the $34(2)$ and $35(2)$ states.

The measured decay time constant for the $46(2)$ state in Fig. 5.9, is larger than expected from the trend in the surrounding states. In this case the presence of both the optically accessible $46\text{f}(2)$ and $53\text{p}(0)$ states within the laser spectral width, and the increasing overlap of Stark manifolds at these high values of n complicate the interpretation of this feature. However, based upon similar arguments to those outlined above, an estimate of the states that can be populated in both of these cases can still be made. Although a rigorous treatment, e.g., by combining particle trajectory calculations with MQDT, will be required to determine the relative populations of each Stark state and the efficiency with which each can be decelerated and trapped, in this instance it is considered that:

- The $46(2)$ Stark states are populated because of electric-field-induced mixing with the $46\text{f}(2)$ states.

- The $50(1)$ Stark states are almost degenerate with the $46(2)$ states and can therefore be populated as a result of charge-dipole interactions that (i) couple the $46\text{f}(2)$ states and $50\text{d}(1)$ or $50\text{g}(1)$ states, or (ii) couple the $53\text{p}(0)$ state with the $50\text{s}(1)$ or $50\text{d}(1)$ states. These are then mixed with the hydrogenic $50(1)$ states in the electric field.

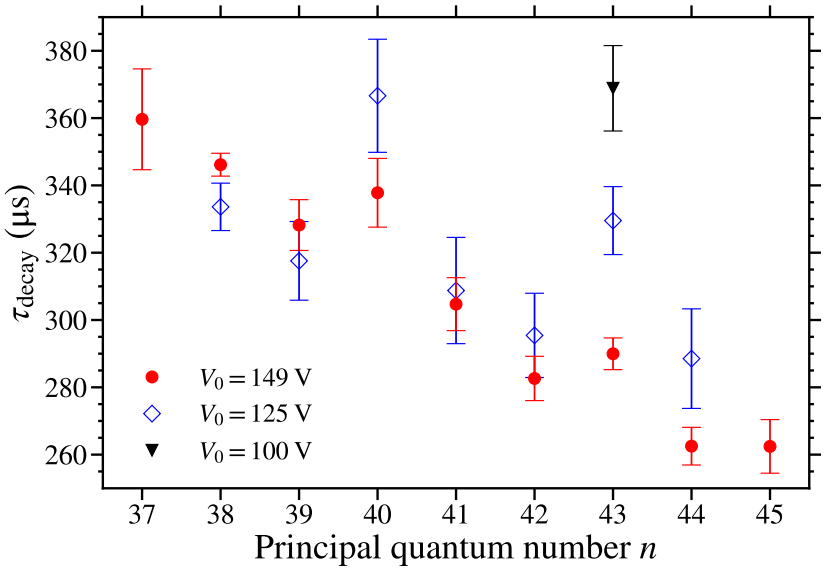

Figure 5.11: Measured values of τ_{decay}, for states in the $N^+ = 2$ series. The data were recorded for $V_0 = 100$ V (black triangle), 125 V (blue open diamonds), and 149 V (red circles).

- Finally, $52(0)$ Stark states can be populated as a result of electric-field-induced mixing with the $53p(0)$ state.

Since, at a particular excitation wavenumber the $N^+ = 0$ Stark states were observed to exhibit longer decay time constants than the $N^+ = 1$ and 2 Stark states (see Fig. 5.9), the presence of $52(0)$ states is expected to increase the value of τ_{decay} measured at the wavenumber associated with the excitation of the $46(2)$ states when compared to the other surrounding states. This is consistent with the experimental observations.

The dependence of τ_{decay} on the trap depth was measured for the $n(2)$ states in the range from $n = 38$ to 44, see Fig. 5.11. The data in this figure were recorded for three different trap depths with $V_0 = 149$ V (red circles), $V_0 = 125$ V (blue open diamonds), and $V_0 = 100$ V (black triangle). From these data, it is seen that in general τ_{decay} is insensitive to the value of V_0, and hence the trap depth. This is consistent with the results of calculations for $F_z = 95$ V cm^{-1} ($V_0 = 149$ V) and $F_z = 80$ V cm^{-1} ($V_0 = 125$ V) in which the reduction in the electric field strength caused τ_{calc} to change by < 5 μs over this range of values of n. However, two exceptions to this general trend are seen in Fig. 5.11. These occur for the $40(2)$ and

$43(2)$ states where the value of τ_{decay} increased as the value of V_0 was decreased.

As discussed above, photoexcitation on the $40\text{f}(2)$ and $43\text{f}(2)$ resonances results in the population of the $40(2)$ and $44(0)$, and the $43(2)$ and $48(0)$ Stark states, respectively. The increase in τ_{decay} on these resonances as V_0 was decreased indicates that in these cases the fractions of trapped molecules in the longer lived $44(0)$, or $48(0)$, states also increase as V_0 decreases. For states with $n > 40$ the trapping efficiency is limited by electric field ionisation during deceleration and trap loading, with the ionising field scaling with n^{-4}. For lower values of V_0, the electric field experienced by the molecules during deceleration and trapping is reduced. This leads to an increase in the trapping efficiency for molecules in higher n states, because of reduced loses from electric field ionisation and the resulting increase in the effective volume of the trap. This increase in trap loading efficiency is greater for states with higher values of n. Therefore, for the measurements performed following excitation on the $40\text{f}(2)$ resonance, the trapping efficiency for molecules in the $40(2)$ states only changes a little between $V_0 = 149$ V and 125 V, whereas the efficiency of trapping molecules in near the degenerate $44(0)$ states increases as the values of V_0 is reduced. This results in an increase in the fraction of molecules in the longer-lived $44(0)$ state present in the trap when $V_0 = 125$ V, compared with $V_0 = 149$ V, and therefore τ_{decay} is observed to increase. The situation is similar for the $43\text{f}(2)$ resonance, where the trapped molecules are in the $43(2)$ and $48(0)$ states, and the fraction of molecules in the longer-lived $48(0)$ states increases as V_0 decreases resulting in an increase in τ_{decay}.

5.3 Conclusions

In this chapter measurements of the decay of electrostatically trapped Rydberg NO molecules were presented. These molecules were excited in Rydberg states in series converging to the $v^+ = 0$ and $N^+ = 0$ to 2 states of the NO^+ cation, with the molecules trapped on timescales up to 1 ms. Trap decay time constants of ~ 300 μs were determined, by fitting a single exponential function to the measured trap decays between trapping times of 50 μs and 350 μs for Rydberg states with principal

quantum numbers n between 32 and 50, and were observed to generally decrease with increasing value of n for each N^+ series. These measured trap decay time constants therefore did not follow the $\sim n^4$ scaling typically expected of atomic Rydberg states. The general trend is therefore attributed to effects of weak intramolecular interactions. Interactions between the long-lived high-n $v^+ = 0$ Rydberg states and short-lived (~ 1 ps) $n = 7$ $v^+ = 1$ states that are located close to the $v^+ = 0$ ionisation limit were identified as being the most likely cause of these effects. These interactions resulted in a mixing of $\sim 10^{-9}$ of this short-lived character into the long-lived Rydberg states, and contributed $\sim 10^3$ s^{-1} to the total decay rate. Deviations from this general trend were also observed, and attributed to the excitation of long-lived $v^+ = 0$ Rydberg states in series converging to multiple values of N^+. These states were populated through a combination of charge-multpole interactions of optically accessible $n\ell(N^+)$ states with $n'\ell'(N^{+\prime})$ states of a different N^+. These $n\ell(N^+)$ and $n'\ell'(N^{+\prime})$ states were then mixed, by time varying electric fields present close to the time of photoexcitation, with the long-lived $n(N^+)$ and $n'(N^{+\prime})$ Rydberg-Stark states.

Chapter 6

Vibrationally and rotationally excited Rydberg NO

In this chapter experiments in which the effects of vibrational and rotational excitation of the NO^+ ion core on the slow decay of cold electrostatically trapped Rydberg NO molecules are presented. In Section 6.1 the first demonstration of the Rydberg-Stark deceleration and trapping of vibrationally excited molecules is described. The rates of decay of these cold trapped samples were measured and compared to those presented in Chapter 5 for $v^+ = 0$ Rydberg states. A systematic study of the effect of rotational excitation on the decay of NO molecules in long-lived Rydberg-Stark states was also carried out with these results presented in Section 6.2. Conclusions are drawn in Section 6.3. The contents of Sections 6.1 and 6.2 draw on work published in Refs. 160 and 169, respectively, with appropriate adaptations made to align with the structure of this thesis.

6.1 Trap decay rates of vibrationally excited Rydberg NO

6.1.1 Experimental methods

In the experiments described in this section, the NO molecules were excited into high-n Rydberg states in series converging to the $v^+ = 1$ state of the NO^+ cation. This was achieved using a similar excitation scheme to that described in Chapter 5,

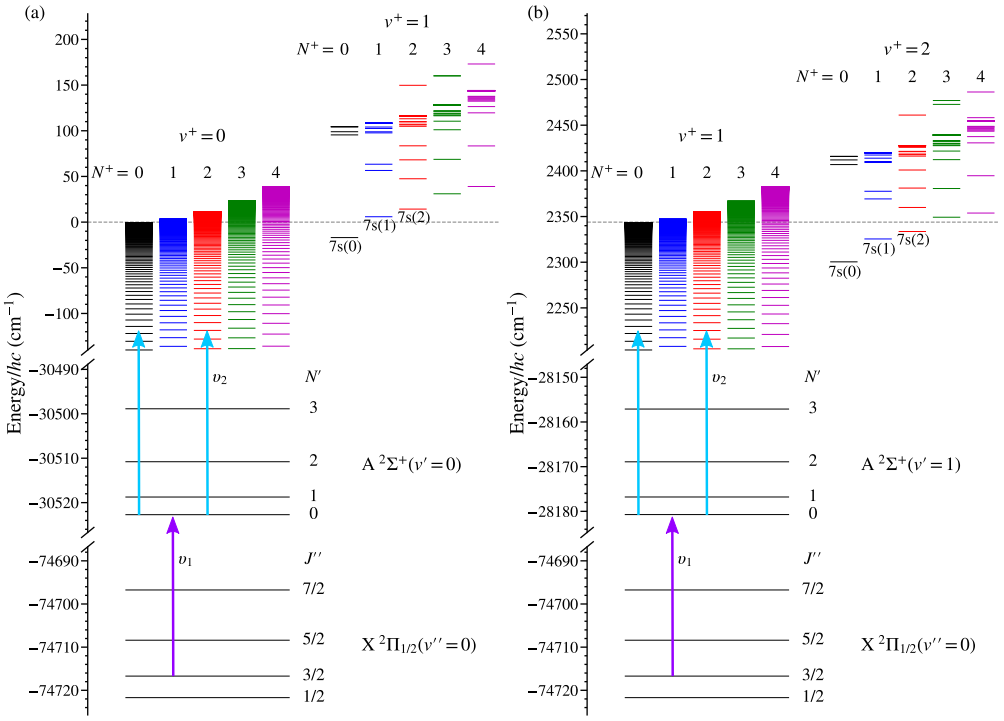

Figure 6.1: Resonance-enhanced two-colour two-photon excitation schemes used to prepare Rydberg states in NO converging to the (a) $v^+ = 0$, and (b) $v^+ = 1$ vibrational states in the $X^+\,^1\Sigma^+$ ground electronic state of NO^+. Low-lying $n = 7$ Rydberg states with $v^+ = 1$ and 2 are also included in each panel. All energies are displayed with respect to the energy of the $N^+ = 0$, $v^+ = 0$ Rydberg series limit.

but with the first step in this case involving the excitation from the $v'' = 0$ vibrational level of the X state to the $v' = 1$, first excited vibrational level, of the A state, i.e., the resonance-enhanced two-colour two-photon

$$\begin{aligned} &X\,^2\Pi_{1/2}\left(v'' = 0, J'' = 3/2\right) \\ &\qquad \rightarrow A\,^2\Sigma^+\left(v' = 1, N' = 0, J' = 1/2\right) \\ &\qquad\qquad \rightarrow n\ell X^+\,^1\Sigma^+\left(v^+ = 1, N^+\right) \end{aligned} \quad (6.1)$$

excitation scheme. A comparison of this excitation scheme to that used for preparation of Rydberg states with $v^+ = 0$ is shown in Fig. 6.1.

Since the intermediate $A\,^2\Sigma^+$ state in NO is a low-lying Rydberg state, it has a similar potential energy curve to the high-n Rydberg states, and that of the ground electronic state of NO^+. Consequently, the Franck-Condon principle results in a

propensity for $\Delta v = v^+ - v' = 0$ transitions from the intermediate A state to the high Rydberg states upon laser photoexcitation. Therefore the preparation of the $A\,^2\Sigma^+(v')$ intermediate state with $v' = 1$ allows access to high Rydberg states in series converging to the $v^+ = 1$ vibrational level in the ground electronic state of NO^+. To implement this excitation scheme the frequency-tripled output of the first laser was set to $\upsilon_1 = 46535.87$ cm^{-1} ($\equiv 214.888$ nm) [~ 80 μJ/pulse] to drive the $X\,^2\Pi_{1/2}(v''=0, J''=3/2) \rightarrow A\,^2\Sigma^+(v'=1, N'=0, J'=1/2)$ transition. The second laser was then adjusted in the range from $\upsilon_2 = 30420$ cm^{-1} to 30500 cm^{-1} ($\equiv 328.7$ nm to 327.8 nm) [~ 1.0 mJ/pulse, collimated to a beam waste of $\sim$ 2-mm] to excite high-n Rydberg states from the intermediate A state.

As discussed in Chapter 5, the long-lived ℓ-mixed Rydberg-Stark states prepared in the experiments discussed here were populated upon the interaction of molecules in optically accessible low-ℓ Rydberg states with time-varying stray electric fields in the apparatus, associated with electrical noise and the presence of charged particles, close to the time of photoexcitation. The procedure employed for deceleration and trapping the molecules was the same as that described in Chapters 4 and 5. Detection of the trapped molecules was performed using both PFI and SFI. For the SFI the form the rising ionisation pulse was the same as in Chapter 5, but with a maximum potential of $V_{\rm max} = -200$ V.

6.1.2 Laser spectroscopy of $v^+ = 1$ Rydberg states

To determine the range of values of n, and N^+, of the Rydberg states in NO with $v^+ = 1$ that could be decelerated and electrostatically trapped, laser photoexcitation spectra were recorded with selective detection of molecules that were successfully trapped. To achieve this, PFI was performed after a trapping time of $t_{\rm trap} = 360$ μs with the resulting spectra presented in Fig. 6.2. All of the resonances in this figure correspond to the excitation of Rydberg states in series for which $v^+ = 1$ and represent resonances on which optically accessible np(0) or nf(2) character is mixed into near-degenerate long-lived Rydberg-Stark states. Spectra recorded for $V_0 = 149$ V and 100 V are displayed in Fig. 6.2(b) and (c), respectively. As in the data in Chapter 5 for the $v^+ = 0$ Rydberg states, the relative intensities of the features in these

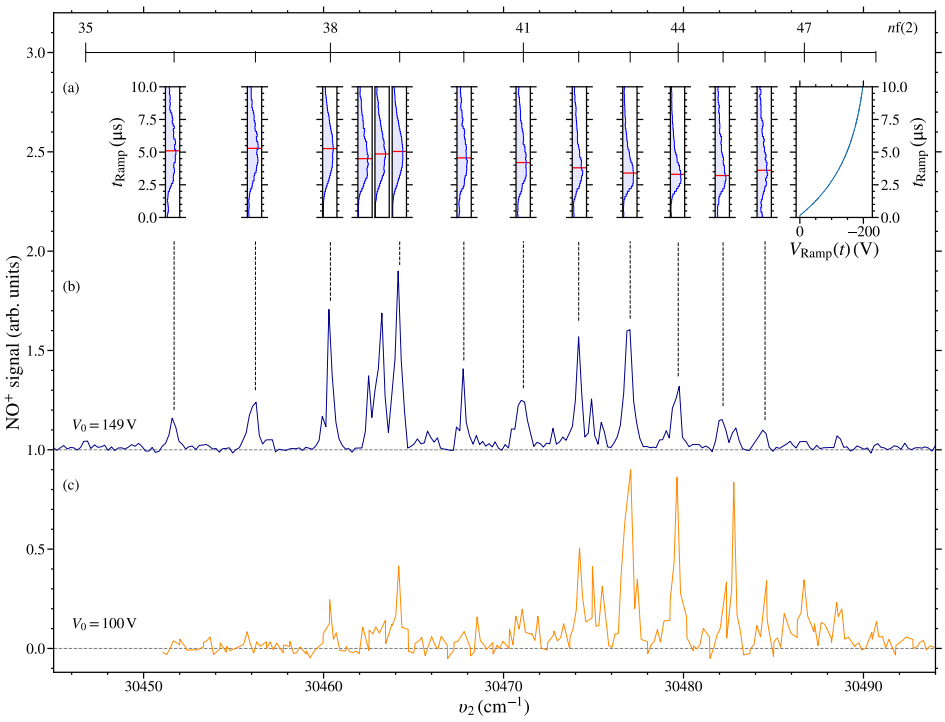

Figure 6.2: Spectra of long-lived $v^+ = 1$ Rydberg states in NO recorded by PFI after deceleration and electrostatic trapping for $t_{\mathrm{trap}} = 360$ μs with $\upsilon_1 = 46535.87$ cm^{-1}. When recording the data in spectrum (b) $V_0 = 149$ V, and (c) $V_0 = 100$ V. The upper part (a) of the figure, contains electron time-of-flight distributions obtained by SFI, using single-event counting, with the ramped ionisation voltage $V_{\mathrm{Ramp}}(t)$ indicated on the top right. These data were recorded for $t_{\mathrm{trap}} = 100$ μs, with $V_0 = 149$ V and excitation on the resonances indicated in (b). The red horizontal line within each panel denotes the intensity maximum in each distribution.

spectra reflect the combined effects of the efficiency with which long-lived LFS Rydberg-Stark states were populated, the deceleration and trap loading efficiency, and the lifetimes of the Rydberg states.

The transitions with maximal spectral intensity in Fig. 6.2 occur for higher values of n when V_0 is reduced to 100 V. For a given value of V_0, i.e., a particular depth of the electric field minima in the travelling electric traps, the optimal range of values of n for which deceleration and trapping can be achieved is determined by the Rydberg-state electric-dipole moments and ionisation electric fields. For lower values of n, the deceleration and trapping efficiency is reduced because of the n^2 dependence of the maximal static electric-dipole moments of the Rydberg-states, and therefore the maximal force that can be exerted on the molecules. On

the other hand, the n^{-4} dependence of the threshold ionisation electric field for high Rydberg states results in a reduction in the deceleration and trapping efficiency for higher values of n [90, 145, 146]. This is because, during the deceleration and trap loading process, molecules in higher n states are more likely to ionise, and the phase-space acceptance of the travelling electric traps for these states reduces. From numerical particle trajectory calculations (see Chapter 4) it was determined that the lower threshold for electric field ionisation of higher-n Rydberg states does not result in a significant increase in field ionisation after the traps are brought to rest.

As was the case for the Rydberg states with $v^+ = 0$, transitions to nf(2) Rydberg states dominate the spectra in Fig. 6.2 because of the comparatively small nf quantum defects of ~ 0.02 in NO, and therefore the close proximity of these states to long-lived higher-ℓ $n(2)$ states. However, ℓ- and N^+-mixing involving optically accessible np(0) states can also lead to the population of $[n-1](0)$ and $n'(1)$ Stark states. In these cases $[n-1](0)$ states are populated as a result of direct electric-field-induced mixing with np(0) states. $n'(1)$ Stark states are populated in situations where mixing with near degenerate np(0) and n'd(1) states occurs because of intramolecular charge-dipole interactions, combined with electric-field–induced mixing of n'd(1) character into the $n'(1)$ states [67, 86]. The measurements of trap decay rates discussed in this section focus primarily on $n(2)$ Stark states excited on the nf(2) resonances indicated by the horizontal bar across the top of Fig.6.2.

In addition to standard laser-photoexcitation spectra, SFI of the Rydberg molecules was performed after deceleration and trapping for $t_{\text{trap}} = 100$ μs with $V_0 = 149$ V [separated panels in Fig. 6.2(a)]. This detection methodology allowed changes in the ionisation fields of the molecules in states with different values of n to be identified. These measurements were made by applying the slowly-rising potential, $V_{\text{Ramp}}(t)$, in the right-hand panel of Fig. 6.2(a) to the side electrodes after switching off the deceleration and trapping potentials. Normalised electron time-of-flight (TOF) distributions recorded by SFI, using single-event counting, following excitation on the resonances with values of n between 36 and 46 are displayed across

the left part of Fig. 6.2(a). The location of the maximum in each time-of-flight distribution is denoted by a red marker. The widths of the distributions in the time domain reflect (i) the distribution of Rydberg-Stark states populated at the time of SFI, (ii) the inhomogeneity of the ionisation fields within the decelerator structure, and (iii) the motion of the molecules during SFI.

In general for the nf(2) resonances, the maxima in the electron TOF distributions in Fig. 6.2(a) occur at earlier times as the value of n increases. This reflects the n^{-4} scaling of the threshold ionisation electric field [66]. SFI measurements performed following excitation on the resonances at $\upsilon_2 = 30462.50$ cm^{-1} and 30463.24 cm^{-1}, i.e., the two resonances between the 38f(2) and 39f(2) features, aided in the characterisation of these states. The maxima in the electron TOF distributions in both of these cases occur at earlier times (4.49 and 4.68 μs, respectively) than those associated with these nf(2) resonances. Therefore the molecules excited on these resonances ionise in lower electric fields. This suggests excitation into states with values of $n > 39$. These states must therefore have values of $N^+ < 2$, and the higher wavenumber feature at $\upsilon_2 = 30463.24$ cm^{-1} must have a higher value of n than the lower one. From the calculated energy-level structure of the Rydberg states, these resonances were attributed to the population of $42(0)$ and $41(1)$ Rydberg-Stark states, respectively.

6.1.3 Trap decay rates

Measurements of the decay of the electrostatically trapped NO molecules in these $v^+ = 1$ Rydberg states were performed in a similar manner to those described in Chapter 5 for $v^+ = 0$. After laser photoexcitation the molecules were decelerated and electrostatically trapped. The integrated NO^+ ion signal, recorded after PFI of the trapped molecules was then measured for values of t_{trap} up to 1 ms. Trap-decay time-constants, τ_{decay}, were then obtained by fitting single exponential functions to these data between $t_{\text{trap}} = 50$ and 350 μs. The results of this process are presented in Fig. 6.3. Each point in this figure corresponds to the weighted mean of up to 15 separate measurements of τ_{decay}. The error bars represent the uncertainties on these mean values.

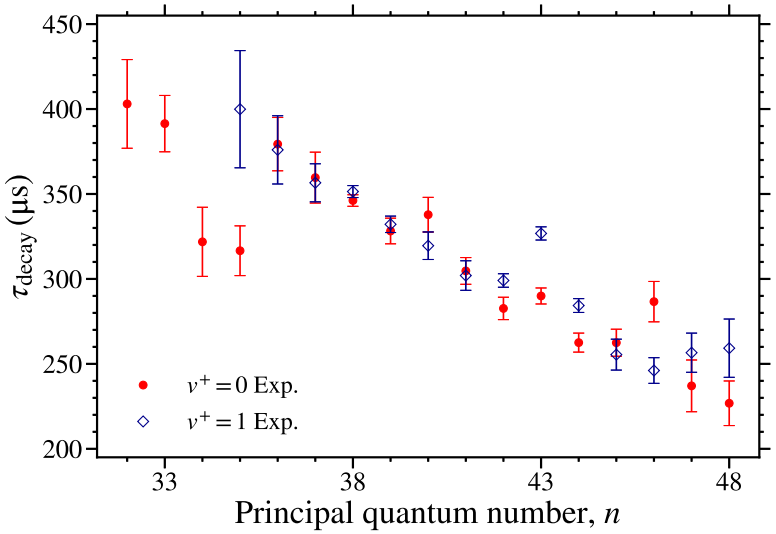

Figure 6.3: Measured trap-decay time constants, τ_{decay}, for $n(2)$ Rydberg states converging to the $v^+ = 0$ [filled red circles – from Fig. 5.9(c) in Chapter 5], and $v^+ = 1$ [open blue diamonds] states in the ground electronic state of NO^+. For all measurements $V_0 = 149$ V.

In Fig. 6.3, the measured values of τ_{decay} for $n(2)$ Rydberg states with $v^+ = 0$ [filled red circles – from Fig. 5.9(c) in Chapter 5] and $v^+ = 1$ [open blue diamonds], are shown for $n = 32 - 48$. All measurements were performed for $V_0 = 149$ V. The general trend seen in these data is that as the value of n is increased, τ_{decay} decreases. This dependence is seen for the $n(2)$ states in both the $v^+ = 0$ and $v^+ = 1$ series, and was previously also observed for $n(0)$ and $n(1)$ states with $v^+ = 0$ in Chapter 5. The measured values of τ_{decay}, for states with $v^+ = 0$ and 1 agree within the measurement uncertainties. For example, in the case of the $38(2)$ states $\tau_{decay} = 346.2 \pm 3.4$ μs when $v^+ = 0$, and 351.4 ± 3.5 μs when $v^+ = 1$. For individual states in both series, deviations from the general trend are observed. These occur, for example, on the $43(2)$ resonance were the measured values of τ_{decay} are larger than expected from the surrounding states.

The trap-decay times, τ_{decay}, in Fig. 6.3, do not follow the $\sim n^4$ scaling expected for the lifetimes of ℓ-mixed Rydberg-Stark states in atoms [66]. The general trend in the measured values of τ_{decay}, and the deviations from this trend result from weak intramolecular interactions. As described in Chapters 4 and 5, contributions from collisions (the number density of the trapped molecules is $\lesssim 10^5$ cm^{-1}), and

black-body-induced transitions (the trap environment being maintained at ~ 30 K), can be ruled out as playing a significant role. Effects of electric field ionisation are also expected to contribute < 1 s^{-1} to the decay rate from the traps for the values of n studied here. In addition to this, the radiative lifetime of the $v^+ = 1$ vibrational state of the NO^+ ion core, in the $X^+\,^1\Sigma^+$ electronic ground state, is known to be ~ 90ms [170], and is therefore not expected to play a significant role on the ~ 1 ms timescale of the experiments reported here.

As in Chapter 5, the general decrease in the values of τ_{decay} with increasing n for both $v^+ = 0$ and $v^+ = 1$ Rydberg states can be attributed to effects of weak vibrational channel interactions. These interactions occur between $v^+ = 0$ high-n Rydberg states, and short-lived $n = 7$ states with $v^+ = 1$. In $v^+ = 1$ high-n Rydberg states these interaction occur with short-lived $n = 7$ states with $v^+ = 2$. As seen in Fig. 6.1 in both cases, the $n = 7$ states with $v^+ = 1$ ($v^+ = 2$) lie energetically above, but close to, the $N^+ = 0$, $v^+ = 0$ ($v^+ = 1$) Rydberg series limit and decay rapidly by fast non-radiative processes with lifetimes of ~ 1 ps [71, 166].

In the data in Fig. 6.3, the values of τ_{decay} for the $n(2)$ Rydberg states with $v^+ = 0$ and 1 are similar, and in both cases decrease as n increases. This leads to the conclusion that the interaction strengths are similar to those of the $v^+ = 0$ Rydberg states, and as a result a comparable amount of mixing occurs between the $n(2)$ states with $v^+ = 1$ and the $n = 7$, $v^+ = 2$ states. As seen in Fig. 6.1, the $n = 7$, $v^+ = 1$ and 2 states lie in similar energetic positions with respect to the $n(2)$, $v^+ = 0$ and 1 states, respectively, which is consistent with similar contributions from vibrational channel interactions in both cases.

For several of the $n(2)$ resonances in Fig. 6.3, deviations from the general trend exhibited by the data are seen for states with $v^+ = 0$ and 1. In each of these cases, because of near degeneracies, Rydberg-Stark states with more than one set of values of n and N^+ are simultaneously populated upon photoexcitation, decelerated and trapped. For the $v^+ = 0$ states, these near degeneracies were also discussed in Chapter 5 . For $v^+ = 1$, the main deviation from the general trend is seen on the $43(2)$ resonance. In this instance, molecules in $43(2)$ and $48(0)$ Rydberg-

Stark states are simultaneously confined in the trap following photoexcitation on the 43f(2) resonance. The 43(2) Rydberg-Stark states are populated because of electric-field-induced mixing with the optically accessible 43f(2) states. Charge-quadrupole interactions, that couple states for which $\Delta N^+ = \pm 2$ and $\Delta \ell = 0$, also mix 43f(2) character into the near degenerate 48f(0) state, which, in the presence of weak stray electric fields mix further with the 48(0) Stark states. Since the 48(0) Stark states decay more slowly from the trap than the 43(2) states – because of their lower value of N^+ and higher value of n – simultaneously trapping molecules in both states results in a value of τ_{decay} that is longer than for surrounding states in the $n(2)$ series.

6.1.4 Deceleration and trapping field strengths

The dependence of τ_{decay} on the strength of the trapping fields was investigated by comparing measurements for $n(2)$ states with $v^+ = 1$ made with $V_0 = 149$ V [open blue diamonds] and 100 V [filled orange squares] as presented in Fig. 6.4. No measurement of τ_{decay} was made for the 40(2) state with $V_0 = 100$ V because the signal was insufficient. In general, for both values of V_0, τ_{decay} decreases with increasing n. However, the values of τ_{decay} for $V_0 = 100$ V are in many instances greater than those for $V_0 = 149$ V. Although, for excitation on the 38(2) and 39(2) resonances the opposite behaviour is seen.

The measurements in Fig. 6.4 demonstrate the persistence of the intramolecular interactions that cause the general reduction in the measured values of τ_{decay} with increasing n at lower trap depths. The slight increase in τ_{decay} for values of n between 41 and 48 when $V_0 = 100$ V, compared to that for $V_0 = 149$ V, reflects the lower time-averaged field-strength experienced by the trapped molecules. This lower field results in smaller Stark shifts, by a factor of $\sim 2/3$, of the trapped molecules. Since the Stark shifts of the LFS Stark states suitable for trapping are positive, reducing them leads to an increase in the average energy separation from the short-lived $n = 7$ states with $v^+ = 2$ which do not shift appreciably in the trapping fields. As a result the amount of mixing with these states that occurs is slightly reduced and the trap decay times are longer.

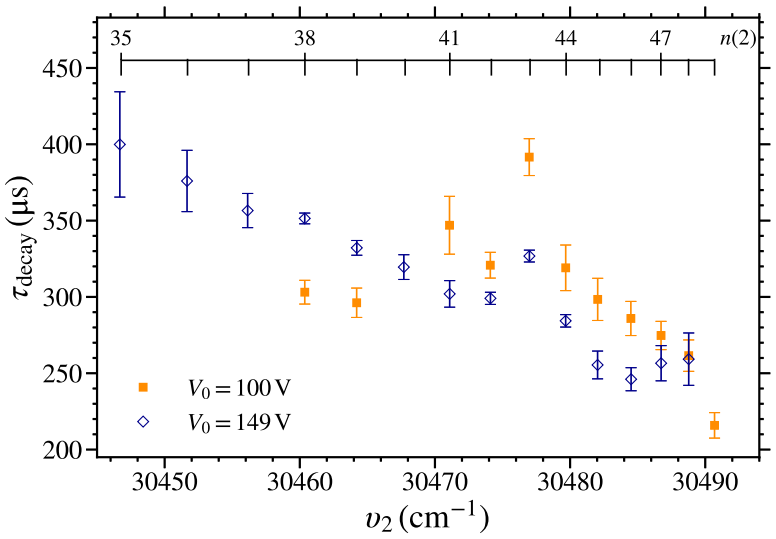

Figure 6.4: Measured trap-decay time constants, τ_{decay}, for $n(2)$ Rydberg states with $v^+ = 1$. The data were recorded for $V_0 = 149$ V (open blue diamonds), and $V_0 = 100$ V (filled orange squares).

The deviation of the value of τ_{decay} for the $43(2)$ resonance in Fig. 6.4, from the general trend exhibited by the surrounding states, is more pronounced when $V_0 = 100$ V than when $V_0 = 149$ V. This is because the difference in the deceleration and trapping efficiency for the $43(2)$ and $48(0)$ Stark states excited on this resonance is more pronounced for lower values of V_0. Consequently, the fraction of trapped molecules in the longer-lived $48(0)$ states is greater under these conditions and τ_{decay} increases.

Finally, the values of τ_{decay} decrease on the $38(2)$ and $39(2)$ resonances when V_0 is reduced to 100 V. This is attributed to a change in the distribution of Stark states populated in the trap. For lower trap potentials, states with smaller dipole moments are trapped less efficiently than those with larger dipole moments. Therefore, for a given value of n, a smaller range of Stark states will be efficiently trapped when $V_0 = 100\,\text{V}$, than when $V_0 = 149\,\text{V}$. The changes in these measured values of τ_{decay} reflect differences in the lifetimes of individual components within a manifold of ℓ-mixed Rydberg-Stark states, and in particular the fact that the outermost Stark states with the largest static electric dipole moments generally exhibit the shortest of these lifetimes.

6.1.5 Vibrational autoionisation

Because the Rydberg-Stark states with $v^+ = 1$ lie above the $v^+ = 0$ series limit, they can decay by vibrational autoionisation. Spontaneous emission from these states, and predissociation are expected to contribute in a similar way to the total decay rates of $n(2)$ Stark states with both $v^+ = 0$ and 1. Therefore, a comparison of the values of τ_{decay} for states in these two Rydberg series allows effects of vibrational autoionisation on the decay of the long-lived $v^+ = 1$ Rydberg-Stark states in the trap to be inferred. Because the values of τ_{decay} for the $v^+ = 0$ and 1 states agree to within the experimental uncertainties, it is concluded that vibrational autoionisation does not play a significant role in the decay of the trapped molecules when $v^+ = 1$. An upper bound on the rate of vibrational autoionisation of these states, $\gamma_{\text{vib-trap}}$, can be obtained by considering the contribution required for τ_{decay} to change by twice the measurement uncertainty. This suggests that for $n = 38$, $\gamma_{\text{vib-trap}} \lesssim 60\ \text{s}^{-1}$.

Studies reported previously of the decay dynamics of Rydberg states in NO with values of $\ell \leq 4$, included detailed analyses of effects of vibrational autoionisation [71, 80, 89, 166, 167]. In these works it was shown that these low-ℓ Rydberg states with $v^+ = 0$ and 1 decay predominantly by fast non-radiative processes. However, in contrast to the $v^+ = 0$ states, for which predissociation is the dominant decay pathway, the $v^+ = 1$ Rydberg states predissociate and autoionise. Recent measurements of the decay rates of $ng(N^+)$ Rydberg states with $v^+ = 1$ and $n = 22$, 25, and 28, yielded total decay rates that were proportional to n^{-3} ($\sim 4 \times 10^{11} n^{-3}\ \text{s}^{-1}$ averaged over all rotations and sub-states, i.e., $\sim 2 \times 10^7\ \text{s}^{-1}$ at $n = 28$) [80]. Calculations of the autoionisation rates, using a long-range potential model [69, 80], indicated that $\sim 70\%$ of the total decay rate of these states could be attributed to autoionisation, with the remaining $\sim 30\%$ associated with predissociation. This is in line with previously measured predissociation rates of $ng(N^+)$ states with $v^+ = 0$ [89]. For all of the short-lived states studied in these works, the spontaneous emission rates were approximately three orders of magnitude lower than the autoionisation rates.

To connect these previous results to the measurements described here for long-

lived, ℓ-mixed Rydberg-Stark states, the vibrational autoionisation rates predicted by the long-range potential model were extrapolated to higher values of ℓ [69, 80]. This allowed an estimate of the order of magnitude of the n- and ℓ-dependent vibrational autoionisation rates, $\gamma_{\rm vib}(n,\ell)$, given by

$$\gamma_{\rm vib}(n,\ell) \simeq 10^{16} n^{-3}\,\ell^{-8}\ {\rm s}^{-1}. \tag{6.2}$$

From this expression it can be determined that the vibrational autoionisation rates of $n = 38$ Rydberg states with values of ℓ between 4 and 12 lie between $\gamma_{\rm vib}(38,4) \sim 10^6\ {\rm s}^{-1}$ and $\gamma_{\rm vib}(38,12) \sim 10^2\ {\rm s}^{-1}$. The spontaneous emission rates of these same states are between 10^4 and $10^3\ {\rm s}^{-1}$.

The molecules that were successfully decelerated and trapped in the experiments reported here were those in outer LFS Rydberg-Stark states. Calculations of the vibrational autoionisation rates of these states, for $n = 38$ and $M_N = 4$, and in Stark manifolds with $\ell_{\rm min} = 4$, 5, and 6 (in an atom these would correspond to $m_\ell = 4$, 5, and 6 manifolds, respectively) were therefore made to aid in the interpretation of the experimental data. In these calculations, the vibrational autoionisation rate of a Stark state $|i\rangle$ was determined by decomposing it into Hund's-case-(d) basis states $|k\rangle = \left|n_k\,\ell_k\,N_k^+\,N_k\,M_{Nk}\right\rangle$, such that

$$\gamma_{{\rm vib-calc},i} = \sum_k |c_{ik}(F_z)|^2\,\gamma_{\rm vib}(n_k,\ell_k), \tag{6.3}$$

where $c_{ik}(F_z) = \langle k|i(F_z)\rangle$ are the coefficients of the corresponding eigenvector in the electric field, F_z. These coefficients were calculated by the matrix diagonalisation methods described in Chapter 3. The mean time-averaged electric field strength of $\overline{F}_z = 95\ {\rm V\,cm^{-1}}$, experienced by the molecules as they move within the traps was determined through numerical particle trajectory calculations, see Chapter 4, and used in the calculations. By accounting for the n- and ℓ-dependence of $\gamma_{\rm vib}(n,\ell)$ using the expression in Eq. 6.2, the vibrational autoionisation rates obtained for the outermost LFS Stark states with $\ell_{\rm min} = 4$, 5, and 6 were $\sim 3\times10^3$, $\sim 7\times10^2$, and $\sim 2\times10^2\ {\rm s}^{-1}$, respectively. These rates are all an order of magnitude, or more,

larger than the experimentally determined bound of $\gamma_{\text{vib}-\text{trap}} \lesssim 60\ \text{s}^{-1}$.

To obtain further insight into the link between the experimental data and these crude order of magnitude estimates, the vibrational autoionisation rates of the field-free $|n\ell\rangle$ Rydberg states were considered more generally to have the form

$$\gamma_{\text{vib}}(n,\ell) = A\, n^{-3}\, \ell^{-p}, \tag{6.4}$$

where A and p are adjustable parameters. To explore the range of values of A and p that could result in Rydberg-Stark state vibrational autoionisation rates $\lesssim 60\ \text{s}^{-1}$, these parameters were constrained to ensure that $\gamma_{\text{vib}}(n,4)$ was equal to the values reported recently for Rydberg states in Ref. 80. This was achieved by adjusting the value of A for each value of p. For these tests the value of p was chosen to lie between 6 and 18 because the intramolecular charge-dipole, charge-quadrupole, and charge-polarisability interactions scale with between $\ell^{-5} - \ell^{-7}$, $\ell^{-3} - \ell^{-9}$, and $\ell^{-5} - \ell^{-7}$, respectively [67]. And, considering Fermi's Golden Rule, the corresponding vibrational autoionisation rates would depend on the square of these quantities.

The calculated values of $\gamma_{\text{vib}-\text{calc}}$ for the outermost LFS Stark states with $n = 38$ and $M_N = 4$ in manifolds with $\ell_{\text{min}} = 4$, 5, and 6 are shown in Fig. 6.5. From these data it is seen that when $\ell_{\text{min}} = 4$, $\gamma_{\text{vib}-\text{calc}}$ converges to $\sim 600\ \text{s}^{-1}$ as the value of p is increased. This represents the contribution to autoionisation rate of the outermost Stark-State from the field-free $\ell = 4$ vibrational autoionisation rate for this value of n. Because the experimental bound on the vibrational autoionisation rates in the work reported here (dashed horizontal line) lies below $\gamma_{\text{vib}-\text{calc}}$ for all values of p under these conditions, it is concluded that the Rydberg states of the decelerated and trapped molecules cannot possess any $\ell \leq 4$ character. For $\ell_{\text{min}} = 5$ and 6, the calculated vibrational autoionisation rates do reduce below $60\ \text{s}^{-1}$ for $p \gtrsim 12$, and 10, respectively. In both of these cases the fluorescence rates of the field-free Rydberg states exceed the vibrational autoionisation rates for $\ell \gtrsim 8$. The ℓ-scaling suggested by these observations is stronger than that in Eq. 6.2. However, because even crude estimates of the kind outlined here of vibrational autoionisation rates

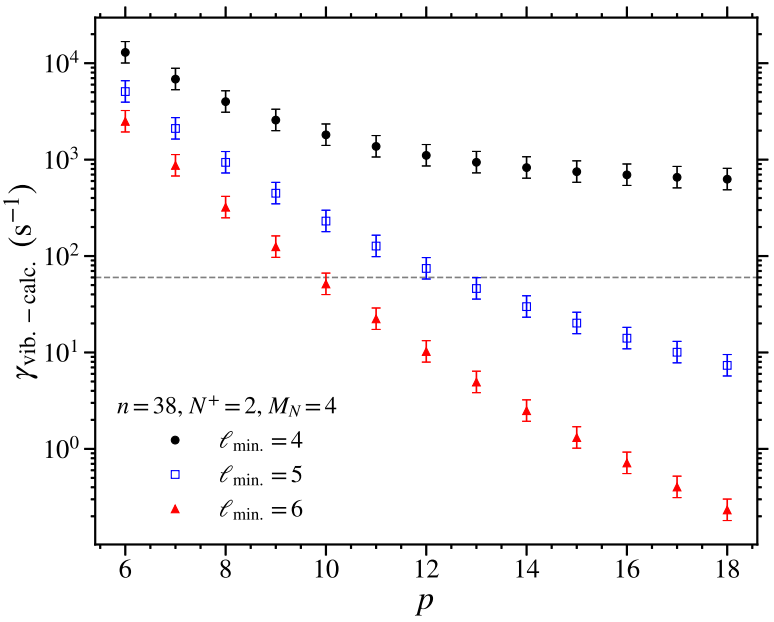

Figure 6.5: Calculated vibrational autoionisation rates of the outermost LFS Stark states with $n = 38$ and $M_N = 4$ in manifolds for which the minimum ℓ character considered was $\ell_{\text{min}} = 4$ (black circles), 5 (open blue squares), and 6 (red triangles) (see text for details).

of ℓ-mixed Rydberg-Stark states are very sensitive to the vibrational autoionisation rates of the field-free low-ℓ states, a more precise interpretation of the experimental results will require more accurate values of the vibrational autoionisation rates of the field-free Rydberg sates with $\ell > 4$.

6.2 Effects of rotational excitation on decay rates of Rydberg NO

6.2.1 Experimental methods

In the experiments presented in this section, the NO molecules were photoexcited using the resonance-enhanced two-colour two-photon

$$\begin{aligned} &\text{X}^2\Pi_{1/2}\left(v''=0, J''=5/2\right) \\ &\qquad\rightarrow \text{A}^2\Sigma^+\left(v'=0, N'=4, J'=7/2\right) \\ &\qquad\qquad\rightarrow n\ell\,\text{X}^{+\,1}\Sigma^+\left(v^+=0, N^+\right) \end{aligned} \quad (6.5)$$

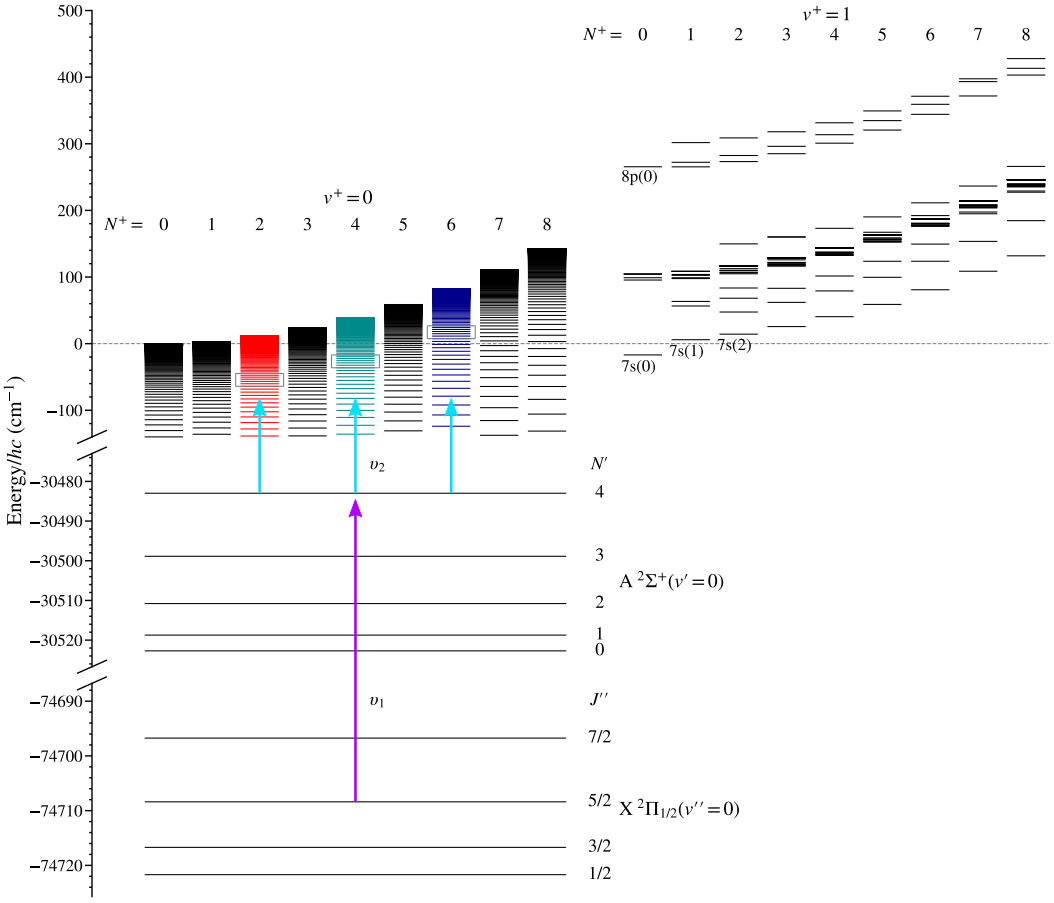

Figure 6.6: Resonance-enhanced two-colour two-photon excitation scheme utilised in the experiment to prepare high-n Rydberg states of NO, in series converging to the $N^+ = 2$, 4, and 6 rotational states of the $v^+ = 0$ vibrational state of NO^+. The grey boxes indicate the zero-field zero-quantum-defect energies of states with $n = 38$ to 44, in their respective series. The zero-field energies of $n = 7$, $v^+ = 1$ states, located close to the $v^+ = 0$, $N^+ = 0$ ionisation limit, are also shown.

excitation scheme depicted in Fig. 6.6. The frequency tripled, υ_1, and doubled, υ_2, outputs of two counter-propagating Nd:YAG pumped dye lasers were used to drive the $X\,^2\Pi_{1/2} \rightarrow A\,^2\Sigma^+$ and $A\,^2\Sigma^+ \rightarrow n\ell\,X^+\,^1\Sigma^+$ transitions, respectively. Here, $\upsilon_1 = 44225.35\,\mathrm{cm}^{-1}$ ($\equiv 226.115$ nm) [$\sim 90\ \mu$J/pulse], and υ_2 was varied in the range of 30384 cm^{-1} to 30511 cm^{-1} ($\equiv 329.12$ nm to 327.75 nm) [~ 0.7 mJ/pulse, collimated to a beam waste of $\sim$ 2-mm]. In addition, the intensity of the tuneable radiation at wavenumber υ_2 was monitored throughout the measurements on a photodiode.

After photoexcitation, three types of measurements were performed. Either

the Rydberg molecules (i) travelled for a short distance beyond the excitation position for a time $t = 1$ μs before detection by SFI; (ii) were loaded into a single travelling electric trap of the Rydberg-Stark decelerator and guided at a constant speed of 795 $\mathrm{m\,s^{-1}}$ to the detection position ~ 100 mm downstream in the apparatus, with delayed PFI then performed at a time $t = 132$ μs after photoexcitation; or (iii) were decelerated in a travelling trap in the decelerator from 795 $\mathrm{m\,s^{-1}}$ to rest in the laboratory-fixed frame of reference, with PFI at times $t \geq 250$ μs after photoexcitation. The deceleration and trapping was performed as described in Chapter 4. The SFI potential in measurement type (i) was applied to electrode E1 [see Fig. 4.1], and had the same form as the SFI potential described in Chapter 5 but with $V_{\mathrm{max}} = -250$ V. For measurement type (ii) and (iii), the rapidly-rising PFI potential of $+500$ V was applied to the side electrodes [see Fig. 4.1]. The ions or electrons generated by PFI or SFI were accelerated out of the decelerator structure and cryogenic region of the apparatus, to either one of two MCP detectors operated at room temperature for collection.

6.2.2 Results and discussions

As in Chapter 5, the photoexcitation scheme used allowed access to Rydberg states in NO with np or nf character. The presence of weak time-varying electric fields gave rise to population transfer from the optically-accessible Rydberg states into longer-lived ℓ-mixed Rydberg-Stark states [76, 91]. This processes occurred most efficiently for states with nf character because of their comparatively small quantum defects of ~ 0.02 [82, 86], and hence their energetic proximity to higher-ℓ states with the same value of n. Because the quantum defects of the nf states are not strongly dependent on the rotational quantum number, N^+, of the NO^+ ion core [82], the mechanisms by which the long-lived Stark states are populated are similar for Rydberg series with different values of N^+. By exciting the molecules through the level in the intermediate A-state with a rotational quantum number $N' = 4$, it was therefore possible to prepare molecules in similar distributions of ℓ-mixed Rydberg-Stark states in series with $N^+ = 2$, 4, and 6.

The spectrum of Rydberg states prepared in the experiments, with lifetimes

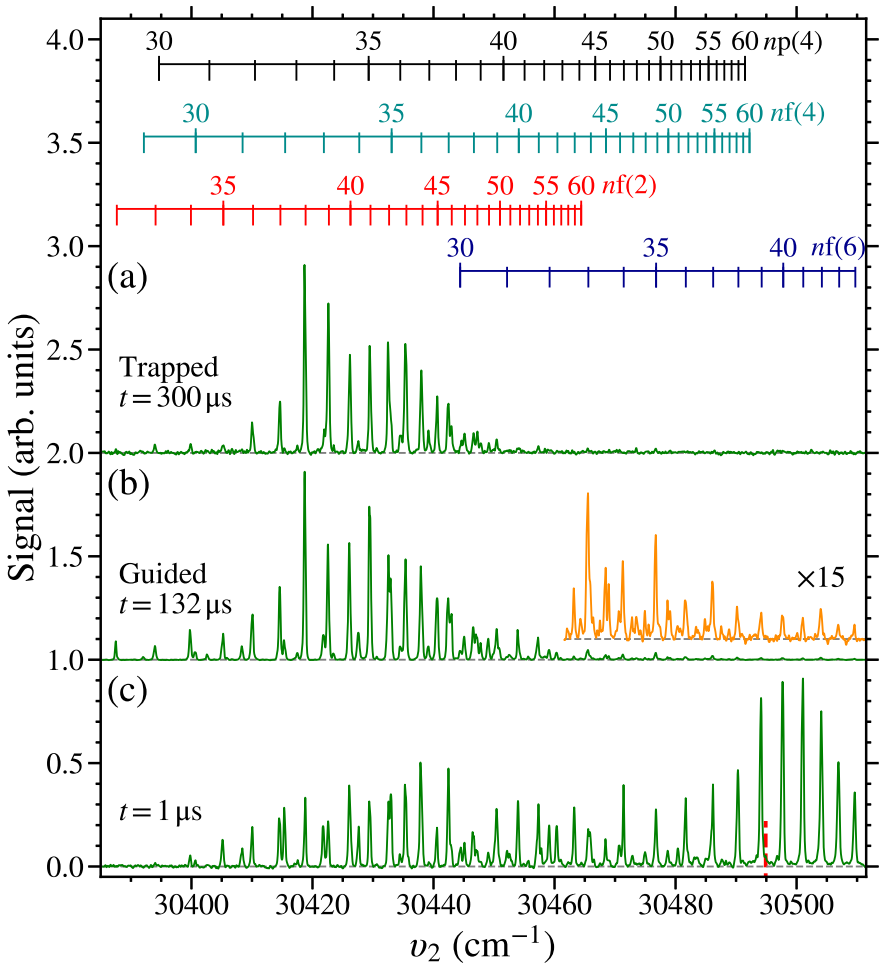

Figure 6.7: Laser photoexcitation spectra of Rydberg states in NO recorded after: (a) deceleration and trapping at $t = 300\,\mu$s, (b) guiding at $t = 132\,\mu$s, and (c) free-expansion at $t = 1\,\mu$s after photoexcitation. All measurements recorded with $\upsilon_1 = 44225.35\,\text{cm}^{-1}$. The vertical red dotted line in (c) represents the position of the $N^+ = 2$ series limit at $\upsilon_2 = 30494.90\,\text{cm}^{-1}$. The spectra shown in (a) and (b) were detecting NO^+ ions using PFI, and in (c) SFI was used with electrons detected.

sufficient for detection 1 μs after excitation, can be seen in Fig. 6.7(c). This spectrum was recorded by SFI so that the signal from the bound Rydberg states displayed, could be separated from that of free electrons generated by direct photoionisation close to, or above the series limits for the lower values of N^+. This, and the other spectra in Fig. 6.7, represent the mean of between 7 and 16 individual measurements. When recording these spectra, the intensity and wavenumber of υ_2 was monitored and recorded for each data point. The NO^+ ion, or the electron signal

recorded on the MCP was then normalised to account for effects of shot-to-shot intensity fluctuations by dividing by the laser intensity. Since the sets of values of υ_2 sampled in each individual spectrum were not exactly the same from one measurement to the next, because of the way in which the tuneable dye laser was scanned, to average the spectra, an equally spaced set of wavenumbers covering the entire measurement range was generated. At each wavenumber in this set, the average spectral intensity was then obtained from the weighted mean of the individual spectra using a Gaussian weighting function with a standard deviation $\sigma = 0.075$ cm^{-1} corresponding to that of the laser spectral profile. Uncertainties were calculated using the standard error on the weighted mean. The absolute signal levels cannot be directly compared between the spectra presented in Fig. 6.7 because of the differing detection efficiencies associated with each spectrum reported.

The spectrum in Fig. 6.7(c) contains transitions to states with values of n between 33 and approximately 55 in the $N^+ = 2$ (lowest wavenumber resonances), $N^+ = 4$ (middle section of the spectrum between $\sim$ 30430 and 30480 cm^{-1}), and $N^+ = 6$ (high wavenumber resonances) series. Each of the features observed can be associated with transitions to the individual Rydberg states in these series as indicated by the vertical bars at the top of the figure. The series observed are those expected from the propensity rules for strong transitions from the intermediate A state to the high Rydberg states, see Section 5.1. The spectra are dominated by transitions to $n\mathrm{f}(N^+)$ Rydberg states. However, there are several features corresponding to excitation on $n\mathrm{p}(4)$ resonances. These typically arise as a result of intramolecular charge-multipole interactions between near degenerate states [67, 86, 90]. Interactions of this kind mix optically accessible $n\mathrm{p}(4)$ character into $n'\ell'(N^{+\prime})$ states which further evolve in the time-varying electric fields close to the time of excitation into long-lived $n'(N^{+\prime})$ ℓ-mixed Rydberg-Stark states. The intensities of the resonances in the spectrum depend on the efficiency with which long-lived Rydberg states are populated in each case. The increase in the intensity of the signal associated with the excitation of $N^+ = 6$ Stark states with values of $n > 38$ and $\upsilon_2 > 30490$ cm^{-1} is attributed to an increase in the number of ions and electrons,

and enhanced electric-field-induced ℓ- and M_N-mixing close to the time of photoexcitation, in this spectral region which is close to or above the $N^+ = 2$ series limit (dashed red vertical line).

The spectrum in Fig. 6.7(b) was recorded by detection of molecules that were loaded into a single travelling electric trap in the Rydberg-Stark decelerator and transported without deceleration over a distance of ~ 100 mm to a second detection region in the apparatus. There, upon switching off the guiding fields, the molecules were detected by PFI at a time $t = 132$ μs after photoexcitation. The resulting spectrum is very different to that in Fig. 6.7(c). It is dominated by the features in the wavenumber range between 30400 and 30460 cm^{-1} that are also present in panel (c). However, the spectral intensity distribution is different. The stronger features in the delayed PFI spectrum correspond to excitation on nf(2) resonances, while the resonances for which $N^+ = 4$ are weaker. Transitions to Rydberg states with $N^+ = 6$ are almost completely absent from this spectrum. They can however be identified in the wavenumber range between 30460 and 30510 cm^{-1} if the signal amplitude is scaled by a factor of 15 [orange spectrum inset and vertically offset in panel (b)]. The intensities of the observed features arise from a combination of (i) the efficiency with which long-lived Rydberg states were populated, (ii) the efficiency with which the molecules were loaded into the travelling electric trap of the decelerator, (iii) the detection efficiency, and (iv) the excited-state decay rates. However, across this spectrum molecules excited to $n(N^+)$ states with the same value of n are expected to be loaded, guided and detected with a similar efficiency because these processes are dominated by the behaviour of the Rydberg electron and not strongly affected by the rotational state of the ion core. The differences in spectral intensities in Fig. 6.7(c) and (b) therefore suggest that the molecules prepared in the more highly excited rotational states, i.e., those with $N^+ = 4$ and 6, decay more rapidly from the travelling electric traps as they are guided to the position where delayed PFI was performed than those in the $N^+ = 2$ states.

Further information on the decay dynamics of the excited molecules was obtained by deceleration to rest in the laboratory-fixed frame of reference and elec-

trostatic trapping. For molecules travelling with an initial longitudinal speed of 795 $\mathrm{m\,s^{-1}}$ this deceleration process took ~ 250 μs. A spectrum recorded with detection after a subsequent trapping time of 50 μs, and therefore at a total time after photoexcitation of $t = 300$ μs is displayed in Fig. 6.7(a). This spectrum contains fewer strong resonances than that in panel (b). The features observed are predominantly those associated with the transitions to Rydberg states in the $N^+ = 2$ series. This further reduction in signal from molecules in the more highly excited rotational states at this later detection time lends additional weight to the suggestion that for a similar range of values of n, the Rydberg states excited in series converging to more highly excited rotational states of the NO^+ ion core decay more rapidly than those associated with lower rotational states.

Quantitative information on the decay rates of the decelerated and electrostatically trapped molecules was obtained by direct measurements of trap loss, as described in Chapter 5. These were carried out for molecules excited on $N^+ = 2$ resonances only. This involved measurements of trap decay time constants for values of n between 38 and 44 inclusive, over times ranging from 300 to 600 μs after photoexcitation, i.e., for trapping times between 50 and 350 μs. The results of these measurements are presented in Fig. 6.8(a). The measured trap decay time constants range from 340 to 275 μs and generally decrease as the value of n increases. These values agree within the experimental uncertainties with those measured upon photoexcitation from the $\mathrm{A}\,^2\Sigma^+\,(v' = 0, N' = 0, J' = 1/2)$ intermediate state, seen in Fig. 5.9. As in Chapter 5, the observed decrease in the trap decay time constant with n was attributed to the increase in the coupling, as the excitation wavenumber is increased, to the short-lived, ~ 1 ps, $n = 7$ states with $v^+ = 1$ located close to the $N^+ = 2$ series limit (see Fig. 6.6). The deviations of the trap decay time constants from this general trend, for example at $n = 43$, can be attributed to effects charge-quadrupole interactions that result in the population of pairs of near degenerate Rydberg states in series with values of N^+ that differ by 2. In the particular case of the Rydberg states with $n = 43$ in the $N^+ = 2$ series, the coupling that occurs is with the longer-lived near degenerate $n = 48$ states in the $N^+ = 0$ series.

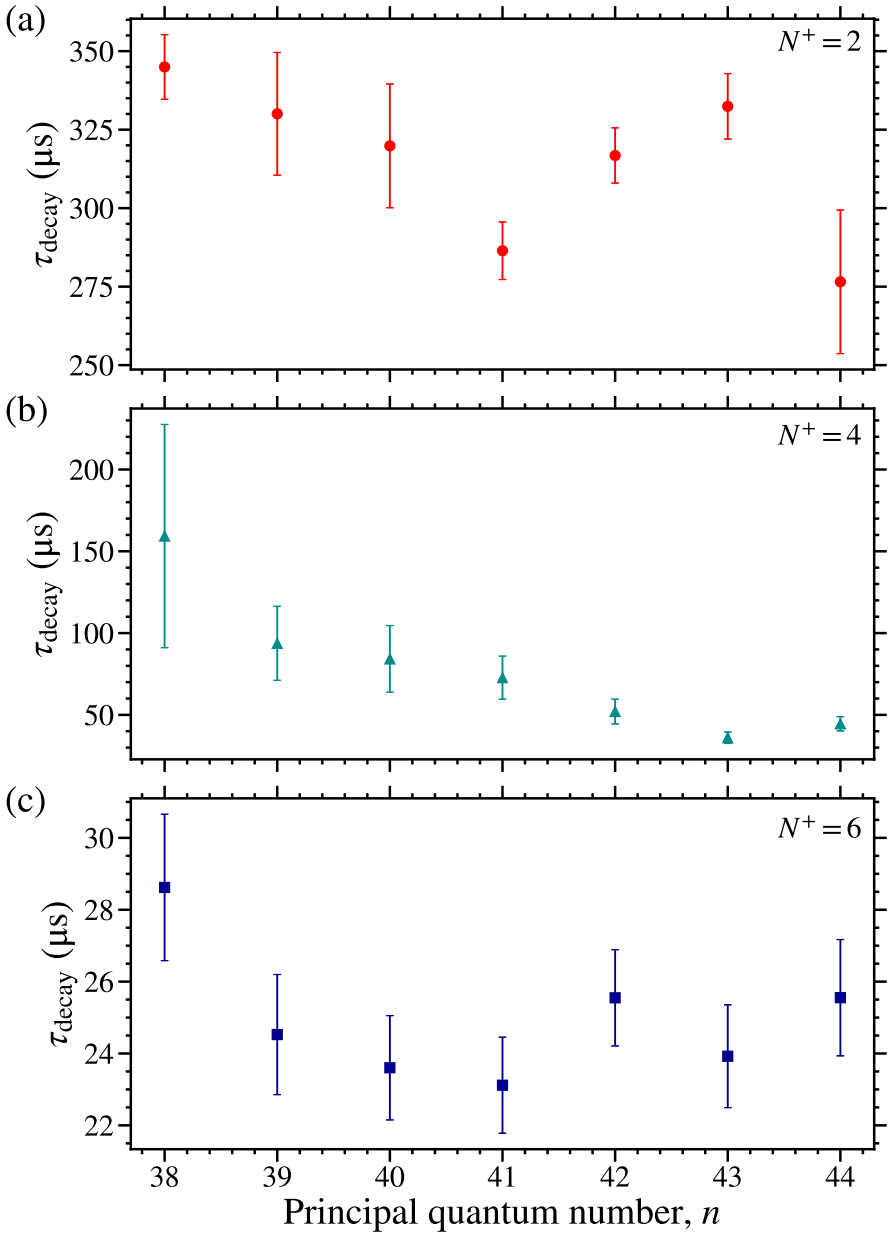

Figure 6.8: (a) Measured trap-decay time constants of long-lived $n(2)$ Rydberg states. Decay time constants for the (b) $n(4)$, and (c) $n(6)$, states inferred from the relative spectral intensities measured at 1 μs and 132 μs after photoexcitation. See text for details.

The decay time constants of molecules excited to states with $N^+ = 4$ and 6 could not be measured by monitoring loss rates from the electrostatic trap because of the insufficient signal strength at later times after photoexcitation.

Although the decay time constants of $n(4)$ and $n(6)$ states could not be obtained from trap decay measurements, they could be determined from the changes

in the relative spectral intensities of the corresponding resonances in the spectra recorded at $t = t_0 = 1$ μs [Fig. 6.7(c)] and $t = t_1 = 132$ μs [Fig. 6.7(b)] after photoexcitation. To achieve this, the decay rates of the molecules in the $n(2)$ Rydberg states measured after deceleration and electrostatic trapping were used for calibration, and the assumption was made that the decay of the molecules in the time between laser photoexcitation and $t = t_0 = 1$ μs could be neglected. This is considered reasonable since this period of time is $< 1\%$ of the typical decay time constant of the molecules in these states.

For each value of n, the efficiency with which long-lived Rydberg-Stark states were populated was assumed to be similar for all values of N^+ studied. This assumption is based on the fact that the quantum defects of the optically accessible nf Rydberg states, and hence their proximity to the manifold of long-lived ℓ-mixed Rydberg-Stark states into which population evolves after excitation, are not strongly dependent on the value of N^+. From this starting point, the differing contributions from the detection and guiding efficiencies in the spectra recorded directly after photoexcitation at $t_0 = 1$ μs, and after confinement and guiding in the travelling trap of the decelerator for $t_1 = 132$ μs, could be accounted for by scaling the data recorded at the later detection time by a factor $C_{\rm scale}(n,t_1)$. The value of $C_{\rm scale}(n,t_1)$ was calculated such that the ratio of the resulting normalised spectral intensities, $C_{\rm scale}(n,t_1)\,I_{n(2)}(t_1)$ to $I_{n(2)}(t_0)$, on the $n(2)$ resonances was equal to that expected from an exponentially decaying function with the corresponding decay time constant, $\tau_{n(2)}$, in Fig. 6.8(a), i.e.,

$$\frac{C_{\rm scale}(n,t_1)\,I_{n(2)}(t_1)}{I_{n(2)}(t_0)} \;=\; \exp\left[-\frac{t_1-t_0}{\tau_{n(2)}}\right]. \qquad (6.6)$$

This same scaling factor was used to normalise the signal amplitude associated with the $n(4)$ and $n(6)$ resonances in the same spectrum. The decay rates of these states could then be obtained by determining $\tau_{n(N^+)}$ from

$$\frac{C_{\rm scale}(n,t_1)\,I_{n(N^+)}(t_1)}{I_{n(N^+)}(t_0)} \;=\; \exp\left[-\frac{t_1-t_0}{\tau_{n(N^+)}}\right] \qquad (6.7)$$

when $N^+ = 4$ and 6. This procedure was repeated for each individual value of n between 38 and 44 for which the measurements were made, with the results presented in Figs. 6.8(b) and (c).

The data in Fig. 6.8(b) and (c) indicate that the decay time constants of the $N^+ = 4$ and 6 Rydberg-Stark states populated in the experiments range from 50 to 150 μs, and from 23 to 29 μs, respectively. These are significantly shorter than the values of $\tau_{n(2)}$ in Fig. 6.8(a). The general trend observed is therefore that the decay time constants for a given value of n reduce as the value of N^+ is increased, i.e., the Rydberg state decay rates increase with N^+. However, the general trend within each individual N^+ Rydberg series, that the decay time constants decrease as the value of n increases, persists for each value of N^+. Although this general trend is less apparent for the shorter-lived states with $N^+ = 6$.

The spontaneous emission rates of the Rydberg states studied are not expected to exhibit a strong dependence on N^+. Therefore, the observation of a decrease in the measured decay time constants with N^+ point to an increase in the rates of non-radiative decay processes, i.e., rotational autoionisation or predissociation, as the value of N^+ increases. Since the $N^+ = 2$ and 4 states studied lie below all lower-N^+ Rydberg series limits (see grey rectangles in Fig. 6.6), these states cannot decay by rotational autoionisation. The change, by a factor of approximately $1/3$, in the lifetimes of the Rydberg states with $N^+ = 4$ compared to those with $N^+ = 2$ in Figs. 6.8(a) and (b) therefore cannot be attributed to rotational autoionisation. As can be seen in Fig. 6.6, the $N^+ = 6$ Rydberg states studied do lie above the ionisation limits of all series with $N^+ \leq 3$. However, the strongest rotational channel interactions that could give rise to rotational autoionisation are the charge-dipole interaction between the Rydberg electron and the static electric dipole moment of the NO^+ ion core, and the charge-quadrupole interaction. The charge-dipole interaction couples states for which $\Delta N^+ = 1$, while the charge-quadrupole interaction couples states for which $\Delta N^+ = 0$ or 2. Since couplings between the bound Rydberg states in the $N^+ = 6$ series and the ionisation continuum with $N^+ \leq 3$ necessitate an interaction for which $\Delta N^+ \geq 3$ this can only occur through higher-order processes

which do not have a strong propensity. For the particular states studied here it is therefore concluded that the observed dependence of the Rydberg state decay rates on the value of N^+ is not dominated by effects of rotational autoionisation, and must therefore be caused by changes in the Rydberg-state predissociation rates.

Changes in the rates of predissociation of the Rydberg states with $N^+ = 2$, 4, and 6 studied are attributed to differences in the amount of low-ℓ character, i.e., $\ell \lesssim 3$, of the Rydberg-Stark states populated in the excitation process as the value of N^+ increases. From the measured decay time constants of the Rydberg states in the $N^+ = 2$ series in Fig. 6.8(a), and the data reported in Sections 5.2 and 6.1, it was concluded that the molecules in long-lived Rydberg states that are successfully decelerated and trapped must be in states with high-$|M_N|$ values, i.e., $|M_N| \gtrsim 4$. For $N^+ = 2$, there exist $2N^+ + 1 = 5$ manifolds of ℓ-mixed Rydberg-Stark states, and when $|M_N| = 4$ the minimal short-lived low-ℓ character in each of these manifolds ranges from 2 to 6 (see Section 3.5 in Chapter 3). Because of this there are many Rydberg-Stark manifolds that do not possess any low-ℓ, i.e., $\ell \lesssim 3$, character. The molecules in these manifolds are therefore most likely to be decelerated and trapped as they are the longest-lived.

This situation is, however, different for $N^+ = 4$ or 6. For $N^+ = 4$, the manifolds of Rydberg-Stark states for which $|M_N| = 4$ can contain values of ℓ down to zero. The short-lived $\ell \lesssim 3$ character in these manifolds of Rydberg-Stark states, results in shorter measured decay times for each value of n than observed when $N^+ = 2$. For $N^+ = 6$, this situation is even further exaggerated, and the decay times of the states populated in the excitation process further reduced. Although the distribution of values of $|M_N|$ of the excited molecules is expected to be similar for each value of N^+, contributions from states with short-lived low-ℓ character differ significantly as the value of N^+ is increased. The observed reduction in the decay time constants of the molecules for each particular value of n with increasing N^+ is therefore attributed to changes in the underlying low-ℓ character of the states that are populated. This is consistent with the behaviour of the trap decay time constants for Rydberg states with $N^+ = 0$, 1, and 2 discussed in Chapter 5.

6.3 Conclusions

The experiments described in this chapter allowed the investigation of the effects of vibrational and rotational excitation on the decay of Rydberg NO molecules in long-lived high-n Rydberg-Stark states. This work included the first demonstration of electrostatic trapping vibrationally excited molecules following Rydberg-Stark deceleration. The trap decay time constants for NO molecules in Rydberg states converging to the $v^+ = 1$ series limit, were found to exhibit the same general trend as those measured for $v^+ = 0$ Rydberg states with the same value of N^+. Indeed, the measured trap decay time constants for molecules in $v^+ = 0$ and 1 Rydberg-Stark states were found to be equal within the measurement uncertainties. It was therefore concluded that the $v^+ = 1$ Rydberg states prepared in the experiments did not exhibit a significant rate of decay by vibrational autoionisation. An upper limit on the of rate of vibrational autoionisation of 60 s^{-1} could be placed on the states prepared in the experiment. Studies of the decay time constants of molecules in $v^+ = 0$ Rydberg series, but converging to more highly excited rotational states of the NO^+ ion core, i.e., those for which $N^+ = 4$ and 6, indicated that molecules in states with higher values of N^+ decayed more rapidly. This observation was attributed to the increase in the amount of short-lived predissociative low-ℓ character as the value of N^+ was increased for similar values of $|M_N|$. These unique measurements demonstrate for the first time that Rydberg states in small molecules that have lifetimes on the order of 100 μs do not simply behave like atomic Rydberg states as is often assumed when simple n-scaling rules are applied. Instead, the same rich decay dynamics that occurs in the short-lived low-ℓ Rydberg states persist and are observable in experiments.

Chapter 7

Spectroscopy and electrostatic-trapping of Rydberg N_2

N_2 is the most abundant molecule in air. Studies of Rydberg states in N_2 are therefore of interest in understanding the physics and chemistry of plasmas generated by electrical discharges including lighting [171–174], and photoionisation by solar radiation [47, 48, 175–177]. Because N_2 has no ground state electric or magnetic dipole moment cold, trapped gas-phase samples have never before been prepared. Samples of this kind offer opportunities for detailed studies of weak transitions, interactions, and slow decay processes. These effects can be otherwise challenging to study quantitatively in the laboratory, but for atmospheric quantities of N_2 irradiated by the sun can have a significant impact. In addition, the preparation of cold electrostatically trapped samples of Rydberg N_2 opens opportunities to study the slow decay dynamics of long-lived Rydberg states in a homonuclear molecule, and allows comparison with the measurements made with NO presented in the previous chapters. In this chapter, laser spectroscopic studies of high-n Rydberg states in N_2 are first presented in Section 7.1. The aim of these experiments was to identify an appropriate excitation scheme by which molecules in long-lived Rydberg-Stark states could be prepared. Following this, in Section 7.2, deceleration and electrostatic trapping N_2 molecules in these long-lived Rydberg-Stark states is demonstrated for the first time.

7.1 Ion-dip and photoabsorption spectroscopy of Rydberg states in N_2

7.1.1 Experimental methods

In the experiments described in this section, photoexcitation of N_2 molecules to long-lived Rydberg-Stark states was studied, with the aim of preparing samples suitable for Rydberg-Stark deceleration and electrostatic trapping. To achieve this pulsed supersonic beams of N_2 were intersected with co-propagating frequency-tripled and fundamental outputs of two Nd:YAG-pumped pulsed dye lasers, between electrodes E1 and E2 in the Rydberg-Stark decelerator apparatus depicted in Fig. 4.1. These lasers were operated at wavenumbers υ_1 and υ_2, respectively, to photoexcite or photoionise the ground-state molecules. Both lasers were focused into the vacuum chamber using the same 300 mm focal length lens, to a minimum beam waist of ~ 100 μm FWHM. In the experiments performed $\upsilon_1 = 49415$ - 49440 cm^{-1} ($\equiv$ 202.37 - 202.27 nm) [at either ~ 35 μJ/pulse or ~ 200 μJ/pulse], and $\upsilon_2 = 26665$ - 26830 cm^{-1} ($\equiv$ 375.02 - 372.72 nm) [at ~ 4 mJ/pulse]. The pulse-length of the laser radiation was ~ 8 ns, with a FWHM spectral width of ~ 0.25 cm^{-1}. The output of the dye lasers was monitored using a fibre-coupled wavelength meter.

After laser photoexcitation or photoionisation, photo-ions and Rydberg N_2 molecules were detected and distinguished by ramped pulsed electric field ionisation. This was carried out by applying a slowly rising potential of the form $V_{\rm ramp}(t) = V_{\rm max}\left[1-\exp\left(-t/\tau_{\rm ramp}\right)\right]$, with $V_{\rm max} = +400$ V and $\tau_{\rm ramp} = 1.55$ μs, to E1, see Fig. 7.1(a). This potential: (i) accelerated the photo-ions extracted at early times in these potentials through a 2 mm diameter aperture in E2 to be collected on an MCP detector, and (ii) ionised the molecules excited into the Rydberg states at higher potentials with the resulting ions accelerated to the MCP. Since the molecules in the Rydberg states ionise at times $t > 0$, in the rising potential, the resulting ions were accelerated through a larger potential difference than the prompt photo-ions. As a result these "Rydberg-ions" arrived at the MCP earlier than the

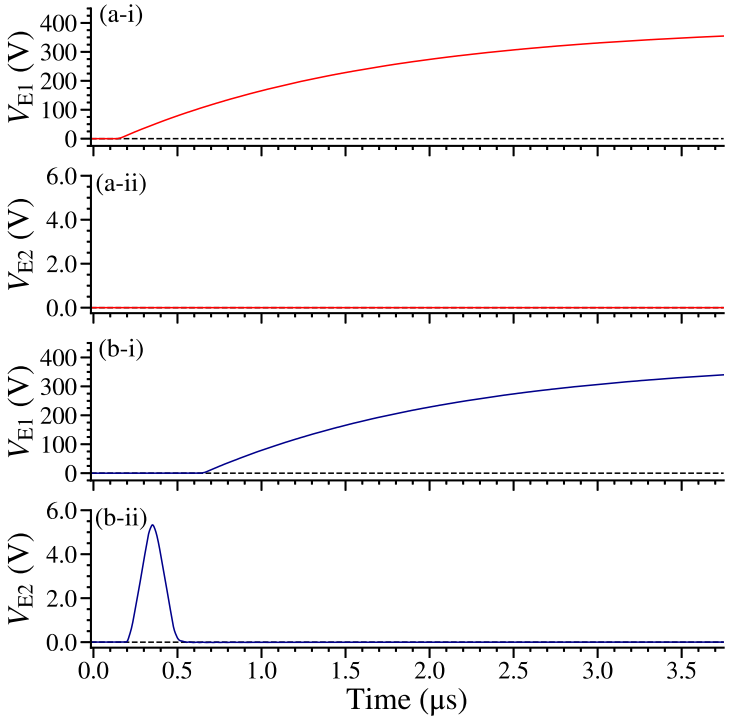

Figure 7.1: Potentials applied to electrodes (i) E1, and (ii) E2, for N_2^+ ion detection at times (a) 150 ns, and (b) 650 ns after photoexcitation.

prompt photo-ions. The ramped ionisation pulse was applied 150 ns after photoexcitation [Fig. 7.1(a)], to allow both the changes in the number of prompt photo-ions and molecules in Rydberg states, to be monitored simultaneously. Examples of the N_2^+ signal recorded at the MCP detector using this detection scheme are shown in Fig. 7.2. The time on the horizontal axis of this figure is the time elapsed after the rising potential was applied to electrode E1. In Fig. 7.2 three time-of-flight distributions are shown for: (i) $\upsilon_2 = 26735.22$ cm^{-1} (orange line), which is not on resonance with any transition to a Rydberg state, (ii) $\upsilon_2 = 26733.41$ cm^{-1} (green line) which is resonant with the transition to the predissociative 35p$(N^+ = J')$ state, that results in depletion of the photo-ion signal, and (iii) $\upsilon_2 = 26776.80$ cm^{-1} (blue line) which is resonant with the transition to the 47f$(N^+ = J')$ state, that leads to the population of Rydberg states that ionise in the rising electric field. These "Rydberg-ions" are indicated by the blue shaded region.

To detect only the bound Rydberg states, a pulsed-potential was applied to E2 200 ns after laser photoexcitation to deflect the prompt photo-ions, see Fig. 7.1(b).

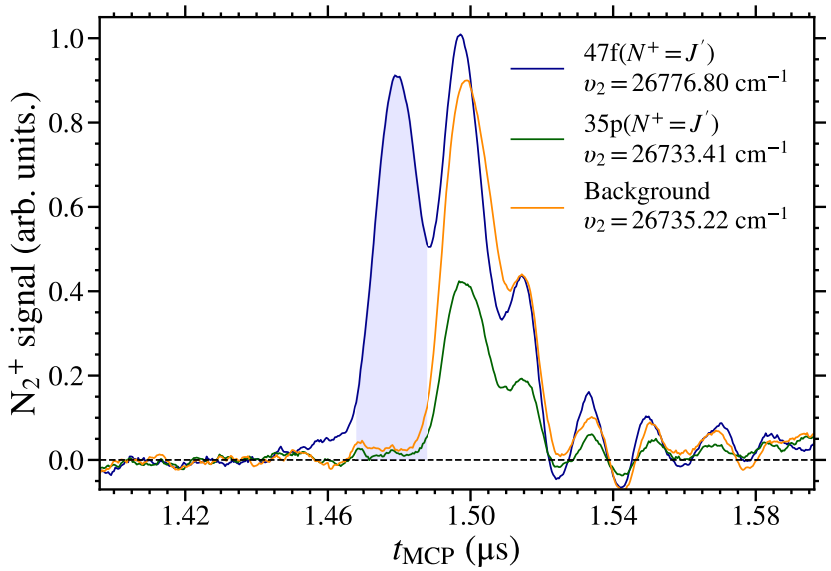

Figure 7.2: Signal from MCP detector with $2\upsilon_1 = 98840.7$ cm^{-1}, and υ_2 as indicated in the legend (see text for details). The time indicated is that elapsed after the rising potential was applied to electrode E1.

This potential had a total duration of ~ 300 ns and a maximum at ~ 5.5 V. The maximal electric field of ~ 18.3 Vcm^{-1} during this pulse also resulted in the diabatic electric field ionisation of molecules in Rydberg states with $n \gtrsim 75$ - 89. This pulsed potential was followed at 650 ns after photoexcitation by the main high voltage ramped ionisation potential that allowed the detection of molecules in Rydberg states at this later time.

7.1.2 Excitation scheme

In the experiments described in this section, N_2 molecules were excited into high-n Rydberg states using the resonance-enhanced two-colour three-photon

$$X\,^1\Sigma_g^+\left(v''=0,J''\right) \;\rightarrow\; a''\,^1\Sigma_g^+\left(v'=0,J'\right) \;\rightarrow\; n\ell X^+\,^2\Sigma_g^+\left(v^+=0,N^+\right) \quad (7.1)$$

excitation scheme [95, 96]. This is depicted schematically in Fig. 7.3. The $X(v''=0) \rightarrow a''(v'=0)$ transition was driven through the absorption of two photons at wavenumber υ_1. Single-colour (2+1) resonance enhanced multi-photon ionisation (REMPI) spectra were recorded to characterise this ground-to-intermediate state transition. Examples of these spectra are shown in Fig. 7.4. The transitions in

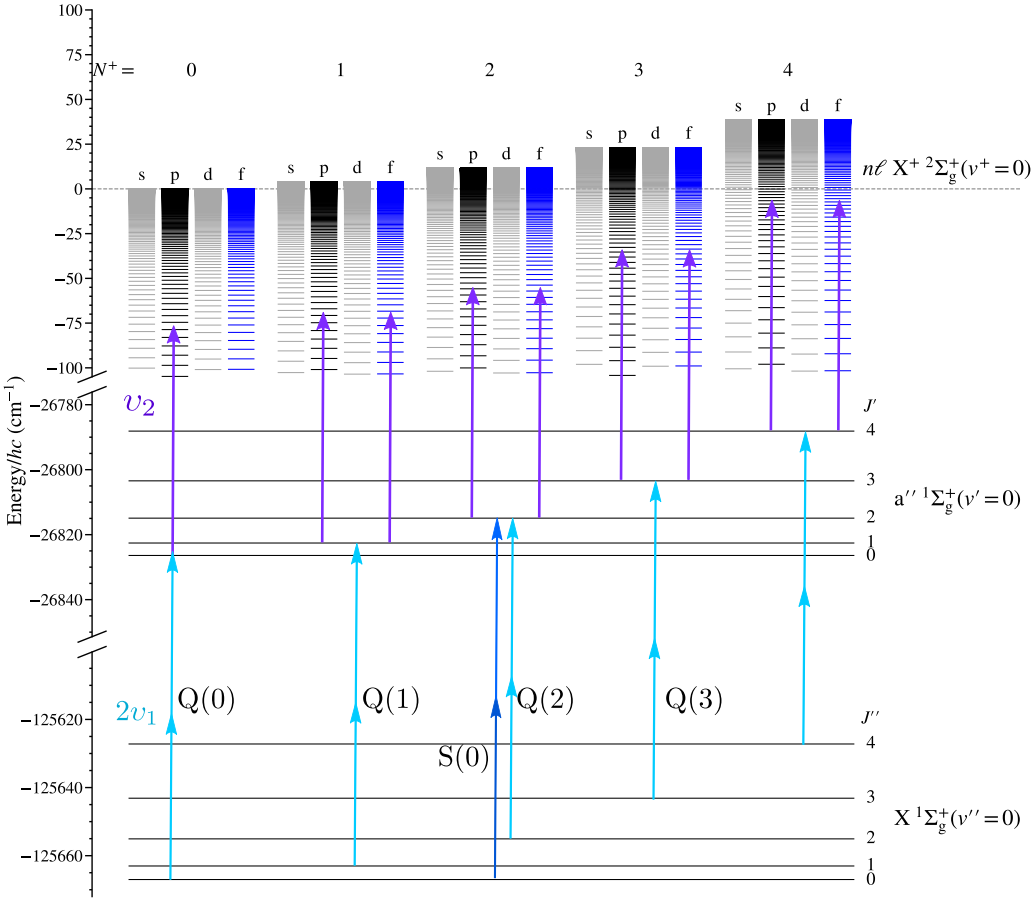

Figure 7.3: Resonance-enhanced two-colour three-photon excitation scheme used to prepare high-n Rydberg states in N_2. For clarity only the $N^+ = J'$ cases of the allowed a$''(v'=0,J') \rightarrow n\ell X^+(v^+=0,N^+)$ transitions are shown (see text for more details).

this figure are labelled using the $\Delta J(J'')$ notation, where the labels Q and S refer to $\Delta J = 0$ and $+2$ transitions, respectively. The energies of the transitions were calculated using the constants in Table 7.1. However, because the rotational constants of the X and a$''$ states are very similar, see Table 7.1, the Q-branch transitions were not rotationally resolved.

The long lifetime of the intermediate a$''$ state of ~ 3.5 μs [178], and the strong Franck-Condon overlap with the ground state of the N_2^+ molecular cation, arises because the a$''$ state is a low-lying Rydberg state, therefore make it an ideal choice of intermediate state from which to access high-n Rydberg states. Transitions from the a$''$ state to the high-n Rydberg states, labelled using the $n\ell(N^+)$ notation, were driven using laser radiation at wavenumber υ_2 in the experiments. This scheme was

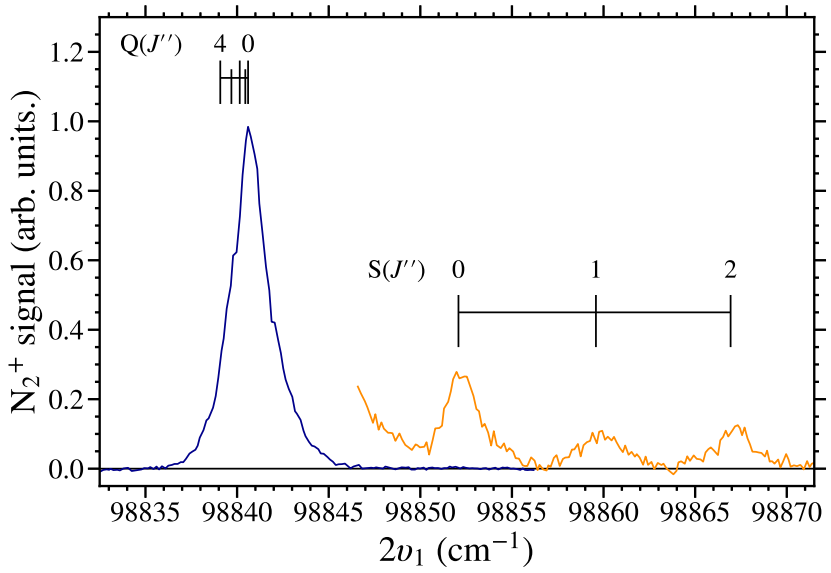

Figure 7.4: Single-colour (2+1) REMPI spectra of the $X\,^1\Sigma_g^+(v''=0,J'') \rightarrow a''\,^1\Sigma_g^+(v'=0,J')$ transitions in N_2. The two spectra shown are not on same scale, with the blue spectrum being recorded with a laser pulse energy of $\sim 35\ \mu$J/pulse, and the orange spectrum with $\sim 200\ \mu$J/pulse.

Table 7.1: Electronic and rotational constants of the $X\,^1\Sigma_g^+(v''=0)$ and $a''\,^1\Sigma_g^+(v'=0)$ states in $^{14}N_2$, and the $X^+\,^2\Sigma_g^+(v^+=0)$ state in $^{14}N_2^+$. All quantities are given in cm^{-1}. Values from Refs. 92, 94, 121 and 179.

Quantity	$X\,^1\Sigma_g^+(v''=0)$	$a''\,^1\Sigma_g^+(v'=0)$	$X^+\,^2\Sigma_g^+(v^+=0)$
T_e	0	98840.59993	125667.0
$B_{rot.}$	1.9895776	1.9137062	1.92234
$D_{rot.}$	5.74137×10^{-6}	6.0000×10^{-6}	6.10×10^{-6}

implemented by excitation to the a$''$ state through: (i) the rotationally unresolved Q-branch transitions at wavenumber $2\upsilon_1 \simeq 98840.7$ cm^{-1} [$\sim 35\ \mu$J/pulse], or (ii) the rotationally resolved S(0) branch at $2\upsilon_1 \simeq 98852.2$ cm^{-1} [$\sim 200\ \mu$J/pulse].

7.1.3 Results and discussions

Before discussing the recorded spectra, it is worth considering which $a''(J') \rightarrow n\ell(N^+)$ transitions are likely to occur. Since the a$''$ intermediate state is nominally a $3s\sigma_g$ Rydberg state, it has predominately $\ell'=0$ character with the most significant higher ℓ' character being $\ell'=2$ [95, 96]. It can therefore be expected that single-

photon electric dipole transitions from the a$''$ to np(N^+) and nf(N^+) Rydberg states are most likely.

More generally, the strong electric dipole transitions that will occur must: (i) conserve total angular momentum, i.e, $\vec{J} = \vec{J}' + \vec{\gamma}$ [where $\vec{\gamma}$ is the photon angular momentum, and $\vec{J}'$ and $\vec{J}$ are the total angular momentum in the a$''$ and high-n Rydberg states, respectively], and (ii) result in a change of total parity, i.e., $p_{\mathrm{a}''} p_{n\ell(N^+)} = -1$ [where $p_{\mathrm{a}''}$ and $p_{n\ell(N^+)}$ are the parities of the a$''$ and high-n Rydberg states, respectively]. In addition, the transitions with the highest propensity will: (i) follow the rotational spectator model [71, 153, 162] where, $\vec{\ell} = \vec{\ell}' + \vec{\gamma}$, i.e., the laser field acts on what is nominally the 3sσ_{g} electron to excite it into a higher-lying Rydberg state, and (ii) not result in a change in total spin, i.e., since the a$''$ state is a singlet state the high-n Rydberg states excited will also be singlet states, such that $\vec{S}' = \vec{S} = \vec{0}$ [where $\vec{S}'$ and $\vec{S}$ are the total spin angular momenta of the a$''$ and high-n Rydberg states, respectively].

The a$''$ state is a $^1\Sigma_{\mathrm{g}}^+$ state. It can therefore be described in Hund's case (b), with a total angular momentum of $\vec{J}' = \vec{N}'$, since $\vec{S}' = \vec{0}$, and a total parity given by $p_{\mathrm{a}''} = (-1)^{J'}$ (since in general the parity is given by $p = (-1)^{N'-\Lambda'}$, where Λ' is the projection of $\vec{N}'$ onto internuclear axis, but $\Lambda' = 0$ for $^1\Sigma_{\mathrm{g}}^+$ states and $J' = N'$) [78]. The high-n Rydberg states, converging toward the $\mathrm{X}^+\,^2\Sigma_{\mathrm{g}}^+$ state of the N_2^+ cation, can be described using Hund's case (d). In this coupling scheme the total angular momentum is $\vec{J} = \vec{N} + \vec{S}$, where $\vec{N} = \vec{N^+} + \vec{\ell}$ and $\vec{S} = \vec{0}$. The total parity of the Rydberg state is $p_{n\ell(N^+)} = (-1)^{N^+ + \ell}$ (since $\Lambda^+ = 0$, where Λ^+ is the projection of $\vec{N^+}$ onto the internuclear axis, for the $\mathrm{X}^+\,^2\Sigma_{\mathrm{g}}^+$ state of the N_2^+ ion core) [77, 78]. By combining these with the conservation of angular momentum and the propensity rules discussed above, it can be determined that the strongest transitions from the a$''$ state to the Rydberg states are those for which:

$$\ell = \ell' \pm 1 \tag{7.2}$$

$$\left|J' - \ell'\right| \leq N^+ \leq J' + \ell' \tag{7.3}$$

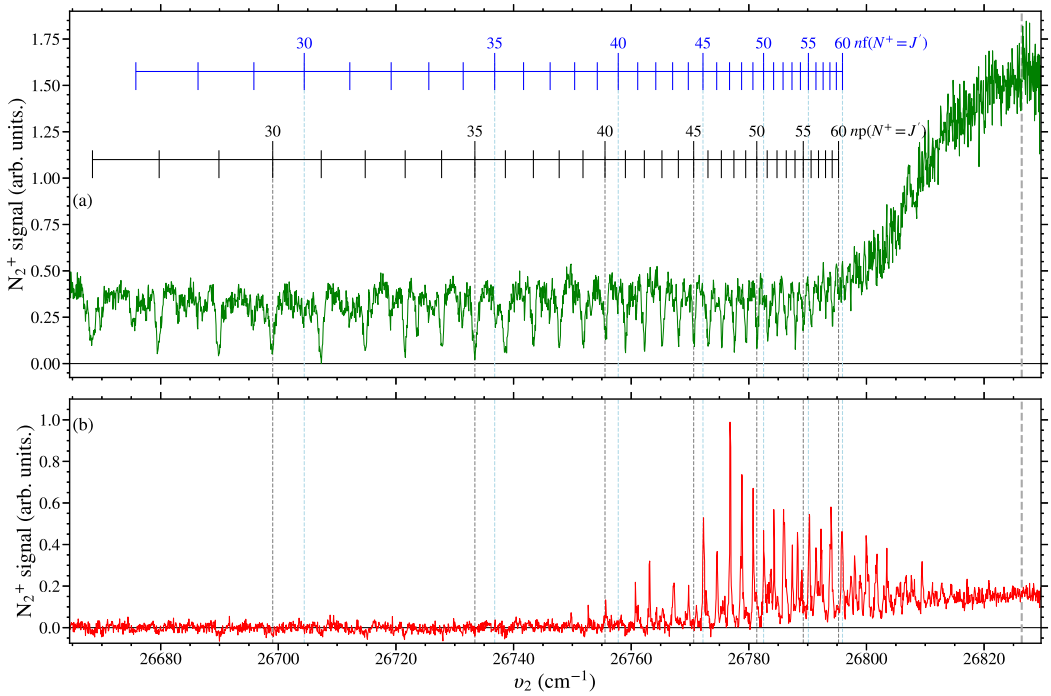

Figure 7.5: Spectra of transitions to high Rydberg states in N_2 recorded with photoexcitation though the rotationally unresolved Q-branch of the X $\rightarrow$ a$''$ transition at $2\upsilon_1 = 98840.7$ cm^{-1}. (a) Prompt N_2^+ photo-ion signal, and (b) Rydberg field ionisation signal. In each case the detection electric field pulse was applied 150 ns after the laser pulse. The thick grey dashed line at 26826.40 cm^{-1} indicates the $N^+ = J' = 0$ series limit.

$$J' + N^+ + \ell = \text{odd}. \tag{7.4}$$

It was therefore expected that transitions will be observed from (i) the $\ell' = 0$ component of the a$''$ state to np(N^+) Rydberg states with $N^+ = J'$, and (ii) the $\ell' = 2$ component of the a$''$ state to np(N^+) and nf(N^+) Rydberg states with $N^+ = J'$, $J' \pm 2$ [although from the $J' = 0$ intermediate state, only transitions to np(2) and nf(2) Rydberg states are likely to occur from the $\ell' = 2$ character component of the a$''$ state]. Transition wavenumbers υ_2, can then be calculated using the molecular constants in Table 7.1, together with the Rydberg formula, and the Hund's-case-(d) quantum defects $\mu_p = 0.646$ and $\mu_f = 0.01$ for $\ell = 1$ and 3 high-n Rydberg states, respectively [93, 94].

Fig. 7.5 shows spectra recorded by scanning the wavenumber of the second laser, υ_2, with the first laser wavenumber set to be resonant with the rotationally unresolved Q-branch X $\rightarrow$ a$''$ transition at $2\upsilon_2 = 98840.7$ cm^{-1}. For these mea-

surements detection was implemented as in Fig. 7.1(a), with the ramped ionisation potential applied 150 ns after the laser pulse. A spectrum representing the change in the prompt photo-ion signal as υ_2 was scanned is shown in Fig. 7.5(a). The corresponding signal resulting from electric field ionisation of molecules in bound Rydberg states is shown in Fig. 7.5(b). The similarity of the rotational constants in the a'' and X^+ states, see Table 7.1, means that transitions to high-n Rydberg states for which $N^+ = J'$ occur at similar transition wavenumbers for $N^+ = J' = 0$ to 4. For example, the difference between the wavenumbers for transitions in which $N^+ = J' = 0$ and $N^+ = J' = 2$ ($N^+ = J' = 4$) is 0.05 cm^{-1} (0.17 cm^{-1}) and is smaller than the laser bandwidth (~ 0.25 cm^{-1}). Therefore when these transitions occur, molecules in all accessible J' intermediate states are excited to Rydberg states of the same values of n and ℓ, leading to strong spectral features. On the other hand, transitions to Rydberg states with $N^+ = J' \pm 2$ can only occur from the $\ell' = 2$ component of the a'' state. In this case rotational state resolution can be achieved, and not all molecules in the a'' state are excited to high-n Rydberg states at any given laser wavenumber.

The spectrum in Fig. 7.5(a) reflects the changes in the prompt photo-ion signal obtained as υ_2 was scanned. The main features in this spectrum are dips in signal, corresponding to the depletion of the number of prompt photo-ions, at wavenumbers of $\upsilon_2 \lesssim 26795$ cm^{-1}. These dips form a Rydberg series. Each resonance corresponds to a transition to an np($N^+ = J'$) Rydberg state, with $n = 27$ to 56. Since no bound Rydberg states survived to be detected by electric field ionisation on these resonances, i.e., see Fig. 7.5(b), it is inferred that the reduction in the number of prompt N_2^+ photo-ions on these resonances reflects the excitation of np Rydberg states that rapidly predissociated into nitrogen atoms which were not detected. The spectral widths of the np($N^+ = J'$) resonances in the spectrum in Fig. 7.5(a) were obtained by fitting a Lorentzian function to each. The n-dependence of the resulting FWHM spectral widths is show in Fig. 7.6. These FWHM spectral widths generally decrease as the value of the principal quantum number, n, increases. However, for values of $n \gtrsim 45$ they converge to a value of ~ 0.25 cm^{-1}. It is therefore concluded

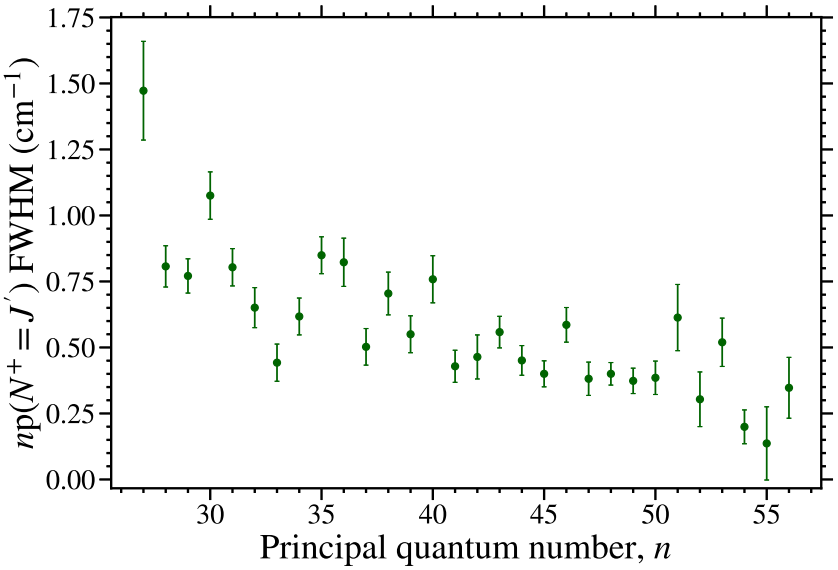

Figure 7.6: Measured FWHM spectral widths of $a'' \rightarrow np(N^+ = J')$ resonances obtained by fitting Lorentzian functions to the ion-dip spectrum in Fig. 7.5(a).

that the FWHM spectral widths at these higher values of n are limited by the laser spectral resolution. On the other hand, at smaller values of n the predissociation lifetimes of the $np(N^+ = J')$ states are sufficiently short that the FWHM become dominated by the short predissociation lifetimes of these Rydberg states.

In Fig. 7.5(a), an enhancement is seen in the prompt photo-ion signal at wavenumbers $\upsilon_2 \gtrsim 26795$ cm^{-1}. This plateaus as the $N^+ = J' = 0$ to 4 series limits are approached, at transitions wavenumbers in range from 26826.40 cm^{-1} to 26826.57 cm^{-1}. This enhancement is therefore attributed to a combination of increased direct near resonant $(2+1')$ photo-ionisation, and the excitation of high Rydberg states that ionise prior to the application of the detection pulse.

Transitions to $nf(N^+ = J')$ Rydberg states dominate the electric field ionisation spectrum in Fig. 7.5(b). However, there are also interloping resonances in this spectrum that can be attributed to transitions to $N^+ = J' \pm 2$ Rydberg states for particularly values of J' in the a'' intermediate state. For $\upsilon_2 \gtrsim 26810$ cm^{-1} a spectrally unresolved signal is observed. This is attributed to a high density of transitions to $N^+ = J'$, $J' \pm 2$ Rydberg states from the rotationally unresolved intermediate state. When $\upsilon_2 \lesssim 26750$ cm^{-1}, no Rydberg states electric field ionisation signal

is observed. The maximum electric field generated by the slowly rising ionisation potential in Fig. 7.1(a) is ~ 1333 Vcm^{-1}. This field exceeds the classical adiabatic ionisation limit for $n \gtrsim 22$, and the diabatic ionisation limit for $n \gtrsim 25-30$. Therefore the absence of nf$(N^+ = J')$ resonances in Fig. 7.5(b) suggests that Rydberg states with sufficiently long lifetimes to allow detection were not populated for $n \lesssim 40$. Indeed there is evidence of weak dip features in the prompt photo-ion signal in Fig. 7.5(a) at the position of the transitions to these nf$(N^+ = J')$ Rydberg states for smaller values of n. Given that the field-free hydrogenic fluorescence lifetimes of such states would range from ~ 15 μs to 70 μs for $25 \leq n \leq 40$ nf Rydberg states, it is suggested here that the decay of molecules excited on these resonances is dominated by fast predissociation.

To further study the Rydberg states populated on the nf$(N^+ = J')$, and nf$(N^+ = J' \pm 2)$ resonances, a second type of spectrum was recorded. In this case the photo-ions were deflected prior to the application of the electric field ionisation pulse used to identify the Rydberg molecule signal. This detection scheme is shown in Fig. 7.1(b). The spectrum in Fig. 7.7 was recorded in this way, with the slowly rising electric field ionisation pulse applied 650 ns after the laser radiation. Transitions to many individual nf$(N^+ = J')$ Rydberg states are resolved for $\upsilon_2 \lesssim 26790$ cm^{-1} in this spectrum. However, the high density of transitions at higher transition wavenumbers leads to an inability to assign individual features. In addition, for $\upsilon_2 \gtrsim 26805$ cm^{-1} there is a general reduction in the intensity of the signal from the bound Rydberg states as υ_2 increases. The electric field associated with the ion deflection pulse, applied before the ionisation pulse, had a maximum value of ~ 18.3 Vcm^{-1}. In this field Rydberg states with $n \gtrsim 75$ - 89 are expected to ionise diabatically. The general reduction in the Rydberg signal at the higher transition wavenumbers, and hence higher values of n in this spectrum, is therefore attributed to this ionisation of Rydberg states excited on nf$(N^+ = J')$ resonances. This, together with the observation that Rydberg states with sufficiently long lifetimes for detection are only seen for $n \geq 38$, suggests that the states detected are long-lived ℓ-mixed Rydberg-Stark states. These hydrogenic Stark state are popu-

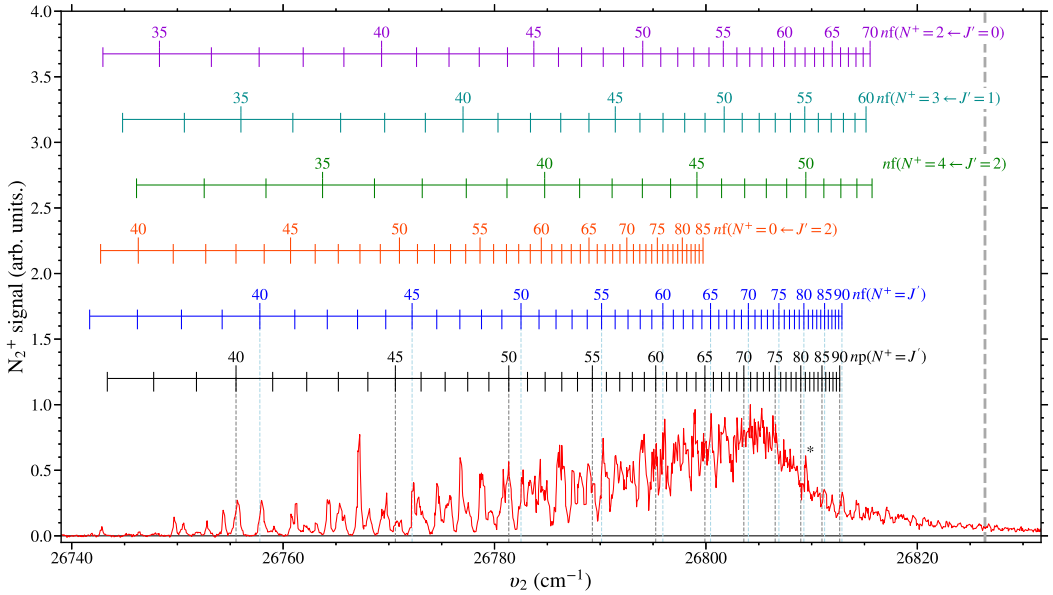

Figure 7.7: Laser photoexcitation spectrum of long-lived Rydberg states in N_2. When recording this spectrum the electric field ionisation pulse for detection was applied 650 ns after the laser pulse as in Fig. 7.1(b). Photoexcitation was carried out though the rotationally unresolved Q-branch of the X $\rightarrow$ a$''$ transition at $2\upsilon_1 = 98840.7$ cm^{-1}. The thick dashed grey line at 26826.40 cm^{-1} indicates the $N^+ = J' = 0$ series limit.

lated by ℓ-mixing of optically accessible $nf(N^+ = J')$ character into the higher-ℓ states by weak stray electric fields close to the time of photoexcitation [76, 91]. These fields can be produced by ions and electrons or laboratory electrical noise. The absence of features associated with excitation on $nf(N^+ = J')$ resonances at lower values of n, in both Fig. 7.5(b) and Fig. 7.7, indicate that the $nf(N^+ = J')$ states were sufficiently separated in energy from the higher-ℓ hydrogenic states such that significant ℓ-mixing did not occur to prevent the decay of the excited molecules by predissociation.

The $nf(N^+ = J')$ Rydberg states in N_2 can be populated from all J' components of the intermediate a$''$ state present. However, the majority of the additionally resolved features in Fig. 7.7 can be attributed to transitions to $nf(N^+ = J' \pm 2)$ states with $J' = 0$, 1, and 2. These also only appear in the spectrum for $n \gtrsim 38$, which is consistent with the situation described above for $nf(N^+ = J')$ states. These $nf(N^+ = J' \pm 2)$ transitions, are also responsible for the sharper features seen at $\upsilon_2 \gtrsim 26805$ cm^{-1}, where the $nf(N^+ = J')$ signal intensity decreases. For exam-

ple, the strong feature indicated by the $*$ at $\upsilon_2 \simeq 26809.5$ cm^{-1} occurs where the 62f($N^+ = 2 \leftarrow J' = 0$), 55f($N^+ = 3 \leftarrow J' = 1$) and 50f($N^+ = 4 \leftarrow J' = 2$) transitions are near degenerate with each other.

In addition to the measurements described above, it was also possible to record spectra by scanning the wavenumber of the second laser, υ_2, while the first laser was tuned to excite the N_2 molecules *via* the rotationally resolved S(0) X $\rightarrow$ a$''$ transition at $2\upsilon_1 = 98852.2$ cm^{-1}. This only leads to the population of the $J' = 2$ rotational level of the a$''$ state. However, because this is a weaker transition than the Q-branch transitions [96], the reduction in signal meant that only spectrum recorded at the earlier detection time, 150 ns after photoexcitation [Fig. 7.1(a)], yielded useful information. These spectra are presented in Fig. 7.8. Fig. 7.8(a) shows the prompt photo-ion signal, while Fig. 7.8(b) shows the corresponding Rydberg state electric-field-ionisation signal.

From the a$''(J' = 2)$ intermediate state the propensity rules, Eq. 7.2 - 7.4, indicate that that the strongest transitions should be to np(N^+) and nf(N^+) Rydberg states for which $N^+ = 0$, 2, and 4. Transitions for which $N^+ = J' = 2$ are expected to be strongest on the np(N^+) resonances as they originate from the majority $\ell' = 0$ character component of the a$''$ state.

In the spectrum recorded by monitoring the prompt photo-ion signal [see Fig. 7.8(a)], the main features are the dips in signal intensity at wavenumbers $\upsilon_2 \lesssim 26790$ cm^{-1}. These dips correspond to depletion of the number of prompt ions. The resonances that dominate this spectrum are those that correspond to transitions to np($N^+ = J' = 2$) Rydberg states, with $n = 35$ to 55. However, no corresponding bound Rydberg-state electric field ionisation signal is observed in Fig. 7.8(b) on these resonances. It may therefore be concluded that these Rydberg states predissociate rapidly upon excitation, resulting in a reduction in the number of N_2^+ photo-ions detected. The transitions to np(N^+) Rydberg states with $N^+ = 0$ and 4, expected from the propensity rules do not give rise to strong features in the spectrum in Fig. 7.8(a), nor do they correspond to any features in the spectrum recorded by Rydberg state electric field ionisation in Fig. 7.8(b).

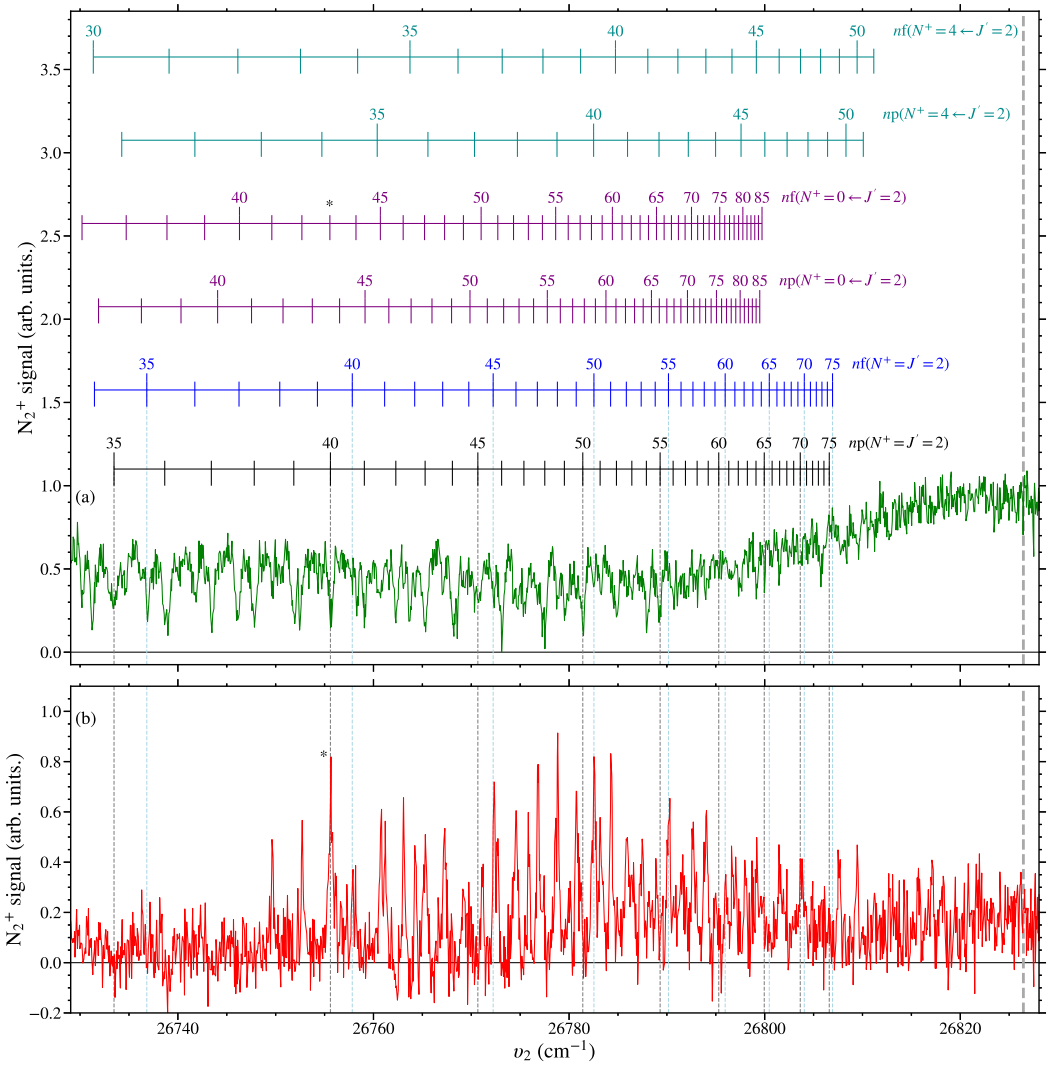

Figure 7.8: Laser photoexcitation spectra of transitions to Rydberg states of N_2 from the intermediate a″ state excited using the the S(0) X → a″ transition at $2\upsilon_1 = 98852.2\ \mathrm{cm}^{-1}$. (a) Shows the prompt N_2^+ photo-ion signal, and (b) shows the Rydberg state field ionisation signal. In both cases the pulsed ionisation electric field was applied 150 ns after the laser pulse. The thick grey dashed line at $26826.45\ \mathrm{cm}^{-1}$ represents the $N^+ = J' = 2$ series limit.

The remaining strong dip features in Fig. 7.8(a) correspond to transitions to $n\mathrm{f}(N^+)$ Rydberg states, with $N^+ = 0$, 2, and 4. These dip features are more pronounced for transitions to $n\mathrm{f}(N^+)$ states with $n \lesssim 40$, where there is no corresponding signal observed from Rydberg states detected by electric field ionisation in Fig. 7.8(b). Examples of such dips in the spectrum in Fig. 7.8(a), that do not correspond to features in Fig. 7.8(b), are seen at the $n\mathrm{f}(N^+ = 4)$ resonances for $n = 30$ to 35. It can be inferred that, for these values of n, sufficient mixing of the optically

accessible $nf(N^+)$ character into the long-lived Rydberg-Stark states does not occur to preclude rapid decay by predissociation.

For higher values of n in Fig. 7.8, i.e. $n \gtrsim 40$, the $nf(N^+)$ resonances do correspond to features in the spectrum in Fig. 7.8(b). In these cases dips are also in the spectrum in Fig. 7.8(a). This suggests that ℓ-mixing does occur to transfer population into long-lived Rydberg-Stark states. The larger spectral intensity of the $43f(N^+ = 0)$ resonance, indicated by the $*$, in Fig. 7.8(b) compared to those surrounding it is likely to reflect the near degeneracy between the $40p(N^+ = 2)$ and $43f(N^+ = 0)$ states, which can mix as the result of the intramolecular interaction of the Rydberg electron with the quadrupole moment of the N_2^+ ion core [67, 86]. In this instance, the strongly optically accessible $40p(N^+ = 2)$ character mixes into the $43f(N^+ = 0)$ state, which further mixes with the long-lived Rydberg-Stark states in the weak stray electric fields.

7.2 Electrostatic-trapping Rydberg N_2 molecules

7.2.1 Experimental methods

In the experiments discussed in this section, the N_2 molecules were excited to long-lived high-n Rydberg states using the two-colour three-photon

$$X\,^1\Sigma_g^+\left(v''=0,J''\right) \;\rightarrow\; a''\,^1\Sigma_g^+\left(v'=0,J'\right) \;\rightarrow\; n\ell X^+\,^2\Sigma_g^+\left(v^+=0,N^+\right) \quad (7.5)$$

excitation scheme presented in Section 7.1, and depicted in Fig. 7.3. The first transition in this excitation scheme is a two-photon transition driven at $2\upsilon_1 = 98841.1\ \mathrm{cm}^{-1}$ [$\sim 150\ \mu$J/pulse, focused with 300 mm focal length lens to a FWHM beam waist of $\sim 100\ \mu$m]. This excited the molecules on the rotationally unresolved $X(J'') \rightarrow a''(J' = J'')$ Q-branch transitions, with $J'' = 0$, 1, and 2 being most populous. Transitions from the a'' state to the high-n Rydberg states were then driven by counter-propagating radiation at $\upsilon_2 \simeq 26735 - 26810\ \mathrm{cm}^{-1}$ [~ 4 mJ/pulse collimated to a beam waste of ~ 2 mm]. This primarily enabled the excitation of Rydberg states with $np(N^+)$ and $nf(N^+)$ character where $N^+ = J'$ (as discussed in

Section 7.1). Time varying electric fields caused by ions, electrons, or laboratory electrical noise, close to the time of photoexcitation cause ℓ-mixing and population transfer into long-lived ℓ-mixed Rydberg-Stark states with high values of $|M_N|$, i.e., $|M_N| \gtrsim 4$, as was discussed in Chapters 5 and 6 for the case of NO [76, 91]. The decay of molecules in these ℓ-mixed Rydberg-Stark state are dominated by fluorescence and not by rapid predissociation. After photoexcitation molecules could be detected at aperture A2 in electrode E2 (see Fig. 4.1), with no decelerating potentials applied in the experiment, or at aperture A1 in electrode E2, after molecules were guided, decelerated, or trapped in the transmission-line decelerator. In all experiments described here the decelerator was operated as described in Chapter 4. In this particular case, the guiding or deceleration potentials were ramped on 6.0 μs after photoexcitation, and a deceleration potential of $V_0 = 149$ V was used. Detection of the Rydberg molecules was performed by PFI, with a fast rising potential of +460 V applied to the side electrodes to ionise the molecules and accelerate the resulting N_2^+ ions out of the cryogenic region of the apparatus to the MCP detector.

7.2.2 Deceleration and trapping

The range of values of n of the long-lived Rydberg states that could be prepared in the experiments was identified by recording laser photoexcitation spectra with detection by delayed PFI 130 μs after photoexcitation. When recording these spectra, the wavenumber, υ_2, of the laser used to drive the $a''\,^1\Sigma_g^+ \rightarrow n\ell X^+\,^2\Sigma_g^+$ transition was scanned while PFI was performed with ion extraction through the aperture A2 on the axis of the molecular beam (see Fig. 4.1). The resulting spectrum is presented in Fig. 7.9(a). Although this spectrum exhibits a high density of spectral features, it can be seen that in general Rydberg states with sufficiently long lifetimes to permit detection 130 μs after photoexcitation were populated following excitation on the $n\mathrm{f}(N^+ = J')$ resonances for values of $n > 35$.

The small quantum defects of $\mu_{n\mathrm{f}} \simeq 0.01$ [94], of the optically accessible $n\mathrm{f}(N^+)$ states in N_2, allow efficient mixing into longer-lived Rydberg-Stark states close to the time of photoexcitation. This mixing can be induced by weak time-varying electric fields – associated with laboratory electrical noise, or arising from

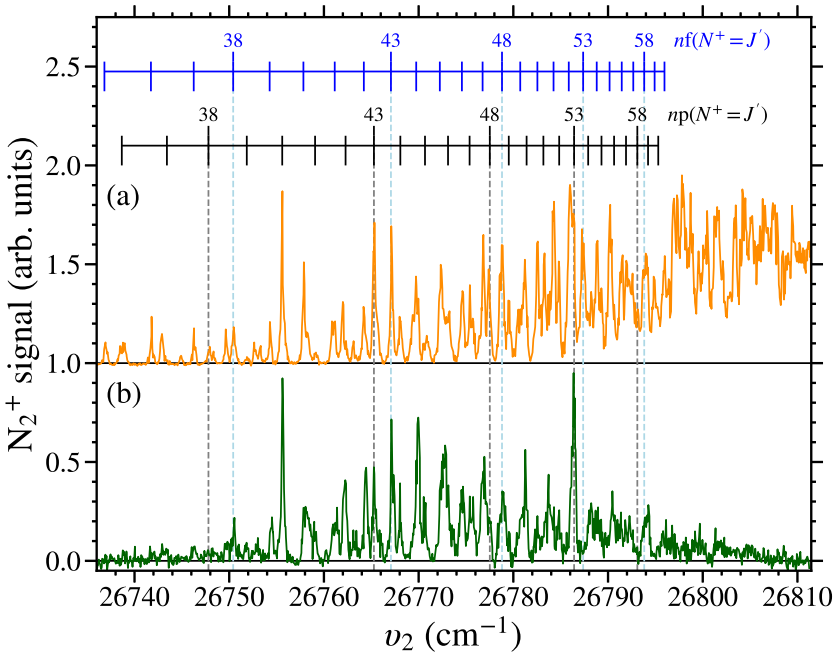

Figure 7.9: Laser photoexcitation spectra recorded by delayed PFI with (a) the decelerator off and detection on the molecular beam axis 130 μs after photoexcitation, and (b) following deceleration and electrostatic trapping for $t_{\text{trap}} = 100$ μs.

collisions with ions and electrons close to the time of laser photoexcitation – and results in the evolution of some excited-state population into the ℓ-mixed Rydberg-Stark states [76, 91]. A subset of these states, with azimuthal quantum numbers $|M_N| \gtrsim 4$ have predominantly high-ℓ, i.e., $\ell \gtrsim 3$, character. For these states rapid predissociation, which typically dominates the field-free decay dynamics of Rydberg states in N_2 for values of $\ell \lesssim 3$, as discussed in Section 7.1, is inhibited. The molecules in these long-lived Rydberg-Stark states were selectively detected in the delayed PFI spectrum in Figure 7.9(a) and are also suitable for deceleration and electrostatic trapping.

The short-lived, predissociative $np(N^+)$ states, with larger quantum defects of $\mu_{np} \simeq 0.646$ [93], which are also accessible in the excitation scheme presented in Fig. 7.1, require larger electric fields to undergo complete ℓ-mixing. Excitation on $np(N^+)$ resonances therefore only leads to the population of long-lived Rydberg-Stark states if intramolecular charge-multipole interactions with accidentally near-degenerate states with smaller quantum defects occur [67, 86]. This is discussed

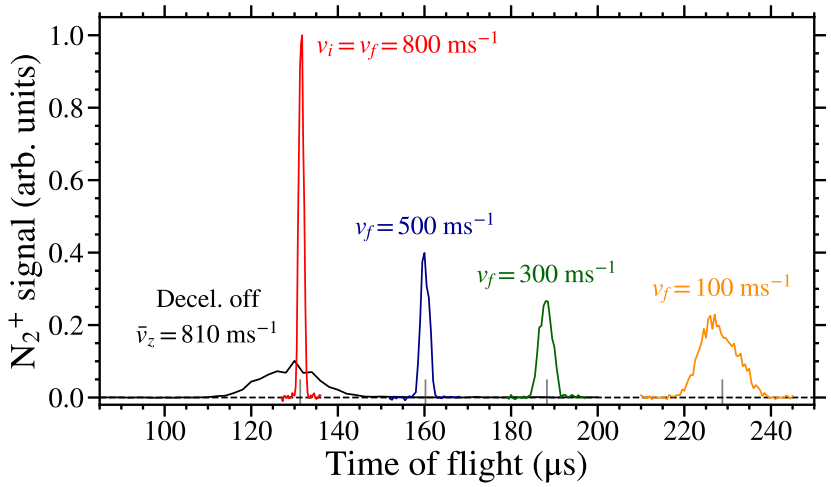

Figure 7.10: TOF distributions of Rydberg N_2 molecules excited on the 43f($N^+ = J'$) resonance with $\upsilon_2 = 26767.10$ cm^{-1} from their position of laser photoexcitation to detection positions $\sim$ 105-mm downstream within the decelerator structure. The TOF distribution recorded with the decelerator off is indicated by the continuous black curve with a maximum close to a time-of-flight of 130 μs. Measurements made with the decelerator on to guide the molecules at 800 m s^{-1} (red curve) and decelerate them from 800 m s^{-1} to final speeds of 500, 300 and 100 m s^{-1} are indicated by the blue, green and orange curves, respectively.

in the context of similar experiments performed with NO in Chapters 5 and 6. An example of this type of channel interaction is seen on the 40p($N^+ = J'$) resonance, at $\upsilon_2 = 26755.55$ cm^{-1} in the spectrum in Fig. 7.9(a) where there is an accidental near degeneracy between the 40p($N^+ = 2$) and 43f($N^+ = 0$) states that can mix as a result of the charge-quadrupole interaction between the Rydberg electron and the N_2^+ ion core.

To observe effects of guiding and deceleration of the long-lived N_2 Rydberg molecules using the chip-based Rydberg-Stark decelerator, υ_2 was tuned to the 43f($N^+ = J'$) resonance in Fig. 7.9(a). This resulted in the population of long-lived hydrogenic Rydberg-Stark states with $n = 43$ and $N^+ = J'$. To determine the mean longitudinal speed of the bunch of excited molecules prepared in this way, a time-of-flight (TOF) spectrum was recorded over the $\sim$ 105 mm distance from the position of laser photoexcitation to the on-axis delayed PFI detection position above aperture A2. This corresponds to the continuous black curve in Fig. 7.10. From this measurement, a mean longitudinal speed of the bunch of excited molecules of

810 m s^{-1} with a standard deviation $\sigma \simeq 40$ m s^{-1} was determined.

With the decelerator potentials on at a peak-to-peak amplitude of $V_0 = 149$ V, molecules in LFS Rydberg-Stark states were loaded into a single travelling electric trap in the decelerator and guided at a constant speed of 800 m s^{-1}. The resulting TOF distribution is shown by the red curve in Fig. 7.10, with the grey vertical line beneath the peak indicating the centre of the TOF distribution expected from numerical calculations. The TOF distribution of guided molecules has a narrower FWHM than that recorded with the decelerator off. This arises because when the molecules are loaded into and transported in the travelling electric trap of the decelerator they all pass the detection position at a similar time. However, in free-flight the same bunch of molecules disperses because of their velocity spread and pass the detection position at a larger range of times.

Molecules loaded into the travelling electric field traps were also decelerated from an initial speed of $v_i = 800$ m s^{-1} to speeds of $v_f = 500$, 300, and 100 m s^{-1} by chirping the frequency of the oscillating deceleration potentials. This can be seen from the corresponding TOF distributions in Fig. 7.10. The final velocities of 500, 300, and 100 m s^{-1} were achieved for tangential accelerations of $a_t = -1.95 \times 10^6$, -2.74×10^6, and -3.14×10^6 m s^{-2}, respectively. The grey vertical lines indicate the calculated mid-point of the TOF distributions of the decelerated molecules, and are in good quantitative agreement with the measurements. The increase in the FWHM of the measured TOF distributions as the value of v_f decreases reflects the longer time taken by the more slowly moving traps to pass the $\sim$ 2-mm-diameter detection region. The reduction in the amplitude of the N_2^+ signal for larger values of $|a_t|$ reflects a combination of the reduction in the phase-space acceptance of the decelerator at higher accelerations, and effects of the decay of the molecules that becomes more pronounced at later times. Minor asymmetries in the measured TOF distributions, are attributed to slight phase-space mis-matching when incoupling the molecules into the travelling electric field trap which was optimised for deceleration to rest.

Deceleration of the molecules from $v_i = 800$ m s^{-1} to $v_f = 0$ m s^{-1}, in the labo-

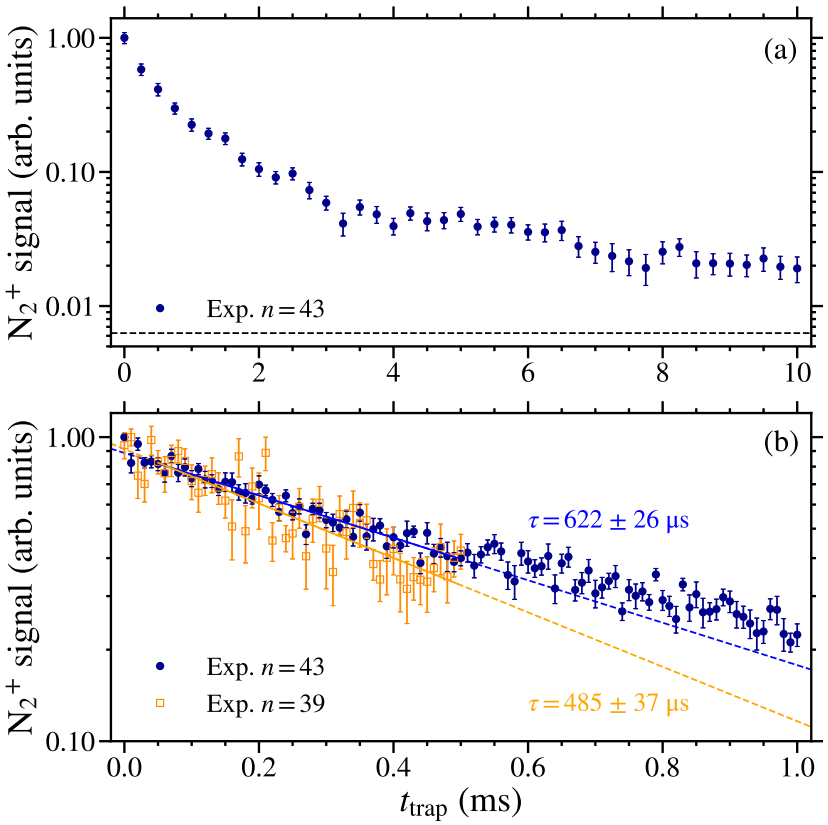

Figure 7.11: Measured decay of Rydberg N_2 molecules from the electrostatic trap, for (a) trapping times up to 10 ms, and (b) trapping times up to 1 ms. The black horizontal line in panel (a) represents one standard deviation of the background signal. The molecules were photoexcited either on the 43f($N^+ = J'$) resonance ($\upsilon_2 = 26767.10$ cm^{-1}), in panels (a) and (b), or the 39f($N^+ = J'$) resonance ($\upsilon_2 = 26754.21$ cm^{-1}), in panel (b) only. In panel (b) single exponential functions were fit to the data between $t_{trap} = 50$ and 500 μs (see text for details).

ratory frame of reference, with a tangential acceleration of $a_t = -3.19 \times 10^6$ m s^{-2}, allowed electrostatic trapping of the N_2 molecules to be achieved at times ≥ 250 μs after photoexcitation. Under these conditions the decay of the molecules from the trap was monitored through the change in the PFI signal with increased trapping time, t_{trap}. Examples of such trap-decay measurements are shown in Fig. 7.11. In these experiments it was possible to trap molecules for up to 10 ms, as shown in Fig. 7.11(a). In this figure the horizontal black line represents the standard deviation of the background signal with the weighted mean of the background data points set to zero. From these data it can be seen that the rate of decay of the molecules

from the trap changes with trapping time. At earlier trapping times the decay is faster while at later times it is slower. The low number density of molecules in the trap of $\sim 10^4$ cm^{-3} with ~ 10 molecules trapped per cycle meant that collisions between the trapped molecules are not expected to significantly contribute to the changing trap decay rate over time. In addition, effects of electric field ionisation have been shown in Section 4.3 to result in contributions of < 1 s^{-1} to the trap decay rates after the traps have been brought to rest. Therefore, the observed changes in the trap decay rate with time are attributed to either (i) effects of blackbody induced transitions, which become important on long timescales, or (ii) the range of Rydberg-Stark states initially populated having a range of lifetimes, such that molecules in shorter-lived states decay more quickly from the trap leaving only molecules in longer-lived states in the trap at later times.

Examples of trap decay measurements, for trapping times of up to 1 ms, are shown in Fig. 7.11(b) for molecules excited on the 43f($N^+ = J'$) [blue circles] and 39f($N^+ = J'$) [orange open squares] resonances. To obtain trap decay time constants, τ_{decay}, from these data, single exponential functions were fitted for trapping times between 50 and 500 μs. This range of times was employed in the fitting procedure because (i) after $t_{\text{trap}} = 50$ μs the motion of the molecules in the trap has equilibrated [136, 143], and (ii) beyond $t_{\text{trap}} = 500$ μs the decay in the signal from the trapped molecules begins to deviate from a single exponential function [see Fig. 7.11(b)]. From this process the data in Fig. 7.11(b) for molecules excited on the 43f($N^+ = J'$) and 39f($N^+ = J'$) resonances yielded trap-decay time constants of 622 ± 26 μs and 485 ± 37 μs, respectively.

The range of states for which the deceleration and trapping could be achieved was ascertained by measuring a laser photoexcitation spectrum with the detection by delayed PFI at $t_{\text{trap}} = 100$ μs. Such a spectrum is shown in Fig. 7.9(b). The relative spectral intensities in this figure reflect the combined effects of (i) the efficiency with which the long-lived Rydberg-Stark states were populated, (ii) the deceleration and trapping loading efficiencies which for lower [higher] values of n are limited by the $\sim n^2$ dependence of the maximal dipole moment [the $\sim n^{-4}$

dependence of the ionisation electric field], and (iii) the decay of the Rydberg states populated. As in Fig. 7.9(a), transitions to states with nf($N^+ = J'$) character can be identified at lower transitions wavenumbers of approximately $\upsilon_2 < 26780$ cm^{-1}. However, at higher transition wavenumbers the high spectral density of $N^+ = J'$ and $N^+ = J' \pm 2$ transitions to long-lived Rydberg states suitable for deceleration and trapping significantly increases resulting in a more complex spectrum. Also clearly observed in Fig. 7.9(b) are the sharp features at $\upsilon_2 = 26755.55$ and 26786.38 cm^{-1} that correspond to the 40p($N^+ = J'$) and 53p($N^+ = J'$) resonances, respectively. On these resonances, the higher spectral intensities are attributed to effects of charge-quadrupole interactions mixing the 40p($N^+ = 2$) [53p($N^+ = 1$)] and 43f($N^+ = 0$) [43f($N^+ = 3$)] states, which are separated by ~ 0.06 cm^{-1} [~ 0.11 cm^{-1}], which allows more efficient population transfer into the long-lived ℓ-mixed Rydberg-Stark states suitable for deceleration and trapping.

7.2.3 Trap decay measurements

For N_2 molecules excited on nf($N^+ = J'$) resonances to Rydberg-Stark states denoted $n(N^+ = J')$, trap decay measurements were made for values of n between $n = 39$ and 48. Between 3 and 11 measurements were made for each value of n. The error weighted mean of the decay time constants, τ_{decay}, associated with these was then computed with the results displayed in Fig. 7.12(a). The error bars associated with each point represent the uncertainty on the mean values. The values of τ_{decay} obtained from these measurements range from ~ 450 to 700 μs and generally increase with n. For comparison, the trap decay time constants for the $n(N^+ = 2)$ long-lived Rydberg-Stark states in NO measured under the same conditions, as discussed in Section 5.2, are included in Fig. 7.12(b). These values of τ_{decay} range from ~ 400 to 200 μs and generally decrease with increasing principal quantum number n.

Comparison of the data for N_2 and NO in Fig. 7.12 indicates that not only are the measured values of τ_{decay} different, for the same range of values of n, but the general trends observed are also different. It may be expected in general that (i) the total decay rate associated with fluorescence and predissociation for both molecules

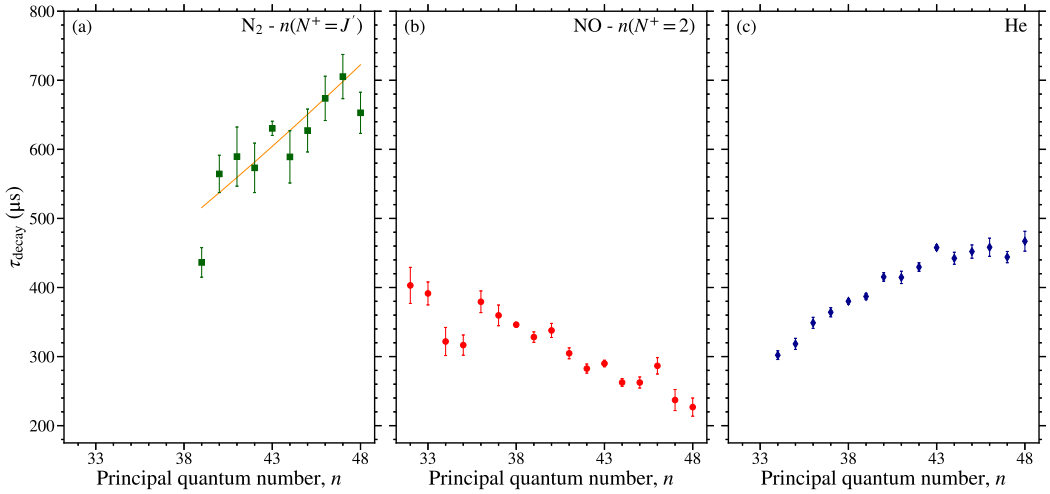

Figure 7.12: Measured trap-decay time constants, τ_{decay}, for: (a) N_2 molecules excited on the $nf(N^+ = J')$ resonances to long-lived $n(N^+ = J')$ Rydberg-Stark states (green squares). The continuous orange line represents the function $\tau = 1.34n^{1.62}$ μs fit to the experimental data. (b) NO molecules excited on $nf(N^+ = 2)$ resonances to long-lived $n(N^+ = 2)$ Rydberg-Stark states (red circles - from Fig 5.9), and (c) He atoms in singlet Rydberg states (blue diamonds).

should decrease with n, and (ii) since all measurements were made in the same apparatus at the same blackbody temperature, that effects of blackbody induced transitions or ionisation should be similar. The differences in the observed trends in the measured values of τ_{decay} for N_2 and NO must therefore be attributed to the difference in the effects of intramolecular interactions. For NO, the general decrease in the value of τ_{decay} with n was attributed in Section 5.2 to effects of vibrational-channel interactions that mixed short-lived ($\sim$ 1 ps) $n = 7$ $v^+ = 1$ character into Rydberg states converging to the $v^+ = 0$ state of NO^+.

To estimate the n-scaling of the N_2 trap decay time constants in Fig. 7.12(a) a least squares fitting procedure was implemented with a scaling factor and the exponent of the n scaling set as free fit parameters. From this it was found that $\tau = 1.34n^{1.62\pm0.05}$ μs. Therefore the measured trap decay time constants for N_2 do not follow the expected scaling of lifetimes of atomic Rydberg states. In this case an $\sim n^4$ dependence of the decay time constants would be expected for individual ℓ-mixed Rydberg-Stark states [76].

To further investigate the role of different decay processes, and the expected

n-dependence of the measured trap decay time constants, additional deceleration and trapping experiments were performed with He atoms in singlet Rydberg-Stark states. This allowed studies of trap decay dynamics to be performed in a system devoid of intramolecular charge-multipole interactions and non-radiative decay processes. In this work, He atoms were excited from the metastable $1s2s\,^1S_0$ level to Rydberg-Stark states with $1snp\,^1P_1$ character in a single-photon transition of ~ 313 nm. The stray time varying electric fields close to the time of photoexcitation then resulted in the population of ℓ-mixed Stark states with a distribution of $|m_\ell|$ values, predominantly $|m_\ell| \leq 2$. These Rydberg He atoms were loaded into the travelling electric traps of the decelerator operated with $V_0 = 149$ V. They were then decelerated from an initial speed of $v_i = 2000\ \mathrm{m\,s^{-1}}$ to a final speed of $v_f = 0\ \mathrm{m\,s^{-1}}$ in a time of $\sim 100\ \mu$s. Trap decay time constants were determined, using the same fitting start and end trapping times as for the case of N_2, for states with values of n from $n = 34$ to 48 with the results presented in Fig. 7.12(c). These measured trap decay time constants ranged from $\tau_{\mathrm{decay}} = 300\ \mu$s to 500 μs and generally increased as the value of n increased. The smaller values of τ_{decay}, than those measured for N_2, reflect the lower-$|m_\ell|$ character of these atomic Rydberg states excited in this single-photon excitation scheme, and the fact that lower-$|m_\ell|$ states in atoms can be decelerated and trapped because the rapid decay by predissociation does not occur.

It is evident from the data in Fig. 7.12(c) that these values of τ_{decay} for He also do not follow an $\sim n^4$ scaling [76]. The decay time constants measured do however increase with n. The observed trend in the measured values of τ_{decay}, with n, in He is attributed the Rydberg-Stark states populated having a distribution of m_ℓ values. Since these states with different values of m_ℓ have a range of lifetimes, that increase as the value of m_ℓ increases, as seen in Section 3.2, the total population in the trap does not decay exponentially. At lower values of n, i.e., $n \lesssim 40$, the measured trap decay time constants are dominated by the decay of the longer-lived $|m_\ell| \geq 2$ Rydberg-Stark states. This is because, even in He, Stark states with $|m_\ell| \leq 1$ are not sufficiently long-lived to contribute to the trap decay signal. For higher values of n, the measured values of τ_{decay} increase more slowly with n. This is because for

these states, the $|m_\ell| \leq 1$ Rydberg-Stark states have sufficiently long fluorescence lifetimes to be trapped, and contribute to the trap decay dynamics at early times. The balance between these changes in the distribution of values of m_ℓ of the trapped atoms meant that the measured decay time constants did not scale in a simple way with n. Because of this, the observation that the measured trap decay time constants for N_2 increased with n but did not scale in a simple way is also not surprising, and considered to be a consequence of the distribution of M_N states in the trap.

7.3 Conclusions

In this chapter, a combination of ion-dip and photoabsorption spectroscopy of high-n Rydberg states in N_2, excited though the intermediate $a''\,^1\Sigma_g^+$ state, allowed the population of Rydberg-Stark states suitable for deceleration and electrostatic trapping to be identified. These spectroscopic studies enabled the predissociative np Rydberg states to be distinguished from the longer-lived states that can be used to populate ℓ-mixed Stark-states. This excitation process is similar to that used for the preparation of Rydberg-Stark states in NO in Chapter 5. The first demonstration of deceleration and electrostatic trapping N_2 molecules was presented. The deceleration and trap loading process relied on the results of the spectroscopic studies. The measured trap decay time constants ranged from 450 μs to 700 μs for states with values of n between 39 and 48. Unlike in NO, these measured trap decay time constants were observed to increase with increasing value of n. This difference in the general trends observed is attributed to the differing effects of intramolecular interactions on these two molecules. Additional experiments performed to decelerate and trap He atoms in singlet Rydberg states aided the interpretation of the data recorded for N_2.

Chapter 8

Conclusions and outlook

The experiments reported in this thesis include the first demonstration of deceleration and electrostatic trapping of neutral NO and N_2 molecules. These advances were enabled through the use of multiphoton excitation schemes to prepare long-lived Rydberg states with high principal quantum numbers in both species. They also exploited a unique state-of-the-art cryogenically-cooled chip-based transmission-line Rydberg-Stark decelerator. These molecules are the heaviest species to have been decelerated to rest in the laboratory-fixed frame of reference using the methods of Rydberg-Stark deceleration. Previous related works were carried out with H, D, H_2, and He [62, 63, 125, 128, 134–136]. Because of the universality of Rydberg-states in all atoms and molecules with a stable ion core, and the large static electric dipole moments associated with these states, these methods represents a species-independent way of decelerating and trapping samples of this kind. The suitability of this approach to the preparation of cold trapped samples of molecules that do not processes electric or magnetic dipole moments in their ground electronic state is exemplified by the case of N_2 presented here. The cold electrostatically trapped samples of NO and N_2 prepared as part of this thesis allowed for studies of the slow decay dynamics of long-lived Rydberg states in theses species over previously inaccessible timescales of up to 10 ms. However, these samples in velocity controlled beams or in traps are also well suited to studies of cold collisions and reactions [54–59].

Measurements of the decay of electronically trapped NO molecules in Rydberg-

Stark states with principal quantum numbers, n, between 32 to 50 were carried out for Rydberg series converging to a range of selected rotational and vibrational states of the NO^+ cation. For NO molecules in $v^+ = 0$ series, measurements were performed for Rydberg states with rotational quantum numbers $N^+ = 0$ to 6. For the series with $N^+ = 0$, 1, and 2, the decay of the molecules was monitored directly through the changes in the trapping signal with time. The trap decay time constants obtained by fitting single exponential functions to the experimental data between trapping times of 50 μs and 350 μs ranged from 200 μs to 400 μs and decreased with increasing values of n. This is contrary to what is typically expected of Rydberg states that decay purely by spontaneous emission. This general trend was attributed to the effects of weak-vibrational channel interactions between the high-n $v^+ = 0$ Rydberg states excited in the experiments, and short lived ($\sim$ 1 ps) $n = 7$ $v^+ = 1$ Rydberg states that lie close to the $v^+ = 0$ ionisation limit. In addition to this, effects of rotational channel interactions between the optically accessible Rydberg states in one Rydberg series with near degenerate states in a different N^+ series were also identified and found to be in good agreement with expectations from the literature.

Measurements performed by excitation of Rydberg states in NO through a rotationally excited intermediate state, allowed access to long-lived $N^+ = 2$, 4, and 6 Rydberg states. The decay time constants of these higher N^+ Rydberg states were determined for the first time by a combination of trap decay measurement and delayed pulsed electric field ionisation measurement. For this range of measurement, it was concluded that the Rydberg states populated with higher values of N^+ decayed more quickly than those with lower values of N^+ for the same value of n. This effect was attributed to an increase in the low-ℓ predissociative character in the states populated at higher N^+ under the assumption that states with similar distributions of values of $|M_N|$ were present in each case.

Experiments performed to decelerate and electrostatically trap NO molecules in the excited $v^+ = 1$ vibrational states allowed direct comparison of the trap decay time constants to those made for $v^+ = 0$ Rydberg states. The decay time constants

of the $v^+ = 1$ Rydberg states were found to follow the same general trend as those of the $v^+ = 0$ states. However, in the $v^+ = 1$ Rydberg states studied, decay by fluorescence, predissociation, and vibrational autoionisation are possible, while in the $v^+ = 0$ state vibrational autoionisation is precluded. The measured trap decay time constants for the $v^+ = 0$ and $v^+ = 1$ Rydberg states agreed to within the measurement uncertainty. This showed for the first time that effects of vibrational autoionisation do not significantly affect the decay of long-lived Rydberg-Stark states suitable for deceleration and trapping. In this work an upper bound of ~ 60 s^{-1} could be placed on the vibrational autoionisation rate of the Rydberg states studied.

In the experiments performed with N_2 a combination of ion-dip and photoabsorption spectroscopy of high-n Rydberg states was used to (i) study the predissociation of the low-ℓ Rydberg states, and (ii) establish an excitation scheme by which long-lived ℓ-mixed Rydberg-Stark states could be populated for deceleration and electrostatic trapping. Molecules prepared in these long-lived Rydberg-Stark states were decelerated and trapped, in the same way as for NO. The trap decay time constants measured in this case ranged from 450 μs to 700 μs and increased with the value of n. The difference in the general trends followed by the N_2 and NO trap decay time constants was attributed to the differing effects of intramolecular interactions in each species.

Although the experiments reported here represent a significant advance in the ability to decelerate and trap molecules heavier than H_2 by Rydberg-Stark deceleration, and opened access to studies of Rydberg-state decay processes on ~ 10 ms timescales, there are still a range of future experiments that must be performed to completely understand the decay dynamics of the molecules studied. First, despite the preparation of the Rydberg-Stark states carried out in the work described here being selective of particular values of n, N^+, and v^+, individual Rydberg-Stark states with selected values of M_N were not resolved or selectively prepared. In the future it would therefore be very beneficial to prepare and trap fully quantum-state-selected molecules. This has been achieved in the trapping experiments with H_2 [62, 63, 180], and could be achieved in NO or N_2 by using narrow band lasers,

or in the case of NO a three-photon excitation scheme though the H state [181], provided that stray fields resulting from electrical noise and the presence of charge particles can also be minimised. This would allow detailed comparison with calculations of the lifetimes of individual Rydberg-Stark states to be performed.

Second, further experiments are required to improve upon the known predissociation decay rates of field-free high-n Rydberg states, and particularly the ℓ-dependence of these decay rates for $\ell \geq 4$. Currently, field-free predissociation decay rates of high-n Rydberg states of NO with $\ell \leq 4$ are known [82, 86, 89, 110], but those for higher-ℓ states are not. This information would be an important input into final comparisons of measured and calculated Rydberg-Stark state decay rates. In N_2, values of the predissociation decay rates of even the low-ℓ high-n states have not been reported.

Third, to further study the role of weak intramolecular charge-multipole interactions on the decay, and ultimately lifetimes, of electrostatically trapped Rydberg molecules it would be desirable to make comparative measurements of trap decay rates for molecules with similar electronic structure but different multipole moments. Of particular interest would be a comparison of decay rates of Rydberg states of heteronuclear and homonuclear molecules with a similar electronic structure. In these cases the respective presence and absence of an electric dipole moment of the ion core could provide insight into the effects of charge-dipole and charge-quadrupole interactions on decays dynamics. A prime pair of candidate molecules for which such a study are the isoelectronic CO and N_2 molecules. The ground electronic states of the neutral CO and N_2 are $X\,^1\Sigma^+$ and $X\,^1\Sigma_g^+$ states, respectively, and the ground electronic states of the CO^+ and N_2^+ cations are $X^+\,^2\Sigma^+$ and $X^+\,^2\Sigma_g^+$ states, respectively. Properties of the ground states of these cations are listed in Table 8.1. From these, it can be seen that the ground electronic states of CO^+ and N_2^+ have similar rotational and vibrational intervals, which will result in Rydberg states converging to these rotational-vibrational states of the molecular cations at similar energies relative to the ionisation limits. They also have similar electric quadrupole moments. However, the CO^+ cation has an electric dipole moment and

Table 8.1: Properties of the electronic ground states of the $^{12}C^{16}O^+$ and $^{14}N_2^+$ molecular cations, at their equilibrium internuclear separation. The values of the electric dipole and electric quadrupole moments are for the $v^+ = 0$ vibrational state of the molecular cations.

Quantity	CO^+ $X^+\,^2\Sigma^+$	Refs.	N_2^+ $X^+\,^2\Sigma_g^+$	Refs.
$(E_{X^+} - E_X)/hc$ (cm^{-1})	113031	[182]	125667.0	[92]
ω_e (cm^{-1})	2214.39	[183]	2207.0	[121]
$\omega_e\chi_e$ (cm^{-1})	15.13	[183]	16.10	[121]
B_e (cm^{-1})	1.976964	[183]	1.93176	[121]
α_e (cm^{-1})	1.8952×10^{-2}	[183]	1.88×10^{-2}	[121]
D_e (cm^{-1})	6.318×10^{-6}	[183]	6.10×10^{-6}	[121]
Electric dipole moment (a.u.)	1.015	[184, 185]	0	
Electric quadrupole moment (a.u.)	1.913	[184, 185]	1.72	[186]

the N_2^+ cation does not. These studies will also benefit from further investigation of the ℓ-dependence of predissociation decay rates, in both species, and the decay dynamics of low-n Rydberg states in vibrationally excited series that lie close to the ionisation limits of lower-lying series.

The demonstration in this thesis of the preparation, deceleration, and electrostatic trapping of molecules heavier than H_2 also opens up the possibility to perform a range of new experiments with such samples. For example, the generation of velocity-controlled beams of these Rydberg molecules in particular rotational and vibrational states are of interest for studies of ion-molecule reactions [55, 56]. The deceleration of Rydberg NO and N_2 therefore opens up the use of this technique to study such collisions involving molecular ions other than H_2^+ and its isotopologues [55, 56, 59, 64]. In addition, experiments could be performed to de-excite the molecules from the Rydberg states to low-lying electronic states, or the ground state, following deceleration. This could allows the preparation of cold samples, with zero mean velocity in the lab frame of reference, of molecules in their ground or low-lying electronically excited states that could not be efficiently prepared by other means. This would be of particular interest, for example, in the preparation

of cold gases of heavy species such as BaF which are of interest in next-generation experiments to place bounds on the electric dipole moment of electrons [187].

Bibliography

[1] V. Andreev, D. G. Ang, D. DeMille, J. M. Doyle, G. Gabrielse, J. Haefner, N. R. Hutzler, Z. Lasner, C. Meisenhelder, B. R. O'Leary, C. D. Panda, A. D. West, E. P. West, and X. Wu, "Improved limit on the electric dipole moment of the electron," *Nature*, vol. 562, p. 355, 2018.

[2] T. S. Roussy, L. Caldwell, T. Wright, W. B. Cairncross, Y. Shagam, K. B. Ng, N. Schlossberger, S. Y. Park, A. Wang, J. Ye, and E. A. Cornell, "An improved bound on the electron's electric dipole moment," *Science*, vol. 381, p. 46, 2023.

[3] J. Baron, W. C. Campbell, D. DeMille, J. M. Doyle, G. Gabrielse, Y. V. Gurevich, P. W. Hess, N. R. Hutzler, E. Kirilov, I. Kozyryev, B. R. O'Leary, C. D. Panda, M. F. Parsons, B. Spaun, A. C. Vutha, A. D. West, and E. P. West, "Methods, analysis, and the treatment of systematic errors for the electron electric dipole moment search in thorium monoxide," *New J. Phys.*, vol. 19, p. 073029, 2017.

[4] E. J. Salumbides, J. C. Koelemeij, J. Komasa, K. Pachucki, K. S. Eikema, and W. Ubachs, "Bounds on fifth forces from precision measurements on molecules," *Phys. Rev. D*, vol. 87, p. 112008, 2013.

[5] S. Schiller and V. Korobov, "Tests of time independence of the electron and nuclear masses with ultracold molecules," *Phys. Rev. A*, vol. 71, p. 032505, 2005.

[6] V. V. Flambaum and M. G. Kozlov, "Enhanced sensitivity to the time varia-

tion of the fine-structure constant and m_p/m_e in diatomic molecules," *Phys. Rev. Lett.*, vol. 99, p. 150801, 2007.

[7] E. Reinhold, R. Buning, U. Hollenstein, A. Ivanchik, P. Petitjean, and W. Ubachs, "Indication of a cosmological variation of the proton-electron mass ratio based on laboratory measurement and reanalysis of H_2 spectra," *Phys. Rev. Lett.*, vol. 96, p. 151101, 2006.

[8] W. Ubachs, R. Buning, K. S. Eikema, and E. Reinhold, "On a possible variation of the proton-to-electron mass ratio: H_2 spectra in the line of sight of high-redshift quasars and in the laboratory," *J. Mol. Spectrosc.*, vol. 241, p. 155, 2007.

[9] H. L. Bethlem and W. Ubachs, "Testing the time-invariance of fundamental constants using microwave spectroscopy on cold diatomic radicals," *Faraday Discuss.*, vol. 142, p. 25, 2009.

[10] B. R. Heazlewood and T. P. Softley, "Towards chemistry at absolute zero," *Nat. Rev. Chem.*, vol. 5, p. 125, 2021.

[11] K. Gawlas and S. D. Hogan, "Rydberg-State-Resolved Resonant Energy Transfer in Cold Electric-Field-Controlled Intrabeam Collisions of NH_3 with Rydberg He Atoms," *J. Phys. Chem. Lett.*, vol. 11, p. 83, 2020.

[12] J. Zou and S. D. Hogan, "Probing van der Waals interactions and detecting polar molecules by Förster-resonance energy transfer with Rydberg atoms at temperatures below 100 mK," *Phys. Rev. A*, vol. 106, p. 043111, 2022.

[13] R. González-Férez, J. Shertzer, and H. R. Sadeghpour, "Ultralong-Range Rydberg Bimolecules," *Phys. Rev. Lett.*, vol. 126, p. 043401, 2021.

[14] H. G. Bennewitz, W. Paul, and C. Schlier, "Fokussierung polarer Moleküle," *Zeitschrift für Physik*, vol. 141, p. 6, 1955.

[15] W. H. Wing, "Electrostatic trapping of neutral atomic particles," *Phys. Rev. Lett.*, vol. 45, p. 631, 1980.

[16] T. Breeden and H. Metcalf, "Stark acceleration of Rydberg atoms in inhomogeneous electric fields," *Phys. Rev. Lett.*, vol. 47, p. 1726, 1981.

[17] S. D. Hogan, M. Motsch, and F. Merkt, "Deceleration of supersonic beams using inhomogeneous electric and magnetic fields," *Phys. Chem. Chem. Phys.*, vol. 13, p. 18705, 2011.

[18] S. Y. Van De Meerakker, H. L. Bethlem, N. Vanhaecke, and G. Meijer, "Manipulation and control of molecular beams," *Chem. Rev.*, vol. 112, p. 4828, 2012.

[19] H. L. Bethlem, G. Berden, and G. Meijer, "Decelerating Neutral Dipolar Molecules," *Phys. Rev. Lett.*, vol. 83, p. 1558, 1999.

[20] S. A. Meek, H. L. Bethlem, H. Conrad, and G. Meijer, "Trapping molecules on a chip in traveling potential wells," *Phys. Rev. Lett.*, vol. 100, p. 153003, 2008.

[21] S. A. Meek, H. Conrad, and G. Meijer, "Trapping molecules on a chip," *Science*, vol. 324, p. 1699, 2009.

[22] S. Hoekstra, J. J. Gilijamse, B. Sartakov, N. Vanhaecke, L. Scharfenberg, S. Y. T. van de Meerakker, and G. Meijer, "Optical Pumping of Trapped Neutral Molecules by Blackbody Radiation," *Phys. Rev. Lett.*, vol. 98, p. 133001, 2007.

[23] P. F. Barker and M. N. Shneider, "Slowing molecules by optical microlinear deceleration," *Phys. Rev. A*, vol. 66, p. 065402, 2002.

[24] R. Fulton, A. I. Bishop, and P. F. Barker, "Optical Stark Decelerator for Molecules," *Phys. Rev. Lett.*, vol. 93, p. 243004, 2004.

[25] P. F. Barker, S. M. Purcell, P. Douglas, P. Barletta, N. Coppendale, C. Maher-McWilliams, and J. Tennyson, "Sympathetic cooling by collisions with ultracold rare gas atoms, and recent progress in optical Stark deceleration," *Faraday Discuss.*, vol. 142, p. 175, 2009.

[26] S. D. Hogan, "Rydberg-Stark deceleration of atoms and molecules," *EPJ Tech. Instrum.*, vol. 3, p. 1, 2016.

[27] R. W. Field, C. M. Gittins, N. A. Harris, and C. Jungen, "Quantum defect theory of dipole and vibronic mixing in Rydberg states of CaF," *J. Chem. Phys.*, vol. 122, p. 184314, 2005.

[28] J. J. Kay, S. L. Coy, B. M. Wong, C. Jungen, and R. W. Field, "A quantum defect model for the s, p, d, and f Rydberg series of CaF," *J. Chem. Phys.*, vol. 134, p. 114313, 2011.

[29] J. Liu, E. J. Salumbides, U. Hollenstein, J. C. Koelemeij, K. S. Eikema, W. Ubachs, and F. Merkt, "Determination of the ionization and dissociation energies of the hydrogen molecule," *J. Chem. Phys.*, vol. 130, p. 174306, 2009.

[30] N. Hölsch, M. Beyer, E. J. Salumbides, K. S. Eikema, W. Ubachs, C. Jungen, and F. Merkt, "Benchmarking Theory with an Improved Measurement of the Ionization and Dissociation Energies of H_2," *Phys. Rev. Lett.*, vol. 122, p. 103002, 2019.

[31] M. Beyer, N. Hölsch, J. Hussels, C. F. Cheng, E. J. Salumbides, K. S. Eikema, W. Ubachs, C. Jungen, and F. Merkt, "Determination of the Interval between the Ground States of Para- and Ortho- H_2," *Phys. Rev. Lett.*, vol. 123, p. 163002, 2019.

[32] L. Semeria, P. Jansen, G.-M. Camenisch, F. Mellini, H. Schmutz, and F. Merkt, "Precision Measurements in Few-Electron Molecules: The Ionization Energy of Metastable $^4He_2$ and the First Rotational Interval of $^4He_2^+$," *Phys. Rev. Lett.*, vol. 124, p. 213001, 2020.

[33] J. Hussels, N. Hölsch, C.-F. Cheng, E. J. Salumbides, H. L. Bethlem, K. S. E. Eikema, C. Jungen, M. Beyer, F. Merkt, and W. Ubachs, "Improved ionization and dissociation energies of the deuterium molecule," *Phys. Rev. A*, vol. 105, p. 022820, 2022.

[34] N. Hölsch, I. Doran, F. Merkt, J. Hussels, C.-F. Cheng, E. J. Salumbides, H. L. Bethlem, K. S. E. Eikema, M. Beyer, W. Ubachs, and C. Jungen, "Ionization and dissociation energies of HD and dipole-induced g/u-symmetry breaking," *Phys. Rev. A*, vol. 108, p. 022811, 2023.

[35] M. Puchalski, J. Komasa, P. Czachorowski, and K. Pachucki, "Nonadiabatic QED Correction to the Dissociation Energy of the Hydrogen Molecule," *Phys. Rev. Lett.*, vol. 122, p. 103003, 2019.

[36] M. Puchalski, J. Komasa, A. Spyszkiewicz, and K. Pachucki, "Dissociation energy of molecular hydrogen isotopologues," *Phys. Rev. A*, vol. 100, p. 020503, 2019.

[37] S. Raouafi, G. H. Jeung, and C. Jungen, "Permanent and transition dipole moments in CaF and CaCl," *J. Chem. Phys.*, vol. 115, p. 7450, 2001.

[38] C. Jungen and A. L. Roche, "Quantum defect theory of dipole-mixed Rydberg states in CaF," *Can. J. Phys.*, vol. 79, p. 287, 2001.

[39] I. L. Beigman and V. S. Lebedev, "Collision theory of Rydberg atoms with neutral and charged particles," *Phys. Rep.*, vol. 250, p. 95, 1995.

[40] G. V. Golubkov, M. G. Golubkov, and M. I. Manzhelii, "Microwave and IR radiation of the upper atmosphere during periods of enhanced solar activity," *Doklady Physics*, vol. 57, p. 461, 2012.

[41] A. Giusti, "A multichannel quantum defect approach to dissociative recombination," *J. Phys. B*, vol. 13, p. 3867, 1980.

[42] A. Giusti-Suzor and C. Jungen, "Theoretical study of competing photoionization and photodissociation processes in the NO molecule," *J. Chem. Phys.*, vol. 80, p. 986, 1984.

[43] T. P. Softley, "Applications of molecular Rydberg states in chemical dynamics and spectroscopy," *Int. Rev. Phys. Chem.*, vol. 23, p. 1, 2004.

[44] I. F. Schneider, I. Rabadán, L. Carata, L. H. Andersen, A. Suzor-Weiner, and J. Tennyson, "Dissociative recombination of NO^+ : calculations and comparison with experiment," *J. Phys. B*, vol. 33, p. 4849, 2000.

[45] J. Z. Mezei, R. D. Backodissa-Kiminou, D. E. Tudorache, V. Morel, K. Chakrabarti, O. Motapon, O. Dulieu, J. Robert, W. Ü. Tchang-Brillet, A. Bultel, X. Urbain, J. Tennyson, K. Hassouni, and I. F. Schneider, "Dissociative recombination and vibrational excitation of CO^+: model calculations and comparison with experiment," *Plasma Sources Sci. Technol.*, vol. 24, p. 035005, 2015.

[46] Y. Moulane, J. Z. Mezei, V. Laporta, E. Jehin, Z. Benkhaldoun, and I. F. Schneider, "Reactive collision of electrons with CO^+ in cometary coma," *Astron. Astrophys.*, vol. 615, p. A53, 2018.

[47] J. R. Peterson, A. Le Padellec, H. Danared, G. H. Dunn, M. Larsson, A. Larson, R. Peverall, C. Strömholm, S. Rosén, M. Af Ugglas, and W. J. Van Der Zande, "Dissociative recombination and excitation of N_2^+: Cross sections and product branching ratios," *J. Chem. Phys.*, vol. 108, pp. 1978–1988, 1998.

[48] S. L. Guberman, "Role of excited core Rydberg states in dissociative recombination," *J. Phys. Chem. A*, vol. 111, p. 11254, 2007.

[49] R. Peverall, S. Rosén, J. R. Peterson, M. Larsson, A. Al-Khalili, L. Vikor, J. Semaniak, R. Bobbenkamp, A. Le Padellec, A. N. Maurellis, and W. J. Van Der Zande, "Dissociative recombination and excitation of O_2^+: Cross sections, product yields and implications for studies of ionospheric airglows," *J. Chem. Phys.*, vol. 114, p. 6679, 2001.

[50] J. P. Morrison, C. J. Rennick, J. S. Keller, and E. R. Grant, "Evolution from a molecular Rydberg gas to an ultracold plasma in a seeded supersonic expansion of NO," *Phys. Rev. Lett.*, vol. 101, p. 205005, 2008.

[51] H. Sadeghi, A. Kruyen, J. Hung, J. H. Gurian, J. P. Morrison, M. Schulz-Weiling, N. Saquet, C. J. Rennick, and E. R. Grant, "Dissociation and the development of spatial correlation in a molecular ultracold plasma," *Phys. Rev. Lett.*, vol. 112, p. 075001, 2014.

[52] F. B. V. Martins, J. S. Keller, and E. R. Grant, "Control of molecular ultracold plasma relaxation dynamics by mm-wave Rydberg–Rydberg transitions," *Mol. Phys.*, vol. 117, p. 3096, 2019.

[53] R. Wang, J. Sous, M. Aghigh, K. L. Marroquín, K. M. Grant, F. B. V. Martins, J. S. Keller, and E. R. Grant, "mm-wave Rydberg–Rydberg transitions gauge intermolecular coupling in a molecular ultracold plasma," *J. Chem Phys*, vol. 157, p. 064305, 2022.

[54] S. T. Pratt, J. L. Dehmer, P. M. Dehmer, and W. A. Chupka, "Reactions of Rydberg states of molecular hydrogen," *J. Chem. Phys.*, vol. 101, p. 882, 1994.

[55] P. Allmendinger, J. Deiglmayr, O. Schullian, K. Höveler, J. A. Agner, H. Schmutz, and F. Merkt, "New Method to Study Ion-Molecule Reactions at Low Temperatures and Application to the $H_2^+ + H_2 \rightarrow H_3^+ + H$ Reaction," *ChemPhysChem*, vol. 17, p. 3596, 2016.

[56] P. Allmendinger, J. Deiglmayr, K. Höveler, O. Schullian, and F. Merkt, "Observation of enhanced rate coefficients in the $H_2^+ + H_2 \rightarrow H_3^+ + H$ reaction at low collision energies," *J. Chem. Phys.*, vol. 145, p. 244316, 2016.

[57] V. Zhelyazkova, F. B. Martins, J. A. Agner, H. Schmutz, and F. Merkt, "Ion-Molecule Reactions below 1 K: Strong Enhancement of the Reaction Rate of the Ion-Dipole Reaction $He^+ + CH_3F$," *Phys. Rev. Lett.*, vol. 125, p. 263401, 2020.

[58] K. Höveler, J. Deiglmayr, J. A. Agner, H. Schmutz, and F. Merkt, "The $H_2^+ + HD$ reaction at low collision energies: H_3^+/H_2D^+ branching ratio

and product-kinetic-energy distributions," *Phys. Chem. Chem. Phys.*, vol. 23, p. 2676, 2021.

[59] K. Höveler, J. Deiglmayr, J. A. Agner, R. Hahn, V. Zhelyazkova, and F. Merkt, "Observation of quantum capture in an ion-molecule reaction," *Phys. Rev. A*, vol. 106, p. 052806, 2022.

[60] J. Schmidt, M. Fiedler, R. Albrecht, D. Djekic, P. Schalberger, H. Baur, R. Löw, N. Fruehauf, T. Pfau, J. Anders, E. R. Grant, and H. Kübler, "Proof of concept for an optogalvanic gas sensor for NO based on Rydberg excitations," *Appl. Phys. Lett.*, vol. 113, p. 011113, 2018.

[61] J. Schmidt, Y. Münzenmaier, P. Kaspar, P. Schalberger, H. Baur, R. Löw, N. Fruehauf, T. Pfau, and H. Kübler, "An optogalvanic gas sensor based on Rydberg excitations," *J. Phys. B*, vol. 53, p. 094001, 2020.

[62] S. D. Hogan, C. Seiler, and F. Merkt, "Rydberg-state-enabled deceleration and trapping of cold molecules," *Phys. Rev. Lett.*, vol. 103, p. 123001, 2009.

[63] C. Seiler, S. D. Hogan, and F. Merkt, "Trapping cold molecular hydrogen," *Phys. Chem. Chem. Phys.*, vol. 13, p. 19000, 2011.

[64] F. Merkt, K. Höveler, and J. Deiglmayr, "Reactions of H_2, HD, and D_2 with H_2^+, HD^+, and D_2^+: Product-Channel Branching Ratios and Simple Models," *J. Phys. Chem. Lett.*, vol. 13, p. 864, 2022.

[65] J. R. Rydberg, "Über den Bau der Linienspektren der chemischen Grundstoffe," *Zeitschrift für Physikalische Chemie*, vol. 5U, p. 461, 1890.

[66] T. F. Gallagher, *Rydberg Atoms*. Cambridge University Press, 1994.

[67] M. Bixon and J. Jortner, "Intramolecular coupling between non-penetrating high molecular Rydberg states," *Mol. Phys.*, vol. 89, p. 373, 1996.

[68] E. E. Eyler and F. M. Pipkin, "Triplet 4d states of H_2: Experimental observation and comparison with ab initio model for Rydberg-state energies," *Phys. Rev. A*, vol. 27, p. 2462, 1983.

[69] E. E. Eyler, "Autoionization of nonpenetrating Rydberg states in diatomic molecules," *Phys. Rev. A*, vol. 34, p. 2881, 1986.

[70] S. Fredin, D. Gauyacq, M. Horani, C. Jungen, G. Lefevre, and F. Masnou-Seeuws, "s and d rydberg series of NO probed by double resonance multiphoton ionization: Multichannel quantum defect analysis," *Mol. Phys.*, vol. 60, p. 825, 1987.

[71] A. L. Goodgame, H. Dickinson, S. R. Mackenzie, and T. P. Softley, "The Stark effect in the $v^+ = 1$ autoionizing Rydberg states of NO," *J. Chem. Phys.*, vol. 116, p. 4922, 2002.

[72] G. Herzberg and C. Jungen, "Rydberg series and ionization potential of the H_2 molecule," *J. Mol. Spectrosc.*, vol. 41, p. 425, 1972.

[73] I. Rabadán and J. Tennyson, "Ab initio potential energy curves of Rydberg, valence and continuum states of NO," *J. Phys. B*, vol. 30, p. 1975, 1997.

[74] I. Rabadán and J. Tennyson, "Ab initio potential energy curves of Rydberg, valence and continuum states of NO," *J. Phys B*, vol. 31, p. 4485, 1998.

[75] C. Jungen, "Rydberg series in the NO spectrum: An interpretation of quantum defects and intensities in the s and d series," *J. Chem. Phys.*, vol. 53, p. 4168, 1970.

[76] W. A. Chupka, "Factors affecting lifetimes and resolution of Rydberg states observed in zero-electron-kinetic-energy spectroscopy," *J. Chem. Phys.*, vol. 98, p. 4520, 1993.

[77] M. S. Child, *Theory of Molecular Rydberg States*. Cambridge University Press, 2011.

[78] H. Lefebvre-Brion and R. W. Field, *The Spectra and Dynamics of Diatomic Molecules*. Academic Press, 2004.

[79] A. Fujii and N. Morita, "Laser investigation of the competition between rotational autoionization and predissociation in superexcited np Rydberg states of NO," *J. Chem. Phys.*, vol. 98, p. 4581., 1993.

[80] T. J. Barnum, G. Clausen, J. Jiang, S. L. Coy, and R. W. Field, "Long-range model of vibrational autoionization in core-nonpenetrating Rydberg states of NO," *J. Chem. Phys.*, vol. 155, p. 244303, 2021.

[81] M. J. Vrakking and Y. T. Lee, "Enhancements in the lifetimes of NO Rydberg states in dc electric fields: Implications for zero-electron-kinetic-energy photoelectron spectroscopy experiments," *Phys. Rev. A*, vol. 51, p. 894, 1995.

[82] M. J. Vrakking and Y. T. Lee, "Lifetimes of Rydberg states in zero-electron-kinetic-energy experiments. I. Electric field induced and collisional enhancement of NO predissociation lifetimes," *J. Chem. Phys.*, vol. 102, p. 8818, 1995.

[83] F. Merkt, "Molecules in high Rydberg states," *Annu. Rev. Phys. Chem.*, vol. 48, p. 675, 1997.

[84] T. Ebata, Y. Anezaki, M. Fujii, N. Mikami, and M. Ito, "High Rydberg states of NO studied by two-color multiphoton spectroscopy," *J. Phys. Chem.*, vol. 87, p. 4773, 1983.

[85] M. Seaver, W. A. Chupka, S. D. Colson, and D. Gauyacq, "Double resonance multiphoton ionization studies of high Rydberg states in NO," *J. Phys. Chem.*, vol. 87, p. 2226, 1983.

[86] M. Bixon and J. Jortner, "The dynamics of predissociating high Rydberg states of NO," *J. Chem. Phys.*, vol. 105, p. 1363, 1996.

[87] N. J. A. Jones, R. S. Minns, R. Patel, and H. H. Fielding, "Observation of the Stark effect in $v^+ = 0$ Rydberg states of NO: a comparison between predissociating and bound states," *J. Phys. B*, vol. 41, p. 185102, 2008.

[88] R. Patel, N. J. Jones, and H. H. Fielding, "Observation of the Stark effect in $\upsilon^+ = 0$ Rydberg states of NO with a matrix-diagonalization analysis," *J. Phys. B*, vol. 40, p. 1369, 2007.

[89] A. Fujii and N. Morita, "Three-color triple resonance spectroscopy of highly excited *n*g Rydberg states of NO: Decay dynamics of high-l Rydberg states," *J. Chem. Phys.*, vol. 103, p. 6029, 1995.

[90] A. Deller and S. D. Hogan, "Excitation and characterization of long-lived hydrogenic Rydberg states of nitric oxide," *J. Chem. Phys.*, vol. 152, p. 144305, 2020.

[91] F. Merkt and R. N. Zare, "On the lifetimes of Rydberg states probed by delayed pulsed field ionization," *J. Chem. Phys.*, vol. 101, p. 3495, 1994.

[92] K. P. Huber and C. Jungen, "High-resolution jet absorption study of nitrogen near 800 Å," *J. Chem. Phys.*, vol. 92, p. 850, 1990.

[93] F. Merkt and T. P. Softley, "Rotationally resolved zero-kinetic-energy photoelectron spectrum of nitrogen," *Phys. Rev. A*, vol. 46, p. 302, 1992.

[94] S. H. S. Wilson, R. J. Rednall, H. H. Fielding, F. Merkt, and T. P. Softley, "Intensity perturbations in the v^+ = 2, 1 and 0 bands of the zero-kinetic-energy (ZEKE) photoelectron spectrum of N_2," *J. Electron Spectrosc. Relat. Phenom.*, vol. 66, p. 151, 1993.

[95] F. Merkt, S. R. Mackenzie, and T. P. Softley, "Rotational autoionization dynamics in high Rydberg states of nitrogen," *J. Chem. Phys.*, vol. 103, p. 4509, 1995.

[96] S. R. Mackenzie, F. Merkt, E. J. Halse, and T. P. Softley, "Rotational state selectivity in N_2^+ $X^2\Sigma_g^+(v^+ = 0)$ by delayed pulsed field ionization spectroscopy via the $a''^1\Sigma_g^+(v' = 0)$ state," *Mol. Phys.*, vol. 86, p. 1283, 1995.

[97] S. W. Sharpe and P. M. Johnson, "Triplet Rydberg states in molecular nitrogen," *J. Chem. Phys.*, vol. 85, p. 4943, 1986.

[98] M. H. Rayment and S. D. Hogan, "Quantum-state-dependent decay rates of electrostatically trapped Rydberg NO molecules," *Phys. Chem. Chem. Phys.*, vol. 23, p. 18806, 2021.

[99] R. N. Zare, *Angular Momentum*. Wiley, 1988.

[100] A. R. Edmonds, *Angular Momentum in Quantum Mechanics*. Princeton University Press, 1957.

[101] N. Šibalić, J. D. Pritchard, C. S. Adams, and K. J. Weatherill, "ARC: An open-source library for calculating properties of alkali Rydberg atoms," *Comput. Phys. Commun.*, vol. 220, p. 319, 2017.

[102] M. L. Zimmerman, M. G. Littman, M. M. Kash, and D. Kleppner, "Stark structure of the Rydberg states of alkali-metal atoms," *Phys. Rev. A*, vol. 20, p. 2251, 1979.

[103] G. W. F. Drake, "High Precision Theory of Atomic Helium," *Phys. Scr.*, vol. T83, p. 83, 1999.

[104] H. A. Bethe and S. E. E., *Quantum Mechanics of One- and Two-Electron Atoms*. Springer Berlin Heidelberg, 1957.

[105] J. M. Brown and A. Carrington, *Rotational Spectroscopy of Diatomic Molecules*. Cambridge University Press, 2003.

[106] C. Jungen and G. Raseev, "Spin-electronic-rotational frame transformation for photoionization and Rydberg spectra of diatomic molecules," *Phys. Rev. A*, vol. 57, p. 2407, 1998.

[107] M. S. Child and C. Jungen, "Quantum defect theory for asymmetric tops: Application to the Rydberg spectrum of H_2O," *J. Chem. Phys.*, vol. 93, p. 7756, 1990.

[108] U. Fano, "Quantum defect theory of ℓ uncoupling in H_2 as an example of channel-interaction treatment," *Phys. Rev. A*, vol. 2, p. 353, 1970.

[109] E. S. Chang and U. Fano, "Theory of electron-molecule collisions by frame transformations," *Phys. Rev. A*, vol. 6, p. 173, 1972.

[110] M. J. Vrakking, "Lifetimes of Rydberg states in ZEKE experiments. III. Calculations of the dc electric field dependence of predissociation lifetimes of NO," *J. Chem. Phys.*, vol. 105, p. 7336, 1996.

[111] R. D. Gilbert and M. S. Child, "Effects of polarization in the field ionization spectrum of H_2O," *Chem. Phy. Lett.*, vol. 187, p. 153, 1991.

[112] M. Fehér and P. A. Martin, "Ab initio calculations of the properties of NO^+ in its ground electronic state $X\,^1\Sigma^+$," *Chem. Phys. Lett.*, vol. 215, p. 565, 1993.

[113] R. Polák and J. Fišer, "A comparative icMRCI study of some NO^+, NO and NO^- electronic ground state properties," *Chem. Phys.*, vol. 303, p. 73, 2004.

[114] F. P. Billingsley, "Calculation of the absolute infrared intensities for the $0-1$, $0-2$ and $1-2$ vibration-rotation transitions in the ground state of NO^+," *Chem. Phys. Lett.*, vol. 23, p. 160, 1973.

[115] O. Asvany, C. R. Markus, A. Roucou, S. Schlemmer, S. Thorwirth, and C. Lauzin, "The fundamental rotational transition of NO^+," *J. Mol. Spectrosc.*, vol. 378, p. 111447, 2021.

[116] H. H. Fielding and T. P. Softley, "Observation of the Stark effect in autoionising Rydberg states of molecular hydrogen," *Chem. Phys. Lett.*, vol. 185, p. 199, 1991.

[117] C. Jungen and E. Miescher, " Absorption spectrum of the NO molecule. IX. The structure of the f complexes, the ionization potential of NO, and the quadrupole moment of NO^+ ," *Can. J. Phys.*, vol. 47, p. 1769, 1969.

[118] D. T. Biernacki, S. D. Colson, and E. E. Eyler, "High resolution laser spectroscopy of NO: The A, $v = 1$ state and a series of nf, $v = 1$ Rydberg states," *J. Chem. Phys.*, vol. 89, p. 2599, 1988.

[119] K. Gawlas and S. D. Hogan, "Rydberg-state ionization dynamics and tunnel ionization rates in strong electric fields," *Phys. Rev. A*, vol. 99, p. 013421, 2019.

[120] T. P. Softley, A. J. Hudson, and R. Watson, "Multichannel quantum defect theory Stark effect calculation of autoionization lifetimes in high- n Rydberg states of Ar, N_2 and H_2," *J. Chem. Phys.*, vol. 106, p. 1041, 1997.

[121] K. P. Huber and G. Herzberg, *Molecular Spectra and Molecular Structure: IV. Constants of Diatomic Molecules*. Boston, MA: Springer US, 1979.

[122] D. Townsend, A. L. Goodgame, S. R. Procter, S. R. Mackenzie, and T. P. Softley, "Deflection of krypton Rydberg atoms in the field of an electric dipole," *J. Phys. B*, vol. 34, p. 439, 2001.

[123] E. Vliegen and F. Merkt, "Stark deceleration of hydrogen atoms," *J. Phys. B*, vol. 39, p. L241, 2006.

[124] E. Vliegen and F. Merkt, "Normal-Incidence Electrostatic Rydberg Atom Mirror," *Phys. Rev. Lett.*, vol. 97, p. 033002, 2006.

[125] S. D. Hogan and F. Merkt, "Demonstration of three-dimensional electrostatic trapping of state-selected Rydberg atoms," *Phys. Rev. Lett.*, vol. 100, p. 043001, 2008.

[126] C. Seiler, S. D. Hogan, H. Schmutz, J. A. Agner, and F. Merkt, "Collisional and radiative processes in adiabatic deceleration, deflection, and off-axis trapping of a Rydberg atom beam," *Phys. Rev. Lett.*, vol. 106, p. 073003, 2011.

[127] S. D. Hogan, P. Allmendinger, H. Saßmannshausen, H. Schmutz, and F. Merkt, "Surface-electrode Rydberg-stark decelerator," *Phys. Rev. Lett.*, vol. 108, p. 063008, 2012.

[128] S. D. Hogan, C. Seiler, and F. Merkt, "Motional, isotope and quadratic Stark effects in Rydberg-Stark deceleration and electric trapping of H and D," *J. Phys. B*, vol. 46, 2013.

[129] S. R. Procter, Y. Yamakita, F. Merkt, and T. P. Softley, "Controlling the motion of hydrogen molecules," *Chem. Phys. Lett.*, vol. 374, p. 667, 2003.

[130] Y. Yamakita, S. R. Procter, A. L. Goodgame, T. P. Softley, and F. Merkt, "Deflection and deceleration of hydrogen Rydberg molecules in inhomogeneous electric fields," *J. Chem. Phys.*, vol. 121, p. 1419, 2004.

[131] P. Allmendinger, J. Deiglmayr, J. A. Agner, H. Schmutz, and F. Merkt, "Surface-electrode decelerator and deflector for Rydberg atoms and molecules," *Phys. Rev. A*, vol. 90, p. 043403, 2014.

[132] P. Lancuba and S. D. Hogan, "Guiding Rydberg atoms above surface-based transmission lines," *Phys. Rev. A*, vol. 88, p. 043427, 2013.

[133] P. Lancuba and S. D. Hogan, "Transmission-line decelerators for atoms in high Rydberg states," *Phys. Rev. A*, vol. 90, p. 053420, 2014.

[134] P. Lancuba and S. D. Hogan, "Electrostatic trapping and in situ detection of Rydberg atoms above chip-based transmission lines," *J. Phys. B*, vol. 49, p. 074006, 2016.

[135] P. Allmendinger, J. A. Agner, H. Schmutz, and F. Merkt, "Deceleration and trapping of a fast supersonic beam of metastable helium atoms with a 44-electrode chip decelerator," *Phys. Rev. A*, vol. 88, p. 043433, 2013.

[136] V. Zhelyazkova, M. Žeško, H. Schmutz, J. A. Agner, and F. Merkt, "Fluorescence-lifetime-limited trapping of Rydberg helium atoms on a chip," *Mol. Phys.*, vol. 117, p. 2980, 2019.

[137] A. Deller and S. D. Hogan, "Confinement of High- and Low-Field-Seeking Rydberg Atoms Using Time-Varying Inhomogeneous Electric Fields," *Phys. Rev. Lett.*, vol. 122, p. 053203, 2019.

[138] E. Vliegen, H. J. Wörner, T. P. Softley, and F. Merkt, "Nonhydrogenic Effects in the Deceleration of Rydberg Atoms in Inhomogeneous Electric Fields," *Phys. Rev. Lett.*, vol. 92, p. 033005, 2004.

[139] E. Vliegen and F. Merkt, "On the electrostatic deceleration of argon atoms in high Rydberg states by time-dependent inhomogeneous electric fields," *J. Phys. B*, vol. 38, p. 1623, 2005.

[140] A. Deller, A. M. Alonso, B. S. Cooper, S. D. Hogan, and D. B. Cassidy, "Electrostatically Guided Rydberg Positronium," *Phys. Rev. Lett.*, vol. 117, p. 073202, 2016.

[141] A. M. Alonso, B. S. Cooper, A. Deller, L. Gurung, S. D. Hogan, and D. B. Cassidy, "Velocity selection of Rydberg positronium using a curved electrostatic guide," *Phys. Rev. A*, vol. 95, p. 053409, 2017.

[142] M. H. Rayment, L. Gurung, R. E. Sheldon, S. D. Hogan, and D. B. Cassidy, "Multiring electrostatic guide for Rydberg positronium," *Phys. Rev. A*, vol. 100, p. 013410, 2019.

[143] A. Deller, M. H. Rayment, and S. D. Hogan, "Slow Decay Processes of Electrostatically Trapped Rydberg NO Molecules," *Phys. Rev. Lett.*, vol. 125, p. 73201, 2020.

[144] J. M. Doyle, B. Friedrich, J. Kim, and D. Patterson, "Buffer-gas loading of atoms and molecules into a magnetic trap," *Phys. Rev. A*, vol. 52, p. R2515, 1995.

[145] R. J. Damburg and V. V. Kolosov, "A hydrogen atom in a uniform electric field. III," *J. Phys. B*, vol. 12, p. 2637, 1979.

[146] M. G. Littman, M. M. Kash, and D. Kleppner, "Field-Ionization Processes in Excited Atoms," *Phys. Rev. Lett.*, vol. 41, p. 103, 1978.

[147] S. A. Meek, H. Conrad, and G. Meijer, "A stark decelerator on a chip," *New J. Phys.*, vol. 11, p. 055024, 2009.

[148] R. J. Sadus, *Molecular Simulation of Fluids: Theory, algorithms and object-orientation*, pp. 228–229. Oxford, UK: Elevier, 2002.

[149] M. E. Tuckerman, *Statistical Mechanics: Theory and Molecular Simulation*, pp. 100–101. Oxford, UK: Oxford Uni. Press, 2010.

[150] S. D. Hogan, "Calculated photoexcitation spectra of positronium Rydberg states," *Phys. Rev. A*, vol. 87, p. 063423, 2013.

[151] R. Patel, N. J. A. Jones, and H. H. Fielding, "Rotational-state-selective field ionization of molecular Rydberg states," *Phys. Rev. A*, vol. 76, p. 043413, 2007.

[152] E. F. McCormack, F. Di Teodoro, J. M. Grochocinski, and S. T. Pratt, "Dynamics of Rydberg states of nitric oxide probed by two-color resonant four-wave mixing spectroscopy," *J. Chem. Phys.*, vol. 109, p. 63, 1998.

[153] N. Jones, *The spectroscopy of bound and predissociating Rydberg states of NO in external electric fields*. PhD thesis, University College London, 2008.

[154] E. Klisch, S. P. Belov, R. Schieder, G. Winnewisser, and E. Herbst, "Transitions between Hund's coupling cases for the X 2Π state of NO," *Mol. Phys.*, vol. 97, p. 65, 1999.

[155] T. Bergeman and R. N. Zare, " Fine structure, hyperfine structure, and Stark effect in the NO $A\,^2\Sigma^+$ state by optical radio-frequency double resonance ," *J. Chem. Phys.*, vol. 61, p. 4500, 1974.

[156] J. A. Gray, R. L. Farrow, J. L. Durant, and L. R. Thorne, "The electric dipole moment of NO $A\,^2\Sigma^+$ $v' = 0$ measured using Stark quantum-beat spectroscopy," *J. Chem. Phys.*, vol. 99, p. 4327, 1993.

[157] T. B. Settersten, B. D. Patterson, and W. H. Humphries, "Radiative lifetimes of NO $A\,^2\Sigma^+$ ($v' = 0$, 1, 2) and the electronic transition moment of the $A\,^2\Sigma^+$-$X^2\Pi$ system," *J. Chem. Phys.*, vol. 131, 2009.

[158] J. M. Brown, J. T. Hougen, K. P. Huber, J. W. Johns, I. Kopp, H. Lefebvre-Brion, A. J. Merer, D. A. Ramsay, J. Rostas, and R. N. Zare, "The labeling of parity doublet levels in linear molecules," *J. Mol. Spectrosc*, vol. 55, p. 500, 1975.

[159] M. Sharma, J. M. Austin, N. G. Glumac, and L. Massa, "NO and OH spectroscopic vibrational temperature measurements in a postshock relaxation region," *AIAA Journal*, vol. 48, p. 1434, 2010.

[160] M. H. Rayment and S. D. Hogan, "Electrostatic trapping vibrationally excited Rydberg NO molecules," *Mol. Phys.*, vol. 121, p. e2160846, 2023.

[161] R. Patel, *Spectroscopy and dynamics of Rydberg states of NO in static and ramped electric fields*. PhD thesis, University College London, 2007.

[162] F. Merkt and T. P. Softley, "Rotational line intensities in zero kinetic energy photoelectron spectroscopy (ZEKE-PES)," *Int. Rev. Phys. Chem.*, vol. 12, p. 205, 1993.

[163] S. N. Dixit, D. L. Lynch, V. McKoy, and W. M. Huo, "Rotational branching ratios in (1+1) resonant-enhanced multiphoton ionization of NO via the $A\,^2\Sigma^+$ state," *Phy. Rev. A*, vol. 32, p. 1267, 1985.

[164] H. Rudolph, S. N. Dixit, V. McKoy, and W. M. Huo, "(1+1) resonant enhanced multiphoton ionization via the $A\,^2\Sigma^+$ state of NO: Ionic rotational branching ratios and their intensity dependence," *J. Chem. Phys.*, vol. 88, p. 1516, 1988.

[165] C. Seiler, J. A. Agner, P. Pillet, and F. Merkt, "Radiative and collisional processes in translationally cold samples of hydrogen Rydberg atoms studied in an electrostatic trap," *J. Phys. B*, vol. 49, p. 094006, 2016.

[166] A. Fujii and N. Morita, "Rotational state dependence of decay dynamics in the superexcited 7f Rydberg state ($v = 1$) of NO," *J. Chem. Phys.*, vol. 97, p. 327, 1992.

[167] R. S. Minns, D. T. Lazenby, F. H. Hall, N. J. Jones, R. Patel, and H. H. Fielding, "A spectroscopic investigation of the ionisation and dissociation decay dynamics of Rydberg states of NO," *Mol. Phys.*, vol. 112, p. 1808, 2014.

[168] J. Jiang, T. J. Barnum, S. L. Coy, and R. W. Field, "Analysis of vibrational autoionization of CaF Rydberg states," *J. Chem. Phys.*, vol. 150, p. 154305, 2019.

[169] M. H. Rayment and S. D. Hogan, "Effects of rotational excitation on decay rates of long-lived Rydberg states in NO," *J. Chem. Phys.*, vol. 159, p. 164309, 2023.

[170] C.-H. Kuo, C. Beggs, P. Kemper, M. Bowers, D. Leahy, and R. Zare, "Experimental measurement of the radiative lifetime of NO^+ ($X\,^1\Sigma^+$, $v = 1$, 2 and 3)," *Chem. Phys. Lett.*, vol. 163, p. 291, 1989.

[171] L. G. Christophorou and R. J. Van Brunt, "SF_6/N_2 Mixtures: Basic and HV Insulation Properties," *IEEE Trans. Dielectr. Electr. Insul.*, vol. 2, p. 952, 1995.

[172] T. A. Paul, M. Porus, B. Galletti, and A. Kramer, "SF_6 concentration sensor for gas-insulated electrical switchgear," *Sens. Actuators A: Phys.*, vol. 206, p. 51, 2014.

[173] C. Köhn, S. Dujko, O. Chanrion, and T. Neubert, "Streamer propagation in the atmosphere of Titan and other N_2:CH_4 mixtures compared to N_2:O_2 mixtures," *Icarus*, vol. 333, pp. 294–305, 2019.

[174] E. E. Ferguson and W. F. Libby, "Mechanism for the fixation of nitrogen by lightning," *Nature*, vol. 229, p. 37, 1971.

[175] K. Kirby, E. R. Constantinides, S. Babeu, M. Oppenheimer, and G. A. Victor, "Photoionization and photoabsorption cross sections of He, O, N_2 and O_2 for aeronomic calculations," *At. Data Nucl. Data Tables*, vol. 23, p. 63, 1979.

[176] D. Strobel, C. Opal, and R. Meier, "Photoionization rates in the night-time E- and F-region ionosphere," *Planet. Space Sci.*, vol. 28, p. 1027, 11 1980.

[177] P. D. Feldman, D. J. Sahnow, J. W. Kruk, E. M. Murphy, and H. W. Moos, "High-resolution FUV spectroscopy of the terrestrial day airglow with the Far Ultraviolet Spectroscopic Explorer," *J. Geophys. Res. Space Phys.*, vol. 106, p. 8119, 2001.

[178] A. W. Kam and F. M. Pipkin, "Measurement of the lifetime of the metastable $a''\,^1\Sigma_g^+$ state of N_2," *Phys. Rev. A*, vol. 43, p. 3279, 1991.

[179] E. J. Salumbides, A. Khramov, and W. Ubachs, "High-Resolution 2 + 1 REMPI Study of the $a''\,^1\Sigma_g^+$ State in N_2," *J. Phys. Chem. A*, vol. 113, p. 2383, 2009.

[180] C. Seiler, *Rydberg-Stark deceleration and trapping of atoms and molecules*. PhD thesis, ETH Zürich, 2013.

[181] F. Munkes, H. Kübler, and T. Pfau, "Private communication." 2023.

[182] P. Erman, A. Karawajczyk, E. Rachlew-Källne, C. Strömholm, J. Larsson, A. Persson, and R. Zerne, "Direct determination of the ionization potential of CO by resonantly enhanced multiphoton ionization mass spectroscopy," *Chem. Phys. Lett.*, vol. 215, p. 173, 1993.

[183] L. R. Ventura, R. S. da Silva, M. Y. Ballester, and C. E. Fellows, "Revisiting $^{12}C^{16}O^+$ first negative system: An experimental and theoretical study," *J. Quant. Spectrosc. Radiat. Transf.*, vol. 256, p. 107312, 2020.

[184] S. Mackenzie, E. Halse, E. Gordon, D. Rolland, and T. Softley, "Pulsed-field ionization spectroscopy of CO via the $E\,^1\Pi$ state and NO via the $B\,^2\Pi$ state," *Chem. Phys.*, vol. 209, p. 127, 1996.

[185] P. A. Martin and M. Fehér, "CASSCF calculations of the multipole moments and dipole polarisability functions of the $X\,^2\Sigma+$ and $A\,^2\Pi$ states of CO^+," *Chem. Phys. Lett.*, vol. 232, p. 491, 1995.

[186] J. Berkowitz and B. Ruscic, "Electric field effects in the photoionization of N_2 near threshold," *J. Chem. Phys.*, vol. 93, p. 1741, 1990.

[187] P. Aggarwal, H. L. Bethlem, A. Borschevsky, M. Denis, K. Esajas, P. A. Haase, Y. Hao, S. Hoekstra, K. Jungmann, T. B. Meijknecht, M. C. Mooij, R. G. Timmermans, W. Ubachs, L. Willmann, and A. Zapara, "Measuring the electric dipole moment of the electron in BaF," *Eur. Phys. J. D*, vol. 72, p. 197, 2018.

“So long, and thanks for all the fish”

Douglas Adams